Parametric numerical study on two-way bending capacity of unreinforced masonry walls Evaluation of the influence of geometric parameters to improve analytical formulations

Chang, L.

DOI
10.4233/uuid:1a99cc80-3fea-4ed3-894f-bf3afeca6745

Publication date
2022

Document Version
Final published version

Citation (APA)
Chang, L. (2022). *Parametric numerical study on two-way bending capacity of unreinforced masonry walls: Evaluation of the influence of geometric parameters to improve analytical formulations*. [Dissertation (TU Delft), Delft University of Technology]. https://doi.org/10.4233/uuid:1a99cc80-3fea-4ed3-894f-bf3afeca6745

PARAMETRIC NUMERICAL STUDY ON TWO-WAY BENDING CAPACITY OF UNREINFORCED MASONRY WALLS

EVALUATION OF THE INFLUENCE OF GEOMETRIC PARAMETERS TO IMPROVE ANALYTICAL FORMULATIONS

PARAMETRIC NUMERICAL STUDY ON TWO-WAY BENDING CAPACITY OF UNREINFORCED MASONRY WALLS

EVALUATION OF THE INFLUENCE OF GEOMETRIC PARAMETERS TO IMPROVE ANALYTICAL FORMULATIONS

Dissertation

for the purpose of obtaining the degree of doctor
at Delft University of Technology,
by the authority of the Rector Magnificus Prof. dr. ir. T. H. J. J. van der Hagen,
chair of the Board for Doctorates,
to be defended publicly on
Monday 26 September 2022 at 17:30 o'clock

by

Langzi CHANG
Master of Engineering in Civil Engineering
Harbin Institute of Technology, China
born in Boli, China

This dissertation has been approved by the promotors.

Composition of the doctoral committee:

Rector Magnificus	chairperson
Prof. dr. ir. J.G. Rots	Delft University of Technology, promotor
Dr. R. Esposito	Delft University of Technology, copromotor

Independent members:

Prof. dr. D. D'Ayala	University College London, UK
Prof. dr. A. Scarpas	Delft University of Technology
Prof. ir. S. N. M. Wijte	Eindhoven University of Technology
Assoc. Prof. dr. G. Castellazzi	University of Bologna, Italy
Assoc. Prof. dr. D. V. Oliveira	University of Minho, Portugal

Reserve member:

Prof. dr. M. Veljkovic	Delft University of Technology

Keywords:	Unreinforced masonry, Out-of-plane, two-way bending, Geometric parameters, 3D simplified brick-to-brick modelling, Analytical formulation
Printed by:	Ipskamp Printing, The Netherlands
Cover design:	Langzi Chang

ISBN 978-94-6384-374-4

An electronic version of this dissertation is available at

http://repository.tudelft.nl/

Philosophers have only interpreted the world
in various ways;
the point is to alter it.

Karl Marx

To my beloved homeland

Summary

Investigations on unreinforced masonry (URM) walls subjected to natural hazards, such as earthquakes and wind loads, identify the out-of-plane (OOP) failure as one of the most common failure mechanisms. Concerning the OOP failure, two types of failure mechanisms can be distinguished in URM walls: one-way bending in which lateral edges of walls are not supported; two-way bending in which at least one lateral edge of walls is supported in addition to the supports at the top and bottom. Compared with walls in one-way bending, walls in two-way bending are more widely encountered in practice considering that the lateral edges of walls are usually connected with pillars or return walls. Therefore, the failure of URM walls in OOP two-way bending can be more common. Even so, research on the geometric parameters that can have a major influence on the two-way bending capacity of URM walls, such as the aspect ratio, pre-compression and opening, is quite scarce. Due to a lack of experimental evidence and systematic numerical study, the current analytical formulations, namely the Yield Line Method (YLM) incorporated in the European Standard Eurocode 6, and the Virtual Work Method (VWM) incorporated in the Australian Standard AS3700 and Dutch Practical Guideline NEN-NPR 9998, assessing these geometric parameters can be limited in accuracy and application range.

This thesis aims at improving the analytical formulations assessing the influence of geometric parameters on the two-way bending capacity of URM walls. As a starting point, the accuracy and application range of the current analytical formulations are assessed and geometric parameters having a crucial influence on the two-way bending capacity are revealed (Chapter 2). A dataset of 46 testing specimens from 8 international testing campaigns is created and used for the assessment. The analytical formulations based on the VWM are found to return the most accurate predictions for the testing specimens. Even so, drawbacks and limitations are identified for the VWM. Besides, the pre-compression, wall aspect ratio and openings are identified to have a crucial influence on the two-way bending capacity of URM walls.

To perform for the first time a systematic study on the influence of the crucial geometric parameters, a 3D simplified brick-to-brick modelling approach was adopted. With this approach, the mortar joints including their connecting areas with the bricks are simplified as zero-thickness interfaces, while the bricks are extended in dimensions to account for the thickness of the mortar joints. The selection was made in comparison with other modelling strategies, namely the 3D detailed brick-to-brick and continuum modelling approaches. The model was further calibrated

and validated against quasi-static monotonic tests (Chapter 3). The numerical study focuses on strong brick-weak mortar masonry and walls with four-sided restrain. A good agreement is found between the numerical and experimental results in terms of the two-way bending capacity, initial stiffness and crack pattern. The two-way bending capacity of URM walls was found to be linearly dependent on the pre-compression and exponentially dependent on the wall aspect ratio. Besides, their influence is interdependent (Chapter4). Regarding the openings, the influence of their size, shape (aspect ratio of windows or doors) and location are investigated (Chapter 5). It is found that the arrangement of the opening area can significantly affect the two-way bending capacity of walls (defined as the peak pressure on the wall net area): when the opening area is non-covered and non-loaded, the two-way bending capacity of the perforated wall is higher than that of its solid counterpart; when the opening area is covered with timber or glass plates and loaded as the rest of the wall, the two-way bending capacity of the perforated wall is lower than that of the corresponding solid wall. In the case of non-covered and non-loaded openings, the numerical parametric study shows that the two-way bending capacity increases as the opening size or its aspect ratio increases, but it is insensitive to the opening position.

Eventually, improvements to the analytical formulation based on the VWM are proposed based on the outcomes of the numerical parametric analysis (Chapter 6). The quantified relationships between the pre-compression, wall aspect ratio, openings features and two-way bending capacity are incorporated within the updated VWM formulation proposed by Willis. The improved formulation provides higher accuracy in the prediction of the two-way bending capacity for the dataset collected in Chapter 2.

In summary, this study systematically explores and quantifies the relationships between the geometric parameters and the two-way bending capacity of URM walls by employing a reliable 3D simplified brick-to-brick modelling approach. The numerical results further contribute to the improvement of the current analytical formulations assessing the two-way bending capacity of URM walls.

Samenvatting

Uit onderzoek naar ongewapend metselwerk (URM) muren die worden blootgesteld aan natuurrampen, zoals aardbevingen en windbelastingen, blijkt dat out-of-plane (OOP) falen een van de meest voorkomende faalmechanismen is. Wat het OOP-falen betreft, kunnen twee soorten faalmechanismen in URM-wanden worden onderscheiden: eenrichtingsbuiging waarbij de laterale randen van de wanden niet worden ondersteund; tweerichtingsbuiging waarbij ten minste één laterale rand van de wanden wordt ondersteund naast de steunen aan de boven- en onderkant. Vergeleken met muren die in één richting buigen, worden muren die in twee richtingen buigen in de praktijk vaker aangetroffen, aangezien de laterale randen van muren gewoonlijk zijn verbonden met pijlers of keermuren. Daarom kan het falen van URM-wanden in OOP in twee richtingen vaker voorkomen. Desondanks is het onderzoek naar de geometrische parameters die een grote invloed kunnen hebben op de tweewegbuigcapaciteit van URM-wanden, zoals de hoogte-breedteverhouding, de voordruk uit bovenbelasting en de opening, vrij schaars. Door een gebrek aan experimenteel bewijs en systematische numerieke studie, kunnen de huidige analytische formuleringen, namelijk de Yield Line Method (YLM) opgenomen in de Eurocode 6, en de Virtual Work Method (VWM) opgenomen in de Australische Standaard AS3700 en de Nederlandse Praktijkrichtlijn NEN-NPR 9998, die deze geometrische parameters beoordelen, beperkt zijn in nauwkeurigheid en toepassingsgebied.

Deze dissertatie heeft tot doel de analytische formuleringen te verbeteren die de invloed van geometrische parameters op de tweezijdige buigcapaciteit van URM wanden beoordelen. Eerst worden de nauwkeurigheid en het toepassingsgebied van de huidige analytische formuleringen beoordeeld en worden geometrische parameters die een cruciale invloed hebben op de tweezijdige buigcapaciteit onthuld (Hoofdstuk 2). Een dataset van 46 proefstukken van 8 internationale testcampagnes wordt samengesteld en gebruikt voor de beoordeling. De analytische formules gebaseerd op de VWM blijken de meest accurate voorspellingen te geven voor de geteste proefstukken. Desondanks worden nadelen en beperkingen voor de VWM vastgesteld. Bovendien blijken de voordruk, de hoogte-breedteverhouding van de wand en de openingen een cruciale invloed te hebben op de tweezijdige buigcapaciteit van URM-wanden.

Om voor het eerst een systematische studie van de invloed van de cruciale geometrische parameters uit te voeren, werd gekozen voor een 3D vereenvoudigde benadering van het modelleren van baksteen tot baksteen. Bij deze benadering worden de mortelvoegen met inbegrip van hun verbindingszones met de bakstenen

vereenvoudigd als interfaces met een dikte van nul, terwijl de bakstenen worden uitgebreid in afmetingen om rekening te houden met de dikte van de mortelvoegen. De keuze werd gemaakt in vergelijking met andere modelstrategieën, namelijk de 3D gedetailleerde benadering van baksteen tot baksteen en continuüm modellering. Het model werd verder gekalibreerd en gevalideerd aan de hand van quasi-statische monotone proeven (hoofdstuk 3). Er is een goede overeenkomst gevonden tussen de numerieke en experimentele resultaten voor wat betreft de twee-weg buigcapaciteit, initiële stijfheid en scheurpatroon. De twee-weg buigcapaciteit van URM wanden bleek lineair afhankelijk te zijn van de voordruk en exponentieel afhankelijk van de wand-aspect-verhouding. Bovendien is hun invloed onderling afhankelijk (hoofdstuk 4). Wat betreft de openingen, is de invloed van hun grootte, vorm (aspectverhouding van ramen of deuren) en locatie onderzocht (Hoofdstuk 5). Gebleken is dat de plaatsing van de opening van grote invloed kan zijn op de buigcapaciteit van de wanden in twee richtingen (gedefinieerd als de piekdruk op het netto wandoppervlak): wanneer de opening niet bedekt en niet belast is, is de buigcapaciteit van de geperforeerde wand hoger dan die van zijn massieve tegenhanger; wanneer de opening bedekt is met hout of glasplaten en belast is als de rest van de wand, is de buigcapaciteit van de geperforeerde wand in twee richtingen lager dan die van de overeenkomstige massieve wand. In het geval van niet-overdekte en niet-belaste openingen blijkt uit de numerieke parametrische studie dat de buigcapaciteit in twee richtingen toeneemt naarmate de grootte van de opening of de hoogte-breedteverhouding toeneemt, maar dat deze ongevoelig is voor de positie van de opening.

Uiteindelijk worden op basis van de uitkomsten van de numerieke parametrische analyse verbeteringen aan de analytische formulering op basis van de VWM voorgesteld (hoofdstuk 6). De gekwantificeerde relaties tussen de voordruk, de wand hoogte-breedteverhouding, de openingskenmerken en de buigcapaciteit in twee richtingen zijn verwerkt in de door Willis voorgestelde bijgewerkte VWM-formulering. De verbeterde formulering geeft een hogere nauwkeurigheid in de voorspelling van de twee-weg buigcapaciteit voor de dataset verzameld in Hoofdstuk 2.

Samenvattend, deze studie onderzoekt en kwantificeert systematisch de relaties tussen de geometrische parameters en de twee-weg buigcapaciteit van URM wanden door gebruik te maken van een betrouwbare 3D vereenvoudigde baksteen-tot-baksteen modelbenadering. De numerieke resultaten dragen verder bij aan de verbetering van de huidige analytische formuleringen voor de beoordeling van de twee-weg buigcapaciteit van URM wanden.

Nomenclature

The frequently used symbols in this thesis are listed as follows.

Latin Symbols

c	Cohesion of interface elements
c_0	Initial cohesion of interface elements
E_b	Elastic modulus of brick units
f_{bt}	Tensile strength of bricks
f_c	Compressive strength of interface elements
f_t	Tensile strength of interface elements
f_{x1}	Flexural strength of masonry having failure plane parallel to bed joints
f_{x2}	Flexural strength of masonry having failure plane perpendicular to bed joints
G	Assumed slope of the crack line (AS3700)
G_f^I	Mode-I fracture energy of interface elements
G_f^{II}	Mode-II fracture energy of interface elements
$G^I_{f,b}$	Mode-I fracture energy of bricks
H_0	Opening height
h_{cr}	Crack band-width
H_d	Design height of the wall
h_u	Brick height
H_w	Wall height
k_1, k_2	Coefficients to assess the two-way bending capacity in AS3700
k_b	A constant used for calculating the diagonal bending moment capacity accordingly to Willis (2004)

k_{nn}, k_{ss}, k_{tt}	Normal and shear stiffness values of surface interface elements
k_p	Prepend spacing factor
L_0	Opening length
L_d	Design length of the wall
l_u	Brick length
L_w	Wall length
M_d	Diagonal bending moment capacity
M_h	Horizontal bending moment capacity
R_f	Restraint factor concerning the vertical boundaries
s_p	Minimum overlap of the brick units in successive courses
t_j	Mortar joint thickness
t_u	Brick thickness
t_w	Wall thickness
u	Normal relative displacement of interface elements
v_s (v_t)	Shear relative displacement
w	Two-way bending capacity of URM walls
w_p	Two-way bending capacity of perforated URM walls
w_s	Two-way bending capacity of solid URM walls
x	Absolute horizontal distance from the opening centroid to the left edge of the wall
x_0	Absolute distance between the central line of the wall and that of the opening
y	Absolute vertical distance from the opening centroid to the bottom edge of the wall
Z	Section modulus of the wall
Z_d	Section modulus of the bedded area
Z_p	Lateral section modulus based on the mortar contact area of the perpend joints
Z_t	Equivalent torsional section modulus
Z_u	Lateral section modulus of the bricks

Greek Symbols

α	Slope factor of the assumed diagonal cracks
α^*	Opening aspect ratio (opening height to length)
α_2	Bending moment coefficient in Eurocode 6
α_f	An aspect factor in AS3700
γ	Wall density
ε_1	Principle strain in the total strain crack model
η	Normalised opening length
κ	Wall aspect ratio
λ	Normalised position of the opening (Chapter 2)
λ_x	Normalised horizontal distance from the opening centroid to the left edge of the wall (Chapter 5)
λ_y	Normalised vertical distance from the opening centroid to the bottom edge of the wall (Chapter 5)
μ	Flexural strength ratio f_{x1}/f_{x2}
ν	Poisson's ratio of the masonry
ν_b	Poisson's ratio of bricks
σ	Normal stress of surface interface elements
σ_1	Maximum principle stress
σ_d	Vertical compressive stress at specific height of the wall
σ_v	Pre-compression at the top of a wall
τ_s, τ_t	Shear stress of surface interface elements
τ_u	Ultimate torsional shear strength of masonry
φ	Capacity reduction factor
φ	Friction angle
ϕ_0	Tangent of the assumed slope of the crack line G
ψ	Dilatancy angle of interface elements

Table of contents

Chapter 1

INTRODUCTION

1.1 Research background

Unreinforced masonry (URM) structure is one of the predominant structural types in many regions such as Europe, North America and Australia. URM walls, as the most important load-bearing components of buildings, are advantageous in carrying gravitational loads thanks to their high compressive strength. However, due to their low tensile strength, URM walls are susceptible to failure caused by horizontal loads such as wind and seismic loads. Subject to horizontal loads, URM walls can undergo two types of actions: in-plane shearing and out-of-plane (OOP) bending. The wall plane is parallel to the horizontal loads with the former, while it is perpendicular to the horizontal loads with the latter (Figure 1.1a). The in-plane failure of URM walls has been sufficiently studied in the past decades (Mojsilović, 2011; Malomo et al., 2018; Morandi et al., 2018; Malomo et al., 2019; Liu & Crewe, 2020; Messali et al., 2020; Malomo & DeJong, 2021; Pereira et al., 2021). By contrast, the available literature on OOP failure of URM walls is much less, though investigations of natural hazards report it to be more prevalent and catastrophic (D'Ayala & Paganoni, 2011; Moon et al., 2014; Penna et al., 2014; Walsh et al., 2015; Sorrentino et al., 2016; Padalu et al., 2020b) (Figure 1.1b-e).

Figure 1.1. (a) Load path in URM buildings subjected to horizontal loads; (b) and (c) OOP failure of URM walls in the 2011 Christchurch Earthquake (Walsh et al., 2015); (d) and (e) OOP failure of URM walls in 2015 Nepal Earthquake (Padalu et al., 2020b).

Subject to OOP bending, two modes can be distinguished for URM walls depending on the boundary conditions: one-way bending in which walls are supported at parallel edges or only at bottom edges; two-way bending in which at least one pair of adjacent edges are supported (Figure 1.2). In contrast with the research efforts put into one-way bending (Derakhshan et al., 2013b; Derakhshan et al., 2013a; Li et al., 2014; Abrams et al., 2017; Galvez et al., 2018; Tomassetti et al., 2018; Isfeld et al., 2021), the research of walls in two-way bending is still limited, even though these walls are more frequently encountered in practice considering that the lateral edges of walls are usually supported by pillars or return walls. In addition, the mechanical behaviour and capacity of URM walls in two-way bending are sensitive to geometric parameters or those related such as aspect ratio, pre-compression and opening (Damiola et al., 2018; Chang, Messali, et al., 2020). However, a lack of sufficient knowledge of their effects hinders the further understanding of the response of URM walls in OOP two-way bending. This raises doubts about the reliability of current analytical formulations assessing the two-way bending capacity (the peak pressure on the wall net area) of URM walls.

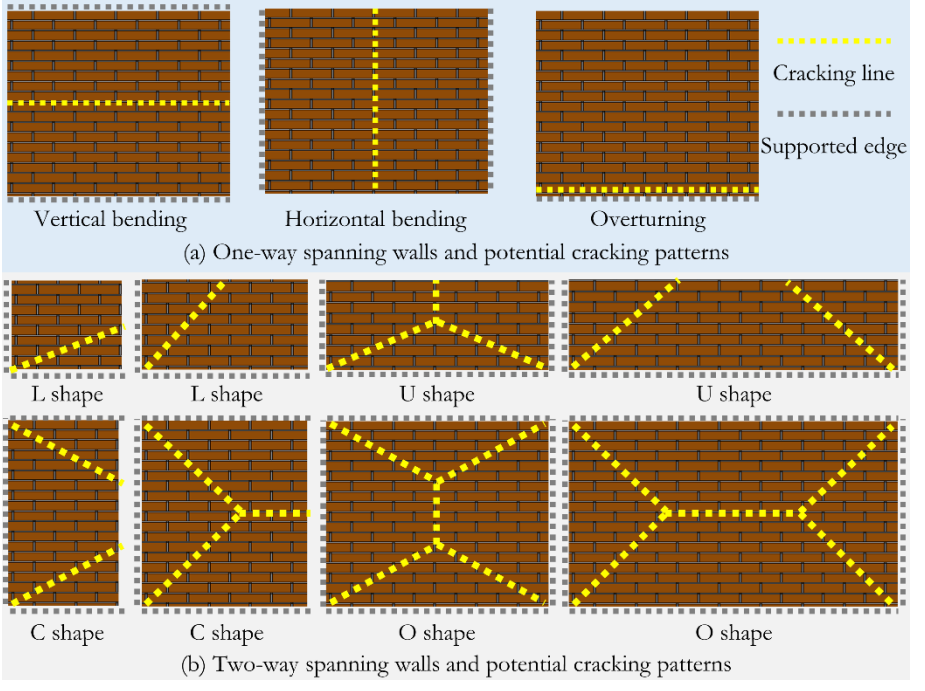

Figure 1.2 One-way and two-way spanning walls and potential cracking patterns (yellow line) considering different lateral constraints (grey line). Adapted from Vaculik (2012).

To improve the understanding of URM walls in OOP two-way bending, testing campaigns have been carried out worldwide. Chong (1993), van der Pluijm (1999b, 2001) and Derakhshan et al. (2018) performed monotonic pushover tests (Figure 1.3a) to determine the two-way bending capacity of URM walls. Besides, URM walls subjected to quasi-static cyclic OOP loading (Figure 1.3b) have been tested to

determine their post-peak behaviour and energy dissipation (Griffith & Vaculik, 2007; Ravenshorst & Messali, 2016; Damiola et al., 2017; Padalu et al., 2020b). Additionally, shake table tests (Figure 1.3c) have been conducted by Vaculik and Griffith (2017b) and Graziotti et al. (2019) to investigate the wall behaviour under dynamic loading. However, the experimental research is limited in quantity, even though a few testing campaigns have been used to evaluate the accuracy of the analytical formulations (Griffith & Vaculik, 2007; Derakhshan et al., 2018; Graziotti et al., 2019). Furthermore, systematic research regarding the influence of geometric parameters on the two-way bending capacity is scarce. Even if some cutting-edge research has attempted to study the influence of geometric parameters such as pre-compression and aspect ratio (Griffith & Vaculik, 2007), the number of testing samples in each comparable group is so small that the influence of these parameters could not be quantified. These research gaps pose limitations in establishing an experimental database that is beneficial to developing the current analytical formulations.

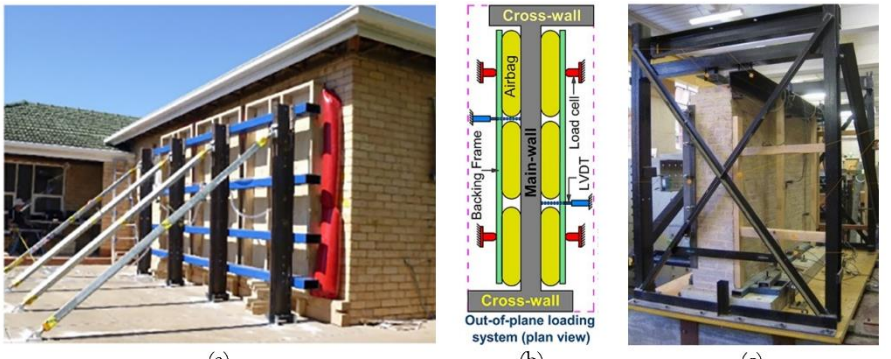

Figure 1.3. Experimental configurations of (a) monotonic pushover tests (Derakhshan et al., 2018); (b) quasi-static cyclic tests (Ravenshorst & Messali, 2016); (c) dynamic tests (Vaculik & Griffith, 2017b).

To transform the knowledge acquired from the experiments into practical assessing and designing methods, analytical formulations assessing the two-way bending capacity of URM walls need to be proposed for standards as guidance for practitioners. Currently, two analytical formulations, namely the Yield Line Method (YLM) incorporated in the Eurocode 6 (2012), and the Virtual Work Method (VWM) incorporated in the Australian Standard AS3700 (2018) and Dutch Practical Guideline NEN-NPR9998 (2018) provide evaluating approaches regarding the two-way bending capacity of URM walls. The former is based on the Yield Line Method (YLM), while the latter is based on the Virtual Work Method (VWM). Besides, suggestions on specific terms (such as the calculation of torsional shear strength) or updated versions have been proposed for these analytical formulations (Willis et al., 2006; Graziotti et al., 2019; Padalu et al., 2020a; Liberatore & AlShawa, 2021). However, there are continuous debates regarding the accuracy of the analytical formulations. These debates mainly originate from the basic assumptions

and empirical parts of the analytical formulations. Considering Eurocode 6 for example, the moment resistance along cracks on URM walls in OOP two-way bending is assumed to develop simultaneously and reach the same level, which is criticised for violating the anisotropic nature of masonry (Vaculik, 2012). Another example is that in AS3700 (whose analytical formulations regarding the two-way bending capacity have not been updated since the old version of 2001), the evaluation of the bending moment capacity is regressed based on a limited experimental database and is therefore empirical, which can result in high inaccuracy when assessing the two-way bending capacity of the walls (Willis, 2004). Apart from these, the analytical formulations can evaluate the influence of the geometric parameters on the two-way bending capacity inaccurately and within a limited application range. Some examples are the evaluation of the effect of pre-compression and opening by these analytical formulations (Chang, Messali, et al., 2020). For a detailed review of the analytical formulations, readers are referred to Chapter 2.

As an alternative to physical experiments, numerical models accounting for nonlinear physical and geometrical effects is more effective, cost-saving and time-efficient. Benefited by the material characterisation of existing masonry (van der Pluijm, 1999a; Jafari et al., 2019, 2020, 2022) and the development of computational capacity, three finite element modelling approaches, namely continuum modelling, detailed brick-to-brick modelling and simplified brick-to-brick modelling were developed to study the fracture process in URM structural components (D'Altri et al., 2019). With the continuum modelling, bricks and mortar joints are not distinguished, and the masonry structure is modelled as a continuum body (Figure 1.4a). With the detailed brick-to-brick modelling, both mortar joints, bricks and interfaces between them are modelled according to real dimensions (Figure 1.4b). With the simplified brick-to-brick modelling, cracks and frictional slip are assumed to mainly take place in mortar joints. Therefore, the mortar joints are modelled as zero-thickness interface elements, while the bricks are extended in dimensions and modelled as solid elements (Rots et al., 1997) (Figure 1.4c). The 3D version of the simplified brick-to-brick modelling is the most suitable for modelling URM structures at the level of components, because it requires less quantity of elements than the detailed brick-to-brick modelling, and is capable of capturing the cracking patterns accurately compared to the continuum modelling. Some studies have been conducted to predict the OOP two-way bending mechanism using the 3D simplified brick-to-brick modelling (Abdulla et al., 2017; D'Altri et al., 2018; D'Altri et al., 2019; Chang, Rots, et al., 2020). Results show that this modelling approach can accurately predict the two-way bending capacity and cracking patterns of URM walls. Nevertheless, the 3D simplified brick-to-brick has not been further applied to study the influence of geometric parameters on the two-way bending capacity of URM walls.

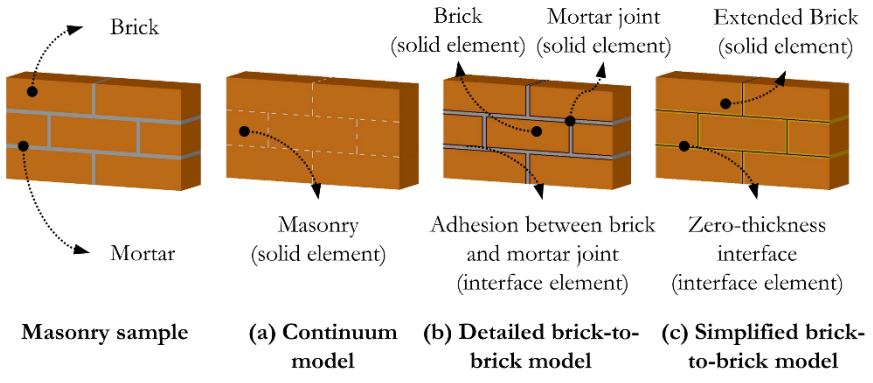

Figure 1.4. Schematic diagram of the modelling approaches for URM structures.

1.2 Research gaps and questions

Based on the previous discussions, research gaps are presented. The experimental study is scarce in terms of the influence of the geometric parameters, such as aspect ratio, pre-compression and opening on the two-way bending capacity of URM walls. Built upon the available experimental studies, the current analytical formulations can evaluate the influence of the geometric parameters inaccurately or within a limited application range. The 3D brick-to-brick simplified modelling technique is a promising tool to efficiently and effectively study this influence, but systematic research has not been carried out.

Corresponding to the research gaps, the main research question is proposed as,

- How to improve the analytical formulations assessing the influence of geometric parameters on the two-way bending capacity of URM walls?

Sub-questions are stated as,

- Sub-question 1: to what extent do the current analytical formulations assess the two-way bending capacity of URM walls inaccurately?
- Sub-question 2: how to establish reliable numerical models to predict the response of URM walls in OOP two-way bending?
- Sub-question 3: according to the predictions by the numerical models, how do the geometric parameters influence the response, such as the two-way bending capacity and crack pattern of URM walls?
- Sub-question 4: how to incorporate the quantitative relations between the geometric parameters and the two-way bending capacity from the numerical results to improve the current analytical formulations?

1.3 Research objectives, methodology and scope

To answer the above-mentioned questions, the following research objectives are identified:

- Creating an experimental database regarding the two-way bending capacity of URM walls. Evaluating the accuracy and application range of current major analytical formulations based on the database.
- Establishing reliable numerical models to predict the response of URM walls in OOP two-way bending.
- Perform numerical parametric studies to evaluate the influence of the geometric parameters, namely, aspect ratio, pre-compression and opening, on the response of URM walls in OOP two-way bending.
- Incorporating the quantitative relations between the geometric parameters and two-way bending capacity from the numerical study and proposing suggestions on improving the analytical formulations.

To predict the two-way bending capacity and capture the crack pattern of URM walls, a 3D simplified brick-to-brick modelling technique is employed to carry out Nonlinear Finite Element Analyses (NLFEA). With this modelling technique, the mortar joints are modelled as zero-thickness interface elements, while the bricks are extended in dimensions and modelled as solid elements. The NLFEA is carried out with the software package DIANA 10.4 (2019). The calibration and validation of the numerical models are based on the experimental study carried out by Griffith and Vaculik (2007). In their study, eight full-size URM walls were built to investigate the influence of wall aspect ratio, pre-compression and openings. Though the testing samples are limited in number, the experimental campaign is the most cutting-edge in studying the influence of the geometric parameters and providing relatively complete experimental data. Parametric studies are conducted to study the influence of the geometric parameters by varying their values in the numerical models. The results of the parametric studies are used to quantify this influence and further incorporated into the analytical formulations.

This research focuses on the influence of wall aspect ratio, pre-compression and openings on the two-way bending capacity of URM walls that are single-wythe and built with running bond. These parameters have been proved to have a prominent influence on the wall response. Other geometric parameters such as bond pattern and slenderness are not extensively investigated due to the time limit of the PhD study. The numerical study focuses on the strong brick-weak mortar masonry type. The loading condition in the numerical study is monotonic static because it is majorly considered in the assumptions of the analytical formulations. The analytical formulations that are primarily compared and improved are the Virtual Work Method-based ones in the Australian Standard AS3700. This is because the fundamental assumptions of the Virtual Work Method are more rational than the others (Vaculik, 2012).

1.4 Thesis outline

This thesis consists of 7 chapters. The chapters are outlined as follows.

Chapter 2 evaluates the accuracy and application range of current major analytical formulations assessing the two-way bending capacity of URM walls. A database of available testing campaigns is created. The accuracy of the analytical formulations is evaluated based on the database. Sensitivity studies are carried out to reveal how the analytical formulations assess the influence of the geometric parameters on the two-way bending capacity.

Chapter 3 introduces the numerical modelling approaches. The 3D brick-to-brick modelling approach is discussed. Numerical models are calibrated and validated on available testing campaigns. In addition, a sensitivity study is carried out to verify the influence of input parameters on the numerical models.

Chapter 4 investigates the influence of the aspect ratio and pre-compression on the two-way bending capacity of URM walls through a parametric study using the validated numerical model. Based on the numerical results, regressed equations are proposed to quantitatively describe the influence of these geometric parameters on the two-way bending capacity.

Chapter 5 explores the influence of openings on the two-way bending capacity of URM walls. A brief review of the available experimental database regarding the perforated URM walls is conducted. The influence of the arrangements of the opening area is studied by applying the Yield Line Method and numerical modelling. A parametric study is carried out to investigate the influence of the geometric parameters of openings, namely, size, shape and position, on the mechanical behaviour of URM walls in OOP two-way bending. By regressing the numerical results, equations are proposed to quantitatively describe the influence of openings on the two-way bending capacity.

Chapter 6 proposes improvements to the current analytical formulations. The numerical results in Chapter 4 and 5 are incorporated to predict the two-way bending capacity more accurately and in a wider application range compared to the original formulations.

Chapter 7 presents the concluding remarks of the thesis and suggestions for future research.

The graphical outline of the thesis corresponding to the research questions is shown in Figure 1.5.

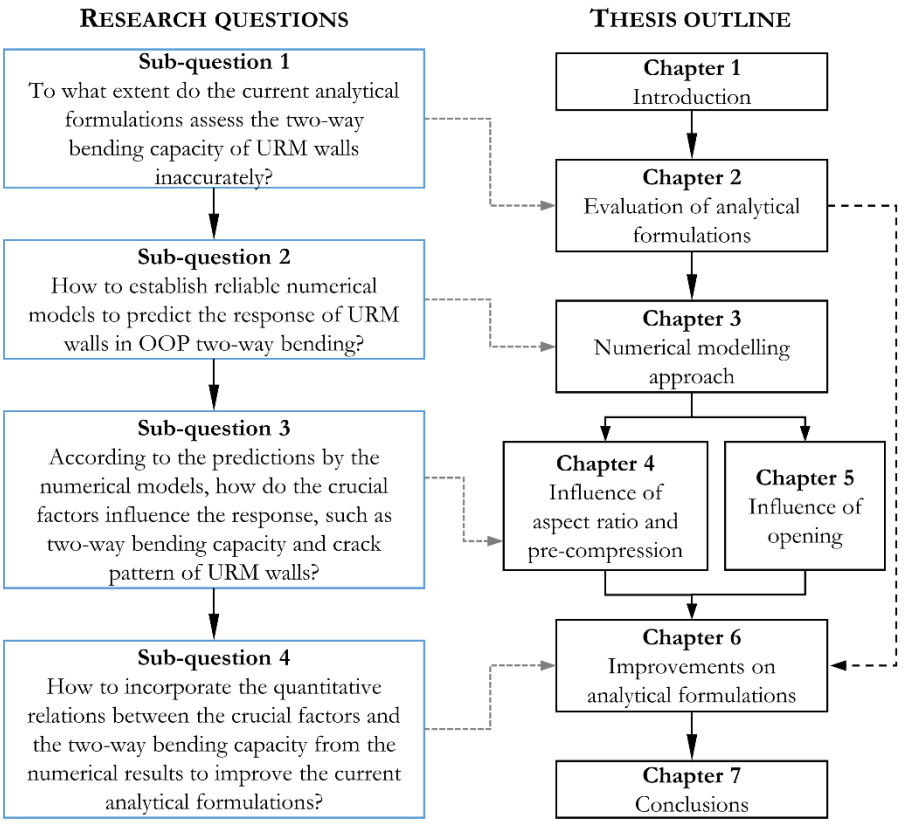

Figure 1.5. Thesis outline corresponding to the research questions.

Chapter 2

TWO-WAY BENDING CAPACITY OF UNREINFORCED MASONRY WALLS: A REVIEW OF ANALYTICAL FORMULATIONS[1]

Investigations of post-seismic events show that the collapse of walls in out-of-plane (OOP) two-way bending can be one of the most predominant failure mechanisms for unreinforced masonry (URM) structures. To assess the force capacity of URM walls in OOP two-way bending, various analytical formulations have been developed during the past decades. However, the accuracy and application range of these analytical formulations have been evaluated against only a limited number of experiments. This chapter aims at assessing the accuracy and the application range of the current analytical formulations that evaluate the two-way bending capacity of unreinforced masonry walls. In particular, the Yield Line Method, adopted by Eurocode 6, and the Virtual Work Method, adopted by Australian Standard AS3700 and modifications by the other two research groups, are compared. A dataset of 46 testing specimens from 8 international testing campaigns was created and used to evaluate current analytical formulations. A general comparison shows that within the listed dataset, the formulations based on the Virtual Work Method returned the most accurate predictions, especially for partially clamped walls and walls with openings. Testing specimens were divided into groups to study the influence of crucial factors, such as material properties, boundary conditions, pre-compression, aspect ratio and openings. However, only in a few cases, clear trends were identified from the testing data. Sensitivity studies were carried out to reveal how the analytical formulations assess the influence of crucial factors on the two-way bending capacity of the walls. Results expose the drawbacks and limitations of the considered analytical formulations. Eventually, potential directions for improving the accuracy and the application range of the analytical formulations are pointed out. The geometric parameters identified to be influential will be investigated in the following numerical studies.

[1] This chapter is based on the published journal article: Chang, L.-Z., Messali, F., & Esposito, R. (2020). Capacity of unreinforced masonry walls in out-of-plane two-way bending: A review of analytical formulations. *Structures*, *28*, 2431-2447. Minor modifications have been made to suit the thesis.

2.1 Introduction

Research shows that the out-of-plane (OOP) failure of structural components can be one of the most predominant failure mechanisms in unreinforced masonry (URM) buildings (D'Ayala & Paganoni, 2011; Moon et al., 2014; Penna et al., 2014; Sorrentino et al., 2016). Various analytical formulations have been developed during past decades to assess the two-way bending capacity of URM walls. Compared with one-way vertically spanning walls, for which analytical formulations have been well developed (Doherty et al., 2002; Derakhshan et al., 2013b; Derakhshan et al., 2014; Walsh et al., 2014), analytical formulations for URM walls in OOP two-way bending require further improvement in accuracy and extension for the application range.

To improve the understanding of URM walls in OOP two-way bending, testing campaigns have been carried out worldwide. Chong (1993), van der Pluijm (1999b, 2001) and Derakhshan et al. (2018) performed monotonic pushover tests to determine the two-way bending capacity of walls. Besides, walls subjected to quasi-static cyclic OOP loading have been tested to determine their post-peak behaviour and energy dissipation (Griffith et al., 2007; Ravenshorst & Messali, 2016; Damiola et al., 2017; Messali et al., 2017; Damiola et al., 2018; Padalu et al., 2020b). Shake table tests have also been conducted by Vaculik and Griffith (2017b) and Graziotti et al. (2019) to observe the wall behaviour under dynamic loading. Several testing campaigns have been used to evaluate the accuracy of the analytical formulations (Griffith & Vaculik, 2007; Derakhshan et al., 2018; Graziotti et al., 2019), even though each campaign has a limited number of testing samples. Furthermore, research on the crucial factors to which the two-way bending capacity of walls can be sensitive, such as boundary conditions, is limited to only a few testing samples. This poses limitations in validating and developing current analytical formulations.

Analytical formulations have been developed in past decades and incorporated into standards to assess the wall capacity in engineering practice. Current analytical formulations are mainly based on the Yield Line Method or the Virtual Work Method. The Yield Line Method by Haseltine, Tutt, et al. (1977), together with its variations, such as the Fracture Line Method by Sinha (1978) and Hendry et al. (2017), contributed to the method currently proposed in Eurocode 6 (2012). The core assumptions of the Yield Line Method are: the masonry is simplified as a homogeneous material; all cracks develop simultaneously; the two-way bending capacity is calculated from the equilibrium between the applied forces and the reaction forces along cracking lines. One drawback of the Yield Line Method is that some crucial factors such as bond patterns are neglected since masonry is considered a homogenous material. This can affect the crack pattern therefore possibly resulting in misevaluation. Another drawback of the Yield Line Method is that all cracks are assumed to develop concurrently, which can lead to inaccuracy for calculating the two-way bending capacity since contributions of all cracks are taken into account. However, some tests suggest that cracks develop in sequence and a central horizontal crack may not contribute to the two-way bending capacity (Griffith et al., 2007; Ravenshorst & Messali, 2016; Damiola et al., 2017). Apart

from the above-mentioned flaws, Eurocode 6, which is based on the Yield Line Method, defines the value of the coefficients needed in the formulations only for a limited number of cases presented in the informative Annex E. There, the boundary conditions of the walls are considered as either hinged or clamped (an intermediate status is not covered), and the openings are not taken into account.

Another category of analytical formulations originates from the Virtual Work Method. Lawrence and Marshall (2000) firstly applied the Virtual Work Method to evaluate the two-way bending capacity of URM walls, and later it was adopted by the Australian Standard AS3700 (2018), though the formulas for moment capacity are empirical and in some cases dimensionally inconsistent. Willis et al. (2006) refined the method by calculating bending moment capacity based on theoretical derivation rather than on empirical formulas as in AS3700. Graziotti et al. (2019) adopted the same theoretical framework as Willis et al. (2006) and experimentally evaluated the torsional strength to avoid the misleading influence of the flexural strength of masonry on the torsional strength. However, new theoretical formulations were not proposed. Furthermore, Derakhshan et al. (2018) modified the Virtual Work Method to include the effects of plaster. The core assumptions of the Virtual Work Method are: the contributions from horizontal cracks are neglected; diagonal cracks start right from the wall corners; the cracking pattern is assumed to follow the mortar joints and is determined by the aspect ratios of the units and the wall; horizontal and diagonal bending moment capacities are calculated independently; the virtual work done by external loads is equal to the strain energy along cracking lines in pre-assumed cracking patterns (Figure 2.1). Additionally, the Virtual Work Method provides coefficients and formulas to consider the presence of openings. However, some limitations still exist. One limitation is related to the restraint factor R_f which is used to evaluate the rotational stiffness of the vertical boundary conditions. Although some researchers including Griffith and Vaculik (2007), suggest that R_f can be taken as 0.5 for partially clamped walls (walls that are neither hinged nor clamped but have a finite rotational stiffness), such as walls with return walls, this cannot be generalised for other forms of boundary conditions. Moreover, the application range of AS3700 formulations is limited to single-wythe walls built in stretcher bond.

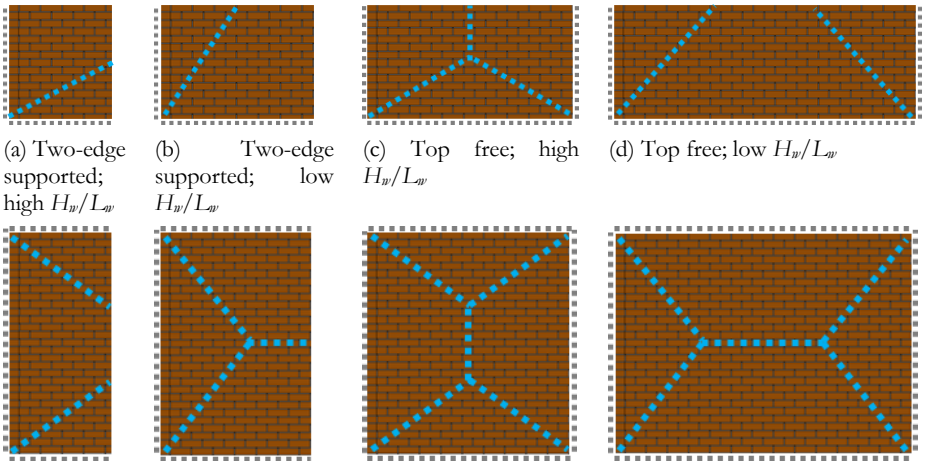

(a) Two-edge supported; high H_w/L_w (b) Two-edge supported; low H_w/L_w (c) Top free; high H_w/L_w (d) Top free; low H_w/L_w

(e) Side free; high H_w/L_w (f) Side free; low H_w/L_w (g) Four-edge supported; high H_w/L_w (h) Four-edge supported; low H_w/L_w

Figure 2.1. Classic pre-assumed cracking patterns used in formulations based on the Virtual Work Method (adapted from Derakhshan et al. (2018)).

The aforementioned formulations are all force-based methods. In recent years, displacement-based methods have also been developed. Vaculik and Griffith (2017a) proposed a displacement-based method to estimate the complete force-displacement relationship of walls. This displacement-based method neglects the contribution given by the flexural strength of masonry and is only suitable for application in the post-peak response of URM walls under two-way bending, which results in a substantial underestimation of the two-way bending capacity. Besides, the application of this formulation is currently limited to a few predefined failure mechanisms.

Based on the discussion above, it can be concluded that much progress has been made, but some drawbacks and limitations still lie within current analytical formulations. Consequently, it is worthy to evaluate the accuracy and application range of these formulations and identify directions to improve them. This chapter aims at evaluating the accuracy and application range of four force-based analytical formulations proposed by Eurocode 6 (EC6), Australian Standard (AS3700), Willis et al. (2006) (W2006) and Graziotti et al. (2019) (G2019). For this purpose, 46 testing specimens from 8 international testing campaigns on URM walls in OOP two-way bending were collected and categorised (Section 2.2); analytical predictions were compared with the testing results to evaluate the accuracy of the analytical formulations (Section 2.3); the testing specimens were divided into groups to assess the influence of crucial factors on the two-way bending capacity in tests; sensitivity studies were carried out to evaluate whether the influence of the crucial factors predicted by the analytical formulations matches with that revealed by the testing results (Section 2.4). Eventually, potential directions for improving the accuracy and application range of the analytical formulations are pointed out (Section 2.5).

2.2 Research methodology

2.2.1 Database of experimental benchmarks

A dataset of 46 testing specimens from 8 international testing campaigns in recent 30 years on URM walls in OOP two-way bending was created. Earlier testing campaigns were not included in this chapter due to the unavailability of the complete testing data. Table 2.1 lists the characteristics of all the selected testing specimens (Chong, 1993; van der Pluijm, 1999b, 2001; Griffith et al., 2007; Ravenshorst & Messali, 2016; Messali et al., 2017; Vaculik & Griffith, 2017b; Damiola et al., 2018; Derakhshan et al., 2018; Graziotti et al., 2019; Padalu et al., 2020b). The dataset consists of tests performed mostly on clay brick and calcium silicate (CS) brick masonry walls. 37 out of 46 testing specimens were subjected to quasi-static cyclic loading, while the others were to dynamic loading. Only 5 testing specimens were made in half-scale. Over half of the walls were supported on four edges, namely "O" shaped walls; 1/3 of the walls were unsupported at the top edge, i.e. "U" shaped walls; only 4 walls were unsupported on one vertical edge, i.e. "C" shaped walls. Vertical supports constructed with return walls to simulate partially clamped edges were in nearly half of the testing specimens. Only less than half of the walls were tested under pre-compression, even though in practice most walls are vertically load-bearing. Concerning aspect ratio, all walls were tested with a height-to-length ratio lower than unity ($H_w/L_w \leq 1$). Approximately 50% of the testing specimens had openings. In the majority of the cases, the walls were single-wythe and built with stretcher bond; only 2 walls were double-wythe and built with English bond.

Table 2.1. Dataset of URM walls in OOP two-way bending.

Testing campaign	Sample	Opening[1]	Bond. Cond.[2]	Unit type	Bond Patt.[3]	Geometry of						Wall density	Pre-compression	Material properties			Testing results
						Unit	Joint	Wall	Aspect ratio	Opening				Flexural/tensile strength (MPa) of			
														Masonry		Unit	
						$l_u \times h_u \times t_u$ (mm^3)	t_j (mm)	$L_w \times H_w \times t_w$ (mm^3)	H_w/L_w	$L0 \times H0$ (mm^2)	$x0$ (mm)	γ (kN/m^3)	σ_v (MPa)	f_{x1}	f_{x2}	f_{bt}	w (kPa)
Chong (1993), full scale quasi-static	SB01	No	U	clay	Stret.	215×65×102.5	14	5615×2475×102.5	0.44	-	-	15.15	0	0.47	1.67	3.82	2.80
	SB02	Yes(C)	U	clay	Stret.	215×65×102.5	14	5615×2475×102.5	0.44	2260×1125	0	15.15	0	0.47	1.67	3.82	2.40
	SB03	Yes(C)	U	clay	Stret.	215×65×102.5	14	5615×2475×102.5	0.44	2935×525	0	15.15	0	0.47	1.67	3.82	2.30
	SB04	Yes(C)	U	clay	Stret.	215×65×102.5	14	5615×2475×102.5	0.44	910×2025	0	15.15	0	0.47	1.67	3.82	2.20
	SB05	No	U	clay	Stret.	215×65×102.5	14	5615×2475×102.5	0.44	-	-	15.15	0	0.47	1.67	3.82	2.70
	SB06	No	O	clay	Stret.	215×65×102.5	14	2900×2450×102.5	0.84	-	-	15.15	0	0.47	1.67	3.82	7.50
	SB07	Yes(C)	O	clay	Stret.	215×65×102.5	14	2900×2450×102.5	0.84	900×900	0	15.15	0	0.47	1.67	3.82	5.50
	SB09	Yes(E)	U(re)	clay	Stret.	215×65×102.5	14	5615×2475×102.5	0.44	900×900	1458	15.15	0	0.47	1.67	3.82	2.40
	DC01	No	U	concrete	Stret.	440×215×100	14	5615×2475×100	0.44	-	-	19.61	0	1.37	1.68	1.20	2.65
	DC02	Yes(C)	U	concrete	Stret.	440×215×100	14	5615×2475×100	0.44	2260×1125	0	19.61	0	1.37	1.68	1.20	1.75
	DC02B	Yes(C)	U	concrete	Stret.	440×215×100	14	5615×2475×100	0.44	2260×1125	0	19.61	0	1.37	1.68	1.20	1.50
	HW01	No	C	clay	Stret.	215×65×102.5	10	2700×2475×102.5	0.92	-	-	28.84	0	0.77	4.12	13.09	3.70
	HW02	Yes(E)	C	clay	Stret.	215×65×102.5	10	2700×2475×102.5	0.92	460×535	110	28.84	0	0.77	4.12	13.09	2.80
	HW03	Yes(C)	C	clay	Stret.	215×65×102.5	10	2700×2475×102.5	0.92	460×1150	0	28.84	0	0.77	4.12	13.09	3.30
	HW04	Yes(C)	C	clay	Stret.	215×65×102.5	10	2700×2475×102.5	0.92	900×535	0	28.84	0	0.77	4.12	13.09	3.70

Table 2.1. Dataset of URM walls in OOP two-way bending.

Testing campaign	Sample	Opening[1]	Bond. Cond.[2]	Unit type	Bond Patt.[3]	Geometry of						Wall density	Pre-compression	Material properties			Testing results
						Unit	Joint	Wall	Aspect ratio	Opening				Flexural/tensile strength (MPa) of			
														Masonry		Unit	
						$l_u \times h_u \times t_u$ (mm³)	t_j (mm)	$L_w \times H_w \times t_w$ (mm³)	H_w/L_w	$L0 \times H0$ (mm²)	$x0$ (mm)	γ (kN/m³)	σ_v (MPa)	f_{x1}	f_{x2}	f_{bt}	w (kPa)
	W01	Yes(C)	U	clay	Stret.	215×65×102.5	10	5615×2475×102.5	0.44	340×235	0	28.84	0	0.77	4.12	13.09	2.30
van der Pluijm (1999, 2001), full scale quasi-static	Panel II	No	O	clay	Stret.	204×50×98	10	3949×1738×98	0.44	-	-	18.18	0	0.26	1.52	4.04	4.41
	CS-b panel	No	O	CS	Stret.	437×198×100	2	3960×1800×100	0.45	-	-	17.50	0	0.68	1.22	1.89	5.60
	CS-e panel	No	O	CS	Stret.	897×598×100	2	3960×1800×100	0.45	-	-	17.50	0	0.66	1.05	1.54	5.59
	sm-RIJ panel	No	O	clay	Stret.	206×50×96	2	3990×1800×96	0.45	-	-	11.55	0	1.03	1.77	2.70	5.52
Griffith et al. (2007), full scale quasi-static cyclic	Wall 1	No	O(re)	clay	Stret.	230×76×110	10	4080×2494×110	0.61	-	-	19.00	0.1	0.61	1.92	3.55	4.76
	Wall 2	No	O(re)	clay	Stret.	230×76×110	10	4080×2494×110	0.61	-	-	19.00	0	0.61	1.92	3.55	3.04
	Wall 3	Yes(E)	O(re)	clay	Stret.	230×76×110	10	4080×2494×110	0.61	1200×1000	780	19.00	0.1	0.61	1.92	3.55	5.05
	Wall 4	Yes(E)	O(re)	clay	Stret.	230×76×110	10	4080×2494×110	0.61	1200×1000	780	19.00	0.05	0.61	1.92	3.55	3.91
	Wall 5	Yes(E)	O(re)	clay	Stret.	230×76×110	10	4080×2494×110	0.61	1200×1000	780	19.00	0	0.61	1.92	3.55	3.59
	Wall 6	Yes(E)	U(re)	clay	Stret.	230×76×110	10	4080×2494×110	0.61	1200×946	780	19.00	0	0.61	1.92	3.55	1.97
	Wall 7	Yes(C)	O(re)	clay	Stret.	230×76×110	10	2520×2494×110	0.99	1200×946	0	19.00	0.1	0.61	1.92	3.55	8.71
	Wall 8	Yes(C)	O(re)	clay	Stret.	230×76×110	10	2520×2494×110	0.99	1200×946	0	19.00	0	0.61	1.92	3.55	8.52
	TUD_COMP-10	No	O	clay	Stret.	212×50×102	10	4000×2751×102	0.69	-	-	16.00	0.06	0.38	1.18	4.78	3.61
	TUD_COMP-11	No	O	CS	Stret.	212×71×102	10	3986×2765×102	0.69	-	-	17.50	0.06	0.26	0.55	2.74	2.45

Table 2.1. Dataset of URM walls in OOP two-way bending.

Testing campaign	Sample	Opening[1]	Bond. Cond.[2]	Unit type	Bond Patt.[3]	Geometry of						Wall density	Pre-compression	Material properties			Testing results
						Unit	Joint	Wall	Aspect ratio	Opening				Flexural/tensile strength (MPa) of			
														Masonry		Unit	
						$l_u \times h_u \times t_u$ (mm³)	t_j (mm)	$L_w \times H_w \times t_w$ (mm³)	H_w/L_w	$L0 \times H0$ (mm²)	$x0$ (mm)	γ (kN/m³)	σ_v (MPa)	f_{x1}	f_{x2}	f_{bt}	w (kPa)
Messali et al. (2017); Damiola et al. (2018), full scale quasi-static cyclic	TUD_COMP-12	Yes(E)	O	CS	Stret.	212×71×102	10	3986×2765×102	0.69	1776×1640	449	17.50	0.06	0.26	0.55	2.74	3.67
	TUD_COMP-26	No	O	clay	Stret.	210×50×100	10	3950×2710×100	0.69	-	-	16.50	0.06	0.16	0.65	6.31	3.37
	TUD_COMP-27	No	O	clay	Eng.	210×50×100	10	3840×2710×210	0.71	-	-	16.50	0.06	0.14	0.41	6.31	7.52
Vaculik et al. (2018), half scale dynamic	d1	No	O(re)	clay	Stret.	110×39×50	5	1840×1232×50	0.67	-	-	21.20	0.1	0.42	1.30	2.40	3.95
	d2	No	O(re)	clay	Stret.	110×39×50	5	1840×1232×50	0.67	-	-	21.20	0	0.42	1.30	2.40	2.47
	d3	Yes(E)	O(re)	clay	Stret.	110×39×50	5	1840×1232×50	0.67	575×528	317	21.20	0.1	0.42	1.30	2.40	2.67
	d4	Yes(E)	O(re)	clay	Stret.	110×39×50	5	1840×1232×50	0.67	575×528	317	21.20	0.05	0.42	1.30	2.40	2.65
	d5	Yes(E)	O(re)	clay	Stret.	110×39×50	5	1840×1232×50	0.67	575×528	317	21.20	0	0.42	1.30	2.40	1.61
Derakhshan et al. (2018), full scale quasi-static	A-3	No	O(re)	clay	Stret.	230×110×76	10	3020×2750×76	0.91	-	-	19.00	0.008	0.15	0.47	0.87	1.9
	B-3	No	O(re)	clay	Stret.	230×110×76	10	3260×2720×76	0.83	-	-	19.00	0.008	0.15	0.47	0.87	1.71
	B-5	No	O(re)	clay	Stret.	230×110×76	10	3040×2720×76	0.89	-	-	19.00	0.008	0.15	0.47	0.87	2.37
Graziotti et al. (2019), full scale dynamic	CS-005-RR	No	O(re)	CS	Stret.	212×71×102	10	3980×2750×102	0.69	-	-	18.05	0.05	0.95	1.29	2.61	3.70
	CS-000-RF	No	U(re)	CS	Stret.	212×71×102	10	3980×2750×102	0.69	-	-	18.05	0.00	0.95	1.29	2.61	2.65
	CSW-000-RF	Yes(E)	U(re)	CS	Stret.	212×71×102	10	3980×2750×102	0.69	1790×1630	445	18.05	0.00	0.95	1.29	2.61	2.34

Table 2.1. Dataset of URM walls in OOP two-way bending.

Testing campaign	Sample	Opening[1]	Bond. Cond.[2]	Unit type	Bond Patt.[3]	Geometry of						Wall density	Pre-compression	Material properties			Testing results
						Unit	Joint	Wall	Aspect ratio	Opening				Flexural/tensile strength (MPa) of			
														Masonry		Unit	
						$l_u \times h_u \times t_u$ (mm^3)	t_j (mm)	$L_w \times H_w \times t_w$ (mm^3)	H_w/L_w	$L0 \times H0$ (mm^2)	$x0$ (mm)	γ (kN/m^3)	σ_v (MPa)	f_{x1}	f_{x2}	f_{bt}	w (kPa)
	CL-000-RF	No	U(re)	clay	Stret.	208×50×98	10	4020×2760×98	0.69	-	-	19.63	0.00	0.41	1.98	7.83	3.30
Padalu et al. (2020),full scale quasi-static cyclic	URM-F	No	O(re)	clay	Eng.	229×72×109	10	3000×3000×229	1	-	-	19.00	0.125	0.45	0.46	2.60	19.26

[1] The presence of openings: Yes(C) and Yes(E) denote that the opening is centrically and eccentrically located, respectively.

[2] Boundary conditions: "U" shape: the top of the wall is free; "C" shape: one vertical edge of the wall is free; "O" shape: all edges of the wall are restrained; (re): the wall is restrained with return walls.

[3] Bond patterns: "Stret." and "Eng." refer to stretcher bond and English bond, respectively.

2.2.2 Current analytical formulations

Figure 2.2 shows the testing configuration with the adopted terminology used to describe the testing specimens. H_w and L_w are the height and the length of the wall, respectively; H_0 and L_0 are the height and the length of the opening, respectively; x_0 is the distance between the centre line of the opening and that of the wall; h_u, l_u and t_u are the height, the length and the thickness of masonry units, respectively; t_j is the thickness of the mortar joints. The red dotted lines denote presupposed diagonal cracking patterns in the Virtual Work Method.

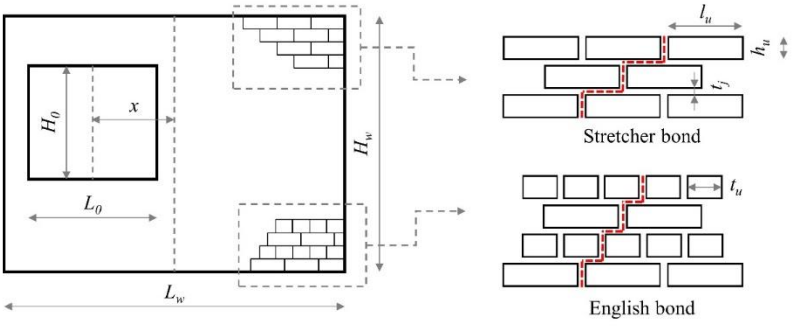

Figure 2.2. The testing configuration of the testing specimens.

Four groups of analytical formulations, namely Eurocode 6 (EC6), AS3700, Willis et al. (W2006) and Graziotti et al. (G2019) were compared to evaluate the two-way bending capacity of the above-mentioned testing specimens. The recently developed displacement-based seismic design method presented in Vaculik and Griffith (2017a) was not considered since it mainly focuses on the determination of the force-displacement relationship, and it neglects the contribution of the flexural strength of masonry. In this sense, it generally results in an over-conservative prediction of the two-way bending capacity.

EC6 evaluates the two-way bending capacity w of a wall by the following equation:

$$w = \frac{(f_{x1} + \sigma_d)Z}{\mu\alpha_2 {L_w}^2} \tag{2.1}$$

where the flexural strength ratio μ is defined as:

$$\mu = (f_{x1} + \sigma_d)/f_{x2} \tag{2.2}$$

with f_{x1} and f_{x2} being the flexural strength of masonry obtained for planes of failure parallel to and perpendicular to the bed joints, respectively; σ_d is the vertical compressive stress at a specific height of the wall caused by self-weight and pre-compression σ_v; Z is the section modulus of the wall; α_2 is the bending moment coefficient. In this work, the values of α_2, which are allowed to be obtained from a

suitable theory, were taken from the Annex E of EC6, where α_2 is provided as a dependent variable of μ, H_w/L_w and boundary conditions in tabular form.

The formulations AS3700, W2006 and G2019 assess the two-way bending capacity w of a wall by the following equation:

$$w = \frac{2\alpha_f}{{L_d}^2}(k_1 M_h + k_2 M_d) \tag{2.3}$$

with the components of Equation (2.3):

$$G = \frac{2(h_u + t_j)}{l_u + t_j} \tag{2.4}$$

$$\alpha = \frac{G L_d}{H_d} \tag{2.5}$$

where H_d and L_d are the design height and design length of the wall, respectively. If the top edge of the wall is unsupported, the design height is the height of the wall ($H_d = H_w$); otherwise, the design height is half of the height of the wall ($H_d = H_w/2$). If one of the vertical edges is unsupported, the design length is the length of the wall ($L_d = L_w$); otherwise, the design length is half of the length of the wall ($L_d = L_w/2$); if an opening is presented, L_d is the length of the longer panel beside the opening. G is the assumed slope of the crack line; α is the slope factor that identifies the expected cracking pattern including a vertical central crack in the case $\alpha < 1$, or a horizontal central crack in the case $\alpha \geq 1$; α_f, k_1 and k_2 are coefficients determined by the presence of the openings, the slope factor α and the number of supported vertical edges. Specifically, k_1 is additionally determined by the restraint factor of vertical boundaries of the wall, R_f, which ranges from 0 (hinged) to 1 (clamped); M_h and M_d are the horizontal and the diagonal bending moment capacity of masonry, respectively.

For the horizontal bending moment capacity (M_h) and diagonal bending moment capacity (M_d), AS3700 adopts the following equations:

$$M_h = the\ least\ of \begin{cases} 2\phi \cdot k_p\left(\sqrt{f_{x1}}\right)\left(1 + \dfrac{\sigma_d}{f_{x1}}\right) Z_d & \text{(stepped failure)} \\ 4\phi \cdot k_p\left(\sqrt{f_{x1}}\right) Z_d & \text{(stepped failure)} \\ \phi\left(0.44 f_{bt} Z_u + 0.56 f_{x1} Z_p\right) & \text{(line failure)} \end{cases} \tag{2.6}$$

$$M_d = \phi(2.25\sqrt{f_{x1}} + 0.15\sigma_d) Z_t \tag{2.7}$$

$$k_p = the\ least\ of \begin{cases} s_p/t_u \\ s_p/h_u \\ 1 \end{cases} \tag{2.8}$$

where ϕ is a capacity reduction factor; s_p is the minimum overlap of masonry units in successive courses; k_p is the perpend spacing factor, for stretcher bond, $k_p = 1$; Z_d, Z_u and Z_p are section modulus of bedded area, section modulus of masonry unit and section modulus of the perpend joints, respectively; Z_t is the equivalent

torsional section modulus. Besides, it is worth noting that M_h in stepped failure cases is dimensionally inconsistent. In this chapter, the capacity reduction factor is set to unity, because the mean value of material properties is considered for comparison with the testing data.

For W2006 and G2019, the following equations are applied to compute M_h and M_d:

$$M_h = lesser\ of \begin{cases} \frac{1}{2(h_u + t_j)}\left[(f_{bt} - \nu \cdot \sigma_d) h_u \cdot \frac{{t_u}^2}{6}\right] & \text{(line failure)} \\ \frac{1}{h_u + t_j}\left[\tau_u k_b \cdot 0.5(l_u + t_j){t_u}^2\right] & \text{(stepped failure)} \end{cases} \tag{2.9}$$

$$M_d = \frac{\sin\varphi_0}{h_u + t_j}\left[(\sin\varphi_0)^3\, \tau_u k_b + \frac{(\cos\varphi_0)^3\,(f_{x1} + \sigma_d)}{6}\right] \cdot 0.5\left(l_u + t_j\right){t_u}^2 \tag{2.10}$$

$$\varphi_0 = \tan^{-1} G \tag{2.11}$$

where ν is the Poisson's ratio of masonry; k_b equalling 0.213 is a coefficient for computing the torsional shear capacity of the bed joints (Willis et al., 2006); τ_u is the ultimate torsional shear strength of masonry in bed joints; φ_0 is tangent of the assumed slope of the crack line G.

For τ_u, W2006 adopts the following equation:

$$\tau_u = 0.9\sigma_d + 1.6 f_{x1} \tag{2.12}$$

while G2019 adopts the following equation:

$$\tau_u = \begin{cases} 1.14\sigma_d + 1.81 & \text{(for CS brick masonry)} \\ 1.55\sigma_d + 1.07 & \text{(for clay brick masonry)} \end{cases} \tag{2.13}$$

The only difference between G2019 and W2006 is the evaluating method on the torsional strength of the bed joints. The equation provided in G2019 was derived from a single testing campaign performing torsional strength tests on CS and clay brick masonry. Though in this chapter G2019 was attempted to be compared with other formulations, its application to other testing campaigns may have limitations and results should be interpreted with care.

Mean values of material properties were adopted in the analytical calculations. When the material properties were not provided in the companion tests, the following procedure was adopted: where f_{bt} was not available, it was taken as 1/10 of the compressive strength of brick f_b (NPR9998, 2018); where f_{x2} was not available, f_{x2} was calculated according to NEN (2018):

$$f_{x2} = lesser\ of \begin{cases} \frac{1}{9}(4\frac{f_{bt}}{f_{x1}} + 5) f_{x1} \\ \left(\frac{s_p}{t_u}\right)^2 \cdot \frac{2.75}{\sqrt{f_{x1}}} \cdot f_{x1} \end{cases} \tag{2.14}$$

Walls with openings are not covered in Annex E of EC6 (2012). For sake of simplicity, panels beside openings were considered independent walls with one vertical side unsupported. The two-way bending capacity was determined as the

minimum of the two-way bending capacity of the entire wall without the opening and that of the longer panel beside the opening. These two scenarios have also been considered in the calculations with the other formulations.

Since the English bond is not considered in AS3700, W2006 and G2019, Equation (2.4) is modified to account for the potential slope of the cracking line (Figure 2.2):

$$G = \frac{2(h_u + t_j)}{t_u + t_j} \tag{2.15}$$

2.3 Comparison of analytical formulations against the database

To compare the accuracy of the formulations, the tested two-way bending capacity from the dataset presented in Section 2.2.1 was predicted according to the equations described in Section 2.2.2. Lower and upper bounds for each testing specimen were calculated. The lower bound of the two-way bending capacity was estimated by considering the wall hinged on all sides in EC6 or assuming $R_f = 0$ in the other formulations; the upper bound of the two-way bending capacity was estimated by considering the wall clamped on all sides in EC6 or assuming $R_f = 1$ for the other formulations.

Table 2.2 lists the percentage of incorrect predictions for each analytical formulation. For each testing specimen, if the tested two-way bending capacity was not comprised between the upper and lower bounds, the analytical prediction was defined as incorrect. More specifically, if the lower bound was higher than the testing result, an incorrect overestimation was marked; if the upper bound was lower than the testing result, an incorrect underestimation was marked. The comparison shows that EC6 has an incorrect prediction rate of 58.7% with the highest overestimation rate of 47.8%. The proposed tactic to account for opening does not provide accurate results considering that EC6 provides more incorrect predictions for walls with openings compared with those without openings. W2006 and G2019 have incorrect prediction rates of 71.7% and 65.2%, respectively. Both these two formulations tend to underestimate the two-way bending capacity. AS3700 provides the lowest incorrect prediction rate of 56.6%. Also, the incorrect prediction rate on walls without openings of AS3700 is the lowest. Nevertheless, the accuracy of AS3700 requires further improvement considering 21.8% and 34.8% of testing specimens are overestimated and underestimated, respectively. The formulations based on the Virtual Work Method provide close incorrect prediction rates for walls with and without openings.

Table 2.2. Percentage of incorrect predictions for the considered dataset.

Analytical formulations		EC6	AS3700	W2006	G2019
Incorrect overestimation	With opening	34.8%	10.9%	2.2%	2.2%
	Without opening	13.0%	10.9%	0.0%	4.3%
Incorrect underestimation	With opening	2.2%	17.4%	39.1%	34.8%
	Without opening	8.7%	17.4%	30.4%	23.9%
Incorrect prediction		58.7%	56.6%	71.7%	65.2%

Considering that nearly half of the testing specimens were built with return walls, similar to constructions in practice, partially clamped conditions may be attained at the vertical supports. To examine the accuracy of the formulations considering the walls as partially clamped, the values of the lower and upper bounds were averaged in the case of EC6, whereas R_f equalling 0.5 was assumed for AS3700, W2006 and G2019. Here it is worthy to mention that R_f is essentially an indicator of not only the moment resistance contribution from vertical boundaries but also the overall crack propagation, as e.g. discussed in Sharma et al. (2020). Figure 2.3 shows the cumulative distribution function for the ratio of the predictions over the testing results. Provided that the ratio of a correct prediction over the testing result is 1 (marked with a black line in Figure 2.3), the probabilities of non-exceedance for the formulations from low to high are: 26% (EC6), 63% (AS3700), 78% (G2019) and 87% (W2006). This suggests that, when the walls are partially clamped, EC6 most possibly overestimates the two-way bending capacity, W2006 and G2019 tend to underestimate the two-way bending capacity, while AS3700 can provide the closest predictions.

Table 2.3 presents the average and the coefficient of variation (CV) of predictions on all testing specimens for each formulation considering the walls as partially clamped, where N(±20%) denotes the number of predictions that deviates from testing results no more than 20%. On average of all testing specimens, EC6 overestimates the two-way bending capacity up to 147%, which corresponds to previous observations. Both W2006 and G2019 underestimate the two-way bending capacity to 71% and 85% on average of all testing specimens, respectively; however, G2019 gives a higher N(±20%) value. AS3700 provides the closest prediction with an accuracy of 98% and the highest N(±20%) value. It can be concluded that within the listed dataset, AS3700 can be the most accurate of all analytical formulations evaluated in this chapter, especially for partially clamped walls or walls with openings.

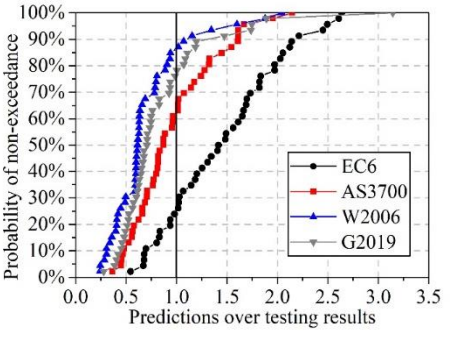

Figure 2.3. The cumulative distribution function for ratios of the predictions over the testing results with partially clamped boundary conditions.

Table 2.3. The average of predictions on all testing specimens by each formulation considering partially clamped boundaries.

Analytical formulations	EC6	AS3700	W2006	G2019
Average of predictions on all testing specimens	147%	98%	71%	85%
CV	0.38	0.43	0.55	0.59
N(±20%)*	12	17	8	12

* N(±20%) denotes the number of predictions that deviates from the testing results by no more than 20%.

Detailed comparisons for all specimens are presented graphically as in Figure 2.4. In Figure 2.4a-d, the ratios between the predicted two-way bending capacity and the experimental one are reported considering hinged (black triangle markers) and clamped boundary conditions (grey rhombus markers). In Figure 2.4e predictions considering specimens as partially clamped (R_f = 0.5 for Virtual Work Method formulations) are compared with the testing results.

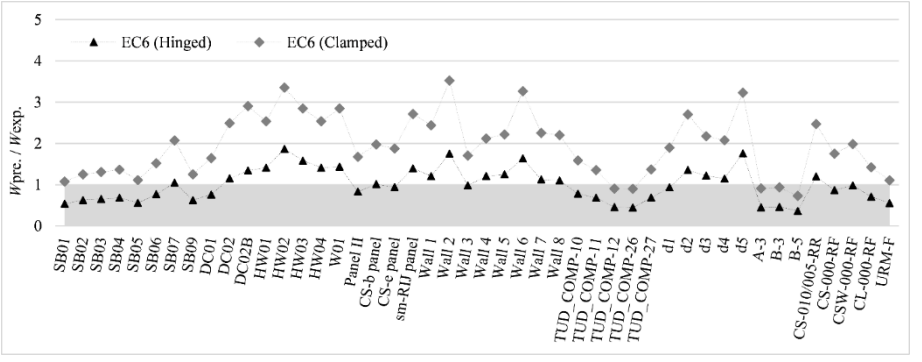

(a) Predictions by EC6 versus the testing results

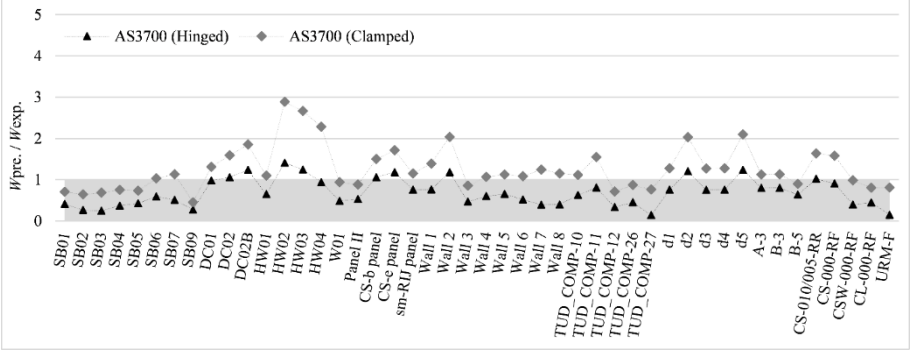

(b) Predictions by AS3700 versus the testing results

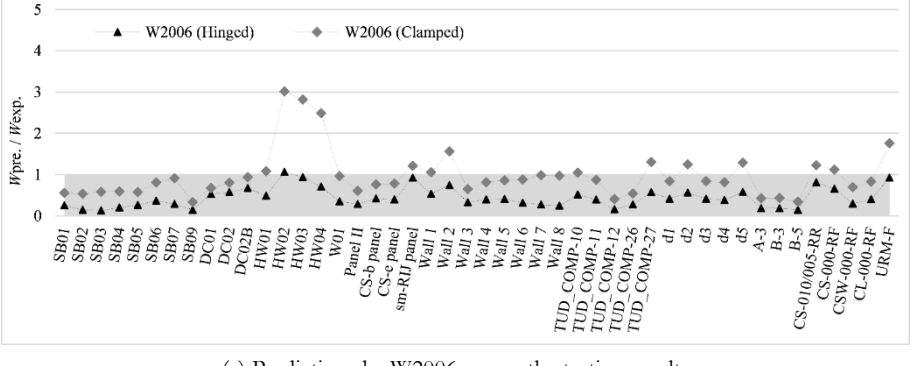

(c) Predictions by W2006 versus the testing results

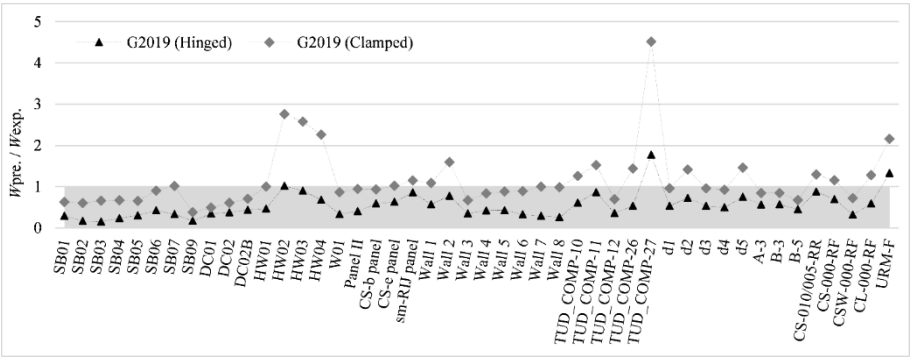

(d) Predictions by G2019 versus the testing results

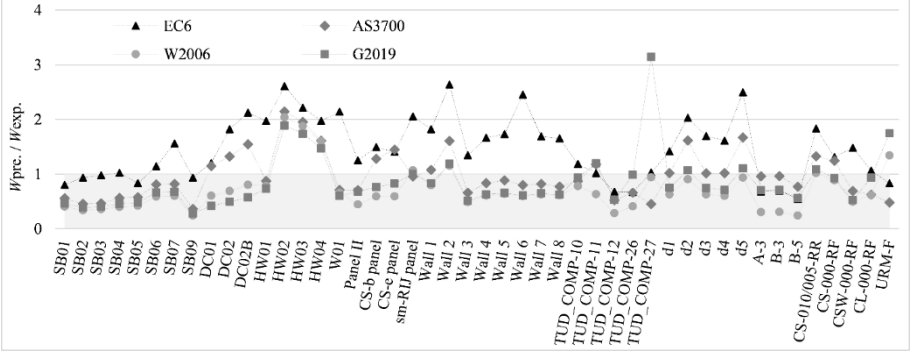

(e) The testing results versus predictions by formulations considering the walls as partially clamped

Figure 2.4.Graphical presentation of the detailed comparison between predictions and the testing results.

2.4 Sensitivity study comparing analytical formulations

In the following sections, the influence of crucial factors on the two-way bending capacity will be studied individually. If not specifically mentioned, partially clamped vertical boundary conditions will be considered for the comparison between the testing results and the analytical predictions.

2.4.1 Boundary conditions

The assumption of different boundary conditions can largely influence the estimation of the two-way bending capacity in current analytical formulations. Table 2.4 presents the ratio of predictions with clamped edges to those with hinged edges on average of all testing specimens for each formulation. All four formulations predict that with the same configuration, the two-way bending capacity of a wall can increase to around 200% as the boundary conditions change from hinged to clamped. Consequently, the parameters related to the vertical boundary conditions could be easily tuned to match testing results, which can result in overlooking the contribution of other parameters. Furthermore, the available testing campaigns provide limited information on the influence of the different degrees of restraint of

the vertical boundary conditions. These together raise the importance and difficulty of studying the influence of the boundary conditions on the two-way bending capacity.

Table 2.4. The ratio of predictions with clamped edges to those with hinged edges on average of all testing specimens.

Analytical formulations	EC6	AS3700	W2006	G2019
$w_{clamped}$ / w_{hinged}	196%	201%	232%	219%

Apart from the vertical boundaries, contributions of horizontal boundary conditions, i.e., the top and bottom edges, were neglected in AS3700, W2006 and G2019. This treatment with horizontal boundary conditions can lead to an incorrect prediction of the cracking pattern (related to the slope factor α) therefore leading to an inaccurate prediction of the two-way bending capacity (Damiola et al., 2018). Unlike testing specimens from other testing campaigns, the walls reported in Damiola et al. (2018) show that diagonal cracks start a few courses away from the wall corners, which suggests a higher degree of constraints at the top and bottom edges. Considering that the Virtual Work Method defines the slope of diagonal cracks as starting from the wall corners, a mismatch between the predicted and the testing crack pattern is observed. In particular, a central vertical crack ($\alpha < 1$) can be predicted instead of a central horizontal crack ($\alpha > 1$), which results in an underestimation of the two-way bending capacity (Damiola et al., 2018).

Based on previous discussions, a sensitivity study with AS3700 was carried out to check both the influence of vertical and horizontal boundary conditions. Testing specimen TUD_COMP-26 (Damiola et al., 2018) was selected as the reference. The wall is 3950×2710 mm², four-side supported, without opening and made of clay brick masonry. Vertical edges were evaluated with the restraint factor R_f. A new coefficient $R_{f,H}$ ranging from 0 to 1 was defined to take the rotational stiffness of horizontal boundary conditions into account. $R_{f,H}$ is used to define the calibrated design height H_d', which replaces H_d, as described in the following equation:

$$H_d' = H_d - n \cdot h_u R_{f,H} \tag{2.16}$$

where n is the number of layers counted between the wall corner and the closest starting point of the diagonal crack.

Equation (2.16) has the following physical meanings: when horizontal edges are simply hinged, i.e. $R_{f,H} = 0$, diagonal cracks start right at the wall corners; when horizontal edges are fully restrained, i.e. $R_{f,H} = 1$, diagonal cracks start n layers of bricks away from the wall corner. In this sensitivity study, n was assumed as 10 based on related testing observations (Ravenshorst & Messali, 2016; Damiola et al., 2017). It should be noted that $R_{f,H}$ is not based on a sufficient number of tests, but it is specified here to study the possible influence of horizontal boundary conditions based on AS3700.

Figure 2.5 shows that the two-way bending capacity increases as R_f or $R_{f,H}$ increases. This is partially inconsistent with the current formulation of AS3700 which suggests

that horizontal boundaries have no contribution to the two-way bending capacity. Even so, R_f does have a larger influence than $R_{f,H}$ on the two-way bending capacity. As R_f increases from 0 to 1, the two-way bending capacity increases by 90%, while as $R_{f,H}$ increases in the same range, the two-way bending capacity increases by 30%. The slope factor α equalling 1 is marked with a solid black line in the graph. In fact, α is not related to R_f but increases as $R_{f,H}$ increases. As $R_{f,H}$ increases, an assumed central vertical crack ($\alpha < 1$) would turn into an assumed central horizontal crack ($\alpha > 1$) which leads to a larger estimated two-way bending capacity. The results stand also for W2006 and G2019 since they evaluate the boundary conditions in the same way AS3700 does.

The results above imply that the two-way bending capacity predicted by the Virtual Work Method is sensitive to the boundary conditions, especially the vertical ones, and to the assumed cracking patterns. Hence, a detailed study on the estimation of the R_f values for different vertical boundary conditions is necessary. Additionally, further investigations regarding the influence of horizontal boundaries on cracking patterns are also suggested.

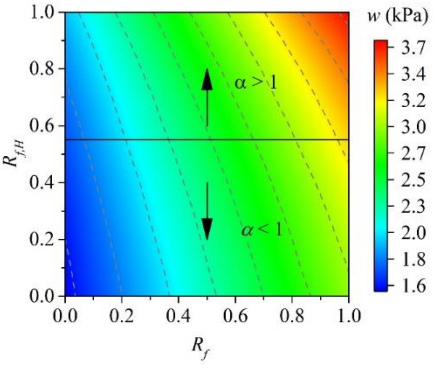

Figure 2.5. Sensitivity study about R_f and $R_{f,H}$ based on TUD_COMP-26 (Damiola et al., 2018).

2.4.2 Material properties

Material properties, such as the flexural strength of masonry f_{x1}, f_{x2} and tensile strength of units f_{bt}, are crucial input parameters for the analytical formulations. Generally, these parameters should be evaluated with dedicated companion material tests (CEN, 1999; SAI, 2018) which, however, are often lacking or incomplete in the considered testing campaigns. Additionally, the material characterisation can often not be performed for existing structures, especially regarding f_{x2}. In this case, mean properties may be estimated by related codes (e.g. [32-33]). Therefore, it is important to evaluate the sensitivity of analytical formulation to material properties and further examine the use of property values provided by codes.

Figure 2.6 presents predictions for 6 testing specimens representing Dutch masonry (Messali et al., 2017; Damiola et al., 2018; Graziotti et al., 2019) using values of material properties from material tests, the Dutch Annex to Eurocode 6 (2018) and

NPR 9998 (2018). For NPR 9998 the values from the category "clay bricks with mortar for general purpose (post-1945)" (NPR9998, 2018) were selected. For each formulation, ratios of predictions with values recommended in codes (w_{codes}) over those with values from material tests ($w_{material\ tests}$) are presented. Figure 2.6a shows that the estimations of material properties by codes can have large differences from those from material tests. Figure 2.6b shows that, in most cases, the predictions obtained using property values from codes, especially NPR 9998, can be over-conservative compared to those using values from the material tests. On the opposite, several predictions according to EC6 using values from the Dutch Annex to Eurocode 6 are even higher than those using values from material tests. Overall, there can be large differences between predictions that adopt material properties from tests and those that use values recommended in codes. This suggests that in practice misevaluating the material properties can result in misevaluating also the two-way bending capacity to a large degree.

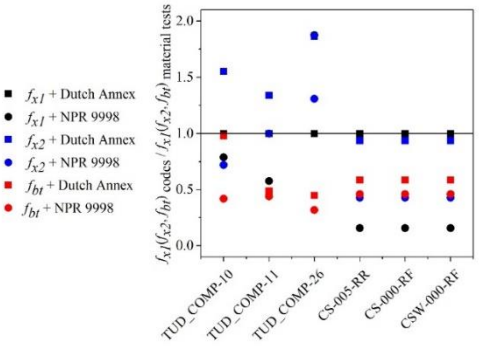

(a) Material properties from material tests and codes

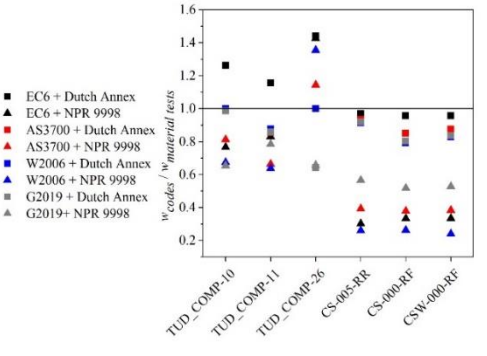

(b) Predictions using various sources of material properties

Figure 2.6. Predictions for 6 testing specimens based on various sources of material properties (Messali et al., 2017; Damiola et al., 2018; Graziotti et al., 2019).

A sensitivity study was carried out to evaluate the influence of material properties on the two-way bending capacity estimated by the analytical formulations.

According to Equations (2.2), (2.6) and (2.10), f_{x1} and f_{x2} are two material properties used in EC6, while f_{x1} and f_{bt} are required for the other formulations. In this sensitivity study, f_{x1}, f_{x2} and f_{bt} have a range of 0.1–1.5 MPa, 0.3–4.5 MPa and 0.5–14.5 MPa, respectively. TUD_COMP-26 (without opening) was selected as the reference. The sensitivity study mainly considered common cases within the range of the dataset in which f_{bt} is larger than or close to f_{x1}.

Figure 2.7 shows the evaluated two-way bending capacity considering various combinations of material properties. According to EC6, the two-way bending capacity increases with the increase of f_{x2}, while the two-way bending capacity is not influenced by f_{x1} when f_{x2} is relatively small. The latter results derive from the fact that when the apparent vertical bending strength ($f_{x1} + \sigma_d$) is larger than f_{x2}, the flexural strength ratio μ will be limited to the unity. In this case, the two-way bending capacity is insensitive to f_{x2} (see Equations (2.1) and (2.2)). Figure 2.7b-d show that with AS3700, W2006 and G2019, the two-way bending capacity increases with the increase of f_{x1}, while f_{bt} has a limited influence. Indeed, if f_{bt} is far larger than f_{x1} ($f_{bt} >> f_{x1}$), the horizontal bending capacity M_h is determined by stepped failure (Equations (2.6) and (2.9)). In this case, the increase of f_{bt} will not lead to an increase in the two-way bending capacity. Further comparing Figure 2.7c and Figure 2.7d shows that f_{bt} has a larger influencing area in W2006 than that in G2019. This is because in W2006 M_h (stepped failure) is dependent on f_{x1}. Hence, the boundary where stepped failure changes into line failure is variable. In contrast, in G2019 M_h (stepped failure) is independent of f_{x1}, therefore, the boundary where stepped failure changes into line failure is consistent. Nevertheless, with G2019 this result is influenced by the defined Equation (2.13) of the torsional strength that does not explicitly consider the dependency of the torsional strength on the flexural strength of masonry as W2006 does. Besides, the equation was derived only from a single testing campaign, and observations are not suggested to be generalised. Moreover, when using the same values of material properties, the predictions of formulations using the Virtual Work Method vary from each other to a large degree. However, due to the lack of related tests, it cannot be determined which formulation quantifies the influence of material properties correctly. This highlights the need for specific studies on the influence of material properties, especially the torsional strength of joints.

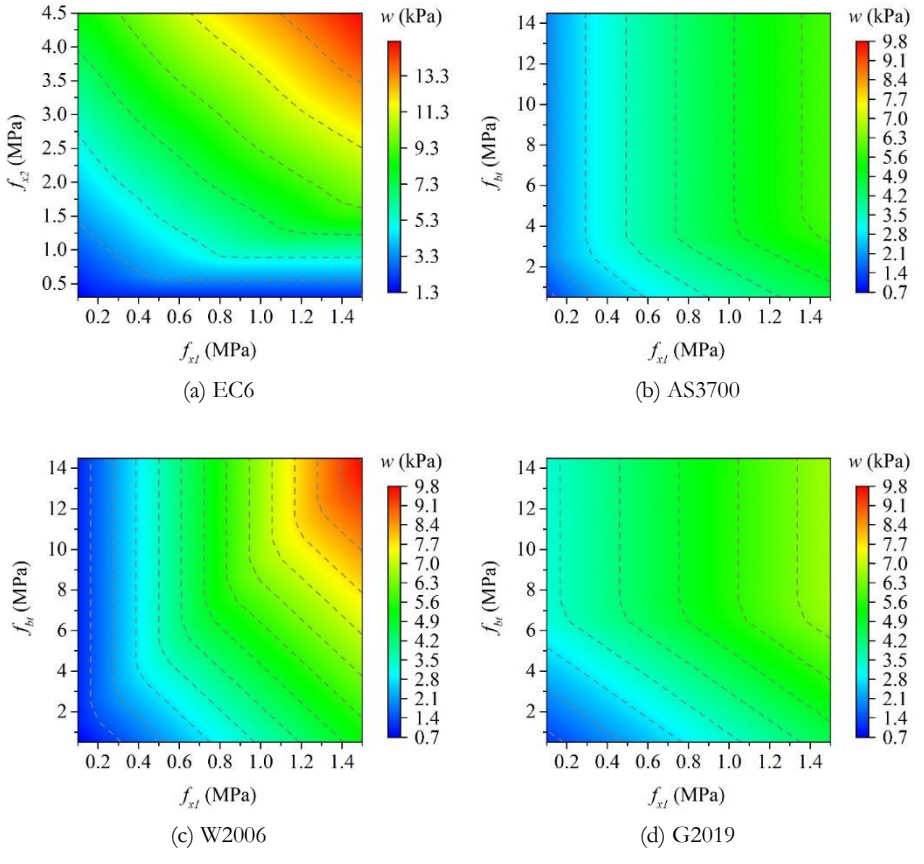

Figure 2.7. Sensitivity study about material properties based on TUD_COMP-26 (without opening).

2.4.3 Pre-compression

To examine how the formulations evaluate the influence of the pre-compression under different wall configurations, testing specimens were selected and divided into five groups (Griffith et al., 2007; Vaculik & Griffith, 2017b). In each group, testing specimens share identical testing configurations, such as the wall geometry, boundary conditions and loading pattern, except for the pre-compression. Groups 1 and 4 do not have openings, while Groups 2, 3 and 5 have. The walls in Groups 1, 2, 4 and 5 have an aspect ratio of around 0.6, while in Group 3 they have an aspect ratio of around 1. Further discussion on the influence of aspect ratio and openings is presented in the following sections.

In Figure 2.8, the markers represent the ratios of the two-way bending capacity of walls that are under pre-compressions over those of zero-pre-compression walls. According to the test results, for walls with aspect ratios 0.61-0.67 (Group 1, 2, 4 and 5), the ratio of the capacity of the walls subjected to 0.1 MPa pre-compression over that of the walls under no pre-compression is approximately 1.5. In contrast,

this comparing ratio drops to 1.02 for the walls with an aspect ratio close to 1 (Group 3). This suggests that the pre-compression has an obvious influence on the two-way bending capacity in the case of walls with lower aspect ratios, while it has a limited influence on walls with larger aspect ratios. None of the formulations can predict this tendency for walls with small aspect ratios. Differently, for walls with a larger aspect ratio (Figure 2.8c), all formulations provide close predictions. Additionally, the testing results show that the two-way bending capacity of the wall subjected to an intermediate pre-compression (0.05 MPa) is also larger than that of the wall under no pre-compression. However, the increase in the two-way bending capacity has a variation in a wide range between 10% and 60% (Figure 2.8b, e).

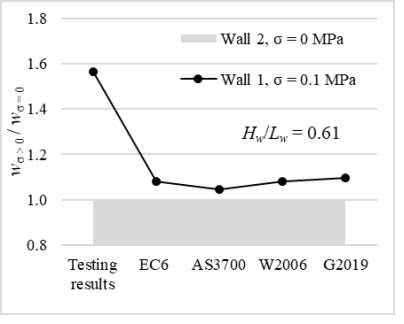

(a) Group 1 (without opening)

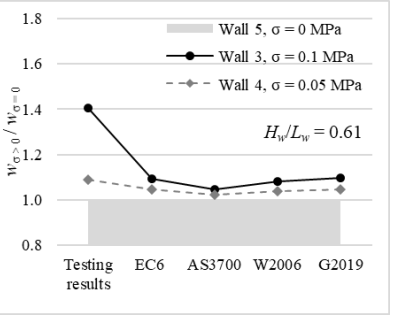

(b) Group 2 (with opening)

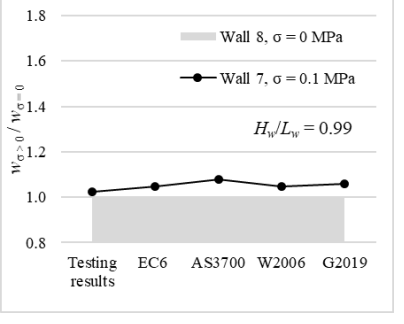

(c) Group 3 (with opening)

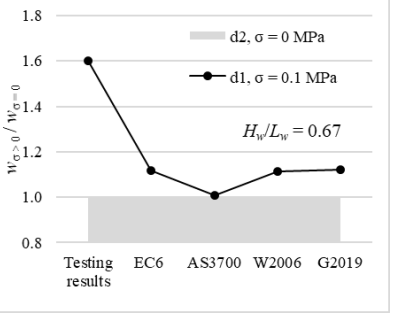

(d) Group 4 (without opening)

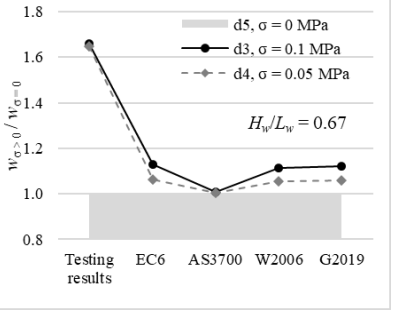

(e) Group 5 (with opening)

Figure 2.8. Comparisons about the pre-compression.

To further evaluate the influence of the pre-compression σ_v on the two-way bending capacity estimated by formulations, a sensitivity study was conducted referring to Groups 1, 2 and 3 (Griffith et al., 2007), with the values of σ_v ranging from 0 to 0.3 MPa. Figure 2.9a and b show that according to the formulations, when the aspect ratio is relatively small (0.61), the two-way bending capacity increases slightly as σ_v increases, no matter if an opening is present; when the aspect ratio is relatively large (0.99), the increase of the two-way bending capacity about σ_v is similar as observed from tests. In general, the two-way bending capacity predicted by AS3700 is less sensitive to the change of the pre-compression, while the two-way bending capacity predicted by the other formulations increases linearly but slightly as the pre-compression increases.

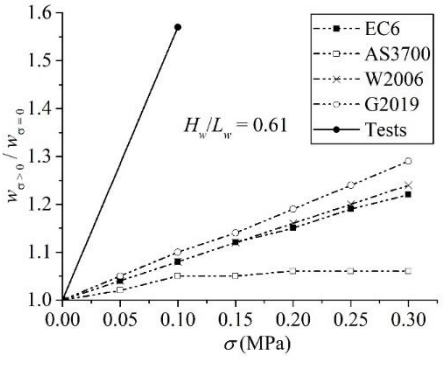

(a) Group 1 (without opening)

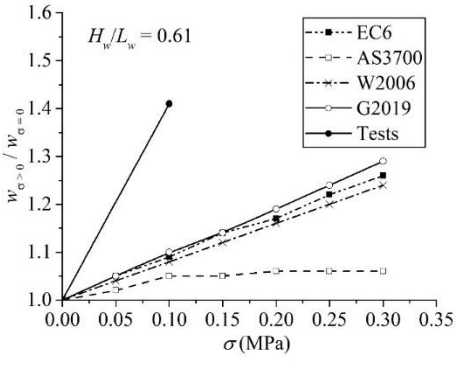

(b) Group 2 (with opening)

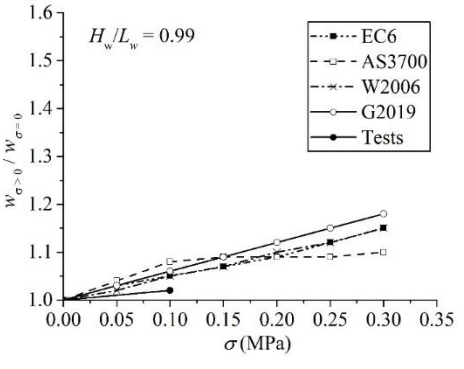

(c) Group 3 (with opening)

Figure 2.9. Sensitivity study about the pre-compression (Griffith et al., 2007).

2.4.4 Aspect ratio

Section 2.4.3 reveals interdependency between the influence of the aspect ratio of the wall (H_w/L_w) and the pre-compression on the two-way bending capacity. This section aims to evaluate the aspect ratio of the walls at different levels of pre-compression. Due to a lack of tests specifically studying the influence of aspect ratio, only two groups including 4 testing specimens were found (Walls 3, 5, 7 and 8)

(Griffith et al., 2007). It should be noted that these four testing specimens are all with openings. The eccentricity and the area of the openings can influence the two-way bending capacity. Consequently, this comparison can provide only an indication of the trend rather than general conclusions.

In Figure 2.10, markers represent the ratios of the two-way bending capacity of walls with aspect ratios of 0.61 over those with aspect ratios of 0.99. The testing results show that if the pre-compression is 0.1 MPa, this comparing ratio is 0.58, while this ratio is 0.42 in the case of no pre-compression. This again suggests that the two-way bending capacity of the walls with lower aspect ratios can be lower than that of the walls with higher aspect ratios. Besides, all formulations can predict the enhancing effect of the increase of the aspect ratio, however, they cannot predict the influence of the change of the pre-compression, as observed in Section 2.4.3.

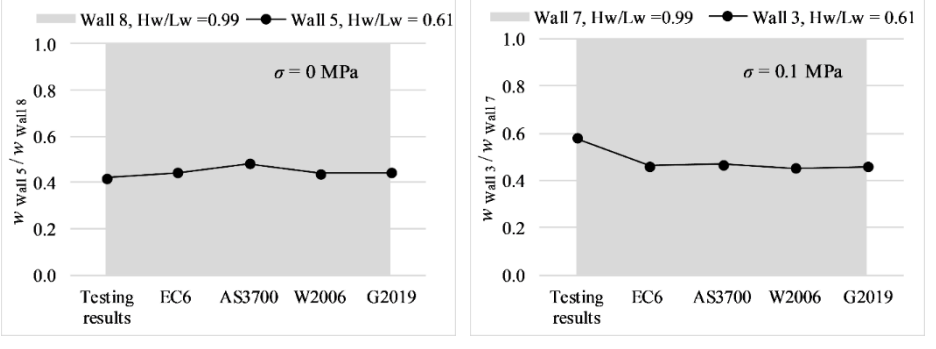

(a) Group 1 (b) Group 2

Figure 2.10. Comparisons about the aspect ratio (Griffith et al., 2007).

A sensitivity study based on Wall 1 and Wall 2 (without openings) (Griffith et al., 2007) was carried out to evaluate the influence of H_w/L_w ranging from 0.5 to 2. Figure 2.11 shows that according to the formulations, the two-way bending capacity increases non-linearly as H_w/L_w increases. All formulations predict similar tendencies. Similarly to what was observed in Section 2.4.3, the analytical predictions predict that the pre-compression has only a slight influence on the two-way bending capacity (Figure 2.11).

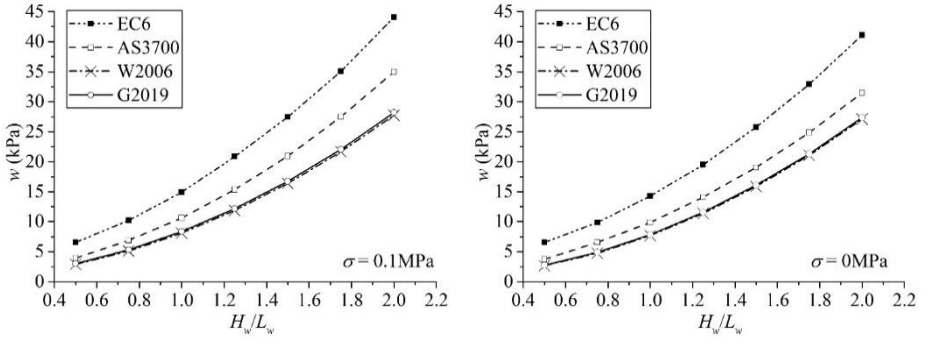

(a) Sensitivity study on Wall 1 (b) Sensitivity study on Wall 2

Figure 2.11. Sensitivity study about the aspect ratio (Griffith et al., 2007).

For the formulations based on the virtual work theory, the aspect ratio of the wall H_w/L_w, and the ratio of the unit $(h_u+t_j)/(l_u+t_j)$ influence the estimation of the two-way bending capacity via the slope factor α (Equation (2.5)). Figure 2.12 shows a sensitivity study considering the combined effects of H_w/L_w and $(h_u+t_j)/(l_u+t_j)$ on Wall 1 with AS3700; the solid black line marks the case of α equals unity. Figure 2.12b shows that the two-way bending capacity is sensitive to H_w/L_w as displayed in Figure 2.11. In contrast, the two-way bending capacity is more sensitive to $(h_u+t_j)/(l_u+t_j)$ in the case $\alpha < 1$ than in the case $\alpha > 1$ when a central horizontal crack is assumed.

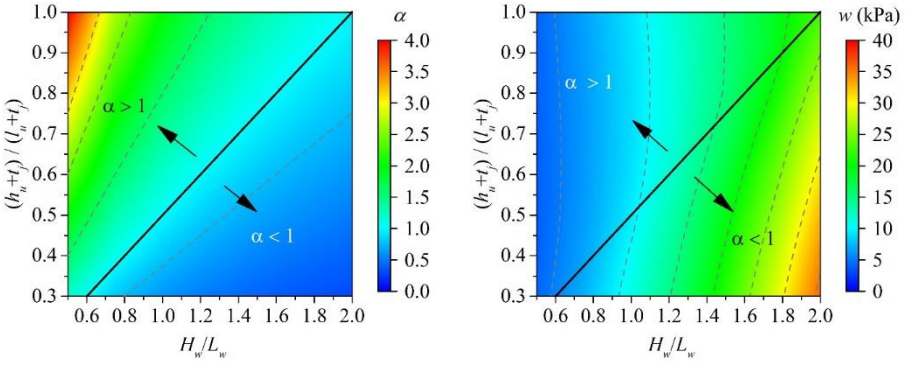

(a) Influence of the unit size and the aspect ratio of the wall on the slope factor α

(b) Influence of the unit size and the aspect ratio of the wall on the two-way bending capacity

Figure 2.12. Sensitivity study about the unit size and the aspect ratio on Wall 1 (Griffith et al., 2007).

2.4.5 Openings

To evaluate the application range of the formulations about walls with openings, 10 groups of testing specimens were compared (Chong, 1993; Griffith et al., 2007; Vaculik & Griffith, 2017b; Damiola et al., 2018; Graziotti et al., 2019). In each group, the first testing specimen is without an opening, while the others are with openings,

as reported in Table 2.5. Openings in Groups 1–4 are centrically located, while in Groups 5–10 they are eccentrically located. Table 2.5 shows that generally, the presence of openings weakens the two-way bending capacity measured in terms of lateral pressure. The walls in Groups 5, 6 and 7 do not show this trend. This is because the lateral pressure was calculated by dividing the reaction force by the net area of the wall. The relatively smaller net area of the wall with the opening can result in an unexpected higher two-way bending capacity. In this sense, in Groups 5 and 7 the presence of the openings still weakens the two-way bending capacity, considering that the reaction forces of the walls without openings are higher than those of the walls with openings in the same group. The only exception is Group 6, where the reaction force of the wall without opening is instead slightly lower than its counterpart (30kN to 31.4kN).

By comparing the predictions with the testing results, Table 2.5 shows that for most cases, especially for walls with centric openings, the proposed simplified method based on Annex E of EC6 to account for openings does not provide satisfactory results. As described in Section 2.2.2, the proposed method for EC6 estimate the wall capacity by considering the minimum between the capacity of the wall without any opening and the capacity of the longer panel beside the opening treated as an independent wall with one vertical side unsupported. According to Equation (2.1), this resulted in the capacity of the panel being larger than that of the entire wall without opening in most cases. Consequently, no distinction is made in the estimation of the capacity for walls with and without openings (e.g. Group 1-4).

In contrast to Annex E of EC6, the formulations based on the Virtual Work Method take the openings into account. Similar to EC6, the two-way bending capacity predicted by these formulations was determined as the minimum of the two-way bending capacity of the entire wall without the opening and that of the longer panel beside the opening. In particular, the presence of the opening affects the estimation of coefficients k_1, k_2, of the design length of the wall L_d, and the aspect factor α_f. Similar to the testing results, most predictions return that the openings weaken the two-way bending capacity. An exception is Group 4, where the two-way bending capacity of the wall with the opening is larger than that of its counterpart. This is because the design length L_d of the wall with the opening is so small that it results in a relatively large two-way bending capacity.

Table 2.5. Grouped testing specimens about openings.

Group	Sample	Opening		OOP pressure (kPa)	OOP force (kN)*	Predictions by			
		Area	Position			EC6 (kPa)	AS 3700 (kPa)	W 2006 (kPa)	G 2019 (kPa)
1	SB01	-	-	2.80	38.91	2.25	1.56	1.14	1.30
	SB02	18%	centric	2.40	33.35	2.25	1.10	0.82	0.93
	SB03	11%	centric	2.30	31.96	2.25	1.07	0.83	0.94
	SB04	13%	centric	2.20	30.57	2.25	1.24	0.88	1.00
2	SB06	-	-	7.50	53.29	8.59	6.10	4.43	4.99
	SB07	11%	centric	5.50	39.08	8.59	4.51	3.30	3.72
3	DC01	-	-	2.65	36.83	3.19	3.04	1.60	1.11
	DC02	18%	centric	1.75	24.32	3.19	2.32	1.21	0.86
4	HW01	-	-	3.70	24.73	7.31	3.23	2.92	2.72
	HW02	4%	centric	2.80	18.71	7.31	6.01	5.71	5.29
	HW03	8%	centric	3.30	22.05	7.31	6.45	6.20	5.73
	HW04	7%	centric	3.70	24.73	7.31	5.97	5.92	5.45
5	Wall 1	-	-	4.76	47.00	8.68	5.13	3.80	3.96
	Wall 3	12%	eccentric	5.05	44.20	6.79	3.34	2.47	2.58
6	Wall 2	-	-	3.04	30.00	8.02	4.89	3.51	3.61
	Wall 5	12%	eccentric	3.59	31.40	6.22	3.19	2.29	2.35
7	TUD_COMP-11	-	-	2.45	27.00	2.49	2.89	1.55	2.93
	TUD_COMP-12	26%	eccentric	3.67	22.40	2.49	1.93	1.05	1.94
8	d1	-	-	3.95	8.96	5.60	4.02	2.49	2.96
	d3	13%	eccentric	2.67	5.25	4.53	2.71	1.68	1.99
9	d2	-	-	2.47	5.60	5.01	3.99	2.24	2.65
	d5	13%	eccentric	1.61	3.16	4.02	2.69	1.51	1.78
10	CS-000-RF	-	-	2.65	29.00	3.47	3.30	2.36	2.45
	CSW-000-RF	27%	eccentric	2.34	18.80	3.47	1.62	1.17	1.23

*The opening area is excluded from the wall surface area in Groups 5-10 when calculating the reaction force since the opening area was non-covered in these testing campaigns.

A sensitivity study was carried out to check the influence of the openings on the two-way bending capacity based on Group 1 considering AS3700. The walls are 5615×2475 mm², top-free and made of clay brick masonry. The eccentricity and the length of the opening were considered variables. The consideration of the length instead of the area of the opening lies in the fact that in AS3700, the height of the opening is not considered. Normalised geometric parameters are introduced as follows:

$$\lambda = \frac{x_0}{(\frac{L_w - L_0}{2})} \in [0, 62] \tag{2.17}$$

$$\eta = \frac{L_0}{L_w} \in [0.1, 0.52] \tag{2.18}$$

where x_0 is defined as the distance between the central line of the opening and that of the wall; L_w and L_o are the length of the wall and the length of the opening, respectively (Figure 2.2); λ is the normalised variable representing the eccentricity of the opening; η is the normalised variable representing the length of the opening. Ranges of λ and η are determined as those covering all testing specimens (η does not start from 0 to avoid calculating error). This is intended to provide a reference for practical configurations of the openings.

Figure 2.13 shows the variation of the two-way bending capacity in terms of pressure (w) and force (F) at varying λ and η. Results show that the further the opening is positioned away from the central line of the wall (λ from 0 to 0.62), the smaller the two-way bending capacity; the two-way bending capacity decreases as the length of the opening increases (η from 0.1 to 0.52) except for a small area where η is less than 0.2 and λ is larger than 0.5. These results provide insights into how the formulations based on the Virtual Work Method evaluate the influence of the openings. Nevertheless, tests are very limited concerning a detailed study on the influence of eccentricity and the area of the openings. Therefore, the predictions by the formulations are not suggested to be generalised.

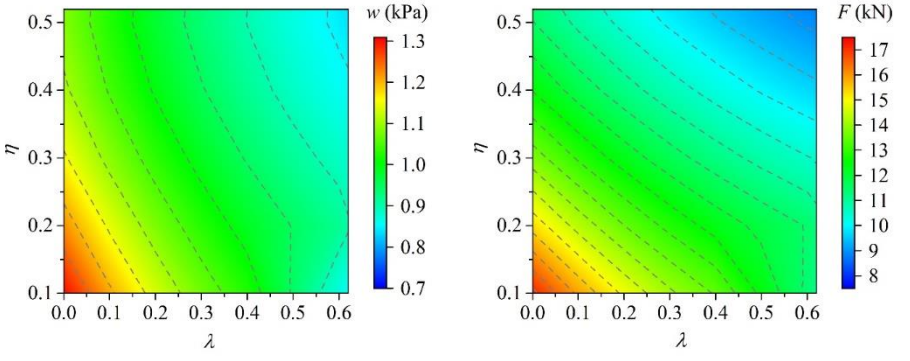

(a) Results presented with lateral pressure w (b) Results presented with reaction force F

Figure 2.13. Sensitivity study about openings based on Group 1 (Chong, 1993).

2.4.6 Wall thickness/bond patterns

Despite the presence of numerous multi-wythe walls in existing URM structures, the majority of testing campaigns (44 out of 46 testing specimens listed in this chapter) focus on single-wythe walls built in stretcher bond. According to Annex E of EC6, walls to be evaluated should be solid walls with thickness less than or equal to 250 mm (CEN, 2012). If the unit thickness is 100 mm, a triple-wythe wall is already beyond the applied range of the code. As for the other formulations, since the assumed cracking pattern is based on stretcher bond, their applications to multi-wythe walls are naturally limited.

In this section, testing specimens TUD_COMP-26 and TUD_COMP-27 are compared since the former is single-wythe and stretcher bonded, while the latter is double-wythe and English bonded. Apart from thickness and bond pattern they have the same testing configurations. Different bond patterns and wall thickness are here compared together since in practice the latter depends on the former. Additionally, the double-wythe wall URM-F tested by Padalu et al. (2020b) is also considered to check the accuracy of formulations treating multi-wythe walls. Here the calculation for the slope factor α related to the assumed cracking pattern is adapted for the English bond as shown in Equation (2.15).

Table 2.6 shows that the two-way bending capacity of TUD_COMP-27 measured in tests is 2.2 times that of TUD_COMP-26. It is not clear whether this enhancing effect is caused by the change in wall thickness or bond pattern. Indeed, increasing the wall thickness increases the section modulus of the wall, while the transverse bricks in English bonded walls provide an interlocking effect between wythes. The formulations based on the Virtual Work Method either underestimate the ratio of double-wythe wall to single-wythe wall (AS3700, 1.5) or extremely overestimate it (W2006, 5.2; G2019, 7.1). AS3700, W2006 and G2019 wrongly predict α for TUD_COMP-26. It should be noted that the horizontal boundary conditions can also play a role as discussed in Section 2.4.1. Considering absolute values, EC6 appears to be the most accurate. As for URM-F, EC6 again predicts the most accurate value, while the other 3 formulations either underestimate or overestimate the wall capacity excessively. The calculated α for URM-F is larger than 1, which is against the testing observation where a central vertical crack took place. This suggests that evaluation for English bonded and multi-wythe walls by AS3700, W2006 and G2019 should be further studied.

Table 2.6. Comparison of the wall thickness and the bond pattern.

Testing samples	Wythe	Bond pattern	Wall thick. (mm)	Test results (kPa)	EC6 (kPa)	α	AS3700 (kPa)	W2006 (kPa)	G2019 (kPa)
TUD_COMP-26	Single	Stretcher	100	3.37	2.27	0.8	2.23	1.38	3.33
TUD_COMP-27	Double	English	210	7.52	7.74	1.6	3.40	7.08	23.65
URM-F	Double	English	229	19.26	16.00	1.4	9.27	25.89	33.65

2.5 Conclusions

This chapter assesses the accuracy and application range of current major analytical formulations assessing the two-way bending capacity of unreinforced masonry (URM) walls. For this purpose, 46 testing specimens from 8 international testing campaigns were collected and categorised. Four sets of current analytical formulations, namely, the Yield Line Method-based Eurocode 6 (EC6), and the Virtual Work Method-based Australian Standard (AS3700), Willis et al. (W2006), and Graziotti et al. (G2019) were considered.

The accuracy of the formulations was evaluated by comparing the predictions with the testing results. The comparison shows that AS3700 provides the highest predicting accuracy rate within the dataset. More specifically, AS3700 is the most accurate assessing walls assumed to be partially clamped and walls with openings. Even so, the incorrect prediction rate of AS3700 is as high as over 50%. EC6 tends to incorrectly overestimate the two-way bending capacity for most testing specimens. W2006 and G2019 tend to incorrectly underestimate the two-way bending capacity equally for walls with or without openings. Nevertheless, among the formulations based on the Virtual Work Method, the approach proposed by Willis et al. (W2006) appears the one with the strongest theoretical framework to be employed for further improvements. The results obtained by G2019 should be treated with care since the proposed equation for the torsional strength was derived from a single testing campaign and not meant to be generalised.

To evaluate the application range of formulations, the influence of the crucial factors on the two-way bending capacity was explored by comparing the available testing results and by performing sensitivity studies for the analytical formulations.

The influence of the boundary conditions was first evaluated. A study on the boundary conditions based on formulations shows that as the boundary conditions of a wall change from hinged to clamped, its two-way bending capacity increases to about 200%. A sensitivity study based on AS3700 shows that the two-way bending capacity is not only sensitive to the rotational stiffness of the vertical boundaries but also the rotational stiffness of the horizontal boundaries, although to a smaller degree. This is contradictory to the assumption in the Virtual Work Method. However, this finding requires further study due to limited testing evidence.

The lack of material characterisation for existing buildings often results in the need of adopting prescribed material properties, which generally leads to a misevaluation of the two-way bending capacity. In most cases, the predictions using values from codes, especially for NPR 9998, are over-conservative compared to those using values from material tests. The sensitivity study shows that with EC6, the two-way bending capacity increases with the increase of horizontal flexural strength of masonry f_{x2}; on the contrary, if the horizontal one f_{x2} is relatively small the two-way bending capacity is not influenced by vertical flexural strength of masonry f_{x1}. With AS3700, W2006 and G2019, the two-way bending capacity increases with the increase of the vertical flexural strength of masonry f_{x1}, while the tensile strength of bricks f_{bt} has a limited influence. However, due to the lack of related tests, it cannot be determined which formulation quantifies the influence of material properties correctly. Additionally, it is worthy to highlight the importance of characterising the torsional shear response of the bed joints, since it can significantly influence the evaluation of the wall capacity.

A study on the influence of the pre-compression shows that the pre-compression has an obvious enhancing effect on the two-way bending capacity of walls with relatively small aspect ratios. In contrast, this effect is quite slight for walls with relatively large aspect ratios. However, none of the formulations can correctly

predict the influence of pre-compression for walls with small aspect ratios. The influence of the aspect ratio of the wall was also examined. Both testing results and predictions show that the two-way bending capacity increases nonlinearly as the aspect ratio of the wall increases.

The testing results show that the presence of openings weakens the two-way bending capacity. A simple extension of Annex E in EC6, made by considering the longer panel beside the opening as an independent wall with one vertical edge unsupported, does not predict this tendency, especially when the opening is centrically located. In contrast, predictions by AS3700, W2006 and G2019 methods match well with the testing observations. A sensitivity study shows that the two-way bending capacity decreases as the eccentricity or the length of the opening increases. Nevertheless, these results are not suggested to be generalised since the continuous varying ranges of the eccentricity and area of the openings discussed in this sensitivity study lack corresponding testing evidence.

The influence of the wall thickness and bond pattern was studied jointly. EC6 is the most accurate formulation for assessing the influence of the thickness, even though the bond pattern is not considered. Formulations based on the Virtual Work Method require further improvements to account for a wider range of wall thickness and bond patterns.

To conclude, the formulations based on the Virtual Work Method returned the most accurate predictions for the testing specimens evaluated in this chapter, especially for partially clamped walls and walls with openings. Nevertheless, drawbacks and limitations were revealed when analytical formulations were applied to assess the influence of crucial factors on the two-way bending capacity. First, the influencing trend of some crucial factors predicted by the analytical formulations is contradictory to the testing results, such as the pre-compression. Second, the application ranges of some crucial factors are limited or not well defined, such as the boundary conditions and the wall thickness/bond patterns. Third, the influence of some crucial factors cannot be determined due to a lack of testing evidence, such as the material properties, and the eccentricity and area of the openings. These together decrease the accuracy and limit the application range of the analytical formulations. To improve the accuracy and application range of the analytical formulations, three geometric parameters, namely the pre-compression, wall aspect ratio and openings that are crucial to the two-way bending capacity, are investigated via the numerical method in the following chapters.

Chapter 3

NUMERICAL MODELLING APPROACH: CALIBRATION AND VALIDATION[2]

Chapter 2 reveals the drawbacks and limitations regarding the evaluation of the influence of the geometric parameters on the two-way bending capacity of the unreinforced masonry (URM) walls. Unfortunately, parametric experimental studies to understand this influence are quite limited. Compared with physical experiments, numerical modelling is an effective alternative since it is economic and time-efficient.

This chapter aims at establishing a reliable numerical model to predict the crucial mechanical features, such as the two-way bending capacity and crack patterns of the URM walls. The two-way bending capacity is here defined as the peak pressure on the wall net area. To achieve this goal, a 3D simplified brick-to-brick modelling approach was applied. A series of 8 quasi-static monotonic tests on URM walls with different pre-compression and wall aspect ratios were selected for the calibration and validation of the model. The model was first calibrated for a solid wall (without opening) and subsequently validated on the remaining walls. To further support the selection of the 3D simplified brick-to-brick modelling approach, a comparison with other modelling strategies, namely the continuum modelling and 3D detailed brick-to-brick modelling, as well as sensitivity studies for mesh size, material properties and boundary conditions were carried out. Numerical results show that the modelling approach employed is reliable to estimate the two-way bending capacity and the corresponding crack pattern in detail, while the prediction of the post-peak response is unsatisfactory. Nevertheless, the approach is suitable to address the purpose of this study which is to evaluate the influence of geometric parameters on the two-way bending capacity of URM walls. This approach is further applied to perform a parametric numerical study on the combined influence of pre-compression and wall aspect ratio (Chapter 4), and opening size, shape and location (Chapter 5).

[2] This chapter is based on the published journal article: Chang, L.-Z., Rots, J. G., & Esposito, R. (2021). Influence of aspect ratio and pre-compression on force capacity of unreinforced masonry walls in out-of-plane two-way bending. *Engineering Structures*, *249*. Minor modifications have been made to suit the thesis.

3.1 Introduction

Numerical modelling, as an alternative to physical experiments, offers the possibility of virtual experiments that are effective and cost/time-efficient. In the past decades, various numerical modelling strategies have been proposed to study unreinforced masonry from material to structural scale. According to the classification by D'Altri et al. (2019), current modelling strategies can be divided into four main categories depending on how the masonry and its constituents are modelled: continuum modelling, brick/block-based modelling, macro-element modelling and geometry-based modelling.

With the continuum modelling, the masonry is modelled as a continuum body without distinguishing between bricks and mortar joints (Figure 3.1a). Orthotropic properties are then attributed to the continuum models to indirectly account for the underlying pattern and properties of bricks and joints (Rots et al., 1997; Lourenco et al., 1998; Milani et al., 2006; Sousamli et al., 2022). In this sense, the cracking, shearing and crushing are represented in a smeared manner. This allows a large mesh size to be applied in the models, therefore, reducing the computing time significantly. The constitutive models can either be acquired by direct experiments (van der Pluijm, 1999a; Bruggi & Taliercio, 2015; Degli Abbati et al., 2019; Jafari et al., 2022) or through homogenisation approaches (Marfia & Sacco, 2012; Leonetti et al., 2018; Zhou, Sluijs, et al., 2022; Zhou, Sluys, et al., 2022). The continuum models can be established either with the 2D plane or shell elements (Noor-E-Khuda et al., 2016) or 3D solid elements (Liberatore et al., 2020). The modelling technique is advantageous in modelling large-scale URM structures in terms of computing efficiency. However, it is not capable of investigating the failure modes of individual mortar joints and is not able to distinguish the detailed stepped crack lines caused by various bond patterns such as the English bond and Flemish bond.

The brick/block-based modelling approach (Figure 3.1b) has two sub-categories, namely, simplified brick-to-brick modelling and detailed brick-to-brick modelling. With the simplified brick-to-brick modelling, the mortar joints including their connecting areas with the bricks are simplified as zero-thickness interfaces, while the bricks are extended in dimensions to account for the thickness of the mortar joints (Rots et al., 1997; Abdulla et al., 2017; D'Altri et al., 2018; D'Altri et al., 2019). With the detailed brick-to-brick modelling, both mortar joints and bricks are modelled according to their real dimensions. The contacting areas at both sides of the mortar joints are modelled directly with interfaces (Rots et al., 1997; Andreotti et al., 2018; Zeng et al., 2021). With the brick/block-based modelling, the bricks/blocks can be modelled with linear elastic or nonlinear constitutive models; the connecting areas between the bricks and mortar joints can be modelled with interface elements within the framework of the finite element method (Lourenco & Rots, 1997; Li et al., 2016; Baraldi & Cecchi, 2017; Chisari et al., 2018; Isfeld et al., 2021; Nie et al., 2022), or contact element within the framework of the Distinct Element Method (Bui et al., 2017; Gonen et al., 2021) or the Applied Element Method (Malomo et al., 2020; Calò et al., 2021). If combing the plane stress

elements for the bricks and line interface elements for the mortar joints (2D version), the brick/block modelling approach is sufficient for modelling the in-plane behaviour of the URM walls, while if combing the 3D continuum elements for the bricks and plane interface elements for the mortar joints (3D version), this technique extends its capacity to model both the in-plane and out-of-plane (OOP) behaviour. One of the primary merits of the brick/block-based modelling is that it can precisely rebuild the structural details (e.g. bond patterns and toothings at the lateral edges) of walls. Thus, crack patterns can be captured in a detailed manner, and failure modes of individual joints can be analysed directly rather than in a smeared-out sense. This advantage is more apparent when the 3D version is applied to simulate the OOP behaviour of URM walls since the failure of the mortar joints in the thickness direction is intuitionally visible. Moreover, unlike the 2D version, the 3D version allows the combined tensile and shear/torsional failures on the planes of the mortar joints to be examined directly. However, the brick/block-based modelling requires much more computational effort compared to the continuum modelling approach. This drawback is even more evident for the detailed brick-to-brick modelling since a more refined mesh size is required for the elements representing the thin mortar joints, which demands substantial computing time and effort. Here it is worth mentioning the "2.5D" modelling technique with which the bricks and mortar joints are modelled concerning the real dimensions with plane or shell elements. Drougkas et al. (2020) applied this technique to the in-plane behaviour of masonry walls and proves that it can predict the stepped cracks in detail as the 3D version of the brick/block-based models. In theory, this technique is applicable for modelling the OOP behaviour of the URM walls. However, the failure of the mortar joints along the thickness direction is difficult to be interpreted, as it is with the continuum models. Moreover, the toothings at the lateral edges of the walls cannot be simulated. Besides, the element size is determined by the thickness of the mortar joints, which greatly raises the number of elements and sharply increases the computing time.

The macro-element modelling approach idealises the masonry structure as a combination of piers and spandrels (Figure 3.1c) as single structural components. Potential cracks between the adjacent components can be modelled with interfaces (Lagomarsino et al., 2013; Xu et al., 2018). This modelling technique is generally fast-computing. However, since the macro-element approach focuses on the global in-plane behaviour, the OOP behaviour is often omitted or treated separately from the in-plane behaviour, which can lead to conservative estimations (D'Altri et al., 2019). The geometry-based approach considers the structure as a rigid body (Figure 3.1d). With this approach, the structural equilibrium and collapse are mainly investigated through limit analysis-based solutions. Focusing on the geometry of the masonry structures from an overall scale, the geometry-based modelling is suitable for masonry vaults and shells (Block & Lachauer, 2013; Chiozzi et al., 2017). However, like the continuum modelling, the detailed crack patterns cannot be predicted. Both the macro-element and the geometric-based modelling approach are not suitable for this work, because the detailed crack patterns cannot be predicted, and the failure modes of individual mortar joints cannot be examined.

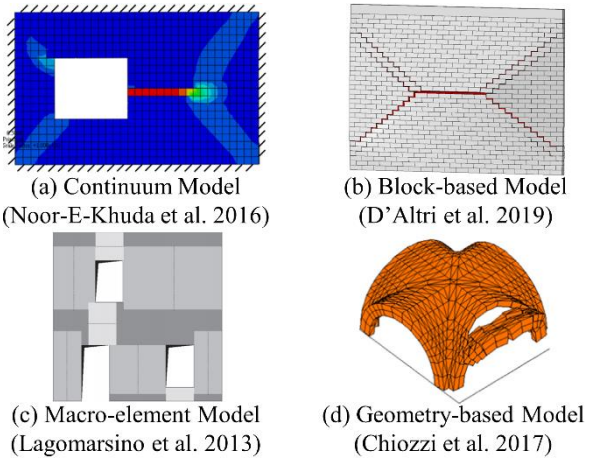

Figure 3.1. Examples of modelling strategies for URM structures.

This chapter aims at building a reliable numerical model to study the influence of the geometric parameters on the OOP two-way bending capacity of URM walls. The 3D simplified brick-to-brick modelling was selected as the modelling approach for the following reasons:

- it can describe the structural details of the walls, such as the bond patterns and the toothings between the main wall and the return walls (which is not applicable with the continuum modelling);
- it predicts the detailed stepped failure caused by various bond patterns (which cannot be distinguished by the continuum modelling);
- it can directly provide the failure modes of individual mortar joints (which is not applicable with the continuum modelling) and the failure of mortar joints in the thickness direction (which is only intuitionally visible via the plane interface elements with the 3D brick-to-brick models);
- it provides a balance between the accuracy and computational costs (the continuum modelling is efficient but loses some details; the 3D detailed brick-to-brick modelling represents the walls with more details but can be much more time-consuming).

A comparison between the selected 3D simplified brick-to-brick modelling against the continuum modelling approach and the 3D detailed brick-to-brick modelling approach is provided in Section 3.6.

3.2 3D simplified brick-to-brick model

The 3D simplified brick-to-brick modelling approach was employed to simulate the mechanical behaviour of URM walls in OOP two-way bending in this study. With this approach, a mortar joint including its two connecting areas with adjacent bricks is modelled as a single zero-thickness 3D plane interface element, while the bricks

are extended in dimensions (brick height and length) and are modelled as 3D continuum elements (Figure 3.2).

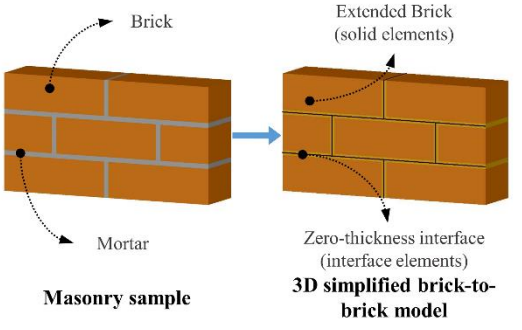

Figure 3.2. Schematic diagram of the 3D simplified brick-to-brick modelling approach.

For the 2D line interface elements, Lourenco and Rots (1997) developed a combined cracking-shearing-crushing model. It is based on multi-surface plasticity, comprising a Coulomb friction model combined with a tension cut-off and an elliptical compression cap. Later, this model was extended to 3D plane interface elements in the finite element software package DIANA, which enables the relative shear-slipping of two planes. The 3D version of the cracking-shearing-crushing model and its variables are shown in Figure 3.3a and b, respectively.

Within the elastic regime, the constitutive relations between the normal stress σ and the normal relative displacement u, and that between the shear stress τ_s (τ_t) and the shear relative displacement v_s (v_t), are described as follows:

$$\begin{Bmatrix} \sigma \\ \tau_s \\ \tau_t \end{Bmatrix} = \begin{bmatrix} k_{nn} & 0 & 0 \\ 0 & k_{ss} & 0 \\ 0 & 0 & k_{tt} \end{bmatrix} \begin{Bmatrix} u \\ v_s \\ v_t \end{Bmatrix} \tag{3.1}$$

with k_{nn} and k_{ss} (k_{tt}) the normal and shear stiffness of the interface elements, respectively.

The tensile stress beyond the tensile strength f_t is assumed to soften exponentially (Figure 3.3c):

$$\sigma = f_t \, e^{-\frac{f_t}{G_f^I} u} \tag{3.2}$$

with G_f^I the Mode-I fracture energy.

The Coulomb friction mode is described by:

$$\tau = \sigma \cdot \tan\varphi + c \tag{3.3}$$

where c is the cohesion of the brick-mortar interface and φ is the friction angle.

The cohesion beyond the initial cohesion of the interface softens exponentially (Figure 3.3d):

$$c = c_0 \, e^{-\frac{c_0}{G_f^{II}} v} \tag{3.4}$$

with c_0 and G_f^{II} the initial cohesion of the brick-mortar interface and Mode-II fracture energy, respectively.

The compressive stress hardens till reaching compressive strength f_c followed by softening. According to the experimental benchmarks by Vaculik (2012), no compressive failure of mortar joints was reported at the end of the pushover tests, and tensile and shear failure mechanisms were observed to be predominant. This is in line with other tests on two-way bending walls (Ravenshorst & Messali, 2016; Damiola et al., 2017). In this sense, it is expected that no crushing of the mortar occurs, so the compressive strength of the interface elements was set to a relatively high value and the post-peak parameters were set with dummy values, which is a common strategy applied with the 3D brick-to-brick modelling (Abdulla et al., 2017; D'Altri et al., 2019). A posteriori check of this assumption was made for each analysis and no crushing of the mortar was detected.

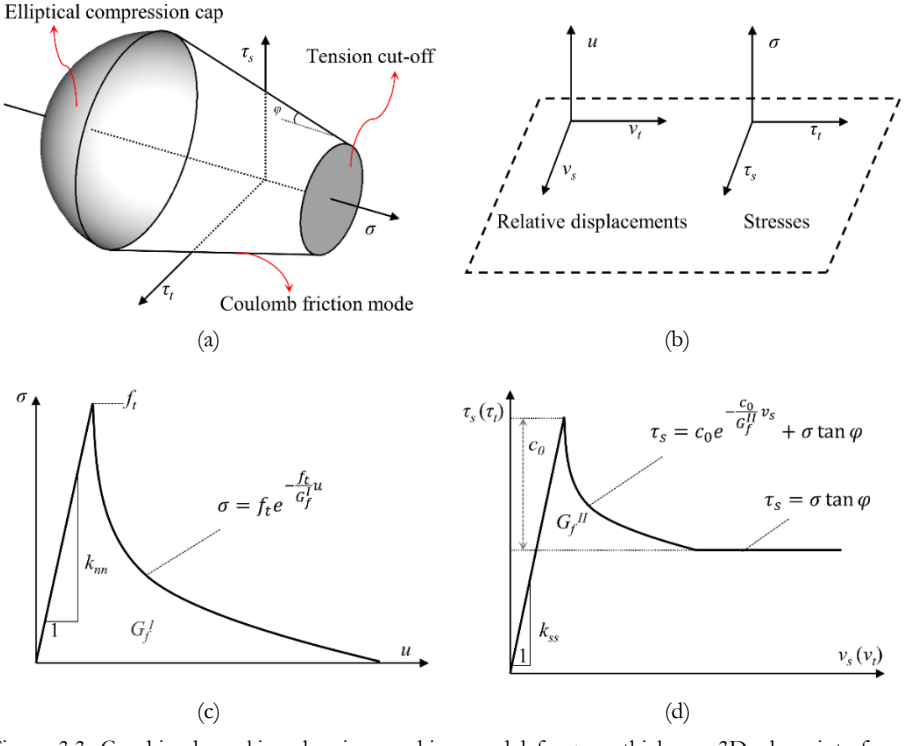

Figure 3.3. Combined cracking-shearing-crushing model for zero-thickness 3D plane interface elements: (a) multi-surface plasticity model; (b) variables of the 3D interface elements; (b) tensile softening; (c) shear softening.

The bricks are modelled with the rotating smeared cracking model proposed by Feenstra (1993), namely the total strain crack model. Due to the general absence of compression failure in bricks for OOP two-way bending experiments (Vaculik, 2012; Damiola et al., 2017), a linear behaviour in compression was adopted for the bricks and a posteriori check was performed. In the tension regime, an exponential softening was adopted for the bricks:

$$\sigma_1 = f_{bt}\, e^{-\frac{f_{bt}}{G^I_{f,b}/h_{cr}}\varepsilon_1} \tag{3.5}$$

with σ_1 and ε_1 the stress and strain along the maximum principal direction, respectively; f_{bt} the tensile strength of bricks; $G^I_{f,b}$ the Mode-I fracture energy of the bricks, and h_{cr} the crack bandwidth (Figure 3.4). It should be noted that with the combination of a discrete modelling approach for the joints and a smeared modelling approach for the bricks, the propagation of a vertical crack may be delayed or discouraged in the bricks. Alternately, the formation of vertical cracks in bricks can be modelled with vertical interface elements pre-set in the middle of the bricks. However, this also leads to more severe numerical instability. Besides, the potential cracks in the bricks can only develop at the presumed position. The comparison of these two modelling strategies regarding the tensile failure of the bricks is presented in Appendix A.

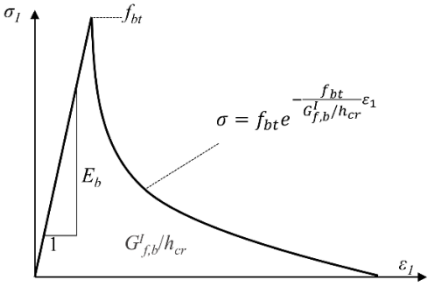

Figure 3.4. Tensile softening in rotating smeared cracking model for the bricks.

3.3 Experimental benchmarks

Quasi-static monotonic airbag experiments on eight walls (labelled as Wall 1-8) carried out by Griffith and Vaculik (2007) were selected as benchmarks. The sketch of Wall 1 and the boundary conditions are shown in Figure 3.5a. In general, all walls were simply supported by steel angles and struts along the top and bottom edges of the main wall (Figure 3.5b, c), except for Wall 6 with a top-free edge. All walls were built with 480 mm-long return walls on the lateral sides of the main wall. The lateral edges of the return walls were constrained by C-shape steel channels which were simply connected to the supporting frame (Figure 3.5d). The experimental configurations of the walls are shown in groups in Table 3.1. These single-wythe stretcher-bonded walls were made of 230×110×76 mm^3 clay bricks and 10 mm-thick mortar joints. All walls were 2,494 mm high. Walls 1-6 were long walls with a length of 4,080 mm, while Walls 7 and 8 were short walls with a length of 2,520 mm. Walls 1 and 2 were solid, while the other walls were with openings. On the top edges of Walls 1, 3 and 7, a pre-compression (σ_n) of 0.1 MPa was applied, while for Wall 4 the pre-compression was 0.05 MPa: the other walls were free of pre-compression. After the application of the pre-compression, an evenly distributed OOP pressure was applied using airbags on the exterior face of the main wall. More

details regarding the experimental configurations can also be found in Vaculik (2012). Here it should be noted that the displacements of the walls recorded in Vaculik (2012) are larger than those recorded in Griffith and Vaculik (2007), although records in these two references were from the same experimental campaign. This is because in the former the displacements of the walls were taken as the absolute displacements at the location of interest, while the displacements of the latter were corrected by reducing the rigid body movements of the supporting frames from the absolute displacements of the walls. In this sense, the corrected load-displacement relations were used as references, since rigid body movements of boundaries are prevented in the numerical models.

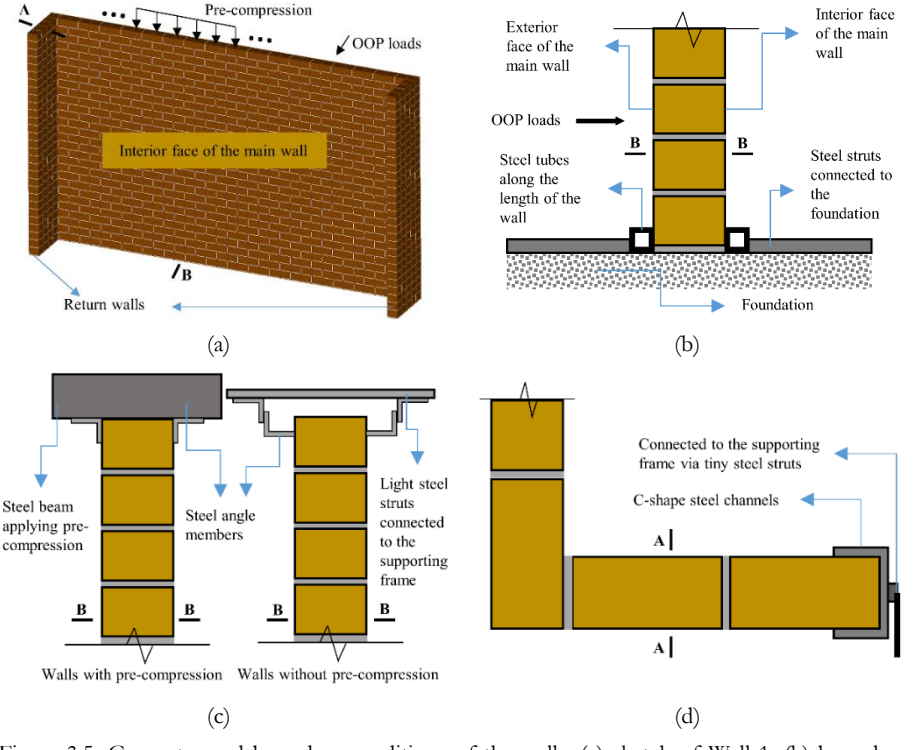

Figure 3.5. Geometry and boundary conditions of the walls: (a) sketch of Wall 1; (b) boundary conditions at the bottom edge of the main wall; (c) boundary conditions at the top edge of the main wall; (d) boundary condition at the lateral edge of the return wall. Adapted from Vaculik (2012).

Table 3.1. Experimental configurations of the walls. Adapted from Griffith and Vaculik (2007).

Experimental configurations* (dimensions in millimetres)	Wall Num./σ_v (MPa)	Experimental configurations (dimensions in millimetres)	Wall Num./σ_v (MPa)
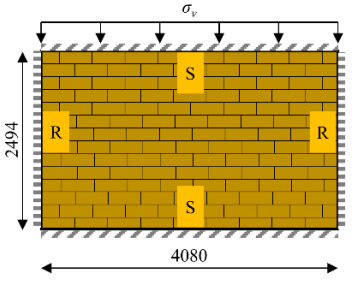	1/0.1 2/0	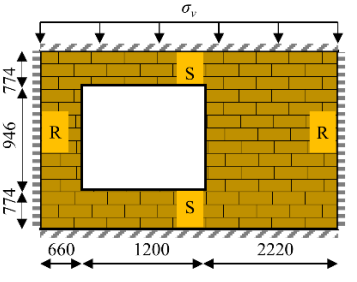	3/0.1 4/0.05 5/0
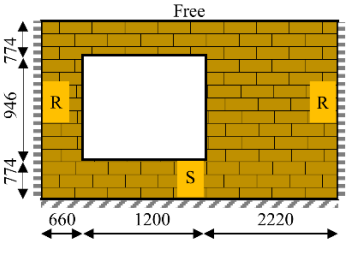	6/0	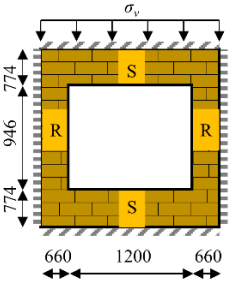	7/0.1 8/0

* "S" refers to being simply supported; "R" refers to being restrained by return walls.

3.4 Calibration of the numerical modelling approach against wall 1

3.4.1 Finite element model

The numerical modelling was carried out with the finite element software package DIANA 10.4 (2019). The calibration of the numerical approach was carried out against Wall 1, while the validation, presented in the following section, is carried out against the remaining seven walls tested in the experimental campaign by Griffith and Vaculik (2007). Clay bricks were extended in dimensions from 230×110×76 mm^3 to 240×110×86 mm^3 and modelled with 3D continuum elements. Mortar joints were modelled with zero-thickness plane interface elements. The mesh of the model is shown in Figure 3.6a. A complete brick was meshed in 2, 1 and 3 divisions in length (l_u), height (h_u) and thickness (t_u) directions, respectively (Figure 3.6b). At the intersections of the main wall and the return walls, half bricks were meshed in a refined manner (3×1×3 divisions), so that 3 elements were constantly kept over the thickness for both the main wall and return walls, avoiding irregular meshed shapes (Figure 3.6c). The mesh manner of the interface elements follows that of the brick surfaces (Figure 3.6d). For the plane interface elements, 8+8 nodes, 3D plane quadrilateral elements (CQ48I in DIANA 10.4) with a 3×3 Newton-Cotes integration scheme were selected, while for the bricks, 20 nodes, 3D quadratic

continuum elements (CHX60 in DIANA) with a 3×3×3 Gauss integration scheme were selected.

Figure 3.6a also shows the boundary conditions of the model. Due to the presence of tubular steel beams at the top and the bottom of the main wall on the internal face (Figure 3.5d), all nodes along these edges of the wall were restrained translationally in the Y direction (OOP direction). To model the mortar layer between the wall and the foundation in the experiments, the bottom face of the wall was connected to the environment using boundary interface elements that shared the same material properties as the other interface elements and were constrained along the Z direction. Return walls were constrained by C-shape steel channels which were simply connected to the supporting frame. For this reason, the translation along the Y direction was constrained at the midlines of the outer surfaces of the return walls. Additionally, along the midline of the outer surface of the left return wall, translations in the X direction were constrained to prevent rigid body movements. Besides, on the outer surfaces of the return walls, all nodes on each vertical edge were tied to its top node in X and Y directions so that these surfaces can keep planes when they rotate (Figure 3.6a). Here it is worthy to note that it can be difficult for the numerical models to accurately capture the boundary conditions in the experiments. For example, the lateral edges of the return walls were restrained with C-shape steel channels and were connected to steel frames with only 3 tiny steel trusses. It is therefore hard to determine whether the in-plane translation (in the X direction) of the wall should be constrained or not. Based on a sensitivity study with various boundary conditions for the return walls (Section 3.4.4), if the in-plane translation of the wall was constrained, two long vertical cracks along the intersections of the main wall and the return walls would take place, which was opposite to the experimental crack patterns and signified over-restraints.

The wall was initially loaded with self-weight and pre-compression in two sequential steps. For both steps, the Newton-Raphson iterative method was applied, and both the displacement and force norms should be satisfied for the convergence. The convergence tolerance was 0.01 for both norms. Next, evenly distributed loads were applied to the exterior face of the main wall. This load was arc-length controlled with the Quasi-Newton iterative method. Either the displacement or force norm should be satisfied. The tolerance norm was 0.01 for both norms. The central points of the solid walls were selected as the control points for the arc-length control. For the perforated walls, the central points of the lintels were selected as the control points for the arc-length control.

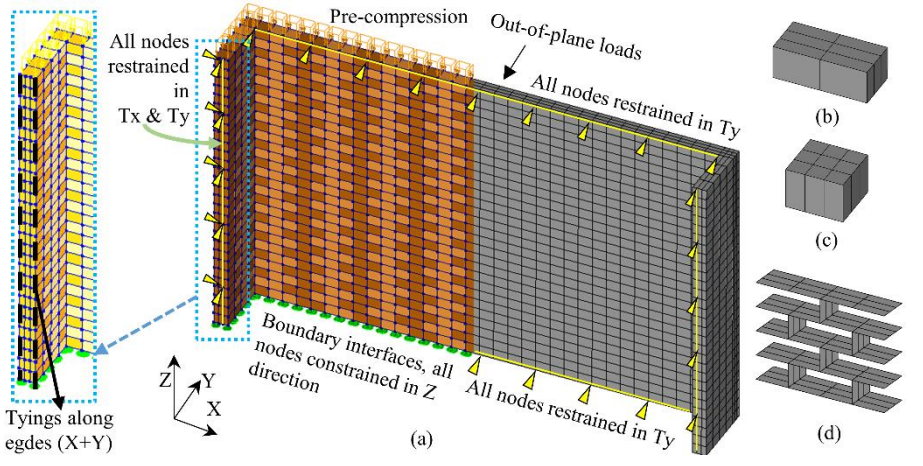

Figure 3.6. Modelling settings: (a) geometry, mesh, boundary conditions and loading of the model. Tx, Ty and Tz: d.o.fs constrained in X, Y and Z directions, respectively; (b) mesh of a complete brick; (c) mesh of a half brick at intersection; (d) mesh of interface elements.

3.4.2 Calibration of the input parameters

For the bricks, as presented in Table 3.2, the elastic modulus (E_b) and tensile strength (f_{bt}) were derived from the compression tests and bond wrench tests on the bricks, respectively, from the same experimental campaign (Griffith & Vaculik, 2007). Values of other parameters were assumed based on the literature since related tests were absent. The experimental study on the Mode-I fracture energy of bricks ($G^I_{f,b}$) is assumed to be 0.018 of the tensile strength of the bricks as recommended by Jafari (2021). As is observed from the experiments and the later numerical study (see Chapter 4), the tensile failure of the bricks is very limited. Therefore, varying the value of $G^I_{f,b}$ has negligible influence on the global structural behaviour. The Poisson's ratio (υ_b) is assumed as 0.16. The crack bandwidth (h_{cr}) was calculated as the cubic root of the element volume as suggested by Rots (1988).

Regarding the input parameters of interface elements (Table 3.3), only the bond wrench tests on the masonry were available from the experiments, from which the tensile strength of the cracking-shearing-crushing model can be deduced indirectly. Therefore, the calibration of the other input parameters was carried out based on available literature. After the boundary conditions of the wall were determined as in Section 3.2, the normal stiffness (k_{nn}) and shear stiffness (k_{ss} and k_{tt}) of the interface elements were calibrated to obtain a good agreement between numerical and experimental results for Wall 1, taking into account the relation between k_{nn} and k_{ss} (k_{tt}) as in Equation (3.6). The same Poisson's ratio adopted for the bricks (ν_b) was used for the calculation of k_{ss} (k_{tt}).

$$k_{ss}\ (k_{tt}) = \frac{k_{nn}}{2(1+\nu_b)} \tag{3.6}$$

The tensile strength of the interfaces (f_t) was assumed as 1/3 of the flexural strength from bond wrench tests (f_{xt}) as recommended by Milani et al. (2006) and Abdulla et al. (2017). The cohesion (c_0) was equal to f_t as recommended by Milani and Lourenço (2013b). Friction angle (φ) was taken as that of the half-scale bricks from a similar experimental campaign by Vaculik (2012). Mode-I fracture energy (G_f^{I}) was taken as 0.05 times of f_t referring to Rots et al. (1997); Milani and Lourenço (2013a, 2013b). Mode-II fracture energy (G_f^{II}) was taken as 10 times the Mode-I fracture energy as suggested by De Villiers (2019); Jafari (2021). Concerning the compressive strength (f_c) for the constitutive model, since crushed mortar joints were not reported at the end of the pushover tests by Vaculik (2012), f_c was set to a relatively high value and the post-peak parameters were set with dummy values. This modelling strategy, also applied by Abdulla et al. (2017) and D'Altri et al. (2019) aims at reducing numerical instability. The dilatancy angle (ψ) was set to zero, implying non-associated plasticity with zero uplifts upon shearing, because van der Pluijm et al. (2000) showed that the dilatancy is insignificant when tensile failure between bricks and mortar joints is the major failure mechanism. A sensitivity study concerning the input parameters is presented in Section 3.4.4.

Table 3.2. Input parameters of bricks

Elastic modulus E_b (MPa)	Poisson's ratio υ_b	Density γ (kg/m³)	Tensile strength f_{bt} (MPa)	Fracture energy $G^I_{f,b}$ (N/mm)
52,700	0.16	1,900	3.55	0.06

Table 3.3. Input parameters of interface elements

Regime	Parameter	Value
Elastic	Normal stiffness k_{nn} (N/mm³)	70
	Shear stiffness k_{ss} (k_{tt}) (N/mm³)	30
Tension	Tensile strength f_t (MPa)	0.21
	Mode-I fracture energy G_f^{I} (N/mm)	0.01
Shearing	Initial cohesion c_0 (MPa)	0.21
	Mode-II fracture energy G_f^{II} (N/mm)	0.11
	Friction angle φ (rad)	0.52
Compression	Compressive strength f_c (MPa)	16

3.4.3 Numerical results: two-way bending capacity and crack pattern

The results of the calibration against Wall 1 in terms of the load-displacement curve and crack progression are presented and discussed in this section. The displacement of Wall 1 was determined in the centre of the wall, as in the experiments. Besides, it is important to determine the state when the wall cracks into several rigid plates, hereinafter referred to as a rigid-plates crack pattern. This is because all analytical formulations evaluate the two-way bending capacity at the moment when the deformed shape of the wall consists of several rigid plane plates. It is, therefore, necessary to verify this assumption with the numerical results. The completion of

the rigid-plates crack pattern development is determined by satisfying the following two criteria at the same time: i) at the mid-span of the wall, the difference between the angle of the upper 1/2 height of the deformed wall and the undeformed wall, and that of the upper 1/4 height of the deformed wall and the undeformed wall (θ_3, and θ_2, respectively) should be less than 10%; ii) the difference between the angle of the upper section of the deformed wall above the central point of the diagonal crack and the undeformed wall (θ_1) and θ_3 should be less than 10% (Figure 3.7). After slight adaptions, these criteria are also suitable for narrow walls having central vertical cracks.

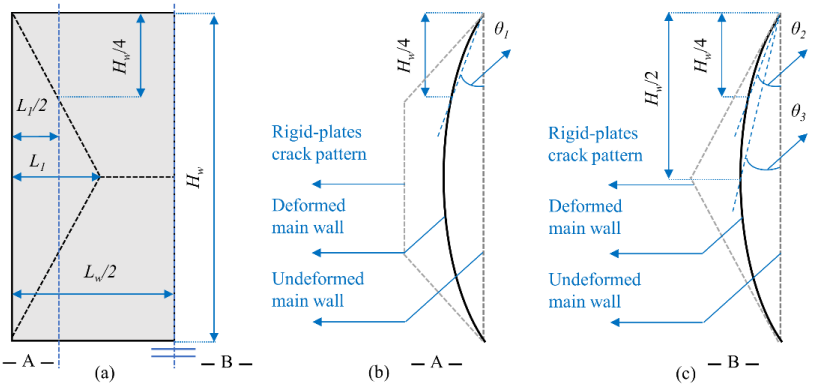

Figure 3.7. Determination of the completion of rigid-plates crack pattern: (a) idealised rigid-plates crack pattern shown with the left symmetric part; (b) deformed shape of the wall at section A; (c) deformed shape of the wall at section B (mid-span).

The deformed shape of Wall 1 at the end of the analysis is shown in Figure 3.8 with a deformation scaling factor of 50. The predicted initial stiffness and two-way bending capacity of the wall are in good agreement with the experimental results (Figure 3.9a). Figure 3.9b, c and d corresponding to 3 marked load levels A, B and C in Figure 3.9a show the onset of pre-peak cracking, the reaching of the two-way bending capacity and the completion of the rigid-plates crack pattern, respectively. Point D indicates the end of the analysis, which resulted from the divergence (for the other models in the following study, they either aborted due to the divergence or no convergence within 1000 iterations at the end). In the legends of interface crack openings, u = 0.003 mm and u = 0.233 mm correspond to the onset of cracking and fully opened crack when the tensile stress has reduced to 1/100 of the tensile strength f_t, respectively. The grey text in the legends indicates the percentage of integration points of the interface elements corresponding to each contour level. At load level A, when the initial stiffness of the wall starts to degrade, only 0.6% of integration points in the interface elements reach the onset of cracking at four corners at the bottom of the wall (Figure 3.9b). When the two-way bending capacity of the wall is reached (load level B), 16% of the integration points surpass the tensile strength and start to soften, though none of them is fully cracked. At the same time, diagonal and central cracks start to form. When 5% of the integration points on the interface elements have fully cracked, the rigid-plates crack pattern starts to form (Figure 3.9d, load level C). At this stage, the model shows the typical crack pattern

of long URM walls in two-way bending, i.e. diagonal cracks and a central horizontal crack, which matches well with the experimental crack pattern shown in Figure 3.9a. After this, the major cracks keep opening, and the deformed shape of the wall remains the same. Compressive failure of interfaces was not detected and stresses remained in the elastic regime. Besides, only a few bricks showed smeared cracking at the corners of the main wall (Figure 3.9d). This is in agreement with the experimental evidence that cracks in bricks are insignificant (Vaculik, 2012; Ravenshorst & Messali, 2016; Damiola et al., 2017). Note that in Figure 3.9d the colour contour of the cracks in bricks is different from that of the interfaces. The largest value of crack width (shown in red in the figure) is 0.41 mm. Additionally, obvious shear sliding along the diagonal cracks was detected, both in in-plane and out-of-plane directions, as shown in Figure 3.9e and f, respectively.

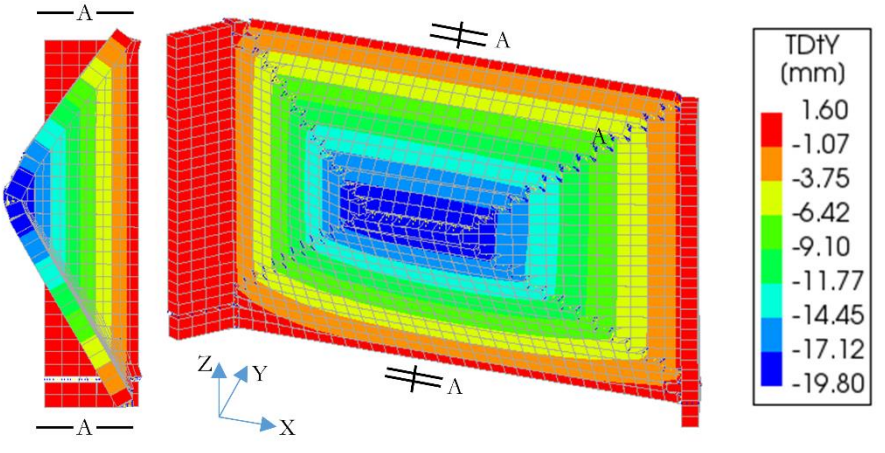

Figure 3.8. Deformation of Wall 1 in the Y direction at the end of the analysis (TDtY in the legend). Deformation scaling factor: 50.

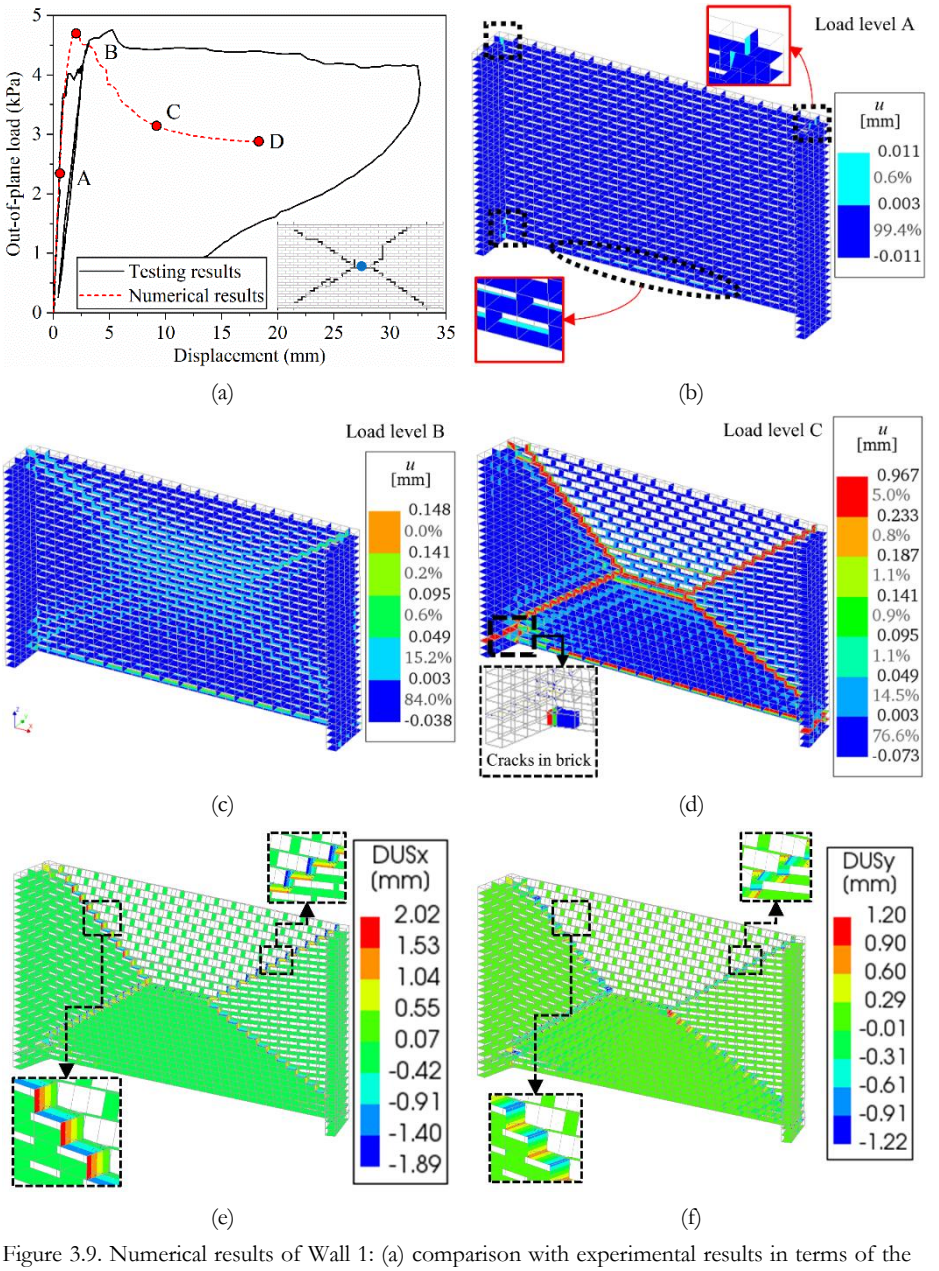

Figure 3.9. Numerical results of Wall 1: (a) comparison with experimental results in terms of the load-displacement curve. The crack pattern from the experiment is shown at the bottom right. The control point of the displacement is marked with a blue solid dot; (b)-(d) discrete crack progression at relevant load levels (u (mm): crack opening); (e) and (f): shear sliding of the interfaces in the in-plane direction (DUSx) and out-of-plane direction (DUSy). Deformation scaling factor: 30.

Although the numerical model matches well with the experimental results in terms of the initial stiffness, two-way bending capacity and crack pattern, the two-way bending capacity drops more sharply than that in the experiment (Figure 3.9a). This

phenomenon has also been observed by Karimi Ghaleh Jough and Golhashem (2020), who also used the 3D simplified brick-to-brick modelling approach to predict the two-way bending capacity of URM walls. Additionally, according to the shake-table tests by Graziotti et al. (2019) and monotonic static tests by Lawrence (1983) on the URM walls in OOP two-way bending, the wall capacity decreased sharply after reaching the peak. In the next section, sensitivity studies will be carried out to investigate if the mesh size, material properties and boundary conditions will influence the post-peak behaviour of the wall.

3.4.4 Sensitivity study on mesh size, material properties and boundary conditions

Sensitivity studies were carried out to examine whether the adjustment of the mesh size, material properties and boundary conditions can reduce the difference between the numerical and experimental results regarding the post-peak behaviour. The first sensitivity study is about the mesh size. Three mesh types have been compared: Mesh type (1) is shown in Figure 3.6b, the bricks are divided into 2×1×3; Mesh type (2) divides the bricks into 2×2×3; while Mesh type (3) divides the bricks into 2×1×4. Figure 3.10 and Figure 3.11 show that the load-displacement relations and crack patterns derived from various meshed models are very similar to each other. In this study, Mesh type (1) with the least number of elements is used for the sake of computational efficiency.

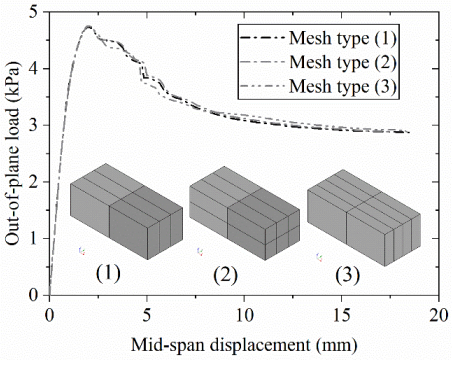

Figure 3.10. Mesh sensitivity study.

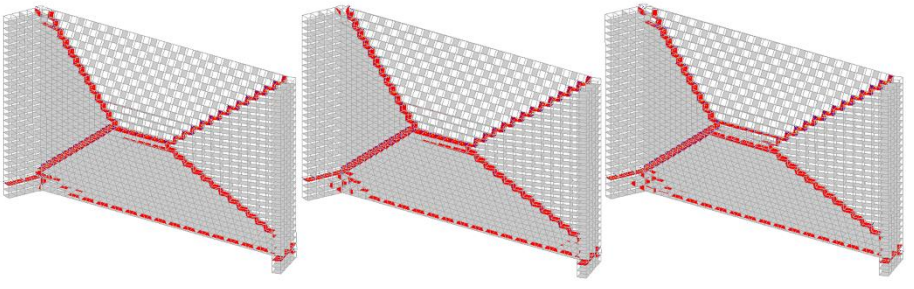

Figure 3.11. Crack patterns at the end of the analysis of the models with various mesh sizes.

The second sensitivity study is about the input parameters. The tested models are listed in Table 3.4. In each model, only one parameter was varied based on the calibrated model, while the other four variables were kept unchanged. At the same time, the condition that c_0 should be larger than $f_t \tan\varphi$ was kept to satisfy Equation (3.3). For this reason, the various cases of the input parameters are on different scales. For example, c_0 varies between 0.5 to 2, while f_t only varies between 0.75 to 1.5. The results of the sensitivity study are shown in Figure 3.12. Figure 3.12a, d, e and f show that within the studied ranges, the two-way bending capacity and residual force of the wall are insensitive to the tensile strength f_t, mode-II fracture energy G_f^{II}, friction angle φ and dilatancy angle ψ. Figure 3.12b and c show that the two-way bending capacity is sensitive to the mode-I fracture energy G_f^{I} and the initial cohesion c_0, while the residual force is not. In all numerical cases, the difference between the two-way bending capacity and the residual force is larger than that in the experiment.

Table 3.4. Inputs for the material sensitivity study.

Variable	Model name of the sensitivity study	Values of					
		f_t (MPa)	G_f^I (N/mm)	φ (rad)	c_0 (MPa)	G_f^{II} (N/mm)	ψ (rad)
-	Calibrated model	0.21	0.0105	0.523	0.21	0.105	0
ft	$0.75f_t$	0.158	0.0105	0.523	0.21	0.105	0
	$1.5f_t$	0.315	0.0105	0.523	0.21	0.105	0
G_f^I	$0.5G_f^I$	0.21	0.00525	0.523	0.21	0.105	0
	$2G_f^I$	0.21	0.021	0.523	0.21	0.105	0
φ	0.75φ	0.21	0.0105	0.392	0.21	0.105	0
	1.25φ	0.21	0.0105	0.654	0.21	0.105	0
c_0	$0.75c_0$	0.21	0.0105	0.523	0.16	0.105	0
	$1.5c_0$	0.21	0.0105	0.523	0.32	0.105	0
G_f^{II}	$0.5G_f^{II}$	0.21	0.0105	0.523	0.21	0.053	0
	$2G_f^{II}$	0.21	0.0105	0.523	0.21	0.210	0
ψ	Dilatancy considered	0.21	0.0105	0.523	0.21	0.105	0.37

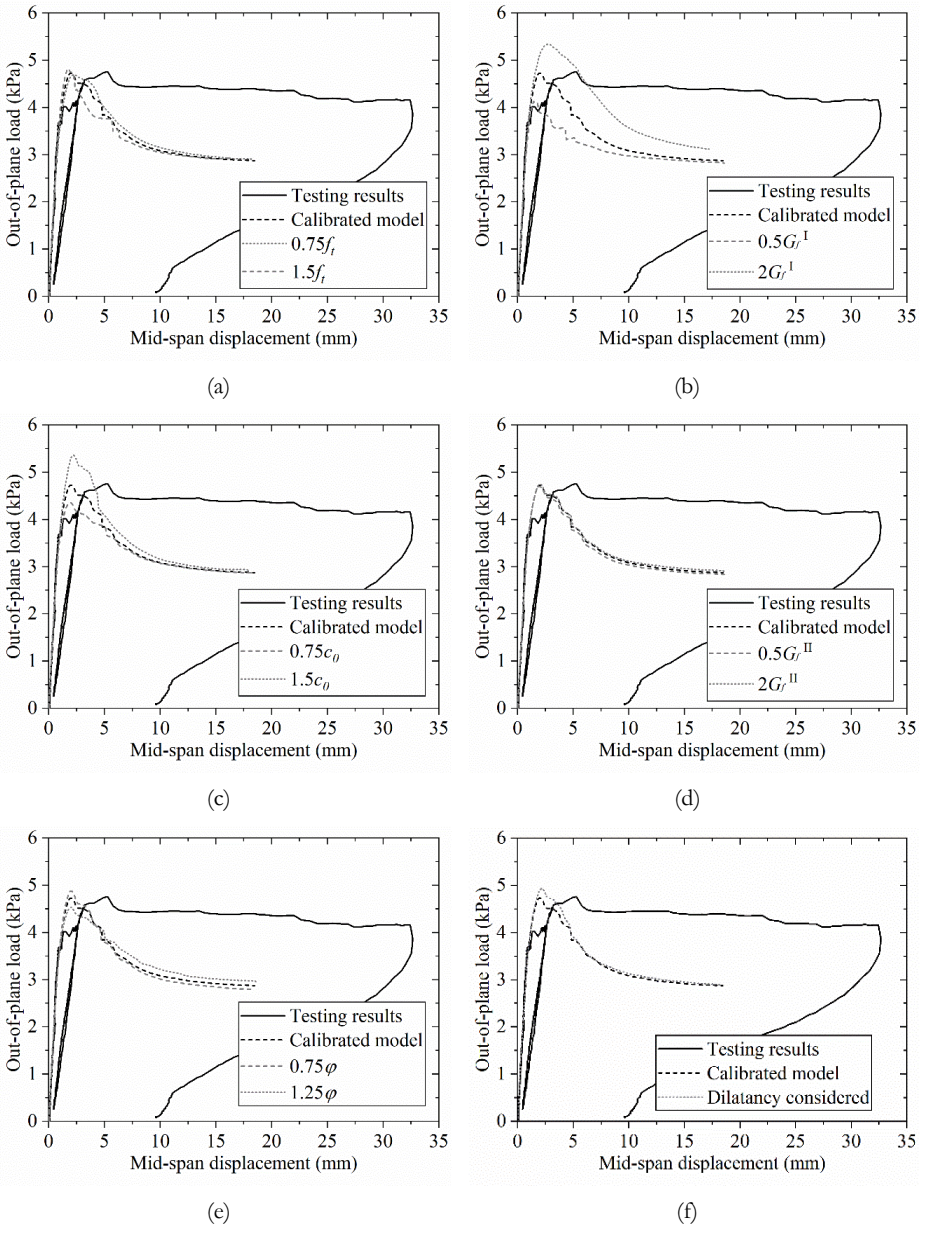

Figure 3.12. Material sensitivity study (a)-(f) on: tensile strength f_t, mode-I fracture energy G_f^I, cohesion c_0, mode-II fracture energy G_f^{II}, friction angle φ and dilatancy angle ψ as a single variable, respectively.

The third sensitivity study has been carried out to examine whether changing the boundary conditions can reduce the post-peak drop and improve the ductility of the wall. Different from the calibrated model, the lateral edges of the return walls are translationally and rotationally constrained. The comparison shows that when

the lateral edges of the return walls are fixed, cracks develop between the intersection of the main wall and the return walls (Figure 3.13a), and the crack pattern is different from that in the experiment (Figure 3.9a). Besides, changing the boundary conditions increases the two-way bending capacity, but does not reduce the post-peak drop, as shown in Figure 3.13b.

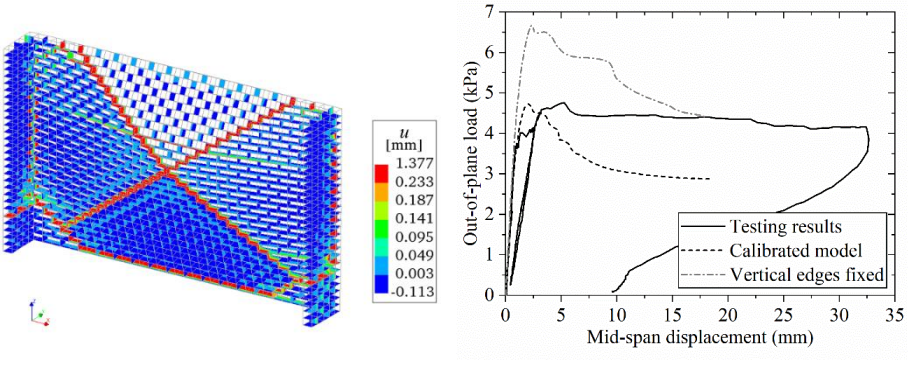

(a) (b)

Figure 3.13. Sensitivity study on the rotational stiffness of the boundary conditions: (a) the crack pattern of the wall with lateral edges fixed; (b) force-displacement curves of the calibrated model and the model with the vertical edges fixed.

3.5 Validation of the numerical modelling approach against walls 2-7

In this section, the calibrated model against Wall 1 is applied in analysing the other seven walls in the same experimental campaign. For Wall 3-8, the steel tubes used as lintels above the openings were modelled with linear elastic solid elements using the material properties of steel (Elastic modulus: 210 GPa; Poisson's ratio: 0.3). Since the presence of openings caused difficulty to determine the completion of the rigid plates, the crack patterns at the end of the analysis were compared with those from experiments for simplicity. Results are shown in Table 3.5 and Table 3.6.

Comparing the numerical and experimental results, it can be seen that the numerical models predict the crack patterns to a rather accurate degree (Table 3.5). Specifically, the stepwise diagonal cracks are well captured. Smeared cracks in the bricks are not presented here, since they only take place at the corners of the walls, similar to Wall 1 (Figure 3.9d). Compressive failure of bricks and interface elements are not detected.

A good agreement is found in terms of initial stiffness and two-way bending capacity (Table 3.6). Special attention should be paid to Wall 2. In the experiment, Wall 2 was not sufficiently constrained at the bottom in the out-of-plane direction, which led to large sliding after being loaded (Vaculik, 2012). Therefore, the predicted initial stiffness K_{ini} and two-way bending capacity w of Wall 2 are higher than those of the experimental results (

Table 3.6). Apart from this, a maximum deviation of 14% is found in terms of initial stiffness. This suggests that the boundary conditions and material properties in the elastic range are well-calibrated. As for the two-way bending capacity, the numerical results match well with the experimental results (Mean Absolute Percentage Error: 11%). These differences can be attributed to not considering the spatial variability in the modelling. According to Li et al. (2016), if the material properties vary randomly among different mortar joints on the same wall, the error between predictions and the tested two-way bending capacity can range from -25% to 30%. In the present study, deterministic values of the material properties were used for all interfaces on the same wall. The predicted differences are likely to be caused by excluding the spatial variability of the material properties. Overall, the accuracy of the calibrated model was validated by applying it to the other seven walls. Therefore, the validated model can be used for further parametric study.

Table 3.5. Validation of the numerical model about the load-displacement curves and crack pattern. Experimental crack patterns are shown in the load-displacement graphics. Positions of recorded displacements are marked with blue dots. Cracks, where ft reduces to its 1/100, are marked with red. Deformation scaling factor: 20.

Wall	Load-displacement curve[1]	Crack pattern of numerical model[2]
2	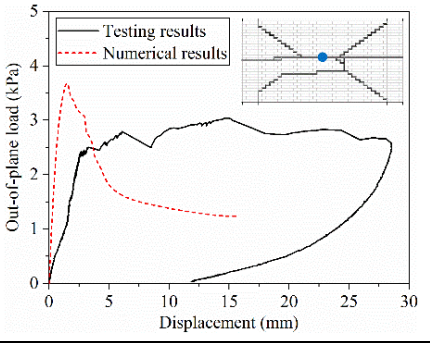	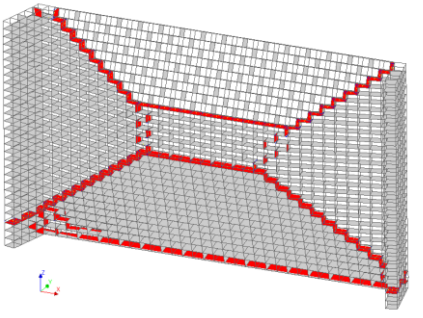
3	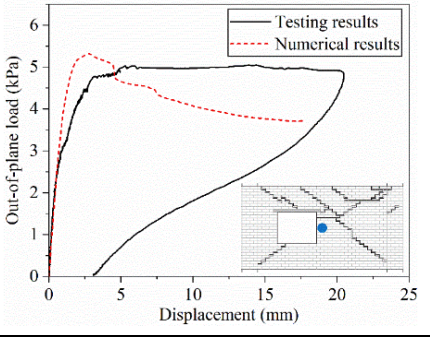	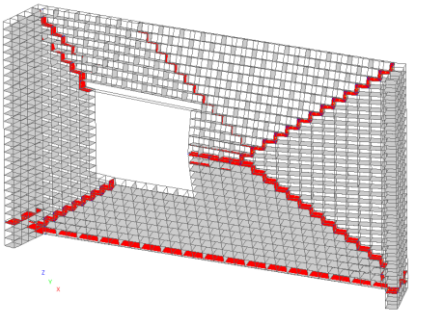

Table 3.5. Validation of the numerical model about the load-displacement curves and crack pattern. Experimental crack patterns are shown in the load-displacement graphics. Positions of recorded displacements are marked with blue dots. Cracks, where ft reduces to its 1/100, are marked with red. Deformation scaling factor: 20.

Wall	Load-displacement curve[1]	Crack pattern of numerical model[2]
4	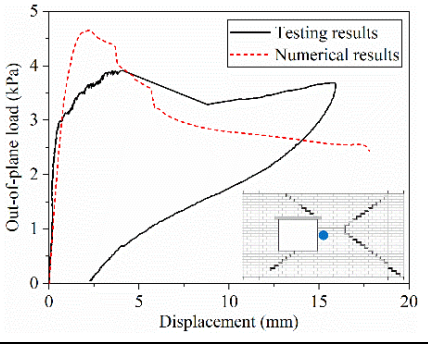	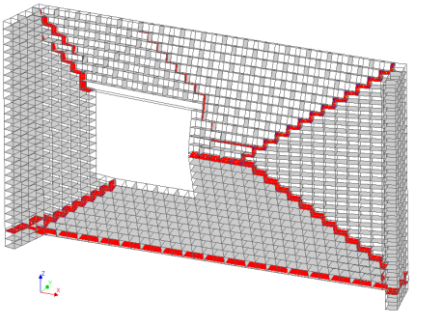
5	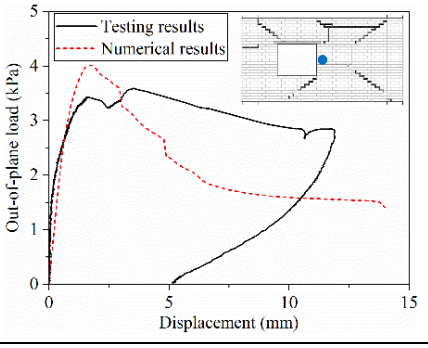	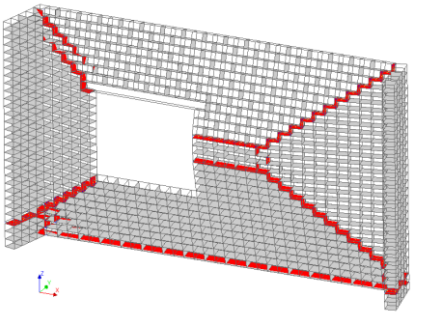
6	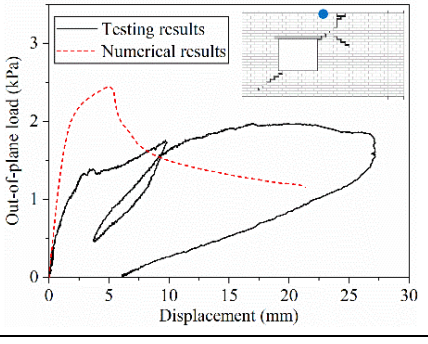	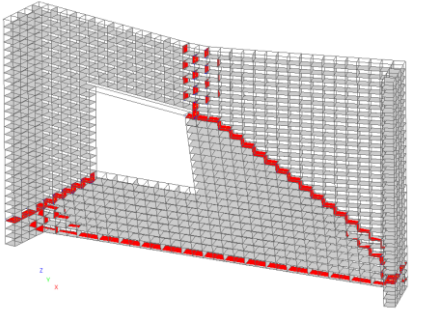

Table 3.5. Validation of the numerical model about the load-displacement curves and crack pattern. Experimental crack patterns are shown in the load-displacement graphics. Positions of recorded displacements are marked with blue dots. Cracks, where ft reduces to its 1/100, are marked with red. Deformation scaling factor: 20.

Wall	Load-displacement curve[1]	Crack pattern of numerical model[2]
7	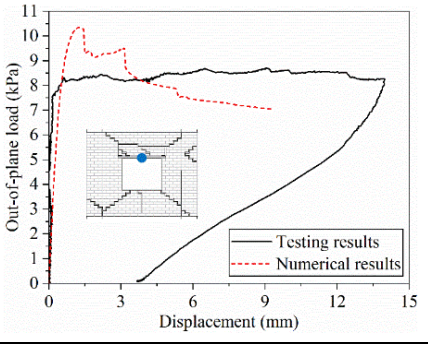	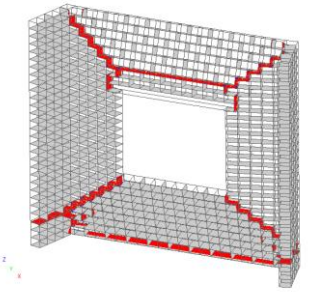
8	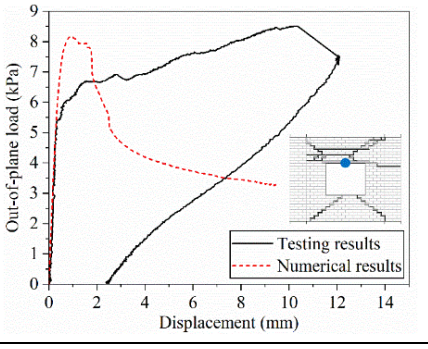	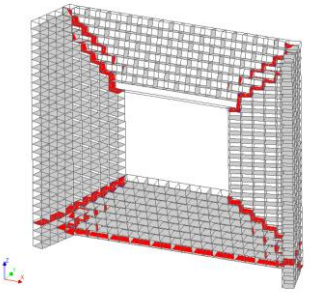

Table 3.6. Comparison in terms of initial stiffness and two-way bending capacity between the numerical and experimental results.

Wall	Experiments		Numerical results		Errors (numerical results to experiments)	
	Initial stiffness K_{ini} (kPa/mm)	Two-way bending capacity w (kPa)	Initial stiffness K_{ini} (kPa/mm)	Two-way bending capacity w (kPa)	Regarding K_{ini}	Regarding w*
1	4.27	4.76	4.37	4.73	2%	-1%
2	0.72	3.04	4.36	3.68	505%	21%
3	5.38	5.05	4.60	5.32	-14%	5%
4	5.34	3.91	4.58	4.65	-14%	19%
5	4.86	3.59	4.53	4.01	-7%	12%
6	1.10	1.97	1.23	2.44	12%	24%
7	19.95	8.71	19.78	10.36	-1%	19%
8	17.37	8.52	19.74	8.17	14%	-4%

* Mean Absolute Percentage Error $\left(\frac{1}{n}\sum\frac{|w_{num}-w_{exp}|}{|w_{exp}|}\right)$: 11% (Wall 2 is excluded).

3.6 Comparison with other modelling approaches

In this section, the results of the 3D simplified brick-to-brick modelling are compared with those of the other two commonly used modelling approaches, namely, continuum modelling and 3D detailed brick-to-brick modelling. With the continuum modelling, bricks and mortar joints are not distinguished, and the masonry structure is modelled as a continuum body. With the detailed brick-to-brick modelling, both mortar joints, bricks and interfaces between them are modelled according to real dimensions (Lourenco & Rots, 1997; D'Altri et al., 2019). The comparison is based on the solid Wall 1 used for the model calibration in Section 3.4. The mesh size, geometry, boundary and loading conditions are kept unchanged. The geometry of models and zoom-in view of masonry constituents are presented in Figure 3.14. Regarding the constitutive models, for the 3D detailed brick-to-brick modelling, the combined cracking-shearing-crushing model is assigned to the interfaces between mortar joints and bricks, while the rotating smeared cracking model with exponential softening in tension and elastic behaviour in compression is assigned to the mortar joints and bricks. For the masonry in the continuum model, the rotating smeared cracking model with exponential softening in tensions and parabolic curve in compression is assigned. The input parameters for the constitutive models are from the experimental records (Griffith & Vaculik, 2007; Vaculik, 2012) or are calibrated according to recommendations from the literature (Jafari, 2021; Jafari et al., 2022). Details about the input parameters are listed in Table 3.7. Note this section aims to simply compare the computational efficiency and the ability to capture the crack patterns of the modelling approaches.

A comprehensive comparison is out of the scope of this study and is suggested to be investigated in separate research.

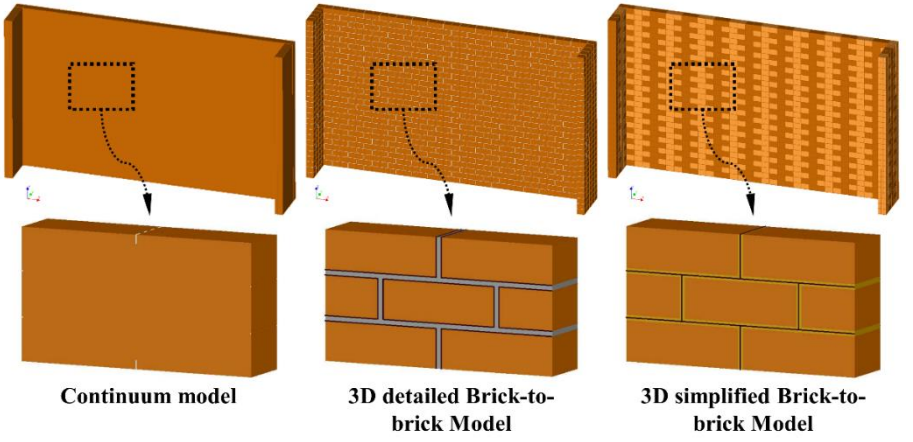

Figure 3.14. The geometry of models and zoom-in view of masonry constituents by various approaches.

Table 3.7. Input parameters for various modelling approaches.

Constitutive model		Input parameter*	Modelled constituents of					
			Continuum model	3D detailed model			3D simplified model	
			Masonry	Brick	Mortar	Interface	Brick	Mortar &Interface
Rotating cracking	Linear material properties	Elastic modulus (N/mm²)	7080	52700	442	-	52700	-
		Poisson's ratio	0.16	0.16	0.16	-	0.16	-
	Tensile behaviour (exponential softening)	Tensile strength (N/mm²)	0.205	3.55	3.92	-	3.55	-
		Mode-I fracture energy (N/mm)	0.0328	0.355	0.036	-	0.355	-
	Compressive behaviour (parabolic)	Compressive strength (N/mm²)	16	Elastic	17	-	Elastic	-
		Compressive fracture energy (N/mm)	31.5		34	-		-
Combined cracking-shearing-crushing	Linear properties	Normal/Shear stiffness (N/mm³)	-	-	-	140/60	-	70/30
	Tensile behaviour (exponential softening)	Tensile strength (N/mm²)	-	-	-	0.21	-	0.21
		Mode-I fracture energy (N/mm)	-	-	-	0.01	-	0.01

Table 3.7. Input parameters for various modelling approaches.

Constitutive model	Input parameter*	Modelled constituents of					
		Continuum model	3D detailed model			3D simplified model	
		Masonry	Brick	Mortar	Interface	Brick	Mortar &Interface
Shear behaviour (exponential softening)	Cohesion (N/mm^2)	-	-	-	0.21	-	0.21
	Friction angle (rad)	-	-	-	0.523	-	0.523
	Mode-II fracture energy (N/mm)	-	-	-	0.105	-	0.105
Compressive behaviour (hardening-softening)	Compressive strength (N/mm^2)		-	-	16	-	16
	Compressive fracture energy (N/mm)	-	-	-	31.5	-	31.5

* The values of the input parameters are from the experimental records (Griffith & Vaculik, 2007; Vaculik, 2012) or are calibrated according to recommendations from the literature (Jafari, 2021; Jafari et al., 2022).

Figure 3.15 presents the load-displacement curves of various modelling approaches. The continuum model predicts a hardening behaviour before the end of the analysis, which is different from the testing results. The 3D detailed and simplified brick-to-brick models predict similar trends in the load-displacement relations, that is the post-peak capacity of the wall drops sharply. Figure 3.16b shows that with the continuum model, the overall crack pattern can be predicted in several wide banded areas, though the detailed stepped failure along the diagonal cracks cannot be shown. By contrast, both the simplified and detailed brick-to-brick modelling can locate the cracks between the bricks therefore more precisely and sharply predicting the crack patterns (Figure 3.16c-e). The detailed modelling can further predict the failure of mortar joints that are not modelled in the simplified modelling (Figure 3.16c).

Table 3.8 compares the computational efficiency of the modelling approaches. When the central point of the wall reaches a displacement of 8 mm, the continuum model consumes the least time (1 hour 9 minutes), the 3D simplified brick-to-brick model requires a longer period, over 4 hours, while the 3D detailed modelling is almost 6 times slower than the simplified model (over 23 hours). This can be explained by the number of elements and degrees of freedom in various models. Though the mesh size is the same among the models, the continuum model consists of the least number of elements, since only solid elements are necessary. By contrast, the simplified model has not only an equivalent number of solid elements as the continuum model but also an extra amount of interface elements, which significantly increases the computing time. The numbers of the solid and interface elements of the detailed model are nearly 4 and 5 times those of the simplified

model, respectively. This is because the mortar joints and adhesions between the bricks and mortar joints are both modelled in the detailed model, which significantly increases the amount of the elements. Besides, all the elements are assigned with physical nonlinearity. Therefore, the detailed model consumes much longer time than the other two approaches. Overall, the 3D simplified brick-to-brick modelling is the most suitable for the scope of this research, considering its ability to precisely capture the crack patterns in URM walls with a reasonable computational time.

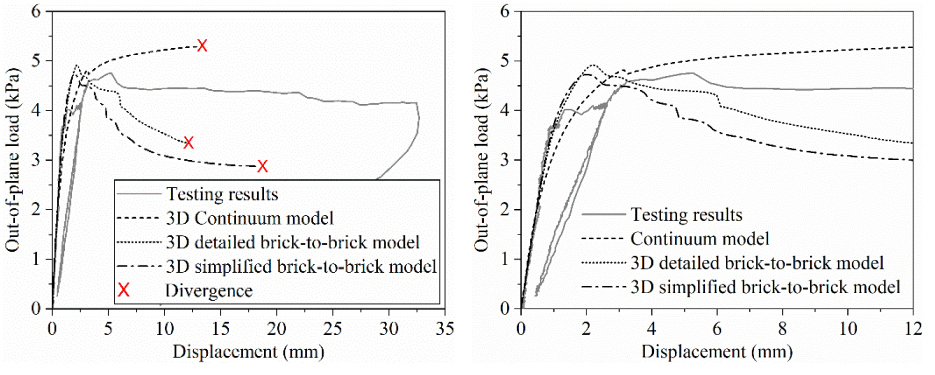

Figure 3.15. (a) Load-displacement curves of various modelling approaches; (b) zoom-in graphic.

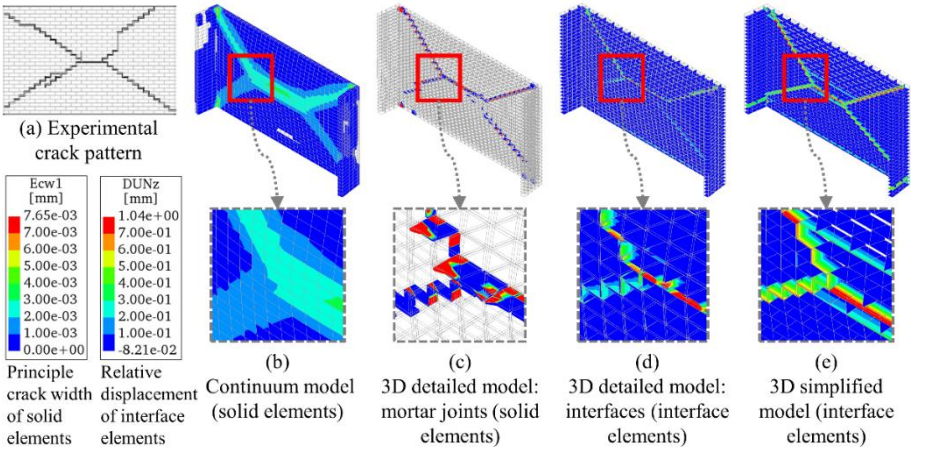

Figure 3.16. Comparison of the crack patterns from various modelling approaches. Crack patterns are taken when the wall's central point reaches a displacement of 8 mm. With the continuum model, the smeared cracks on the inner surface of the main wall are presented. Ecw1: principle crack width. DUNz: normal relative displacement. Deformation scale factor: 20.

Table 3.8. Comparison of the computational efficiency of the modelling approaches.

Modelling approach	3D Continuum model	3D detailed brick-to-brick model	3D simplified brick-to-brick model
Number of solid elements	4,089	14,535	4,089
Number of interface elements	-	25,662	5,775
Number of degrees of freedom	245,340	2,103,876	522,540
Computing time to reach a displacement of 8 mm *	1 hour 9 minutes	23 hours 15 minutes	4 hours 18 minutes

* The processor of the employed desktop is Intel(R) Xeon(R) CPU E5-1650.

3.7 Conclusions

This chapter aims at building reliable numerical models to study the influence of the geometric parameters on the two-way bending capacity of URM walls. First, the 3D brick-to-brick modelling approach is introduced, followed by its calibration of the numerical models based on the selected experimental benchmark. Then, a sensitivity study is carried out to examine the influence of the material properties on the numerical results. Next, the validation of the numerical models is carried out on the remaining samples in the same experimental campaign. Finally, a comparison between the applied approaches with other strategies is presented. The conclusions are drawn as follows.

A good agreement is found between the numerical and experimental results in terms of the two-way bending capacity, initial stiffness and crack pattern. Even so, the numerical results show a drop in the wall capacity in the post-peak stage, while the quasi-static experiments provide a more ductile post-peak behaviour. A sensitivity study shows that the low post-peak capacity in the calibrated model is insensitive to the material properties and boundary conditions. However, the numerically observed post-peak response is in line with other findings in the literature regarding experimental and numerical works (Lawrence, 1983; Graziotti et al., 2019; Karimi Ghaleh Jough & Golhashem, 2020).

Compared with the continuum modelling and the 3D detailed brick-to-brick modelling, the 3D simplified brick-to-brick modelling is a good compromise to capture the response at the component level, in terms of wall capacity and crack pattern, with limited computational costs. In conclusion, the employed 3D simplified brick-to-brick modelling approach and the calibrated input parameters are evaluated to be reliable to address the purpose of this study.

Chapter 4

INFLUENCE OF PRE-COMPRESSION AND ASPECT RATIO[3]

As discussed in Chapter 2, of various geometric parameters influencing the two-way bending capacity of URM walls, the pre-compression and aspect ratio (defined as the wall height to length with the height kept constant) have not been sufficiently studied. To better understand their influence, in this chapter, an extensive parametric study was conducted by employing the 3D simplified brick-to-brick modelling approach calibrated and validated in Chapter 3. Results show that the two-way bending capacity of the URM walls is exponentially related to the aspect ratio and linearly related to the pre-compression. Besides, the influence of the pre-compression and aspect ratio on the two-way bending capacity can be interdependent. Additionally, when the pre-compression is relatively low, a wall does not crack in a localised manner into several rigid plane plates at the two-way bending capacity. Instead, the deformed shape of the wall approximates a curved surface, indicating distributed rather than localized cracking at two-way bending capacity. Furthermore, the two-way bending capacity is much higher than the residual force when the rigid-plates crack pattern is formed in the post-peak stage. The parametric study also shows that torsional failure of bed joints is the predominant failure mechanism for URM walls in OOP two-way bending, and its contribution to the two-way bending capacity generally increases as the pre-compression or aspect ratio increases. Finally, the numerical results were compared with the predictions by three major analytical formulations, namely Eurocode 6, Australian Standard for Masonry Structures (AS 3700) and Willis et al. (2006). As a result, the relations between the two-way bending capacity and the aspect ratio or pre-compression derived from the numerical models could not be accurately predicted by the analytical formulations. The quantitative relationships between the pre-compression/aspect ratio and the two-way bending capacity determined in this chapter will be incorporated into the improved analytical formulation proposed in Chapter 6.

[3] This chapter is based on the published journal article: Chang, L.-Z., Rots, J. G., & Esposito, R. (2021). Influence of aspect ratio and pre-compression on force capacity of unreinforced masonry walls in out-of-plane two-way bending. *Engineering Structures, 249*. Minor modifications have been made to suit the thesis.

4.1 Introduction

Investigations on unreinforced masonry (URM) walls subjected to natural hazards, such as earthquakes, identify the out-of-plane (OOP) failure as one of the most common failure mechanisms (D'Ayala & Paganoni, 2011; Moon et al., 2014; Penna et al., 2014; Sorrentino et al., 2016). Concerning the OOP failure, two modes can be distinguished in URM walls: one-way (mainly vertical) bending in which lateral edges of walls are not supported; two-way bending in which at least one lateral edge of walls is supported in addition to the supports at the top and bottom. Compared with walls in one-way bending, walls in two-way bending are more widely encountered in practice considering that the lateral edges of walls are usually supported by pillars or return walls. Therefore, the failure of URM walls in OOP two-way bending can be more common. According to the investigations by Dizhur and Ingham (2015), failure of URM cavity walls in two-way bending was responsible for 57% of all OOP wall failures during the 2010/2011 Canterbury earthquakes. However, unlike the OOP one-way bending mechanism which has been well studied both experimentally and analytically (Doherty et al., 2002; Derakhshan et al., 2013b; Walsh et al., 2015; Graziotti et al., 2016), research on the OOP two-way bending mechanism is relatively limited. Furthermore, the research on the crucial factors which can have a major influence on the two-way bending capacity (defined as the peak pressure of walls) of URM walls in OOP two-way bending, such as the aspect ratio and pre-compression, is even rarer, especially in experiments (Chang, Messali, et al., 2020). Consequently, the accuracy of the evaluation of the influence of these crucial factors on the two-way bending capacity of walls by the analytical formulations can be hardly validated.

Experimental campaigns have been carried out worldwide to improve the understanding of the OOP two-way bending mechanism, but the total database is limited in numbers. These experiments include monotonic pushover tests (Chong, 1993; Ng, 1996; van der Pluijm, 1999a, 2001; Derakhshan et al., 2018), quasi-static cyclic tests (Griffith et al., 2007; Messali et al., 2017; Damiola et al., 2018; Padalu et al., 2020b) and shake-table tests (Vaculik & Griffith, 2017b; Graziotti et al., 2019). Although these experiments successfully verified the most significant characteristics of the URM walls in OOP two-way bending such as the initial stiffness, two-way bending capacity and crack pattern, the influence of crucial factors, namely the aspect ratio (defined as the wall height to length with the former kept constant) and pre-compression, was either not specifically studied or not sufficiently studied due to a limited number of experimental samples in the experimental campaigns (Chang, Messali, et al., 2020). For example, based on 15 experimental samples with aspect ratios (height to length) of 0.67, 1 and 1.5, Ng (1996) observed that the two-way bending capacity of the walls increases as the aspect ratio increases; based on 8 experimental samples subjected to pre-compression of 0, 0.05 or 0.1 MPa, Griffith and Vaculik (2007) found that the two-way bending capacity of the walls increases as the pre-compression increases. These results provided general tendencies of the influence of the aspect ratio and pre-compression on the two-way bending capacity of URM walls. However, the number of comparable samples is too limited to

quantify the relations between these crucial factors and the two-way bending capacity. This brings difficulty in validating the accuracy and application range of current analytical formulations. Additionally, 4 tested walls from (Griffith & Vaculik, 2007) combining aspect ratios of 0.6 and 1 and pre-compression levels of 0 and 0.1 MPa showed that as the aspect ratio changes, the increment of the two-way bending capacity caused by the pre-compression can be quite different. Although this phenomenon was observed from a limited number of experimental samples, it indicates that the influence of the aspect ratio and pre-compression on the two-way bending capacity can be interdependent, which requires a more extensive study.

As an alternative to physical experiments, finite element analysis offers the possibility of virtual experiments which are effective and cost- and time-efficient provided the models are well-calibrated. Among various finite element modelling approaches, the 3D simplified brick-to-brick modelling is one of the most promising methods to simulate at the structural components level. The 3D simplified brick-to-brick modelling assumes that cracks and frictional slip mainly take place in mortar joints. Therefore, the mortar joints are modelled as zero-thickness interface elements, while the bricks are extended in dimensions and modelled as solid elements (Rots et al., 1997). With this method, a balance can be found between the computational efficiency and accurate identification of the crack pattern of walls. Some studies have been conducted to predict the OOP two-way bending mechanism using the 3D simplified brick-to-brick modelling (Abdulla et al., 2017; D'Altri et al., 2018; D'Altri et al., 2019). Results show that major characteristics, such as stepped diagonal cracks of walls could be well captured. However, according to the author's knowledge, this modelling method has not been applied in an attempt to quantify the relations between the aspect ratio/pre-compression and the two-way bending capacity of URM walls.

Even though experimental and numerical samples are limited in number to compose an abundant database for various wall geometries and pre-compression levels, various analytical formulations have been proposed to evaluate the two-way bending capacity of URM walls. Most analytical formulations are based on the following two methods or their variations: the Yield Line method proposed by Haseltine, Tutt, et al. (1977) and the Virtual Work method proposed by Lawrence and Marshall (2000). The two methods share the following similar assumptions: i) when reaching the two-way bending capacity, a wall cracks into several plane plates, ii) the crack pattern is pre-assumed, and diagonal cracks start right from wall corners, iii) the two-way bending capacity is evaluated by the principle of energy conservation, namely, moment resistance contributions along the predefined cracks are equal to the bending moment caused by OOP loads. Some fundamental differences between the two methods are i) the calculation of the moment resistance capacity along cracks, ii) the Yield Line method assumes that all cracks develop simultaneously and the moment resistance along all cracks contributes to the two-way bending capacity; in contrast, the Virtual Work method assumes that horizontal cracks at the centre of the wall develop quite early, thus their contribution to the two-way bending capacity can be omitted, iii) the Yield Line method evaluates the

slope of the diagonal cracks as an independent variable, while the Virtual Work method determines this slope based on the dimension of bricks. The correctness of these assumptions is still debatable in academia. For example, Vaculik (2012) argued that the Yield Line Method can be unconservative due to the assumption that cracks develop simultaneously. In opposite, Padalu et al. (2020a) concluded that this assumption can be accurate in evaluating the two-way bending capacity based on a Crack-line Method (a variation of the Yield Line Method). This requires further evidence about crack progression in the need of justifying the assumptions and evaluating the two-way bending capacity of walls. The Yield Line Method was adopted by Eurocode 6 (2012). Eurocode 6 is limited to an application range provided by its Annex E for single-leaf walls with a thickness of less than 250 mm. Beyond this scope, supplementary analysis is required for the users. Besides, the predictions by Eurocode 6 are in general unconservative (Chang, Messali, et al., 2020). The Virtual Work Method was adopted by the Australian Standard for Masonry Structures AS 3700 (2018), of which the expressions for bending moment capacity are empirical and dimensionally inconsistent. Based on rational deductions, Willis et al. (2006) proposed new formulas for the calculations of bending moment capacities. However, the torsional strength of bed joints which is crucial to the two-way bending capacity is still empirical and requires further evaluations (Graziotti et al., 2019; Chang, Messali, et al., 2020).

Apart from the above-mentioned drawbacks, a comparison by Chang, Messali, et al. (2020) between the predictions by the analytical formulations and the experimental results shows that limitations also lie in the formulations on evaluating the influence of the pre-compression and aspect ratio. For example, the formulations predict that the two-way bending capacity is not sensitive to the pre-compression, which is against the experimental results. Moreover, the predictions on the influence of the aspect ratio cannot be validated due to a lack of sufficient experimental or numerical results. Also, it is still unknown whether the analytical formulations can predict the potential interdependency between the influence of the aspect ratio and pre-compression as elaborated above. Overall, these call for an extensive study on the influence of the aspect ratio and pre-compression level on the two-way bending capacity of URM walls.

Based on the discussions above, research gaps can be revealed here: i) the available experimental samples and numerical results are limited in number in the need of sufficiently evaluating the influence of the aspect ratio/pre-compression; ii) the evaluation by the analytical formulations on the influence of the aspect ratio/pre-compression on the two-way bending capacity needs to be improved. Corresponding to these research gaps, the aims of this study are built up: i) quantify the relations between the aspect ratio/pre-compression and the two-way bending capacity of walls; ii) find the improving directions for the analytical formulations in evaluating the influence of the aspect ratio/pre-compression on the two-way bending capacity. For these purposes, nonlinear finite element analyses adopting 3D simplified brick-to-brick models are employed in this study. A combined cracking-shearing-crushing model is used for interface elements at bed joint and

head joint locations, while a total-strain based rotating smeared cracking model is used to simulate the cracks in bricks. A parametric study considering the aspect ratio and pre-compression as variables is carried out based on the validated model. The influence of the pre-compression/aspect ratio on the load-displacement curves, two-way bending capacity, crack progression, deformation profiles and joint failure mechanisms have been explored. The relations between the two-way bending capacity and the aspect ratio/pre-compression are established with nonlinear curve fitting (Section 4.2). Eventually, results are compared with three analytical formulations including Eurocode 6, AS 3700 and Willis et al. (2006). Differences between the predictions by the analytical formulations and the numerical results are pointed out and explained. Suggestions regarding improvements to the analytical formulations are proposed. (Section 4.3).

4.2 Parametric study

To study the influence of aspect ratio and pre-compression, a parametric study was carried out based on the calibrated and validated numerical model in Chapter 3. Six different values of aspect ratio and nine values of pre-compression were selected for a total of 54 analysis combinations (Figure 4.1). The aspect ratio κ (wall height to length, H_w/L_w) ranged between 0.3 and 2 as suggested by Annex E in Eurocode 6 (2012). For each wall geometry, the values of pre-compression σ_v range from 0 to 0.5 MPa. The value of 0.5 MPa was estimated in the following way. Considering a typical two-storey detached or terraced house with an attic (Esposito et al., 2019; Miglietta et al., 2021), the pre-compression from one concrete floor (spanning 6 m and 0.2 m thick) can be 0.15 MPa, the variable load on each floor can be 0.03 MPa, the self-weight from the upper masonry walls can be 0.05 MPa per storey, the load from the roof can be 0.05MPa. The pre-compression on the top edge of the bottom wall then sums up to values close to around 0.5 MPa. Apart from the aspect ratio and pre-compression, all the other settings, e.g. input parameters of materials, return walls, bonding patterns and boundary conditions, are the same as presented in Section 3. Please note the results of the parametric study are limited to typical weak mortar/strong brick masonry which generally represents aged or historical masonries.

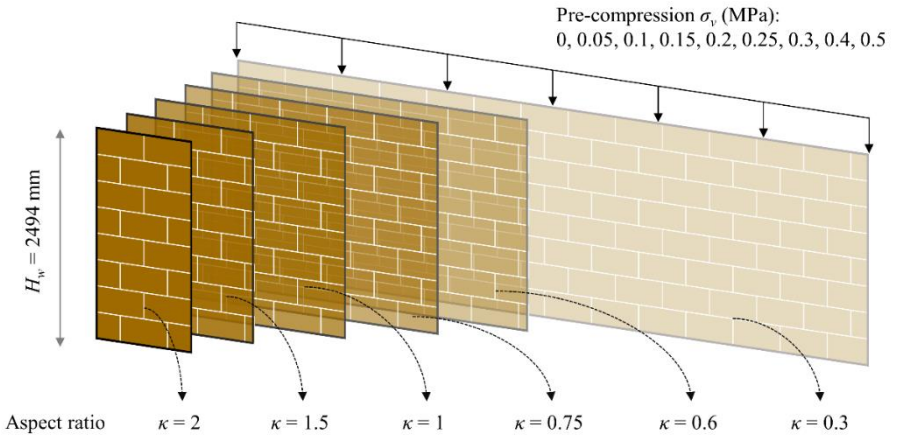

Figure 4.1. Schematic diagram of wall configurations in the parametric study (return walls are not presented).

4.2.1 Load-displacement curve and two-way bending capacity

Figure 4.2 shows the load-displacement curves of all walls in the parametric study. In this figure, the two-way bending capacity is marked with blue dots; the instants of forming rigid-plates crack patterns are determined according to the criteria proposed in Section 3.4 and marked with solid red dots; for walls that did not reach the rigid-plates crack patterns, instants of crack patterns are marked with empty red dots at the end of the analysis. A general tendency observed is that as the aspect ratio κ or pre-compression σ_v increases, the two-way bending capacity increases accordingly. The relation between the two-way bending capacity and the aspect ratio, and the relation between the two-way bending capacity and the pre-compression, are graphically presented in Figure 4.3a and b, respectively. Results show that the two-way bending capacity can follow an exponential relation with aspect ratio and a linear relation with pre-compression, respectively. This was confirmed by a preliminary fitting analysis selecting aspect ratio or pre-compression as the single independent variable and the two-way bending capacity as the dependent variable. Additionally, Figure 4.3b shows that as the aspect ratio increases, the slopes of the curves also increase. This implies that the influence of the pre-compression and aspect ratio can be interdependent.

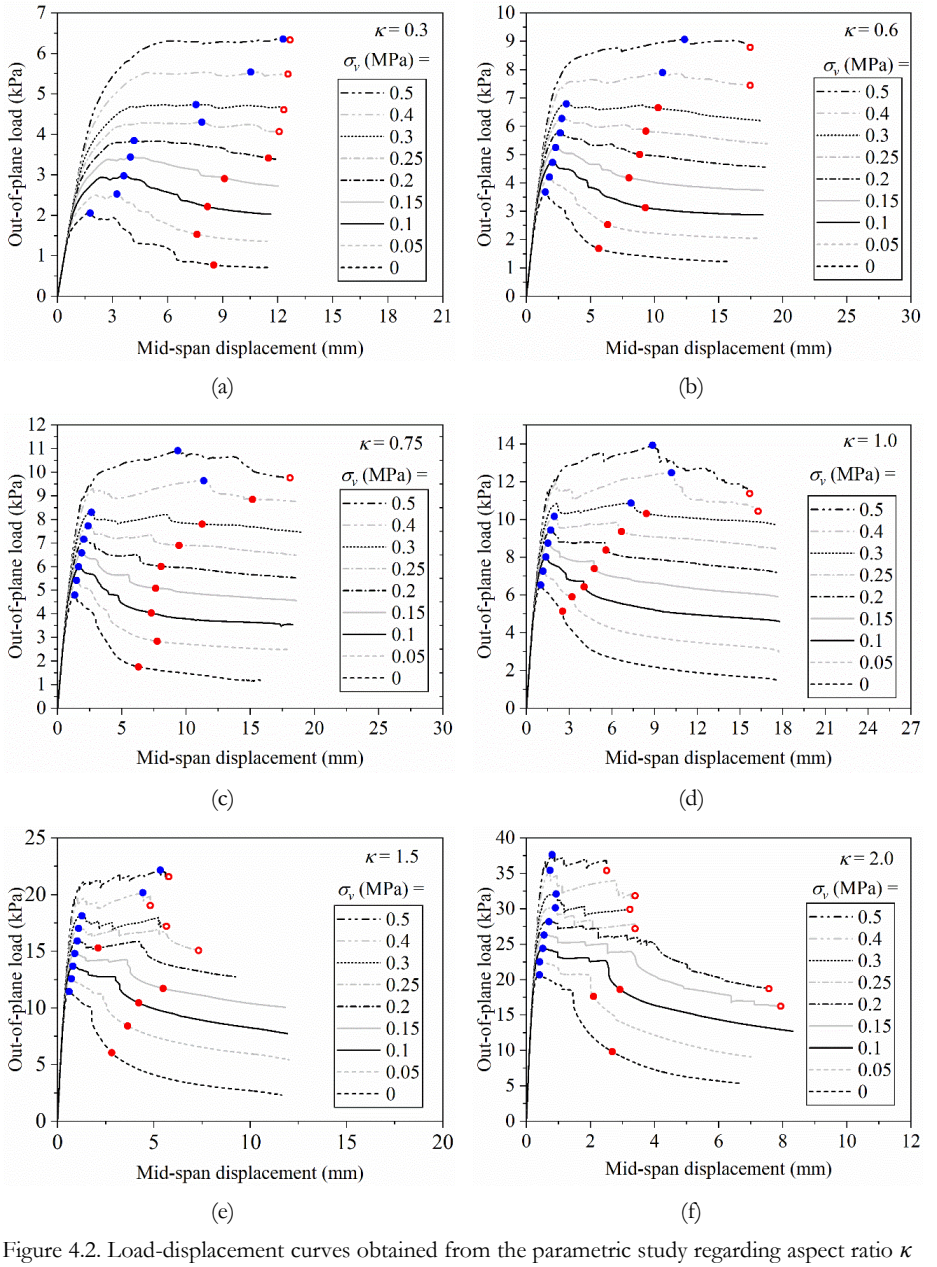

Figure 4.2. Load-displacement curves obtained from the parametric study regarding aspect ratio κ and pre-compression σ_v: (a) κ = 0.3; (b) κ = 0.6; (c) κ = 0.75; (d) κ = 1.0; (e) κ = 1.5; (f) κ = 2.0. Two-way bending capacity w is marked with blue dots. Instants of forming rigid-plates crack patterns are marked with solid red dots. For walls that did not reach the rigid-plates crack patterns, instants of crack patterns are marked with empty red dots at the end of the analysis.

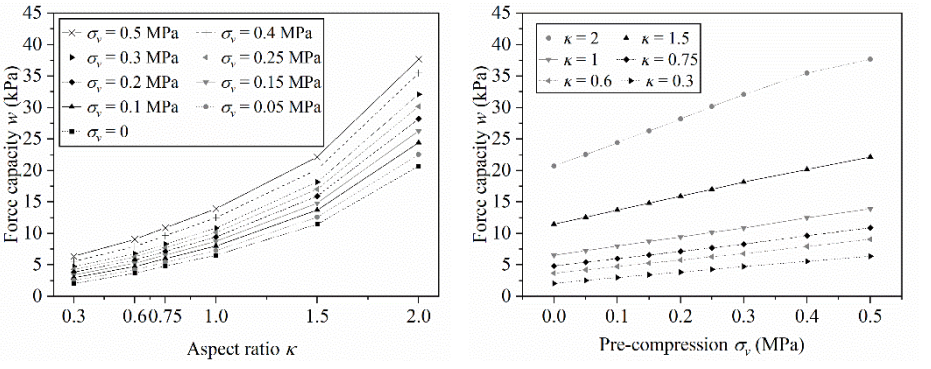

(a) (b)

Figure 4.3. Two-way bending capacity w concerning (a) aspect ratio κ and (b) pre-compression σ_v.

4.2.2 Crack propagation and deformation profile

Table 4.1 presents the crack progression of walls with all aspect ratios subjected to pre-compression of 0.1, 0.3 and 0.5 MPa. For each wall, crack progression is shown at two stages, namely at the two-way bending capacity and final crack pattern. Concerning the latter, crack patterns of the walls corresponding to the instants marked with solid and empty red dots in Figure 4.2 are presented. At the two-way bending capacity, interface crack opening u larger than 0.003 mm (onset of the crack of integration points) and smaller than 0.233 mm (integration points fully crack) is marked in blue; u larger than 0.233 mm is marked in red. At the final crack pattern, u is only marked in red when it is larger than 0.233 mm. Table 4.1 shows that when the walls reach the two-way bending capacity, multiple diagonal and central cracks develop simultaneously. Furthermore, at this stage integration points on interface elements hardly fully crack unless the pre-compression is over 0.3 MPa. At the final crack pattern, the pre-compression has very limited influence on the deformed shapes of the walls, while the crack patterns change obviously as the aspect ratio increases, i.e., the central horizontal crack transforms into a central vertical crack. The tensile failure of the bricks in various cases is shown in Figure 14. The results show that the failure of the bricks is primarily taking place at the corners of the wall and has almost no effect on the overall behaviour regardless of the pre-compression and aspect ratio.

Table 4.1. Crack progression of walls (deformation scaling factor: 30).

	κ = 0.3		κ = 0.6	
	at two-way bending capacity*	at final crack pattern#	at two-way bending capacity	at final crack pattern
σ_v = 0.1 MPa	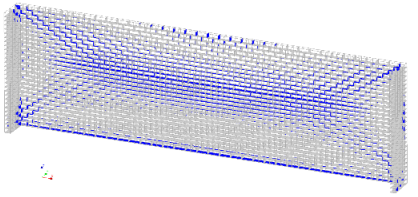	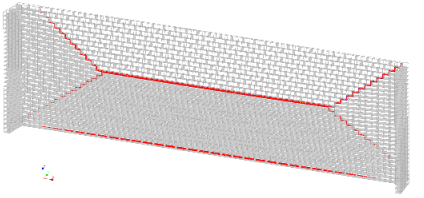	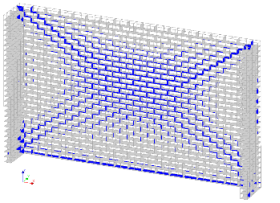	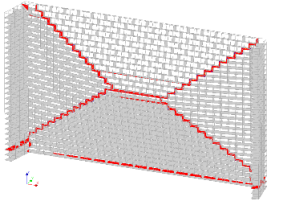
σ_v = 0.3 MPa	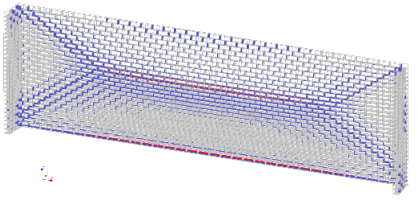	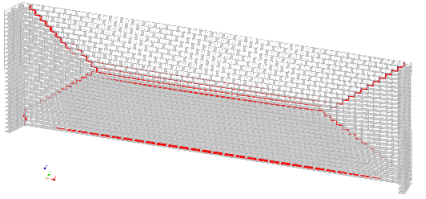	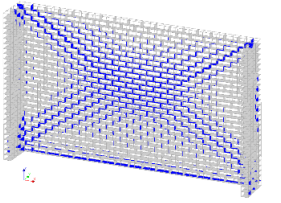	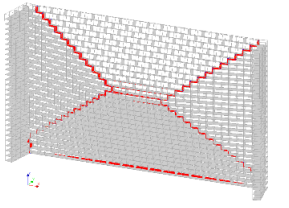
σ_v = 0.5 MPa	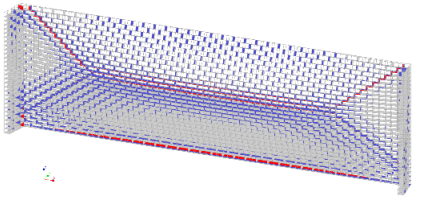	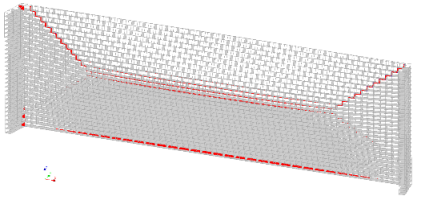	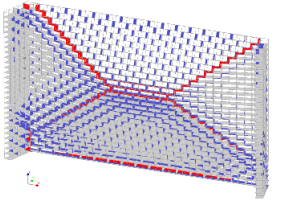	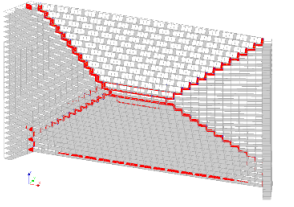

	κ = 0.75		κ = 1		κ = 1.5		κ = 2	
	at two-way bending capacity	at final crack pattern	at two-way bending capacity	at final crack pattern	at two-way bending capacity	at final crack pattern	at two-way bending capacity	at final crack pattern
σ_v = 0.1 MPa	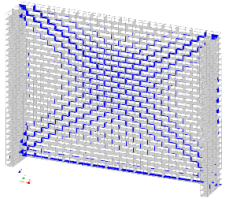	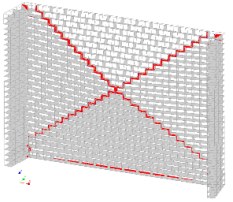	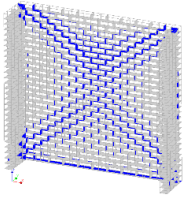	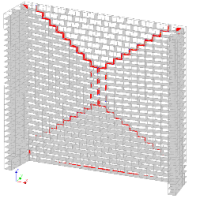	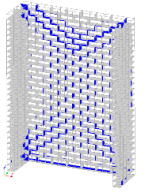	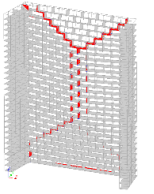	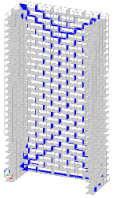	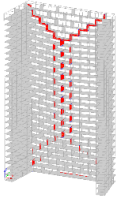
σ_v = 0.3 MPa	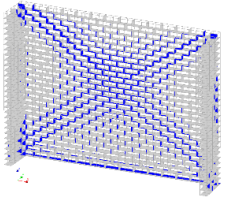	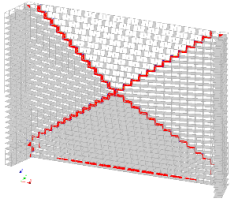	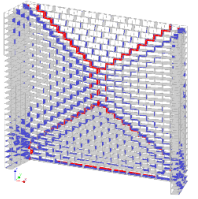	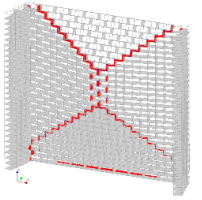	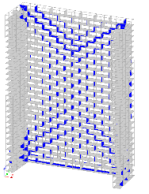	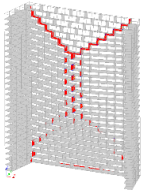	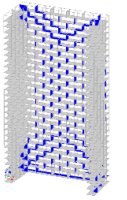	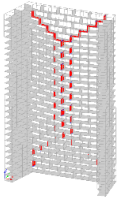
σ_v = 0.5 MPa	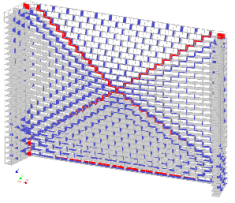	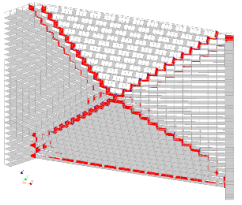	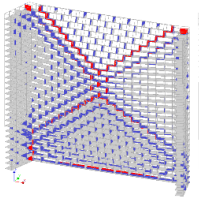	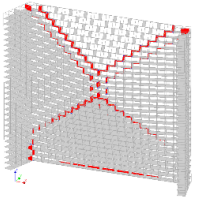	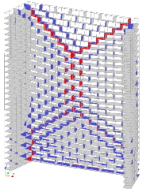	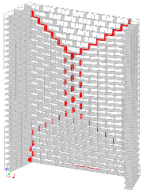	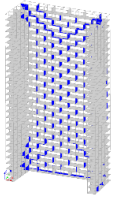	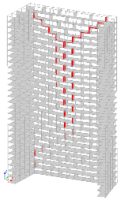

* Crack openings (u) larger than 0.003 mm and smaller than 0.233 mm are marked in blue; crack openings larger than 0.233 mm are marked in red.

\# Only crack openings larger than 0.233 mm are marked in red.

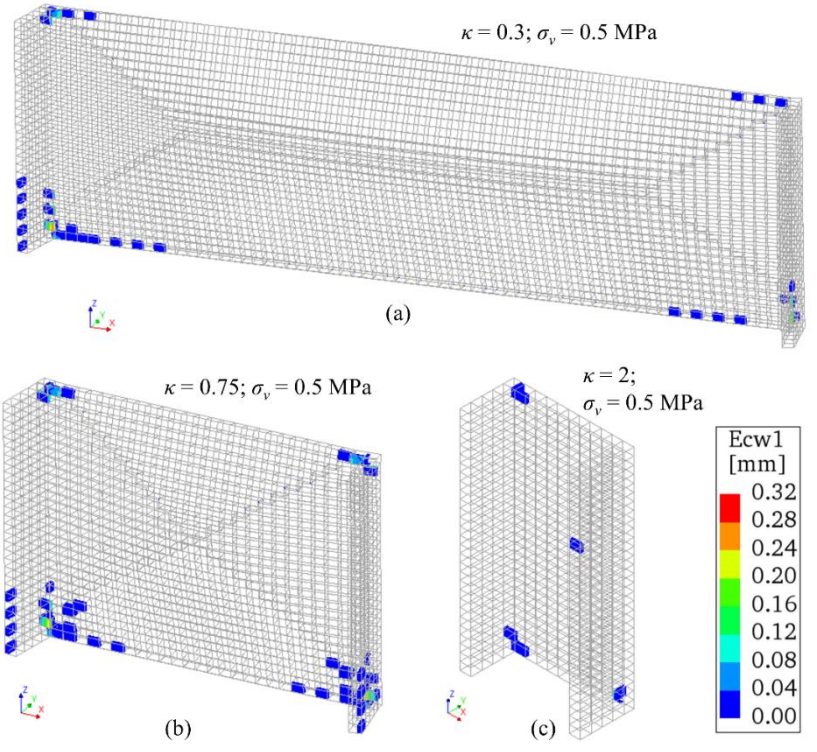

Figure 4.4. The tensile failure of the bricks in cases: (a) $\kappa = 0.3$, $\sigma_v = 0.5$ MPa; (b) $\kappa = 0.75$, $\sigma_v = 0.5$ MPa; (c) $\kappa = 2.0$, $\sigma_v = 0.5$ MPa. Ecw1 is the principle crack width.

The deformation profiles of four representative walls at different instants are shown in Figure 4.5. Results show that when the pre-compression is low (0.1 MPa), the deformation profiles of the walls at the two-way bending capacity approximate curved surfaces, while those at the rigid-plates crack pattern are identical to each other and are close to bi-linear lines (Figure 4.5a,c). When the pre-compression is high (0.5 MPa), the rigid-plates crack pattern does not form at the end of the analysis, although the deformation profiles are close to bi-linear lines (Figure 4.5b, d). Furthermore, the differences between the two-way bending capacity w and the force at rigid-plates crack pattern w_{cp} of the walls can be large especially when the pre-compression is relatively small, as shown in Figure 4.6. This is because on one hand, the increase of the pre-compression increases the arching effect. On the other hand, the increase of the pre-compression increases the friction and shear fracture energy between the interfaces. Therefore, the wall needs to dissipate more energy to reach the two-way bending capacity. These effects together increase the ductility of the wall. In contrast, current analytical formulations assume that the two-way bending capacity is reached at the rigid-plates crack pattern. The above-mentioned observations from numerical results, however, indicate that this assumption can

lead to large inaccuracy in evaluating the two-way bending capacity, especially for walls under low pre-compression. Therefore, the deformation shape at the two-way bending capacity is suggested to be re-evaluated to improve the accuracy of the analytical formulations.

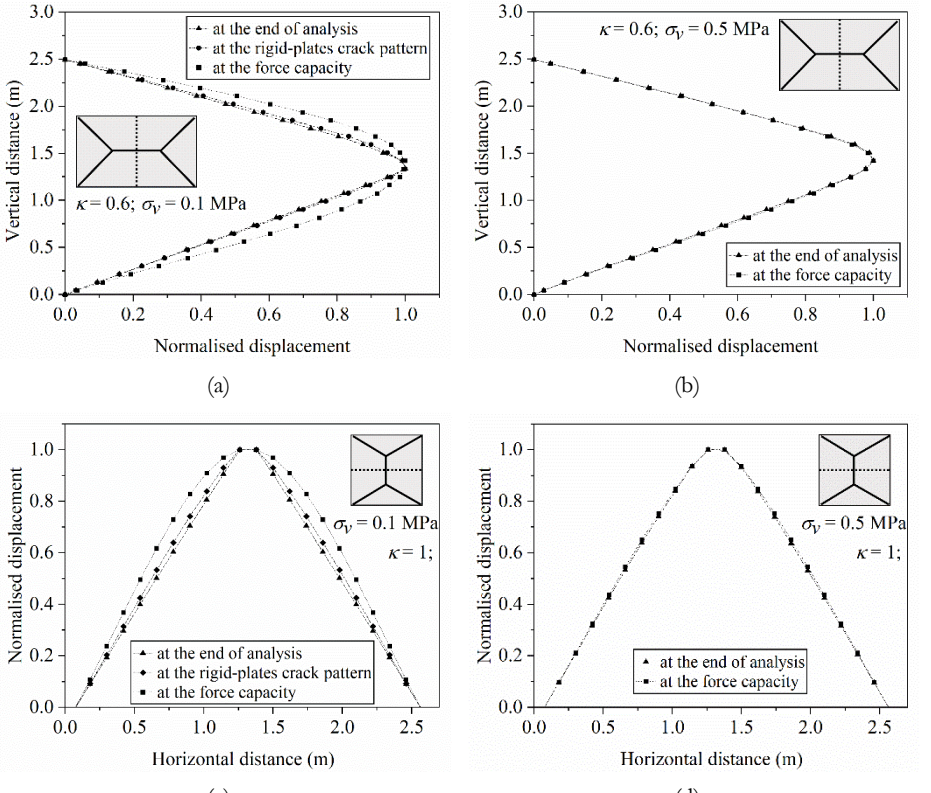

Figure 4.5. Deformation profiles of cases: (a) κ = 0.6, σ_v = 0.1 MPa at mid-span; (b) κ = 0.6, σ_v = 0.5 MPa at mid-span; (c) κ = 1, σ_v = 0.1 MPa at mid-height; (d) κ = 0.6, σ_v = 0.5 MPa at mid-height.

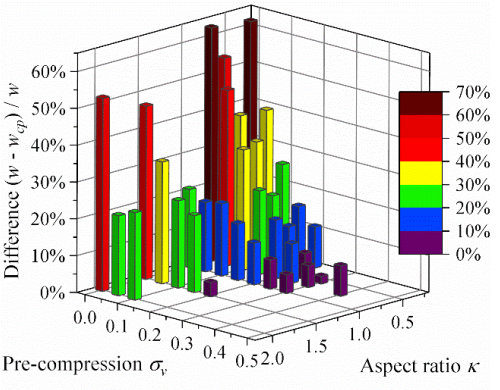

Figure 4.6. Differences between the two-way bending capacity w and the force at the final crack pattern w_{cp} (walls not reaching rigid-plates crack pattern are excluded).

4.2.3 Failure mechanisms of joints

Under OOP two-way bending, generally, the crack pattern of the URM walls is "X" shaped (Figure 4.7a). Besides, four kinds of joint failure mechanisms, namely bending and torsional failure of bed and head joints, majorly contribute to the two-way bending capacity of walls (Figure 4.7b) (Willis et al., 2006). Considering this, it is important to determine how the pre-compression or aspect ratio influences the performance of these failure mechanisms, therefore, influencing the two-way bending capacity. With this purpose, the following procedure was built for the comparison of the dissipated energy among different walls: i) major cracks, in which diagonal and horizontal/vertical cracks can be easily distinguished, were determined based on the final crack patterns as shown in Figure 17a and Table 7; ii) along the major cracks, crack failure was categorised into five kinds: bending and torsional failure of bed and head joints at diagonal cracks, and bending failure of bed joints at central horizontal cracks or bending failure of head joints at central vertical cracks; iii) dissipated mode-I and mode-II fracture energy of interface elements were selected as indicators of the bending and torsional behaviour of joints, respectively; iv) dissipated mode-I and mode-II fracture energy of a single joint were calculated separately from the start of loading to the moment of reaching the two-way bending capacity; v) dissipated energy of counted joints on the major cracks was summed according to crack failure categories; vi) contributions of dissipated energy of different joint mechanisms were compared.

On one single joint, the total dissipated mode-I and mode-II fracture energy due to bending and torsion, respectively, were calculated using the following equations:

$$E_{GfI} = \left(\sum_{j=1}^{n} \sum_{i=1}^{t} \sigma_{j,i} \cdot (u_{j,i} - u_{j,i-1}) \right) \cdot \frac{A_{joint}}{n} \tag{4.1}$$

$$E_{GfII} = \left(\sum_{j=1}^{n} \sum_{i=1}^{t} \tau_{j,i} \cdot (v_{j,i} - v_{j,i-1}) \right) \cdot \frac{A_{joint}}{n} \tag{4.2}$$

where E_{GfI} and E_{GfII} are total fracture energy dissipated by bending and torsion in a single joint, respectively; t is the step when the wall reaches the two-way bending capacity; n is the number of integration points on one joint; σ and τ are normal and shear stress, respectively; u and v are normal and shear relative displacement, respectively; A_{joint} is the area of a joint.

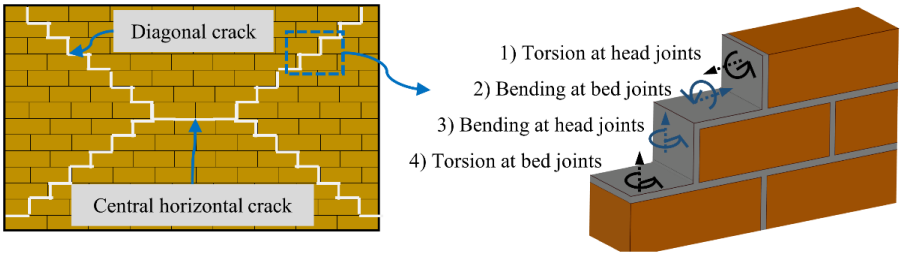

Figure 4.7. The calculation for fracture energy dissipated in joints: (a) major cracks along which fracture energy is calculated; (b) joint failure mechanisms.

To study the influence of the pre-compression on the performance of the joint failure mechanisms, walls of aspect ratio 0.6 were compared. The positions of the major cracks are the same for all walls. Results in Figure 4.8a show that generally the fracture energy dissipated by all joint failure mechanisms increases as the pre-compression increases. This suggests that all failure mechanisms contribute to the increase of the two-way bending capacity as the pre-compression increases. When the pre-compression is above 0.3 MPa, the dissipated fracture energy increases sharply. This is because the walls subjected to high pre-compression reach their two-way bending capacity quite late, and the cracks develop more completely thus leading to a high dissipation of fracture energy. Proportions of contributions by different joint failure mechanisms at different levels of pre-compression are shown in Figure 4.8b. Results show that the contribution by the torsional failure of bed joints at diagonal cracks is predominant and increase as the pre-compression increases. The contributions by the torsional failure of head joints and bending failure of bed joints at diagonal cracks are close to each other and decrease as the pre-compression increases. The contribution of the bending failure of head joints at diagonal cracks is relatively small and decreases when the pre-compression is over 0.3 MPa. The contributions of the bending failure of bed joints at the central horizontal cracks are nearly negligible.

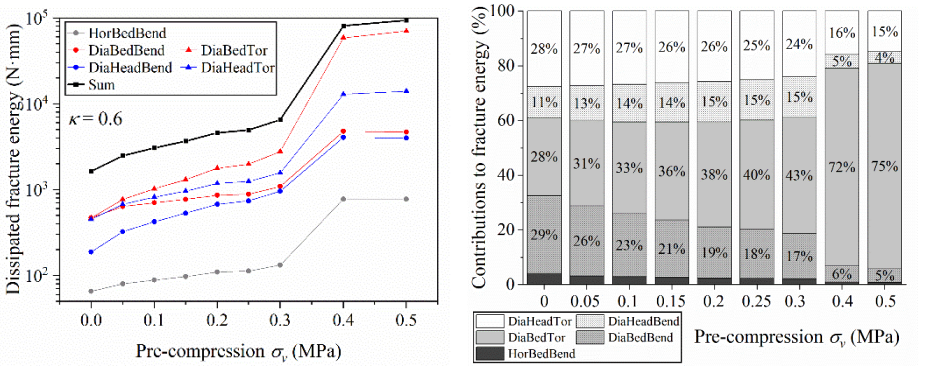

(a) (b)

Figure 4.8. Influence of the pre-compression on the joint failure mechanisms: (a) dissipated fracture energy by the failure mechanisms; (b) proportions of contributions by the failure mechanisms (abbreviations in the legend: "Dia": diagonal cracks; "Hor": central horizontal cracks; "Bed": bed joints; "Head": head joints; "Bend": bending; "Tor": torsion).

To study the influence of the aspect ratio on the performance of the joint failure mechanisms, walls subjected to 0.1 MPa pre-compression were compared. The total dissipated fracture energy of each wall was divided by the wall area. Results in Figure 4.9a show that the dissipated fracture energy per unit area is following an exponential relation with the aspect ratio, which is similar to that between the two-way bending capacity and the aspect ratio (Figure 4.3a). In Figure 4.9b, contributions of the joint failure mechanisms show that when the aspect ratio is very low (0.3), the bending failure of bed joints at central horizontal cracks is predominant. When the wall aspect ratio is low, the wall behaviour is more close to one-way bending (Table 4.1). Apart from this case, the torsional failure of bed joints at diagonal cracks is predominant in other cases. Besides, the torsional failure of head joints at diagonal cracks is also important. In general, the sum contributions of the torsional failure of bed and head joints increase as the aspect ratio increases. In contrast, the contributions by the bending failure at diagonal cracks decrease as the aspect ratio increases.

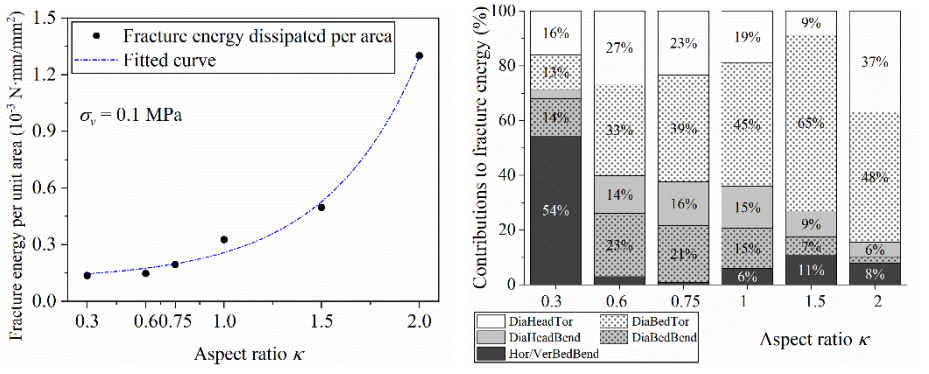

(a) (b)

Figure 4.9. Influence of the aspect ratio on the crack failure mechanisms: (a) fracture energy dissipated per unit area of walls with various aspect ratios; (b) contributions by the failure mechanisms (abbreviations in the legend: "Dia" – diagonal cracks; "Hor/Ver" – central horizontal or vertical cracks; "Bed": bed joints; "Head": head joints; "Bend": bending; "Tor": torsion).

4.2.4 Quantification of the influence of the pre-compression and aspect ratio

In an attempt to quantify the influence of the aspect ratio and pre-compression on the two-way bending capacity, a function of two variables based on the numerical results was nonlinearly fitted selecting the two-way bending capacity as the dependent variable and the aspect ratio and pre-compression as double independent variables. In Equation (4.3), w_{fitted} is the fitted two-way bending capacity, while a_1-a_5 are constants. Figure 4.10 shows that the difference between the fitted function and the numerical results is quite small. The standard error of the regression (SER) was introduced to evaluate the average distance that the numerical results deviate from the regression line. A smaller value of SER indicates that the numerical results are closer to the regression line. The SER of Equation (9) is 0.39 kPa, which means the regression is quite successful. The constants a_1-a_5 represent other crucial factors, such as material properties and boundary conditions, which are non-variables in the equation. It should be noted that till now this equation is more statistical meaning rather than mechanical meaning. Nevertheless, it perfectly reflects the numerical results. Therefore, Equation (4.3) will be compared with current major analytical formulations in the following section to further explore the limitations of the latter.

$$w_{fitted} = a_1 e^{a_2 \kappa} \cdot (a_3 \sigma_v + a_4) + a_5$$
$$\begin{cases} a_1 = 1.6302 \\ a_2 = 0.9724 \\ a_3 = 3.1721 \\ a_4 = 1.9568 \\ a_5 = -1.7759 \end{cases} \quad (4.3)$$

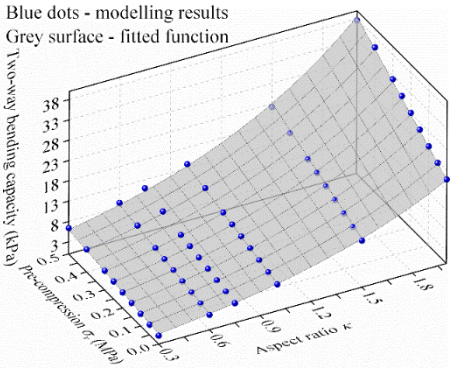

Figure 4.10. Numerical results versus fitted function (blue dots: the numerical results; grey surface: the surface of the fitted function). SER = 0.39 kPa.

4.3 Comparison with current analytical formulations

In this section, predictions by three state-of-the-art analytical formulations are compared with the results of the parametric study in Section 5. The three analytical formulations are Eurocode 6 (2012), Australian Standard for Masonry Structures AS 3700 (2018) and formulations proposed by Willis et al. (2006). The aim is to further reveal the limitations of these formulations and to find the direction for improving them.

The methods of applying the analytical formulations are first introduced. The aspect ratio and pre-compression have the same ranges as those in Section 4.2. The top, bottom and lateral boundaries of the walls were considered as simply supported and partially clamped, respectively. Since partially clamped boundaries are not included in Eurocode 6, the two-way bending capacity of the walls can either be evaluated as hinged or clamped at lateral boundaries, which correspond to support conditions E and G in Annex E of Eurocode 6, respectively (CEN, 2012). Therefore, the results of these two cases were averaged and considered partially clamped. As for AS3700 and the formulation by Willis et al. (2006), the restraint factor of the lateral boundaries R_f was assumed to be 0.5 to account for partially clamped lateral boundaries, as suggested by previous studies (Griffith & Vaculik, 2007; Derakhshan et al., 2018; Graziotti et al., 2019). The flexural strength of masonry having the failure plane perpendicular to the bed joints, f_{x2}, which is required as input for Eurocode 6, is not available from the experimental results (Griffith & Vaculik, 2007; Vaculik, 2012). Therefore, f_{x2} was evaluated according to Dutch National Annex to Eurocode 6 (NEN, 2018). The evaluated value of f_{x2} is 1.92 MPa. For a detailed discussion regarding the application of the analytical formulations, the readers are referred to Chapter 2 (Chang, Messali, et al., 2020).

Figure 4.11 shows the comparison of the predictions by the analytical formulations with the numerical results. Results show that: Eurocode 6 tends to overestimate the two-way bending capacity in general; AS 3700 tends to overestimate the two-way bending capacity when the aspect ratio is over 1; Willis et al. (2006) provide the

closest predictions. About the relation between the two-way bending capacity and the aspect ratio predicted by the analytical formulations, an extra fitting analysis shows that this relation is approximately quadratic, which is different from the numerical results reflected in Equation (4.3). Concerning the pre-compression, the numerical results show that the two-way bending capacity becomes more sensitive to the pre-compression as the aspect ratio increases, while this is not reflected by the considered analytical formulations. Considering that the contributions to the two-way bending capacity by the torsional strength of bed joints are predominant and increase as the pre-compression increases (Section 5.3), also that the evaluation of the torsional capacity of bed joints by the analytical formulations is empirical and insufficient (Willis et al., 2006; SAI, 2018), it is suggested that more studies should be conducted to determine the relationship between the torsional capacity of bed joints and the pre-compression.

More interestingly, the numerical results predict that the influence of the pre-compression and aspect ratio on the two-way bending capacity can be interdependent, which is not predicted by any of the three analytical formulations. Equation (4.3), which precisely fits with the numerical results, indicates that the two-way bending capacity is linearly dependent on the pre-compression. As the aspect ratio increases, the slope of the function regarding the pre-compression increases. Consequently, for a wall with a higher aspect ratio, the same increment of pre-compression can have a larger increment of two-way bending capacity than that of a wall with a lower aspect ratio. In fact, as observed from Section 5.3, as the pre-compression or aspect ratio increases, the contribution of the torsional capacity of joints increases accordingly. It is therefore rational to deduce that when the aspect ratio increases, the contribution of the torsional capacity of joints increases, and the increase of the pre-compression promotes this effect, thus greatly increasing the two-way bending capacity.

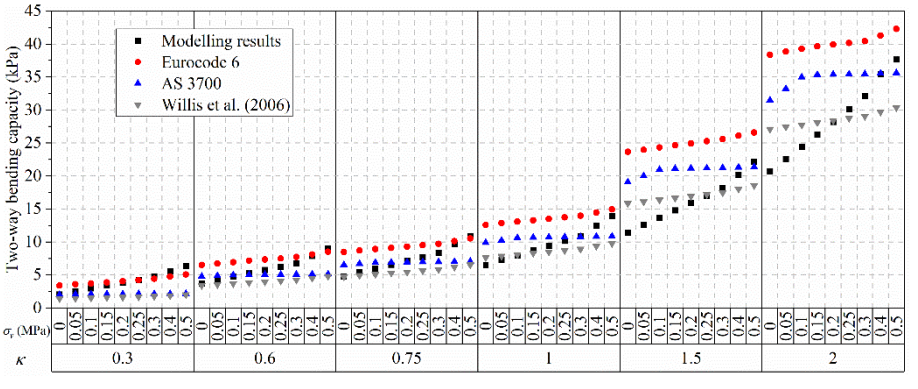

Figure 4.11. Comparison of predictions by analytical formulations with numerical results.

The final crack pattern predicted by the Virtual Work Method is shown in Table 4.2. According to the Virtual Work Method, if the slope factor α is larger than 1, a central horizontal crack is predicted; otherwise, a central vertical crack is predicted (SAI, 2018). Results show that when the aspect ratio is smaller than 0.6, central

horizontal cracks will appear. Besides, the pre-compression does not influence the crack pattern. These results are following the numerical results, as shown in Table 4.2. However, it should be noted that according to the numerical results, the walls have not reached a rigid-plate crack pattern at the two-way bending capacity. The two-way bending capacity can be much higher than the force when the wall forms the rigid-plates crack pattern, especially when the pre-compression is low. Besides, the deformation shape of a wall at the two-way bending capacity is more close to the curved surface rather than rigid plane plates. These observations are against the assumptions of the Virtual Work Method. Therefore, the assumption of the deformed shapes of walls at the two-way bending capacity is suggested to be re-evaluated.

Table 4.2. Final crack patterns predicted by the Virtual Work Method.

Aspect ratio κ	0.3	0.6	0.75	1.0	1.5	2.0
Slope factor α	2.39	1.19	0.96	0.72	0.48	0.36
Central crack	Horizontal	Horizontal	Vertical	Vertical	Vertical	Vertical

4.4 Conclusions

This study focuses on the influence of the aspect ratio (wall height to length) and pre-compression on the two-way bending capacity of unreinforced masonry (URM) walls subjected to out-of-plane (OOP) loads. The main objective is to quantify the relations between the aspect ratio/pre-compression and the two-way bending capacity. For this purpose, the 3D simplified brick-to-brick modelling approach was employed. The calibrated and validated numerical models (Chapter 3) were applied in a parametric study in which the aspect ratio (ranging from 0.3 to 2) and pre-compression (ranging from 0 to 0.5 MPa) were double variables. The influence of the pre-compression and aspect ratio on the two-way bending capacity, crack progression, deformation profiles and joint failure mechanisms were studied. Based on the results of the parametric study, a nonlinear fitted equation was proposed to quantify the relations between the aspect ratio/pre-compression and the two-way bending capacity. The results of the parametric study were compared with the predictions by three major analytical formulations, namely Eurocode 6 (2012), the Australian Standard for Masonry structures AS 3700 (2018) and Willis et al. (2006). The main findings and conclusions are drawn here.

The parametric study shows that the two-way bending capacity is exponentially related to the aspect ratio and linearly related to the pre-compression. An interesting finding is that the influence of the aspect ratio and pre-compression on the two-way bending capacity can be interdependent. That is, as the aspect ratio increases, the same increment of the pre-compression can lead to a larger increment of the two-way bending capacity.

The parametric study also shows that the two-way bending capacity of walls is much higher than the force at the instant of reaching the rigid-plates crack pattern in the post-peak stage, especially when the pre-compression is low. Also, the deformed

shapes of the walls at the two-way bending capacity are more close to curved surfaces rather than a group of rigid plane plates. This is against the assumption of the analytical formulations that when the two-way bending capacity is reached, the rigid-plates crack pattern has been formed. It is therefore suggested that the deformed shape of the wall at the two-way bending capacity (especially when the pre-compression is low) should be studied further.

The torsional failure of bed joints is the predominant failure mechanism for URM walls in OOP two-way bending. As the pre-compression or aspect ratio increases, the proportion of contribution by the torsional capacity of bed joints increases. This suggests that when the aspect ratio increases, the contribution of the torsional behaviour of joints increases, and the increase of the pre-compression enhances this effect thus significantly increasing the two-way bending capacity.

The predictions by the analytical formulations show that: Eurocode 6 tends to overestimate the two-way bending capacity in general; AS3700 tends to overestimate the two-way bending capacity when the aspect ratio is over 1; W2006 provides the closest predictions. Besides, the interdependency of the influence of the pre-compression and aspect ratio on the two-way bending capacity cannot be predicted by any of the considered analytical formulations.

Based on the aforementioned findings, the following suggestions are proposed aiming at improving the analytical formulations in the standards: the quantitative relations between the two-way bending capacity and pre-compression/aspect ratio from the numerical study should be considered; the assumption of rigid-plates cracking pattern forming at the two-way bending capacity should be reappraised; the influence of the torsional failure of bed joints on the energy dissipation and two-way bending capacity should be studied both experimentally and numerically. At last, it should be clarified that the quantified relationships and proposed equations in this chapter are limited to weak joint/strong brick masonry and certain boundary conditions. The quantitative relationships between the pre-compression/aspect ratio and the two-way bending capacity determined in this chapter will be incorporated into the improved analytical formulation proposed in Chapter 6.

Chapter 5

INFLUENCE OF OPENINGS[4]

Perforated unreinforced masonry (URM) walls in out-of-plane (OOP) two-way bending are commonly encountered in natural hazard investigations. However, a systematic study on the influence of the openings is lacking, either experimentally or numerically, as discussed in Chapter 2. This chapter focuses on the influence of openings on the two-way bending capacity of URM walls. An experimental database about the perforated URM walls in OOP two-way bending was created. A brief review of the experimental results shows that the arrangement of the opening area can significantly affect the two-way bending capacity of walls (defined as the peak pressure on the wall net area): when the opening area is non-covered and non-loaded, the two-way bending capacity of the perforated wall is higher than that of its solid counterpart; when the opening area is covered with timber or glass plates and loaded as the rest of the wall, the two-way bending capacity of the perforated wall is lower than that of the corresponding solid wall. These observations from the experiments were confirmed by an analytical estimation using the Yield Line Method (YLM). Next, by applying the calibrated and validated numerical model in Chapter 3, the influence of the arrangement for the opening area from the experimental results and YLM evaluation was confirmed. Further, a parametric study focusing mainly on cases with the opening area non-covered and non-loaded was conducted. The influence of the geometric parameters of openings, namely, the opening size, shape and position was investigated on walls with different aspect ratios. Results show that the two-way bending capacity increases as the opening size or aspect ratio (height to width) increase, but it is insensitive to the opening position. Eventually, based on the numerical results, analytical equations were proposed to account for the influence of the considered parameters on the two-way bending capacity. A comparison with the Australian Standard (AS3700) indicates that the proposed equations incorporate more opening parameters such as opening shape. The quantitative relationships between the openings and the two-way bending capacity determined in this chapter will be incorporated into the improved analytical formulation proposed in Chapter 6.

[4] This chapter is based on the published journal article: Chang, L.-Z., Rots, J. G., & Esposito, R. (2022). Influence of openings on two-way bending capacity of unreinforced masonry walls. *Journal of Building Engineering, 51*. Minor modifications have been made to suit the thesis.

5.1 Introduction

Perforated walls, i.e. walls with openings (windows and doors), are commonly encountered in unreinforced masonry (URM) buildings. In some countries, such as the Netherlands, openings can be relatively large, as shown in Figure 5.1. Therefore, the presence of openings can alter the mechanical behaviour of walls to a large degree. Recent research concerning perforated URM walls focuses on their in-plane performance (Ahani et al., 2019; Liu & Crewe, 2020; Yekrangnia & Asteris, 2020). In contrast, the research on the walls in out-of-plane (OOP) two-way bending, in which at least one lateral edge of a wall is supported in addition to its top and bottom edges, is relatively limited. However, investigations have identified OOP failure of URM walls subjected to natural hazards, such as earthquakes, as one of the most occurring failure mechanisms (D'Ayala & Paganoni, 2011; Moon et al., 2014; Penna et al., 2014; Dizhur & Ingham, 2015; Sorrentino et al., 2016). It is thus of significance to further study the influence of openings on the two-way bending capacity of URM walls.

Figure 5.1. Unreinforced masonry walls with large openings in the Netherlands.

Research on this topic started from laboratory experiments back in the 1970s. Most of the experimental campaigns applied quasi-static tests using airbags (West et al., 1977; de Vekey et al., 1986; Southcombe & Tapp, 1988; Chong, 1993; Chen, 2002; Griffith & Vaculik, 2007; Ravenshorst & Messali, 2016), while a few others adopted dynamic tests (Vaculik, 2012; Graziotti et al., 2019). However, the existing experimental database is limited in quantity, and crucial data such as opening size and position is unavailable, especially in early experimental records. Moreover, different experiments adopted different arrangements for the opening area. Some covered the opening area with timber or glass plates and loaded it with uniformly distributed pressure as the rest of the wall, while the others left the opening area empty and non-loaded. This led to contradictory conclusions on the influence of the openings on the two-way bending capacity of the walls. Furthermore, only a few experiments systematically studied the geometric parameters of the opening, namely size, shape and position. Thus, solid conclusions about these parameters cannot be drawn due to the limited number of samples (Chong, 1993; Chen, 2002). A brief

review of the available database elaborating on the experimental details and findings is provided in Section 5.2.

Numerical modelling, especially nonlinear finite element analysis, has been introduced to study the mechanical behaviour of URM walls in OOP two-way bending. Among various modelling techniques, the 3D simplified brick-to-brick modelling has been proved to be an effective method in studying solid URM walls, considering that it can well present the wall crack pattern (Li et al., 2014; Abdulla et al., 2017; D'Altri et al., 2018; Chang et al., 2021; Isfeld et al., 2021). Concerning perforated walls, Nasiri and Liu (Nasiri & Liu, 2019) used 3D simplified brick-to-brick modelling to study the influence of a central window on masonry infills within reinforced concrete frameworks. However, according to the author's knowledge, there is no research applying this modelling technique to systematically study the influence of openings on the two-way bending capacity of URM walls.

The insufficient research regarding perforated URM walls in OOP two-way bending results in incomplete analytical formulations in current building standards. In some major standards, such as Eurocode 6 – Design of Masonry Structures (2012), large openings that potentially influence the wall behaviour are required to be evaluated using additional analysis tools. By contrast, the Australian Standard – Masonry Structures (AS3700) (2018) takes the opening length and horizontal position into account. Within limited ranges, the two-way bending capacity of the perforated walls is reported to decrease as the opening length increases, or as the opening moves from the wall centre towards the lateral edges (Chang, Messali, et al., 2020). However, the predictions by AS3700 can be contradictory to some experimental results and can overly underestimate the two-way bending capacity of the perforated walls. Besides, the opening aspect ratio is not considered in AS3700. This poses questions regarding the accuracy of the related analytical formulations in AS3700 and calls for further study on perforated URM walls in OOP two-way bending.

This study focuses on the influence of openings on the two-way bending capacity of URM walls. The influence of the arrangement of the opening and the opening geometric parameters, i.e. size, shape and position are specifically explored. First, available experimental records were collected and analysed to provide a brief review of the observations and limitations of existing experimental campaigns (Section 5.2). A preliminary evaluation of the influence of openings by the Yield Line Method was conducted in Section 5.3. Then, the 3D simplified brick-to-brick finite element models calibrated and validated in Chapter 3 were applied. The influence of the arrangement of the opening area was studied with various virtual settings in Section5.4. Further, a parametric study was carried out to evaluate the influence of the opening geometric parameters, such as type (window or door), size, shape and position on both long and short walls (Section 5.5). Eventually, proposed equations based on the numerical results were proposed and compared with AS3700 (Section 5.6).

5.2 A brief review of the available experimental database about the perforated walls

As introduced in Section 5.1, experiments on perforated URM walls in OOP two-way bending have been carried out from the 1970s onwards. A database dating from 1977 is collected and presented in Table 5.1. The database consists of 9 testing campaigns and 19 groups of samples. Each group contains at most one solid wall as a reference and at least one perforated wall having identical testing configurations as the former. In the majority of the cases, quasi-static tests were performed by applying a uniformly distributed pressure on the wall surface with airbags (Figure 5.2a). In a few cases, dynamic loads were applied using shake-tables. Besides, two arrangements of the opening area can be distinguished. In the first case, the opening area is non-covered and non-loaded, as shown in Figure 5.2b; in the second case, the opening area is covered with timber or glass plates and loaded as the rest of the wall, as shown in Figure 5.2c. Although the intentions for these different arrangements have not been explained by the researchers, the former arrangement can be considered representative of seismic scenarios, while the latter can be considered representative of wind-loaded scenarios. In this chapter, the two-way bending capacity of URM walls is defined as the peak pressure applied to the wall net area. In the case of the opening area covered and loaded, the opening area is included in the wall net area. This definition has the following advantages over defining the wall capacity in terms of the resultant force. First, it follows the conventions of the experiments and current standards such as Eurocode 6 (2012) and the Australian Standard (2018) and is beneficial for future improvements in the analytical formulations. Second, this definition reflects the most common loading conditions, namely evenly distributed loads caused by wind or earthquake, of URM walls in OOP two-way bending. Third, comparisons of capacity among walls with various dimensions are possible with this definition since it reflects the dissipated fracture energy per wall surface area.

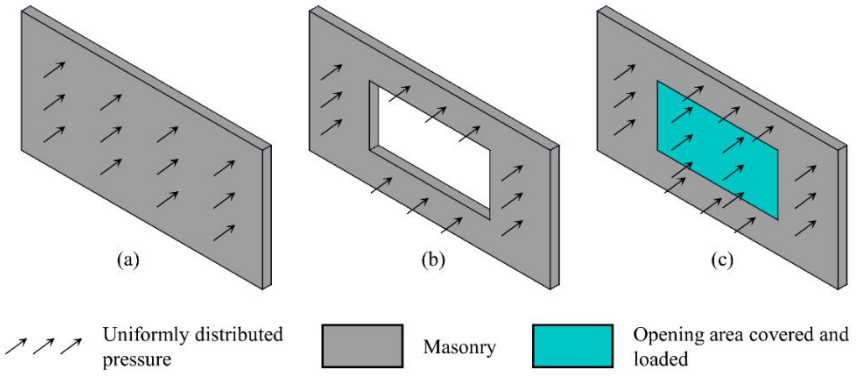

Figure 5.2. Schematic diagrams of wall configurations and opening arrangements in the experiments: (a) solid wall; (b) perforated wall with opening area non-covered and non-loaded; (c) perforated wall with the opening area covered with timber or glass plates, and loaded as the rest of the wall.

Despite the database being diverse in terms of the testing method, unit type, boundary condition, wall aspect ratio and opening geometric parameters, the limited number of the perforated walls (only 49 samples) brings difficulty in generalising the experimental observations to a wider application range. Besides, in most of the groups, only one perforated wall can be compared with the solid wall. This can lead to doubts regarding the accuracy of the experimental results since high variability of material properties was widely reported by the testing campaigns. What is more important, different groups draw contradictory conclusions regarding the influence of the openings on the wall capacity. Some experimental results show that the presence of the opening increases the wall capacity, while the others show the opposite. The review of the database shows that these contradictory results can be related to the arrangements of the opening area, namely, whether the openings were covered and loaded. More details of the testing campaigns are elaborated in the following.

The first recorded experiments on perforated URM walls in OOP two-way bending were conducted by British Ceramic Research Association (BCRA) (Haseltine & Tutt, 1986; West et al., 1986). Although 15 perforated walls were tested, only 4 of them can be compared with a referencing solid wall (group 1 in Table 5.1). Results show that the presence of openings reduces the two-way bending capacity of URM walls. Besides, although walls of different aspect ratios with small (0.9×0.9 m^2) and large (2.1×1.3 m^2) openings were tested, the influence of the opening size was unclear (Fig. 5 in (Haseltine & Tutt, 1986)). The arrangements of the openings are ambiguous from available records (Haseltine & Tutt, 1986; West et al., 1986). In (Haseltine & Tutt, 1986), Haseltine and Tutt simply reported that the effect of glazing had been investigated on some walls with openings, and the glazing of the openings had little impact on the wall capacity. Whether the opening area was loaded is unknown. Following BCRA's testing campaign, Tapp and Southcombe

(Tapp, 1985; Southcombe & Tapp, 1988) conducted two groups of experiments. Results show that the presence of the openings reduces the wall capacity, and the position of the opening has no effect on the wall capacity. The arrangements for the openings are unknown. However, it can be assumed that since their successor Chong, who covered the opening area with chipboard and loaded it, introduced his testing campaign as "a continuation of the work carried out by Tapp and incorporates a wider range of panels and materials" (page 3 in (Chong, 1993)), it is reasonable to assume that Tapp and Southcombe applied the same arrangement to the openings. Apart from this, Chong (1993) observed a similar effect of the openings on the wall capacity (group 6-9 in Table 5.1). de Vekey et al. (1996) covered and loaded the openings. Based on comparable groups and available results (reported by Edgell and Kjaer (2000)), it was found that even though two identical walls with openings were tested, the effect of the openings on the wall capacity can be uncertain (group 10 and 11 in Table 5.1). Chen (2002) tested URM walls with openings of various sizes and positions (group 13 in Table 5.1, reported by Baker et al. (2005)). With the openings covered and loaded, results again show that the presence of the openings reduced the two-way bending capacity. However, a general pattern of the influence of the opening size and position cannot be found.

Different from previous researchers, Griffith and Vaculik (Griffith & Vaculik, 2007; Griffith et al., 2007) did not place any frame or covering board, except for the lintel, in the opening area. Therefore, the opening area was non-covered and non-loaded. Counter-intuitively, the two-way bending capacity of the perforated walls is higher than those of the referencing solid walls (groups 14 and 15). Here it should be noted that sample Wall 2 in group 15 was not initially well constrained at the bottom edge as its counterpart, Wall 5, which has an opening. OOP sliding was reported along the bottom edge of Wall 2 (Vaculik, 2012). Therefore, the actual influence of the opening in this group is remaining questionable. A similar testing campaign was carried out by Ravenshorst and Messali (2016). The experimental results (group 18) support the observations by Griffith and Vaculik. Vaculik (2012) further conducted experiments on half-scale walls subjected to dynamic actions (groups 16 and 17). Though the openings were also non-covered as in his previous experiments, the presence of the openings reduces the wall capacity. However, he also reported that additional timber supports were added to the vertical edges of the solid walls (samples d1 and d2, page 72 in (Vaculik, 2012)), which could enhance the fixity of vertical boundary conditions, therefore increasing the wall capacity. Graziotti et al. (2019) performed dynamic tests on full-scale URM walls with the opening area left non-covered and non-loaded as well. The reducing effect of the opening on the two-way bending capacity was relatively minor (group 19). A special observation of group 19 is that the crack patterns are quite different between the solid wall (CS-000-RF) and the perforated wall (CSW-000-RF). The former collapsed due to the formation of long vertical line cracks passing through the bricks in the middle and vertical edges of the wall, while the latter only formed local diagonal stepped cracks upon the upper portion of the longer panel beside the opening. This difference is not found in previous testing campaigns in which the solid and perforated walls share the same crack pattern.

Concluding from the experimental database, it is found that, i) the influence of the openings on the wall capacity is related to the arrangements of the openings in the experiments; if the openings were covered and loaded like the masonry part of the wall, the presence of openings could reduce the wall capacity, whereas experiments with openings non-covered and not loaded showed higher wall capacity as compared to a solid wall; ii) the results from the limited number of experimental samples cannot reveal the influence of the geometric parameters of openings on the wall capacity. In an attempt to solve these problems, analytical and numerical methods are adopted in the following sections.

Table 5.1. Database of experiments on the influence of openings on the two-way bending capacity of URM walls (1977-2019).

Testing campaign	Grp.	Test. Met.[1]	Unit type	Boun. Cond.[2]	Wall dimensions $H_w \times L_w \times t_w$ (Cubic mm.)	No. of samp.	Label of		Open. Area. Rat.[3]	Open. Eccen.[4]	Opening covered and loaded?	Ratio. Of Cap.[5]
							Solid wall	Perforated wall				
BCRA (1977-1986)	1	Mon.	Clay Brick	U	2600×2700×100	5	1135	1142, 1143, 1155, 1175	11%(2), 38%(2)	Cen.	Unkn.	0.68 - 0.98
	2	Mon.	Clay Brick	U	2600×3700×100	4	None	1196, 1197, 1200, 1204	8%(3), 28%(1)	Cen.	Unkn.	Unkn.
	3	Mon.	Clay Brick	U	2600×5500×100	7	None	1128, 1129, 1131, 1132, 1134, 1139,1141	6%(4), 19%(3)	Cen.	Unkn.	Unkn.
Tapp and Southcombe (1985 &1988)[6]	4	Mon.	Clay Brick	U	2417×4840×102.5	3	None	Panel 1, 2, 3	10%, 14%, 18%	Cen.	Yes[7]	Unkn.
	5	Mon.	Clay Brick	U	2465×4715×102.5	6	ART01	ART02 - 06	14%(3), 15%(2)	Cen.(4); Ecc.(1)	Yes[7]	0.57 - 0.63
Chong (1993)	6	Mon.	Clay Brick	U	2475×5615×102.5	4	SB01	SB02, 03, 04	18%, 11%, 13%	Cen.	Yes	0.76 - 0.85
	7	Mon.	Clay Brick	U	2450×2900×102.5	2	SB06	SB07	12%	Cen.	Yes	0.73
	8	Mon.	Concrete Block	U	2475×5615×100	2	DC01	DC02	18%	Cen.	Yes	0.66
	9	Mon.	Clay Brick	C	2475×2700×102.5	4	HW01	HW02 - 04	4%, 8%, 7%	Cen.	Yes	0.76 - 1
de Vekey et al. (1996)[8]	10	Mon.	Brick	O	2600×5500×(Unkn.)	3	1a-control	1a(i), 1a(ii)	27%(2)	Cen.	Yes	0.77, 1.77
	11	Mon.	Block	O	2600×5500×(Unkn.)	3	1b-control	1b(i), 1b(ii)	27%(2)	Cen.	Yes	0.93, 1.47
	12	Mon.	Brick	C	2600×5500×(Unkn.)	2	2-control	2a(ii)	28%	Cen.	Yes	1
Chen (2002)[9]	13	Mon.	Unknown	O	2800×5800×(Unkn.)	8	1	2 - 8	9% - 27%	Cen.(5); Ecc.(2)	Yes	0.68 - 0.89

Table 5.1. Database of experiments on the influence of openings on the two-way bending capacity of URM walls (1977-2019).

Testing campaign	Grp.	Test. Met.[1]	Unit type	Boun. Cond.[2]	Wall dimensions $H_w \times L_w \times t_w$ (Cubic mm.)	No. of samp.	Label of		Open. Area. Rat.[3]	Open. Eccen.[4]	Opening covered and loaded?	Ratio. Of Cap.[5]
							Solid wall	Perforated wall				
Griffith and Vaculik (2007)[10]	14	Mon.& Cyc.	Clay Brick	O	2494×4200×110	2	Wall 1	Wall 3	12%	Ecc.	No	1.06
	15	Mon.& Cyc.	Clay Brick	O	2494×4200×110	2	Wall 2	Wall 5	12%	Ecc.	No	1.18
Vaculik (2012)[11]	16	Dyn.	Clay Brick	O	1232×1840×50	2	d1	d3	13%	Ecc.	No	0.68
	17	Dyn.	Clay Brick	O	1232×1840×50	2	d2	d5	13%	Ecc.	No	0.65
Ravenshorst and Messali (2016)	18	Cyc.	Calcium silicate	O	2765×3986×102	2	TUD_COMP -11	TUD_COMP -12	26%	Ecc.	No	1.49
Graziotti et al. (2019)	19	Dyn.	Calcium silicate	O	2750×3980×102	2	CS-000-RF	CSW-000-RF	27%	Ecc.	No	0.88
Total	-	-	-	-	-	65	-	-	-	-	-	-

Footnotes and remarks:
[1] Testing methods: Mon. = monotonic quasi-static test; Cyc. = cyclic quasi-static test; Dyn. = dynamic test.
[2] Boundary conditions: U = top free; C = one vertical edge free; O = four-side constrained.
[3] Ratio of the opening area to the wall gross area.
[4] Opening eccentricity: Cen. = centric; Ecc. = eccentric.
[5] Ratio of the two-way bending capacity of the perforated wall to that of the solid wall.
[6] Reported by Chong (1993).
[7] Speculated from information provided in (Chong, 1993).
[8] Reported by Edgell and Kjaer (2000)
[9] Reported by Baker et al. (2005)
[10] The bottom edge of Wall 2 was less constrained than other samples, which caused OOP sliding
[11] Additional constraints were applied to the vertical edges of d1 and d2.
Others: Unkn. = unknown; quantity is marked in the parenthesis.

5.3 Evaluation of the opening arrangement via Yield Line Method

Section 5.2 reveals that the arrangements of the opening area can affect the two-way bending capacity of walls. This section aims at evaluating this aspect by applying the Yield Line Method (YLM). The YLM was firstly developed for reinforced concrete slabs and then modified for URM walls by Haseltine, West, et al. (1977). This method was then adopted by the British Masonry Standard (2005) which was withdrawn and inherited by Eurocode 6 (2012). However, there has been a longstanding argument that YLM tends to overestimate the two-way bending capacity. This is due to its unrealistic assumptions that moment capacities are reached along all cracks simultaneously, and that the diagonal crack angle is an independent variable (Lawrence & Marshall, 2000; Vaculik, 2012). Nevertheless, some researchers have shown that YLM can provide acceptable predictions if material properties and boundary conditions were carefully calibrated (Haseltine & Tutt, 1986; Padalu et al., 2020a; Liberatore & AlShawa, 2021). What is more important, YLM is capable of including the openings after minor adaptions (Baker et al., 2005).

The YLM applied in this section is based on the method for reinforced concrete slabs (Darwin et al., 2016). The relatively more complicated YLM presented in (Padalu et al., 2020a; Liberatore & AlShawa, 2021) and Eurocode 6 were not considered here. This aims at comparing the influence of different opening characteristics by YLM via simple examples in a relative sense rather than precisely predicting the wall capacity. The assumptions are, i) moment capacity (m) is equal along all presumed cracks; ii) cracks along boundaries are not considered (simply supported); iii) the diagonal crack angle (θ) is a constant; iv) the OOP load is evenly distributed on the wall; v) the plates divided by yield lines are rigid. Two arrangements of the opening area mentioned in Figure 5.2 were considered.

The presumed yield line patterns of a representative solid wall and wall with a central opening are presented in Figure 5.3a and b, respectively. In Figure 5.3, H_w and L_w are the height and length of the wall, respectively; H_0 and L_0 are the height and length of the opening, respectively; m is the unit moment capacity of the yield lines; θ is the diagonal crack angle; δ is the virtual OOP displacement. About the solid wall (Figure 5.3a), the internal work dissipated along the yield lines is summed as:

$$W_{int} = 4\left(\frac{1}{\sin\theta\cos\theta} + \frac{L_w}{H_w} - \cot\theta\right)\delta m \tag{5.1}$$

The external work done by the OOP uniformly distributed pressure w is:

$$W_{ext} = \left(\frac{1}{2}H_w L_w - \frac{1}{6}{H_w}^2\cot\theta\right)\delta w \tag{5.2}$$

Equating the internal and external work, the two-way bending capacity w can be determined.

Similarly, in the scenario where the opening area is non-covered and unloaded, the internal work dissipated along the yield lines of the perforated wall (Figure 5.3b) is:

$$W_{int} = 4\left(\frac{L_w - L_0}{H_w(\cos\theta)^2}\right)\delta m \tag{5.3}$$

Correspondingly, the external work is:

$$W_{ext} = \left(\frac{1}{2}\frac{L_0(H_w - H_0)^2}{H_w} + \frac{1}{2}\tan\theta\,(L_w - L_0)^2 - \frac{1}{6}(\tan\theta)^2\frac{(L_w - L_0)^3}{H_w}\right)\delta w \tag{5.4}$$

In the scenario where the opening is covered and loaded, the external work done by the OOP pressure is calculated by Equation (5.2), while the internal work dissipated by the yield lines is calculated by Equation (5.3).

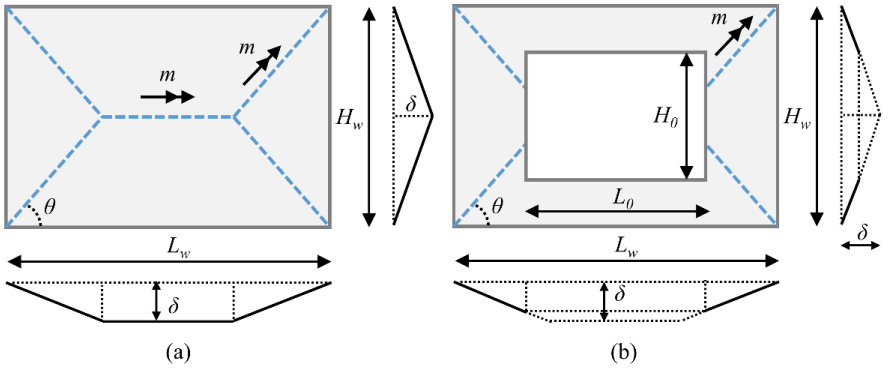

Figure 5.3. Yield line patterns: (a) solid wall; (b) perforated wall with a central window.

A parametric study was conducted selecting Wall 1 (Griffith & Vaculik, 2007) as the reference. The dimensions of the wall are wall-length L_w = 3960 mm; wall height H_w = 2494 mm. The diagonal crack angle (θ), which equals 0.622 rad, was calculated based on the dimensions of the units and the bonding pattern as suggested by AS3700 (2018). The dimensions of the opening are limited to the following conditions considering the presumed crack pattern presented in Figure 5.3b:

$$\frac{H_w - H_0}{L_w - L_0} < \tan\theta \qquad L_0 > L_w - H_w\cot\theta \qquad H_0 < H_w \qquad L_0 < L_w \tag{5.5}$$

The normalised two-way bending capacity of the perforated wall to the solid wall (w_p / w_s) is presented in Figure 5.4. Provided that the opening is non-covered and non-loaded, YLM predicts that the presence of the opening can increase the wall

capacity (w_p / w_s > 1) in most cases. Besides, the two-way bending capacity of the perforated wall increases as the height or length of the opening increases. Figure 5.4b indicates that the presence of the opening weakens the two-way bending capacity ($w_{opening}$ / w_{solid} < 1) in all cases where the opening area was covered and loaded. Additionally, the two-way bending capacity decreases as the opening length increases but is not affected by the opening height. The general tendency of the influence of the openings on the wall capacity predicted by YLM is in accordance with the experimental observations reported in Section 5.2.

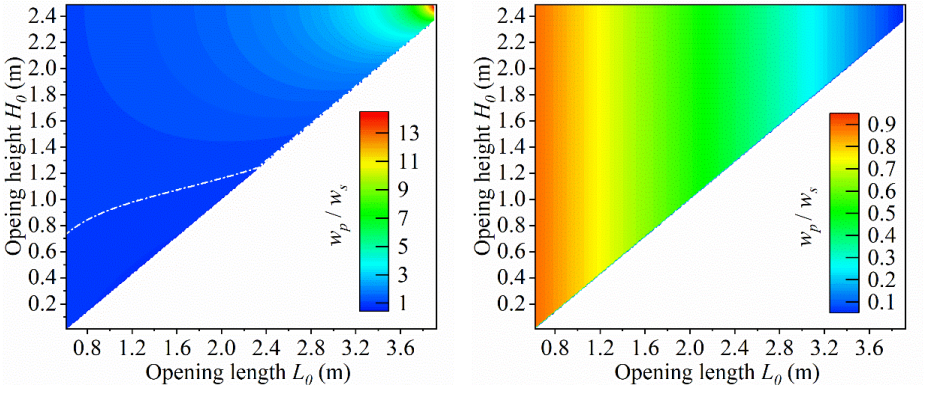

Figure 5.4. Normalised two-way bending capacity of the perforated wall to the solid wall based on YLM evaluations in two scenarios: (a) the opening is non-covered and unloaded; (b) the opening is covered and loaded.

5.4 Evaluation of opening arrangement via numerical analyses

To examine the effect of different arrangements of the opening area on the two-way bending capacity of URM walls, five numerical models labelled Model 1–Model 5 were created, as shown in Figure 5.5. The modelling configurations were the same as those in Chapter 3. In Model 1 the opening was non-covered and non-loaded, which follows Wall 3 in Griffith and Vaculik's experiments (Griffith & Vaculik, 2007). In Model 2, the outer face of the opening area was covered with linear elastic shell elements of which the thickness was set as 18 mm and the elastic modulus was set as 10,000 N/mm^2. These mechanical attributes follow those of a timber plate (Chong, 1993). In Model 3, shell elements were replaced with solid elements of which the elastic modulus was set as 1,000 N/mm^2. The opening was connected with the wall via interface elements. This arrangement takes the interaction between the opening frame and the masonry part into account. In Model 4, an equivalent load, q_{eq} was applied to four faces along the surrounding area of the opening. This arrangement is similar to that of the YLM calculation by Baker et al. (2005). The equivalent load q_{eq} was calculated by

$$q_{eq} = \frac{q \cdot H_0 \cdot L_0}{2(H_0 + L_0)t_w} \tag{5.6}$$

where q is the load applied to the wall; H_0 and L_0 are the opening height and length, respectively; t_w is the wall thickness. Model 5 simulates the behaviour of the panel beside the opening as an independent C shape wall (one vertical edge free); this aims at examining additional checks required by the Australian Standard (article 7.4.4.1 (e) in AS3700 (2018)).

The modelling results are presented in Figure 5.5. The normalised two-way bending capacity of the perforated wall to the solid wall (w_p / w_s) shows that if the opening area is non-covered, the presence of the opening increases the two-way bending capacity, as observed from Model 1. If the panel beside the opening is independently considered, as in Model 5, the two-way bending capacity is even higher than that of Model 1. In contrast, the two-way bending capacity reduces if the opening area is covered and loaded, even though the opening is covered in different ways, as shown in Models 2, 3 and 4. The crack pattern shows that if the opening is non-covered, the diagonal cracks do not develop sufficiently at two-way bending capacity, as shown in Models 1 and 5. Differently, in Models 3 and 4, the diagonal cracks develop more sufficiently at two-way bending capacity. While in Model 2, diagonal cracks develop slightly at two-way bending capacity, even though its opening area is covered as in Model 3. The differences among the crack patterns are attributed to different local failure mechanisms triggered by the arrangement of the opening area. Overall, the numerical models validate the contradictory trends of the influence of openings on the two-way bending capacity caused by various arrangements of the opening area, as observed from experimental results and YLM evaluations.

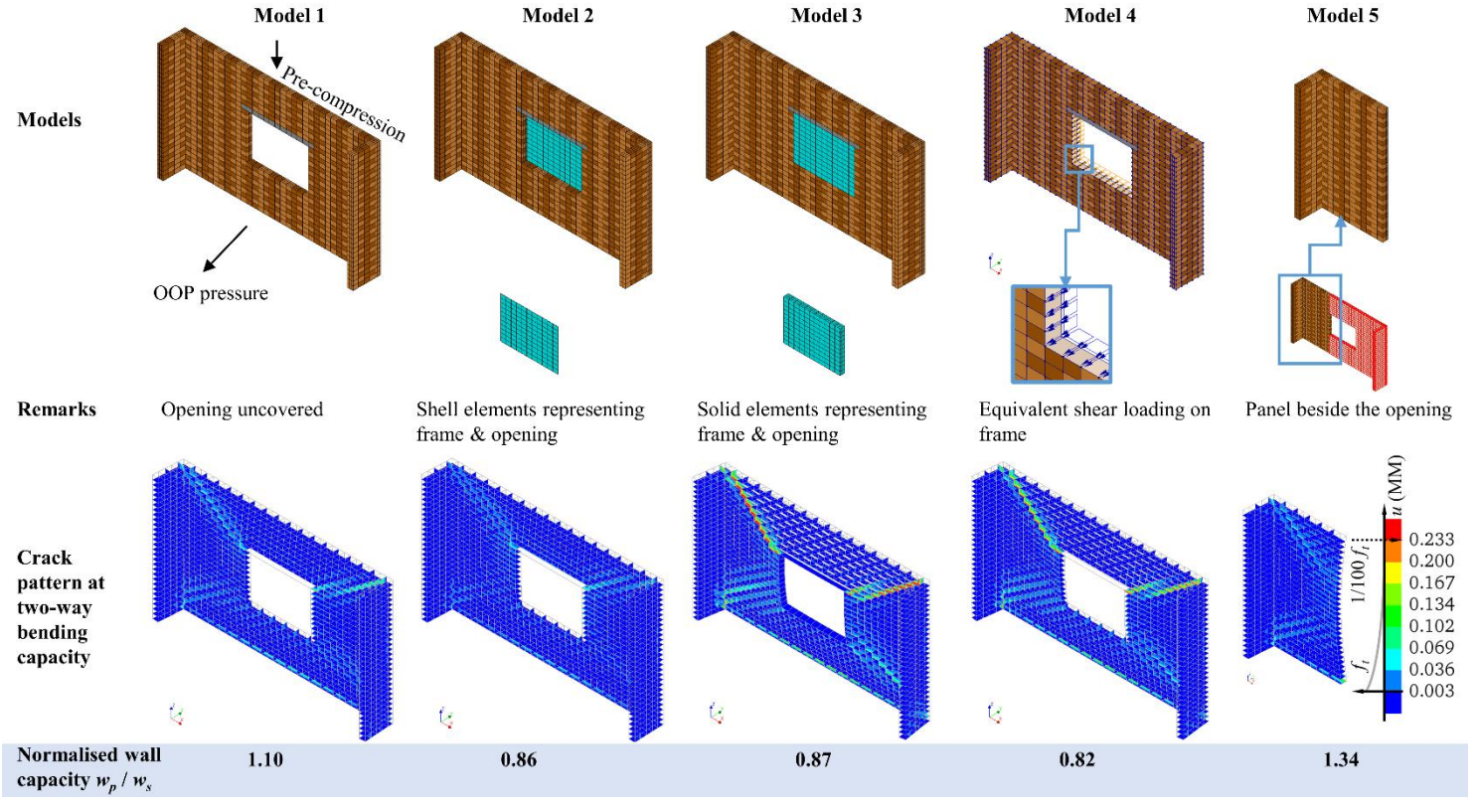

Figure 5.5. Numerical models considering various arrangements of the opening area and corresponding modelling results. Deformation scale factor: 50.

5.5 Parametric study on the influence of opening

In this section, the influence of the opening on the two-way bending capacity of URM walls is numerically studied. The opening areas are non-covered and non-loaded in numerical models as in Model 1 in Section 5.4. This arrangement is considered because in seismic scenarios, dynamic loads majorly take effect on the masonry part rather than the opening since the mass of the former is much larger than the latter. Three parameters related to the opening, i.e. size, shape and position, which can fully determine the opening geometry, are explored separately. As shown in Figure 5.6, these parameters are defined in the following ways in this study. The opening size is defined as the normalised length of the opening to that of the wall ($\eta = L_0/L_w$). The opening shape is defined as the aspect ratio ($\alpha^* = H_0/L_0$) for windows. For doors, a nominal height H_0^* is defined as ($2H_0$-H_w), which is equivalent to the height of a window located at the mid-height of the wall. In this way, the aspect ratio of the doors is defined as ($\alpha^* = H_0^*/L_0$) which makes the shape and position of the doors comparable to those of the windows. The opening position is defined as the normalised horizontal and vertical distances between the opening centroid to the left and bottom edges of the wall, respectively:

$$\lambda_x = \frac{x - L_0/2}{L_w - L_0} \qquad x \in (\frac{L_0}{2}, L_w - \frac{L_0}{2}) \tag{5.7}$$

$$\lambda_y = \frac{y - H_0/2}{H_w - H_0} \qquad y \in (\frac{H_0}{2}, H_w - \frac{H_0}{2}) \tag{5.8}$$

where x and y are the absolute horizontal and vertical distances from the opening centroid to the left and bottom edges of the wall, respectively. With this definition, both λ_x and λ_y range from 0 to 1.

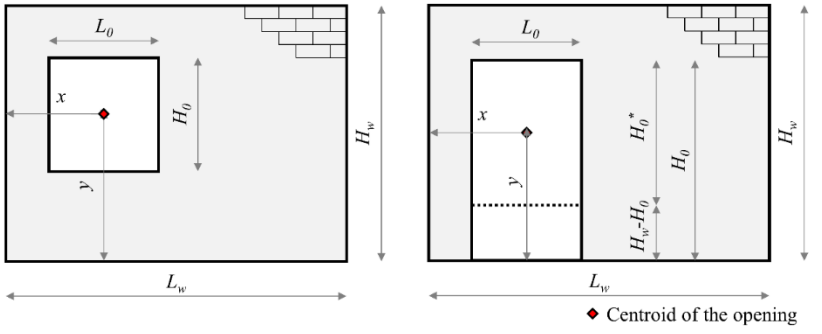

Figure 5.6. Geometric parameters related to the wall with a window or door.

5.5.1 Influence of opening size

5.5.1.1 Modelling types and cases

Four modelling configurations were designed to study the influence of the opening size, as shown in Figure 5.7. The modelling configurations are labelled in such ways: L and S denote a long wall with an aspect ratio (H_w/L_w) of 0.6 and a short wall with an aspect ratio of 1.0, respectively; WIN and DOOR denote a central window and central door, respectively. For each configuration, different opening sizes were considered, as shown in Table 5.2. The aspect ratios of the windows and doors are constant according to previous definitions.

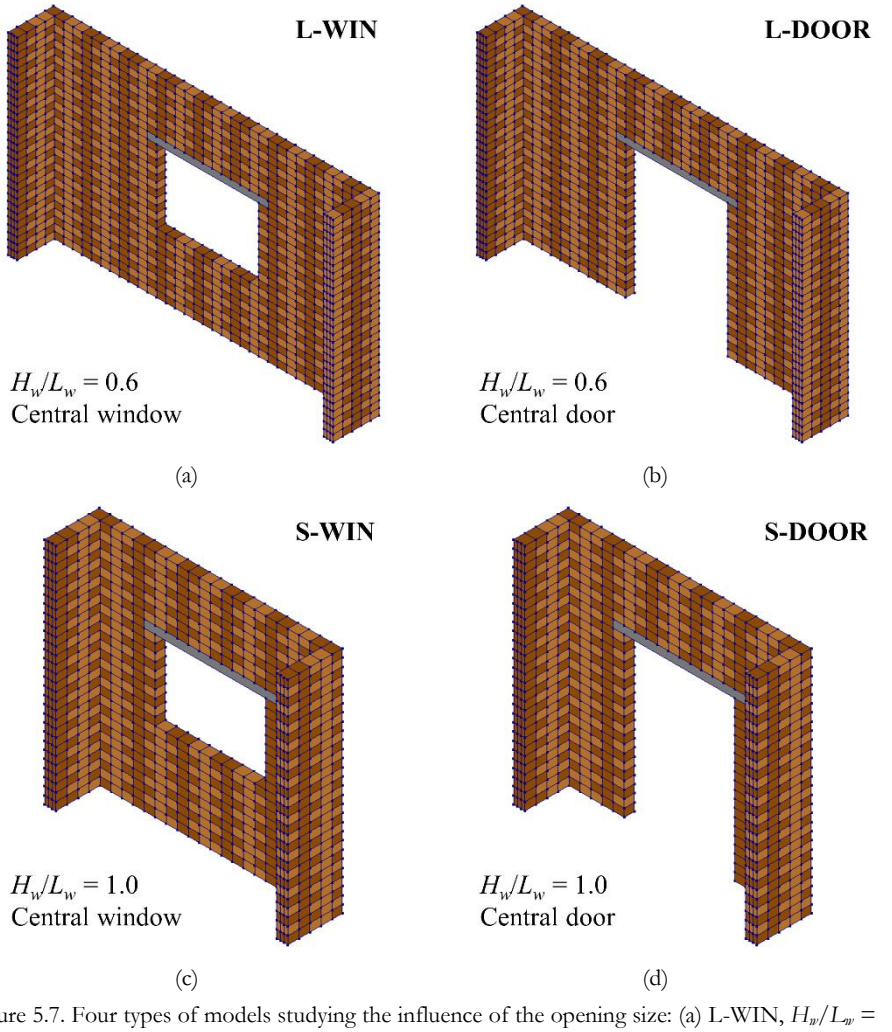

Figure 5.7. Four types of models studying the influence of the opening size: (a) L-WIN, H_w/L_w = 0.6, central window; (b) L-DOOR, H_w/L_w = 0.6, central door; (c) S-WIN, H_w/L_w = 1.0, central window; (d) S-DOOR, H_w/L_w = 1.0, central door.

Table 5.2. Cases corresponding to four modelling types.

Long walls with windows (L-WIN)			Long walls with doors (L-DOOR)		
Case	Opening area* (mm^2)	Opening size η #	Case	Opening area(mm^2)	Opening size η
L-WIN-SZ1	840×602	0.21	L-DOOR-SZ1	840×1548	0.21
L-WIN-SZ2	1080×774	0.27	L-DOOR-SZ2	1080×1634	0.27
L-WIN-SZ3	1320×946	0.33	L-DOOR-SZ3	1320×1720	0.33
L-WIN-SZ4	1560×1118	0.39	L-DOOR-SZ4	1560×1806	0.39
L-WIN-SZ5	1800×1290	0.45	L-DOOR-SZ5	1800×1892	0.45
L-WIN-SZ6	2040×1462	0.52	L-DOOR-SZ6	2040×1978	0.52
L-WIN-SZ7	2280×1634	0.58	L-DOOR-SZ7	2280×2064	0.58
L-WIN-SZ8	2520×1806	0.64	L-DOOR-SZ8	2520×2150	0.64
Short walls with windows (S-WIN)			Short walls with doors (S-DOOR)		
Case	Opening area (mm^2)	Opening size η	Case	Opening area (mm^2)	Opening size η
S-WIN-SZ1	720×516	0.30	S-DOOR-SZ1	720×1548	0.30
S-WIN-SZ2	960×688	0.40	S-DOOR-SZ2	960×1634	0.40
S-WIN-SZ3	1200×860	0.50	S-DOOR-SZ3	1200×1720	0.50
S-WIN-SZ4	1440×1032	0.60	S-DOOR-SZ4	1440×1806	0.60
S-WIN-SZ5	1680×1204	0.70	S-DOOR-SZ5	1680×1892	0.70
S-WIN-SZ6	1920×1376	0.80	S-DOOR-SZ6	1920×1978	0.80

* Opening area: $H_0 \times L_0$;
\# Opening size: $\eta = L_0/L_w$

5.5.1.2 Influence of opening size on the two-way bending capacity

The OOP pressure versus the mid-span displacement curves of L-WIN cases are shown in Figure 5.8. In this figure, the OOP pressure is shown concerning the wall net area. The middle point of the top edge of L-WIN-SZ8 is selected as the displacement control point. The control points of the other cases are in the same position on the walls. Figure 5.8 shows that as the opening size increases, both the initial stiffness and the two-way bending capacity of the wall increase. Besides, at the same position of all walls (red dot, namely the displacement control point marked in Figure 5.8), when reaching the two-way bending capacity, the deflection becomes larger as the opening size increases. This finding is counter-intuitive but is in accordance with similar numerical studies by Nasiri and Liu (2019) and Liberatore et al. (2020). The influence of the opening size (η) on the two-way bending capacity is shown in Figure 5.9. The two-way bending capacity in terms of pressure on the net area of the perforated wall is normalised by dividing the capacity of the corresponding solid wall. The figure shows that assuming that the opening area is non-covered and non-loaded, increasing the opening size leads to an increase in the two-way bending capacity at an approximately exponential pace regardless of the wall aspect ratio and the opening type (window or door). For all cases the trend is similar. For long walls ($H_w/L_w = 0.6$), given a certain opening size, the normalised

two-way bending capacity increases slightly when windows are replaced by doors, as shown in Figure 5.9a. In contrast, for the short walls (H_w/L_w = 1.0), as the opening size increases, the two-way bending capacity of the wall with a door increases a bit more as compared to that of the wall with a window (Figure 5.9b). In Figure 5.10, the influence of the opening size on the OOP force is compared. The OOP force is calculated as two-way bending capacity timing the wall net area. Figure 5.10 shows that for all four modelling types, compared with the solid wall, the OOP force decreases firstly as the opening size increases. When the opening size increases to a certain degree, the OOP force increases as the opening size increases, even though the wall net area keeps reducing.

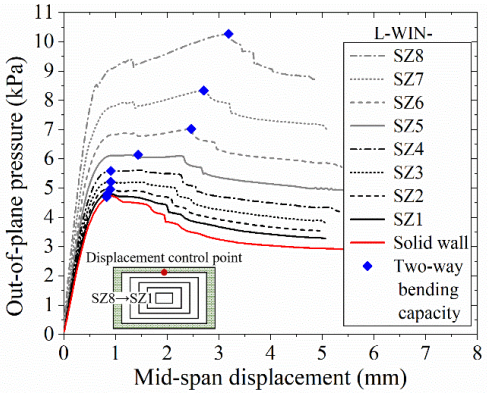

Figure 5.8. Out-of-plane pressure versus mid-span displacement of L-WIN cases. For all cases, the mid-span displacement is calculated at the location of the control point for wall L-WIN-SZ8 (red dot in the figure above).

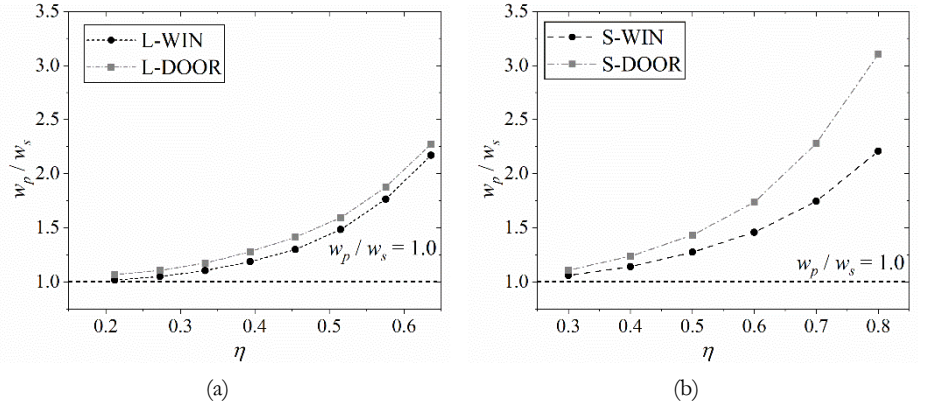

(a) (b)

Figure 5.9. The influence of the opening size η on the normalised two-way bending capacity: (a) for long walls (L-WIN and L-DOOR); (b) for short walls (S-WIN and S-DOOR).

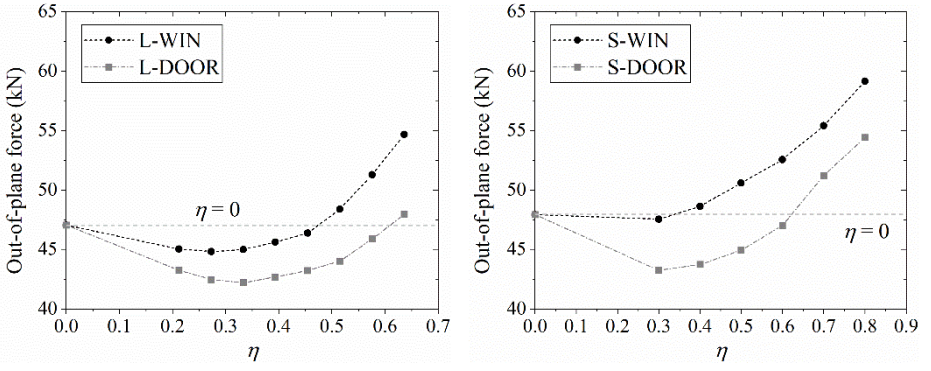

Figure 5.10. The influence of the opening size η on the out-of-plane force: (a) of long walls (L-WIN and L-DOOR); (b) of short walls (S-WIN and S-DOOR).

5.5.1.3 Influence of opening size on crack pattern

Figure 5.11 and Figure 5.12 present the crack patterns of selected cases at the two-way bending capacity. In these figures, cracks start to develop when the normal relative displacement (crack width u) is larger than 0.003 mm; cracks are considered to be fully developed when the tensile stress reduces to 1% of the tensile strength, which corresponds to a crack width u of 0.233 mm. For all cases of each modelling configuration, the presence of an opening does not alter the positions of the major diagonal cracks and horizontal bottom cracks. Different trends are observed between the long and short walls. For the long walls, as the opening size increases, the diagonal cracks on the top corners have more fully opened, and multiple diagonal cracks appear around the bottom corners. In contrast, these trends are relatively subtle concerning the short walls.

The area of the cracked interfaces per unit wall area of L-WIN and S-WIN cases are shown in Figure 5.13a and c, respectively. For each wall, the cracked interfaces were grouped by the normal relative displacement (u) considering partially cracked (0.003 mm < u <0.233 mm) and fully cracked (u > 0.233 mm) interfaces. The gross area of each cracked interface group was divided by the wall net area. Results show that for both the long and short walls, the summed area of the cracked interfaces per unit wall area increases as the opening size increases. The increment for the long walls is larger than that for the short walls. For all cracked interfaces concerning each wall, the percentages of each grouped cracked interfaces per unit wall area are shown in Figure 5.13b and d for L-WIN and S-WIN cases, respectively. Results show that as the opening size increases, per unit wall area, the percentage of the cracked interface with large normal relative displacement (u > 0.210 mm) increases, while the percentage of the cracked interface with smaller normal relative displacement decreases (0.003 mm < u < 0.026 mm) or remained constant (0.026 mm < u < 0.072 mm). The results presented in Figure 5.13 imply that as the opening size increases, more cracks have fully opened per unit area of the wall, therefore dissipating more fracture energy and leading to a higher two-way bending capacity.

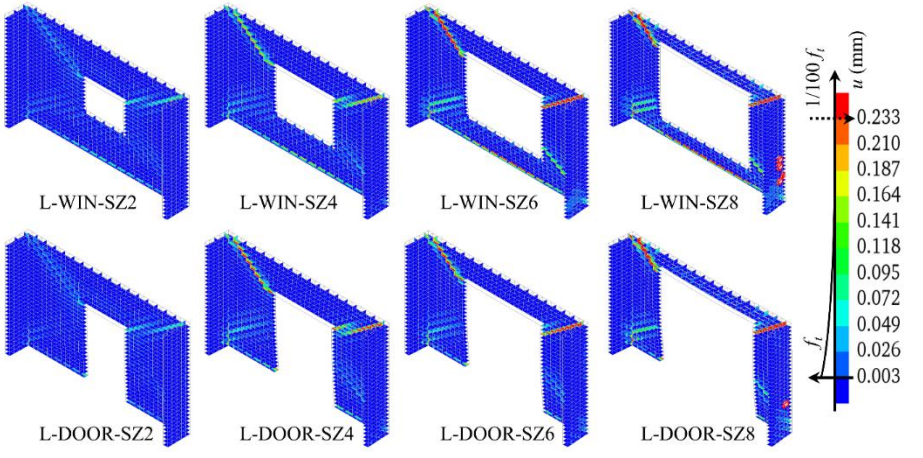

Figure 5.11. Cracking patterns of selected cases of modelling types L-WIN and L-DOOR at the two-way bending capacity.

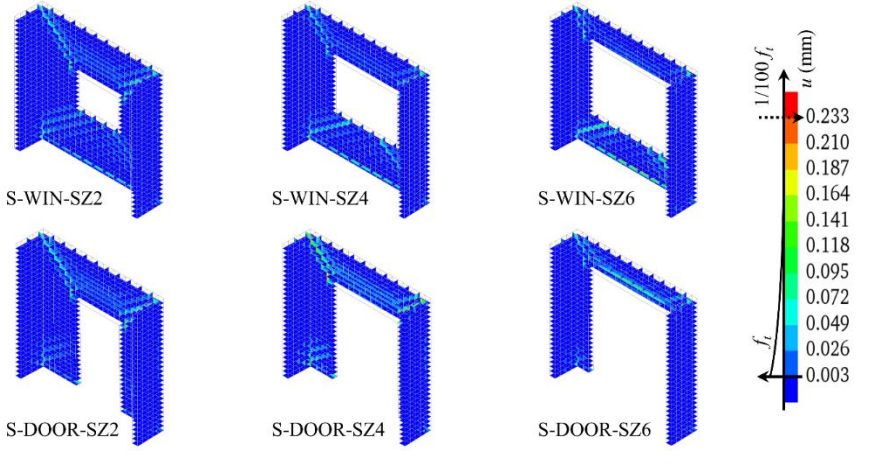

Figure 5.12. Crack patterns of selected cases of modelling types S-WIN and S-DOOR at the two-way bending capacity.

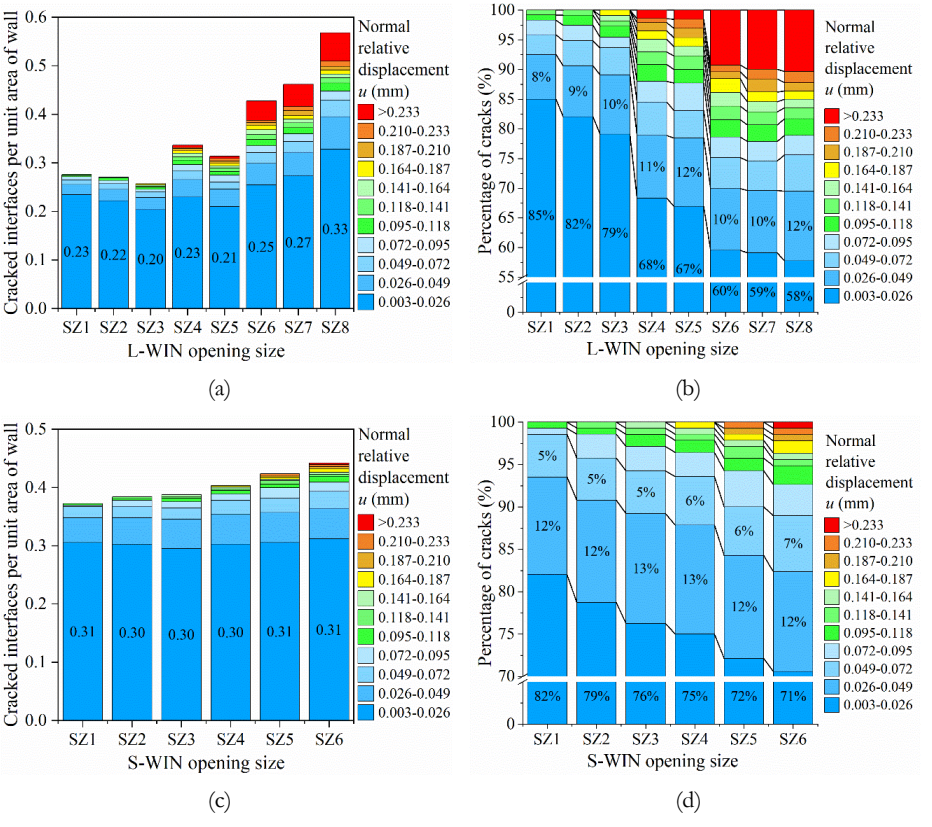

Figure 5.13. The area of the cracked interfaces per unit wall area of (a) L-WIN and (c) S-WIN cases; the percentage of each grouped cracked interface per unit wall net area of (b) L-WIN and (d) S-WIN cases.

5.5.1.4 Influence of opening size on deformation profile

At the two-way bending capacity, deformation profiles at the mid-height of the walls with openings non-covered are presented in Figure 5.14. For long walls (H_w/L_w = 0.6), deformation at mid-height generally increases as the opening size increases (Figure 5.14a), although some deviations are shown for walls with similar opening size, e.g. SZ1-SZ3 of L-WIN and SZ3-SZ6 of L-DOOR. In contrast with the long walls, at the same position as the short walls (H_w/L_w = 1.0), the increase of the opening size only increases the deformation slightly. The deformation profile can be roughly related to the summed cracked interfaces per unit wall area. As the opening size increases, for the long walls, both the summed area of cracked interfaces per unit wall area and the deformation profile increase; for the short walls, these two variables only increase slightly.

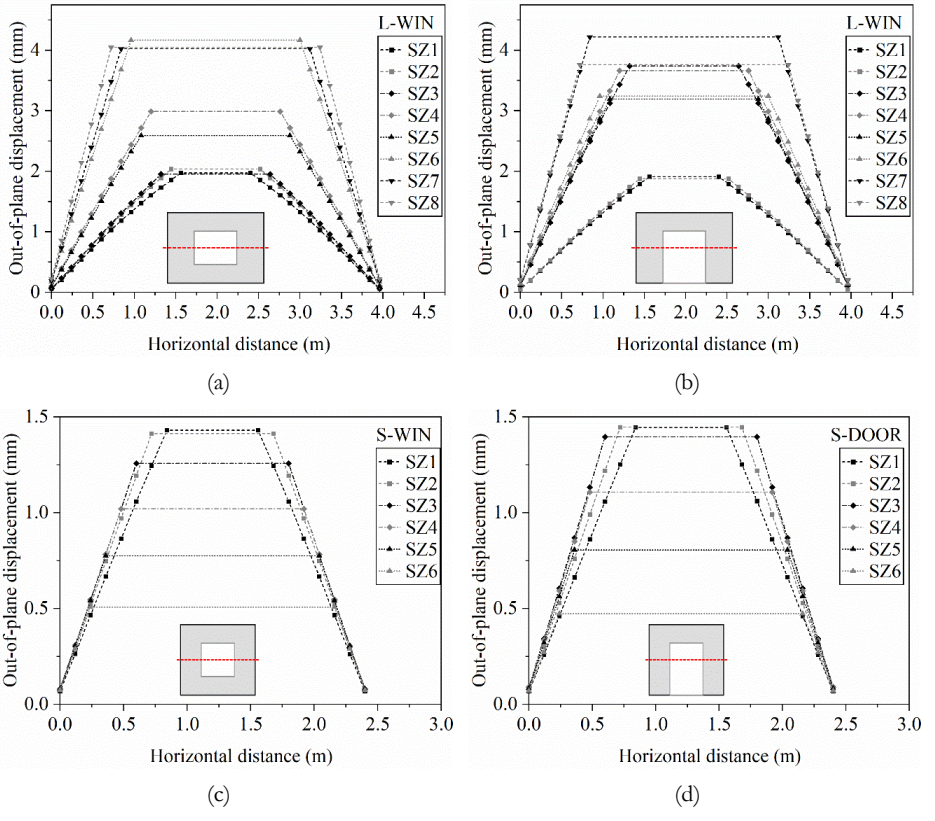

Figure 5.14. Deformation profiles at the mid-height of walls reaching the two-way bending capacity: (a) L-WIN; (b) L-DOOR; (c) S-WIN; (d) S-DOOR.

5.5.1.5 Comparison of the influence of the opening size with different arrangements

In this section, the influence of opening size is studied considering the arrangement of covered and loaded opening areas. The cases of long walls with a window opening are considered (L-WIN). The loading of the opening area is simulated by equivalent loads along the surrounding surfaces of the opening (Model 4 in Section 5.4). Figure 5.15 shows that when the opening area is loaded, as the opening size increases, the normalised two-way bending capacity w_p/w_s decreases followed by a constant value. The difference between these and previous results can be explained as follows. When the opening area is non-covered and non-loaded, as the opening size increases, the bending moments caused by the OOP loads distribute more evenly on the masonry part of the wall. Therefore, the initial stiffness and ductility of the wall increase. Consequently, the wall dissipates more energy, thus reaching a higher two-way bending capacity compared to the solid wall. In contrast, when the opening area is covered and loaded, extra high bending moments carried by the opening area are imposed on the wall. These bending moments are distributed by

the masonry parts, which leads to the reduction of the normalised two-way bending capacity.

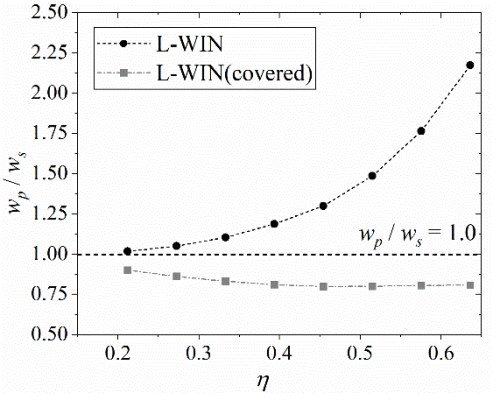

Figure 5.15. Comparisons between different scenarios.

5.5.2 Influence of opening shape

5.5.2.1 Modelling types and cases

In this section, the influence of the opening shape is studied. Based on each case of the long and short wall with a central window (L-WIN and S-WIN) from Section 5.5.1.1, the aspect ratio of opening (α^*) was varied while the opening size (η) and position (λ_x, λ_y) were kept constant. In total, 42 cases were studied including 14 cases from Section 5.5.1.1. The sketches of models and aspect ratios of all cases are present in Figure 5.16.

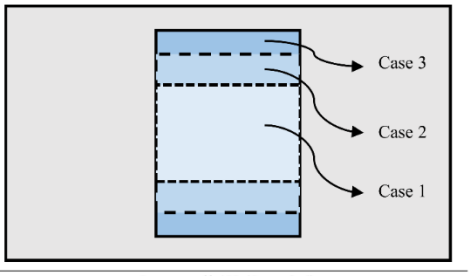

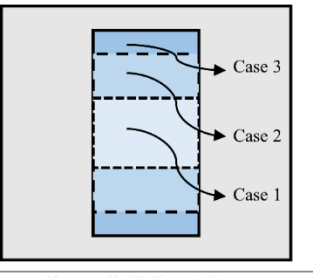

Long wall ($H_w/L_w = 0.6$)

η (L_0/L_w)	0.21	0.27	0.33	0.39	0.45	0.52	0.58	0.64
α^* (H_0/L_0)	0.72	0.72	0.46	0.39	0.33	0.30	0.26	0.24
	1.33	1.19	0.72	0.72	0.72	0.72	0.49	0.51
	2.15	1.67	1.37	1.16	1.00	0.89	0.72	0.72

Short wall ($H_w/L_w = 1.0$)

η (L_0/L_w)	0.30	0.40	0.50	0.60	0.70	0.80
α^* (H_0/L_0)	0.72	0.72	0.43	0.36	0.31	0.27
	1.43	1.08	0.72	0.72	0.51	0.45
	1.91	1.43	1.15	0.96	0.72	0.72

Figure 5.16. Sketches of models and cases concerning the influence of opening shape.

5.5.2.2 Influence of opening shape on two-way bending capacity

The influence of the opening shape on the two-way bending capacity is shown in Figure 5.17. For long walls, when the opening size is constant, the two-way bending capacity increases as the opening aspect ratio increases. Besides, this increasing

effect is small when the opening size is small (η = 0.27), increasing the normalised two-way bending capacity (w_p/w_s) from 1.01 to 1.19 as the opening aspect ratio α^* increases from 0.72 to 2.15. In contrast, this increasing effect is relatively large when the opening size is large, increasing the normalised two-way bending capacity from 1.34 to 2.17 as the opening aspect ratio increases from 0.24 to 0.72. For short walls, when the opening size is smaller than 0.4, the two-way bending capacity decreases first and then increases again as the opening aspect ratio increases. When the opening size is larger than 0.4, the two-way bending capacity constantly increases with the increase of the opening aspect ratio.

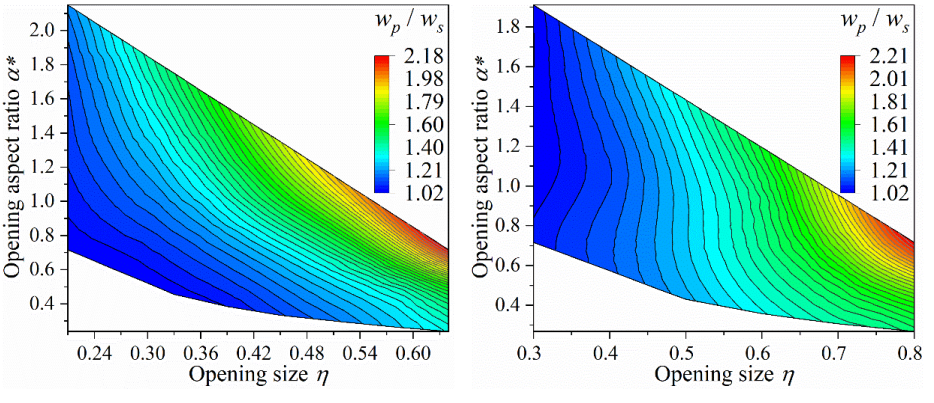

Figure 5.17. Influence of the opening shape on the two-way bending capacity. Cases based on (a) L-WIN; (b) S-WIN. The contour plots are interpolated based on the data boundary.

5.5.2.3 Influence of opening shape on crack pattern

The influence of the opening shape on the wall crack pattern at the two-way bending capacity is shown in Figure 5.18. Cases of the long walls with the opening size of 0.27 and 0.58, and of the short walls with the opening size of 0.4 and 0.7 are selected. Each column presents cases with the same wall aspect ratio and opening size, but varied opening shapes. A general tendency observed is that the locations of the major diagonal cracks remain the same as the opening shape changes. In some cases, secondary diagonal cracks, which are parallel with the major diagonal cracks, can originate from the top corners of the openings, especially with short walls.

The area of the cracked interfaces and the percentage of each grouped cracked interfaces per unit wall area is presented in Figure 5.19a and b, respectively. For long walls and short walls with large opening sizes, both the area of the cracked interfaces per unit wall net area and the percentage of larger cracked interfaces increases with the increase of the opening aspect ratio. In contrast, for short walls with a small opening, the area of the cracked interfaces per unit wall net area decreases first and then increases as the opening aspect ratio increases. This implies that by increasing the opening aspect ratio, a larger number of integration points

are fully cracked; this results in a higher dissipation of fracture energy and results in a higher two-way bending capacity.

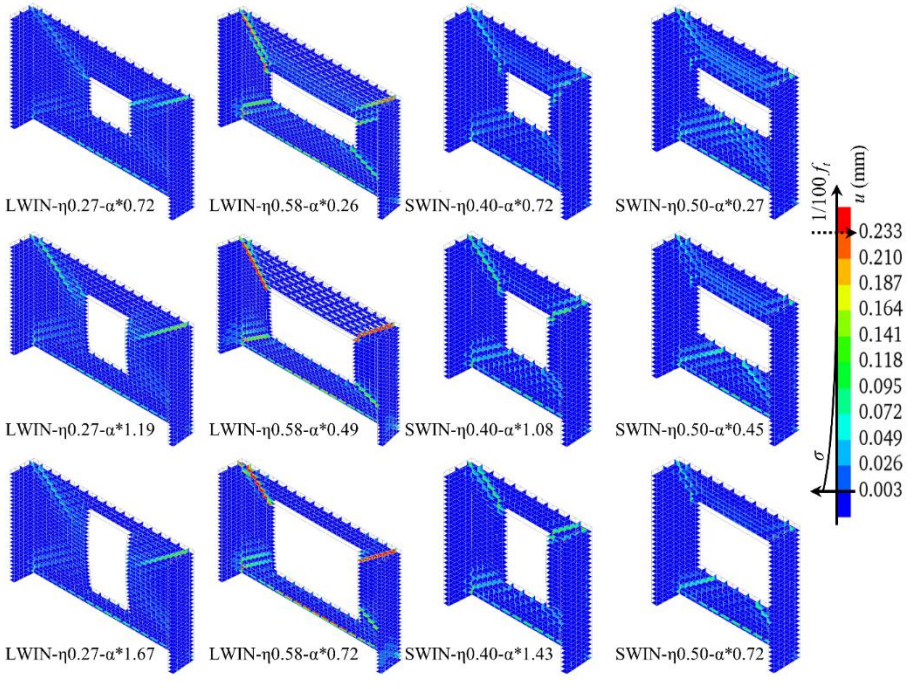

Figure 5.18. Influence of the opening shape on the crack pattern.

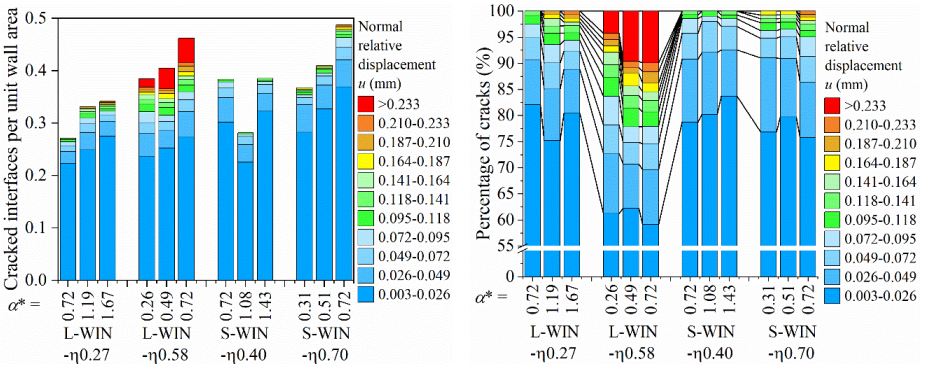

Figure 5.19. Area of the cracked interfaces (a) and the percentage of each grouped cracked interfaces (b) per unit wall net area of selected cases.

5.5.3 Influence of opening position

5.5.3.1 Modelling types and cases

The influence of the opening position is studied in this section. Two models, Type L-WIN-SZ3 and Type S-WIN-SZ2 from Section 5.5.1.1 were selected as reference models. For each reference model, the size and shape of the opening were constant, while the opening position varied. Since the walls are symmetric, the position of the opening only varies on one side. In Figure 5.20, the cases are labelled as "PTXX", and the coordinates of the opening centroids are marked with (λ_x, λ_y) as defined at the beginning of Section 5.5.

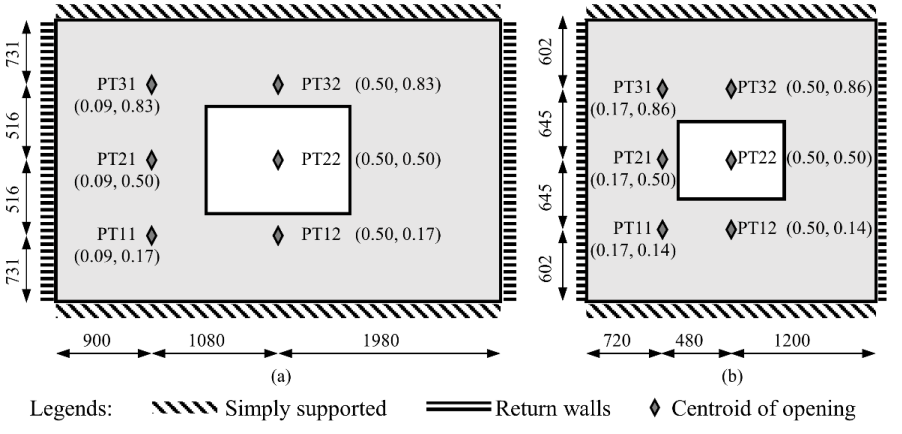

Figure 5.20. Modelling cases exploring the influence of opening position based on (a) L-WIN-SZ3; (b) S-WIN-SZ2.

5.5.3.2 Influence of opening position on two-way bending capacity

The influence of the opening position on the two-way bending capacity is presented in Figure 5.21. Results of cases PT11, 21, and 31 are mirrored in the other symmetric half of the walls. Results show that the influence of the opening position on the two-way bending capacity is limited. For the long walls, the varying opening position causes the normalised two-way bending capacity to change between 1.01 and 1.15. Similarly, for short walls, a variation of the normalised two-way bending capacity between 1.02 and 1.14 is observed. Regardless of the wall aspect ratio, walls with an opening located on the bottom corner show the lowest capacity, while walls with an opening centrally place show the highest capacity.

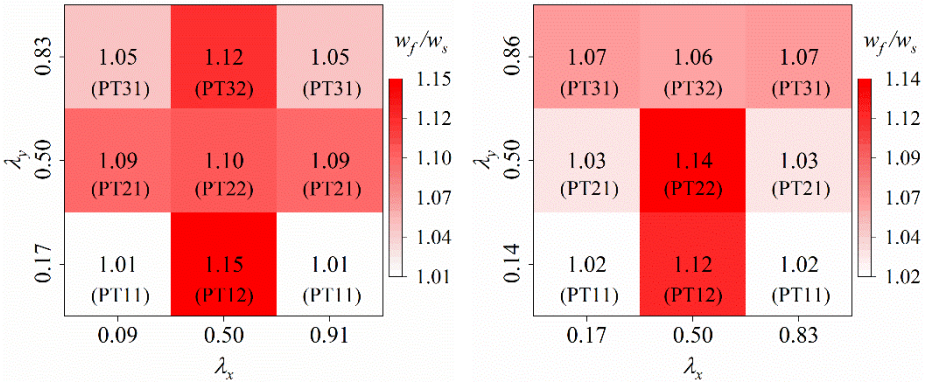

Figure 5.21. Influence of opening position on two-way bending capacity. Cases based on (a) L-WIN-SZ3; (b) S-WIN-SZ2.

5.5.3.3 Influence of opening position on crack pattern

The influences of the opening position on the crack patterns of the long walls and short walls are presented in Figure 5.22 and Figure 5.23, respectively. In the grey-dot-lined boxes of each figure, the crack patterns of each case at the two-way bending capacity are shown to the left, and those at the end of the analysis are shown to the right to provide a reference for the further development of the crack patterns. Unlike the opening size and shape, the opening position can modify the crack pattern to some degree. For the long walls, when the opening is located at the bottom or top corner (L-WIN-PT11 or L-WIN-PT31), a major diagonal crack that should appear in its corresponding solid wall is missing, and the two-way bending capacity is the lowest. If the opening is located at the central left part (L-WIN-PT21), the diagonal crack above the opening originates from the opening corner rather than the wall corner, and multiple secondary diagonal cracks develop above and under the opening. In the case where the opening is located at the centre (L-WIN-PT22) or central top (L-WIN-PT32) of the wall, the positions of the major diagonal cracks are the same, and the central horizontal crack is missing in both cases. If the opening is located at the central bottom part (L-WIN-PT12), the horizontal crack occurs in the upper part of the wall, which together with the diagonal cracks contributes to the highest two-way bending capacity of all cases of L-WIN-SZ3. For the short walls, when the opening is located at the top (S-WIN-PT31), central top (S-WIN-PT32) and central left (S-WIN-PT21) part, the crack patterns are slightly affected except that multiple localised cracks develop from the wall corners. In the case where the opening is located at the bottom part (S-WIN-PT11), the diagonal crack shift to the top corner of the opening, and the bottom right diagonal crack elongates. If the opening is at the centre (S-WIN-PT22), the central vertical crack that should appear in the corresponding solid wall turns to be the horizontal crack above the opening. If the opening is at the central bottom part (S-WIN-PT12), the bottom diagonal cracks start from the wall corners, but develop upwards when they encounter the opening, and elongate diagonally again towards the wall centre.

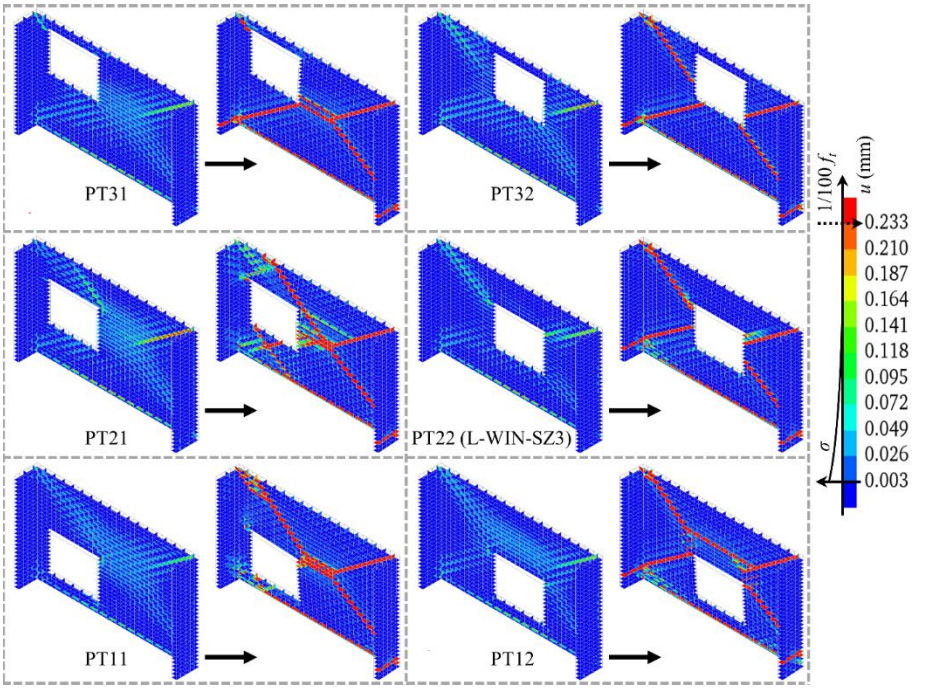

Figure 5.22. The influence of the opening position on the crack pattern of the long walls (L-WIN-SZ3). Within each grey-dot-lined box, the crack patterns at the two-way bending capacity and the end of the analysis are shown to the left and right, respectively.

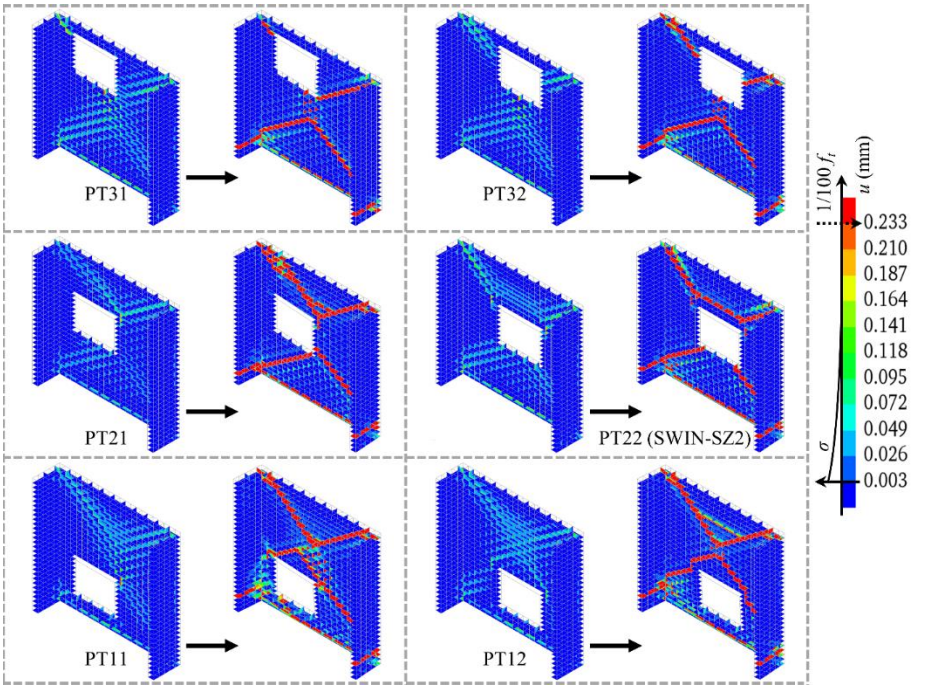

Figure 5.23. The influence of the opening position on the crack pattern of the short walls (S-WIN-SZ2). Within each grey-dot-lined box, the crack patterns at the two-way bending capacity and the end of the analysis are shown to the left and right, respectively.

5.6 Proposed equations and comparison with AS3700

In this section, fitting equations are proposed based on the influence of the opening on the two-way bending capacity studied in Section 5.5. The tendencies of these influences can be summarised as follows: i) the two-way bending capacity is exponentially related to the opening size (η), and this influence is interdependent on the wall aspect ratio (κ) (Figure 5.9); ii) the two-way bending capacity is positively correlated to the opening aspect ratio (α^*) (Figure 5.17); iii) the vertical position of the opening (λ_x) has a very subtle influence on the two-way bending capacity; iv) the influence of the horizontal position (λ_y) of the opening is slight, but increases as the opening moves from the vertical edge towards the central line of the wall (Figure 5.21); v) assuming the same opening size, aspect ratio and position, the difference between the two-way bending capacity of the walls with a window or door is small when the wall aspect ratio is small, but it increases to a large degree if the window is replaced with a door when the wall aspect ratio and opening size are large (Figure 5.9). Based on these observations and applying nonlinear regression techniques, the proposed equations for the normalised two-way bending capacity are proposed as follows.

$$\frac{w_p}{w_s} = \beta_1 \cdot \exp\left(\beta_2 \eta \cdot \kappa^{\beta_3}\right) \cdot (\alpha^*)^{\beta_4} \cdot (\beta_5 |\lambda_x - 0.5| + \beta_6) + \beta_7 + \Delta \tag{5.9}$$

$$\Delta = \begin{cases} 0 & (for\ window) \\ \beta_8 \cdot \eta^{\beta_9} \cdot \alpha^{\beta_{10}} & (for\ door) \end{cases}$$

$$\begin{cases} \beta_1 = 0.14;\ \beta_2 = 5.61;\ \beta_3 = -0.39;\ \beta_4 = 1.03;\ \beta_5 = -0.25; \\ \beta_6 = 0.14;\ \beta_7 = 1.00;\ \beta_8 = 1.74;\ \beta_9 = 3.10;\ \beta_{10} = 1.38 \end{cases}$$

where β_1-β_{10} are constant coefficients; Δ is the supplement coefficient of the opening type. Here it is noted that the range of the opening size (λ) is restricted between 0.2 and 0.8, which excludes cases of extremely small or large openings.

The comparisons of the proposed equations and the numerical results are presented in Figure 5.24. Figure 5.24a and b show that the results of the proposed equations are very close to the numerical results when evaluating the influence of the opening type (door or window), size and wall aspect ratio. Figure 5.24c, together with Figure 5.17c, shows that the influence of the opening aspect ratio with varying opening sizes can also be well represented by the proposed equations. Figure 5.24d shows that the proposed equations predict that the two-way bending capacity increases as the opening moves from the vertical edge to the central line, but is unrelated to the vertical position. The latter prediction is slightly different concerning the numerical results but is acceptable. The standard error of the regression is 0.07, which suggests the numerical results are quite close to the regression results. Overall, the proposed equations can evaluate the general tendency of the influence of the opening on the two-way bending capacity of the wall.

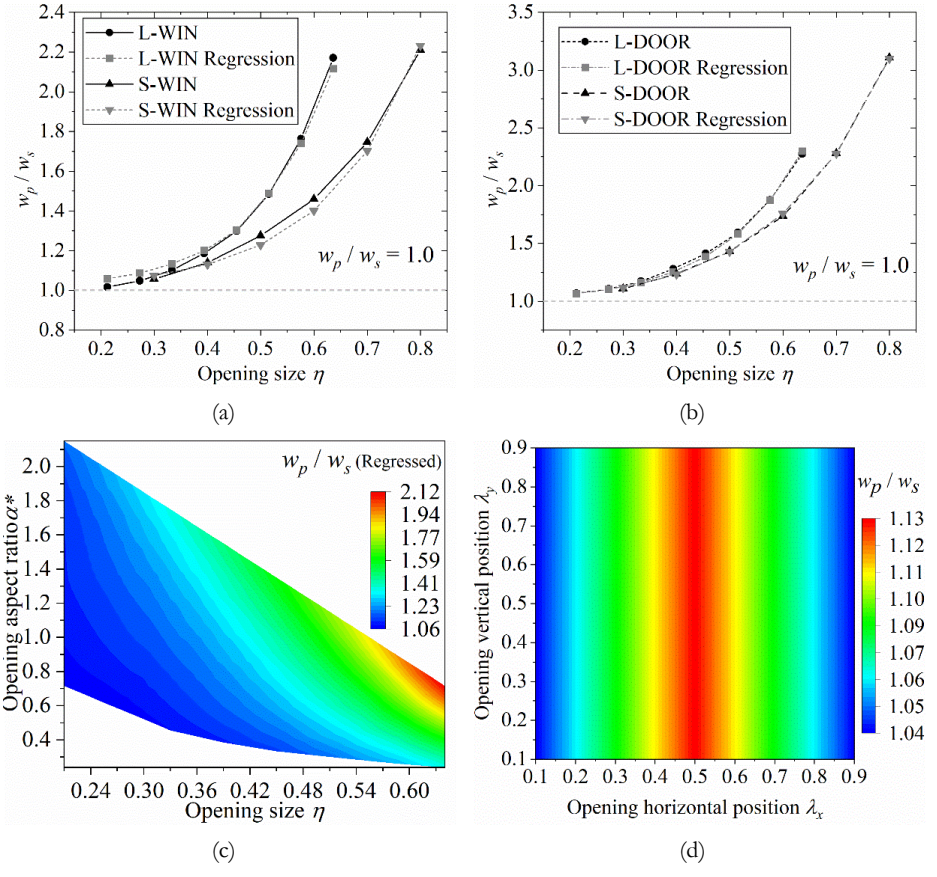

Figure 5.24. Results of the proposed equations concerning, (a) and (b): the wall aspect ratio/opening size considering a central window and door, respectively; (c) the aspect ratio and size of the opening; (d) the opening position.

The proposed equations are further compared with Australian Standard – Masonry Structures AS3700 (2018). In AS3700, the opening area is considered non-covered and non-loaded. Even though AS3700 is more advanced compared to other codes and standards in terms of taking the influence of openings into account, it only considers the influence of the opening size (η) and horizontal position (λ_x). The influence of the wall aspect ratio (κ) and the opening shape (α^*), which was found important to the two-way bending capacity of the perforated walls in this study, is not taken into account.

The comparison of the proposed equations and AS3700 is based on the experimental results of Wall1 (solid wall) and Wall 3 (perforated wall) in (Griffith & Vaculik, 2007). Results are shown in Figure 5.25. According to Figure 5.25a, AS3700 predicts that the presence of an opening reduces the two-way bending capacity ($w_p/w_s < 1$) except a very few cases in which the opening is located in the wall centre and is either very small or large ($\eta < 0.2$ or $\eta > 0.8$). In contrast, the proposed equations suggest that the presence of an opening increases the two-way bending

capacity (w_p/w_s > 1) for most cases. Besides, AS3700 predicts that the two-way bending capacity varies irregularly as the opening size increases (Figure 5.25a), while the proposed equations predict that the former increases constantly as the increase of latter (Figure 5.25b). Additionally, both formulas are in accordance that as the opening moves from the vertical edge towards the wall central line, the two-way bending capacity increases. These results reveal that large differences between AS3700 and the proposed equations exist regarding evaluating the influence of the opening on the two-way bending capacity of URM walls. Further physical experimental research is suggested to supplement more data for walls with various opening sizes, shapes and positions.

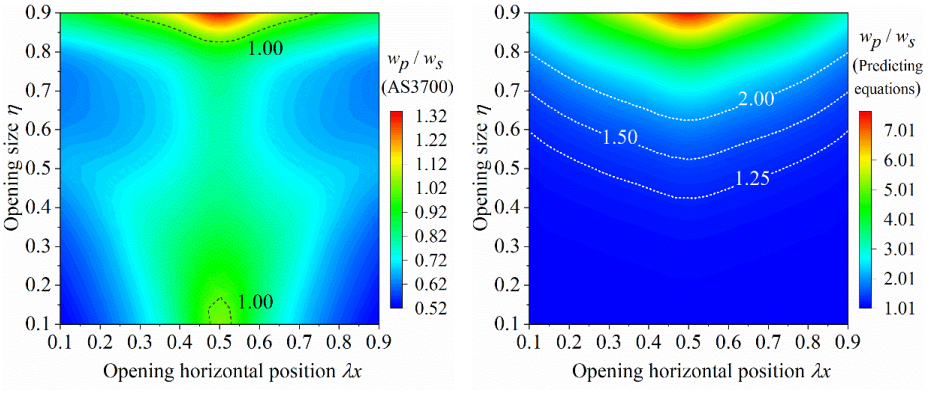

Figure 5.25. Evaluations of the influence of the opening size and horizontal position on the two-way bending capacity by (a) AS3700 and (b) proposed equations.

5.7 Conclusions

In this study, the influence of openings on the two-way bending capacity (defined as the peak pressure on the wall net area) of unreinforced masonry (URM) walls was investigated. First, a brief review was presented to reveal the major findings and limitations of the existing experimental campaigns on the comparable perforated and solid URM walls. Then, an evaluation of the arrangements of the openings, namely the facts of whether the opening area is covered or non-covered, and whether it is loaded or non-loaded, by the Yield Line Method (YLM) was carried out. Next, numerical models were calibrated and validated based on selected experimental benchmarks and were further applied to study the influence of the arrangements of the opening area. Subsequently, a parametric study was carried out to evaluate the influence of the opening geometric parameters, namely size, shape and position for walls with different aspect ratios. Eventually, analytical equations based on the numerical results were proposed and compared with the Australian Standard (AS3700). Conclusions can be drawn as follows:

The existing experimental database concerning perforated URM walls in OOP two-way bending is limited in quantity. Even in each comparable testing group, the

number of samples is quite small, so the high variability of material properties can affect the consistency of the results. Besides, the influence of opening size, shape and position has not been systematically studied by the experiments. Nevertheless, by comparing all the experimental results, the influence of the openings is found to be related to the arrangement of the opening area. The two-way bending capacity of a perforated wall is generally lower than that of its solid counterpart, provided that the opening area is covered and loaded as the rest of the wall; if the opening area is non-covered and non-loaded, the two-way bending capacity of a perforated wall can be higher than that of its corresponding solid wall.

The YLM evaluation confirms that the arrangement of the opening area substantially influences the two-way bending capacity. This is in agreement with the experimental observations. However, it should be noted that relatively rough assumptions were made for this evaluation. For example, the moment capacity was assumed to be equal for both horizontal and diagonal cracks.

The parametric study indicates that when the opening area is non-covered and non-loaded, as the opening size (normalised as the ratio of the opening length to the wall length) increases, the normalised two-way bending capacity of the perforated wall (defined as the ratio of the capacity of the perforated wall to that of the solid wall) increases exponentially. With the same opening size, the two-way bending capacity of a wall with a door is higher than that of a wall with a window. This difference gets larger as the wall aspect ratio and opening size increase. Besides, at the two-way bending capacity, as the opening size increases, the deformation at the mid-height of the wall generally enlarges, and the crack pattern remains similar. Additionally, as the opening size increases, more cracks fully open per unit wall net area, which suggests more fracture energy is dissipated. This results in a higher two-way bending capacity.

As the opening aspect ratio (the opening height to length) increases, the two-way bending capacity increases, but the crack pattern remains similar. The influence of the opening position on the two-way bending capacity is limited. As the opening moves horizontally from the lateral edge towards the wall central line, the two-way bending capacity increases slightly. However, as the opening position varies, either vertically or horizontally on the wall, the diagonal cracks can shift positions, and more secondary diagonal cracks can appear.

The proposed equations were proposed based on a close regression of the numerical results (standard error of the regression: 0.07). Compared with the proposed equations, AS3700 predicts that the presence of the opening weakens the wall capacity. Besides, AS3700 predicts that the two-way bending capacity varies irregularly as the opening size increases. Both the proposed equations and AS3700 predict a similar influence of the opening position on the two-way bending capacity. However, the influence of opening shape and wall aspect ratio on the perforated walls is not considered in AS3700 but can be predicted by the proposed equations.

In summary, a systematically experimental study on the influence of openings on the two-way bending capacity of URM walls is scarce but necessary. Such a study is

beneficial for further development of the knowledge of the wall behaviour and can provide the basis for numerical study. Furthermore, the quantitative relations between the geometric parameters of openings and the two-way bending capacity of URM walls are acquired from the numerical study. Finally, it should be noted that the two-way bending capacity is defined in terms of pressure rather than force. This follows the conventions of current standards and is advantageous for comparing walls with various geometry. However, this definition can lead to irrational results for extremely large or extremely small opening sizes, which, however, are not common in practice. Therefore, the range of the opening size in the proposed equations is restricted according to practical scenarios. The quantitative relationships between the openings and the two-way bending capacity determined in this chapter will be incorporated into the improved analytical formulation proposed in Chapter 6.

Chapter 6

IMPROVED ANALYTICAL FORMULATION BASED ON VIRTUAL WORK METHOD

As discussed in Chapter 2, the current analytical formulations evaluating the two-way bending capacity of the URM walls are limited in accuracy and application range, which can reduce their reliability in practical engineering. Therefore, further improvements to the current analytical formulations are necessary.

This chapter presents an improved analytical formulation based on the Virtual Work Method (VWM) by making use of the findings of the parametric numerical study. To achieve this, the influence of the geometric parameters, namely the wall aspect ratio, pre-compression and openings, on the two-way bending capacity of URM walls observed in the parametric numerical study (Chapter 4 and Chapter 5) was incorporated into the VWM. After determining the material properties as input, the improved analytical formulation was calibrated against the numerical study. Then, the validation of the analytical formulations was carried out against the experimental dataset presented in Chapter 2. Besides, the influence of the lateral boundary conditions and the failure of head joints were discussed. Results show that the improved analytical formulation provides more accurate predictions than the former versions of VWM. Finally, issues and limitations lying in the improved analytical formulation, are further discussed.

6.1 Establishment of the improved analytical formulation

In this section, an improved analytical formulation evaluating the two-way bending moment capacity of URM walls is proposed. The improved analytical formulation is based on the Virtual Work Method rather than the Yield Line Method, because the former has more rational assumptions and a wider application range than the latter, as discussed in Chapter 2. First, the basic assumptions and principles of VWM applied in AS3700 (2018)[5] and its updated version by Willis et al. (2006) are introduced and discussed. Then, the numerical findings presented in Chapter 4 and Chapter 5, namely, the relations between various geometric parameters and the two-way bending capacity are incorporated into the improved analytical formulation. Afterwards, a discussion regarding the influence of the lateral boundary conditions and the failure of head joints is made. Eventually, the improved formulation is compared with past VWM formulations to evaluate its accuracy.

6.1.1 Current Virtual Work Method formulations

The basic assumptions of the VWM applied in the AS3700 (2018) are mainly based on the crack patterns of walls observed in the experiments by Lawrence (1983). The major experimental findings are that:

- If four-edge restrained walls are long enough, the horizontal crack takes place along the bed joints at the mid-height of the walls in the early stage of loading. The upper and lower panels of the wall separated by this crack work independently as three-edge restrained walls.
- Vertical cracks develop along the lateral edges of walls provided that the rotation of these edges is sufficiently restrained.
- The diagonal cracks follow the mortar joints in a stepped manner. The direction of the diagonal crack is dominated by the dimensions and bond patterns of the bricks. For example, if the wall is in a stretcher bond, the diagonal cracks start from the corners, move along half a bed joint, go through a head joint, turn to the next bed joint in the same direction and so on (Figure 6.1).
- For short walls, if the diagonal cracks from the bottom (or top) edge intersect, a vertical crack forms and goes upwards (or downwards) at the central area of the wall.

[5] The 2018 version of the AS3700 inherits the analytical formulation regarding the two-way bending capacity of the URM walls in the 2001 version of the code.

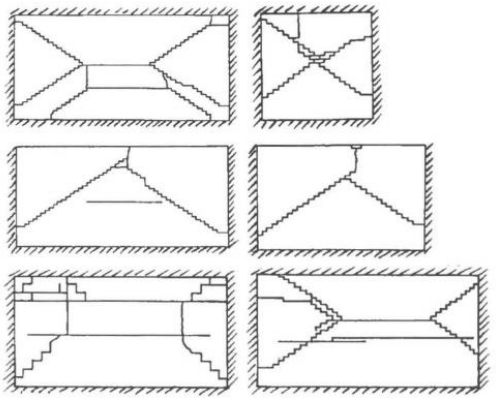

Figure 6.1. Examples of wall crack patterns (Lawrence & Marshall, 2000).

The analytical formulation based on the VWM proposed by Lawrence and Marshall (2000) and incorporated in AS3700 makes the following assumptions in the case when a wall reaches its two-way bending capacity:

- The contribution of the central horizontal crack to the two-way bending capacity is omitted because it is assumed that these cracks form way before the two-way bending capacity was reached and thus do not contribute to the resisting mechanism.
- The dimensions and bond patterns of the bricks determine the angle of the diagonal cracks because cracks are assumed to form at the brick-to-mortar interface or in mortar joints.
- The ratio of the angle of the diagonal crack to the wall aspect ratio determines the presence of a central vertical crack.
- The rotational stiffness of the lateral edges determines the presence of vertical cracks along these edges.
- Cracks along the top and bottom edges are omitted.
- The wall separated by the crack lines works as a mechanism composed of several rigid flat plates. The wall edges and crack lines are considered the hinges of these plates. The relative rotation between adjoining panels is proportional to the OOP deflection of the wall.

Considering these assumptions, the potential crack patterns of walls can be categorised into eight types depending on the wall aspect ratio and boundary conditions, as shown in Figure 6.2.

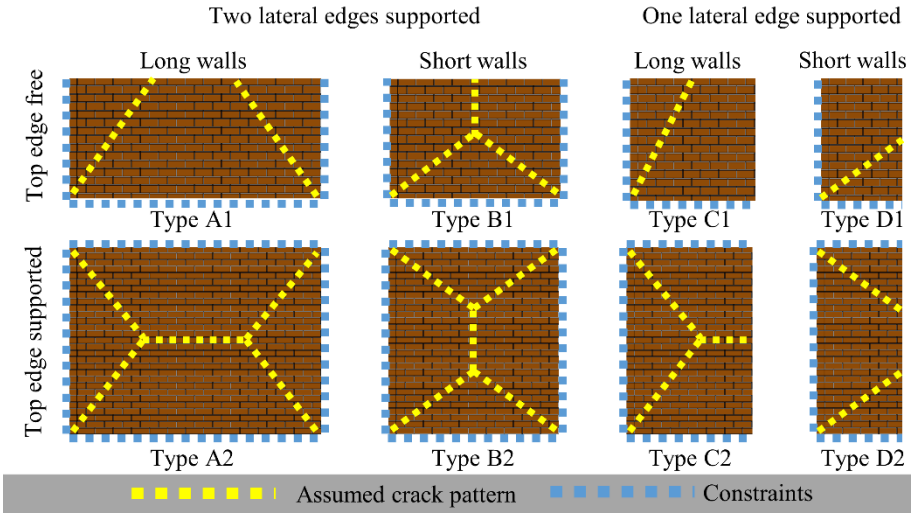

Figure 6.2. Various types of crack patterns of walls based on the assumption by Lawrence and Marshall (2000).

Based on the above-mentioned assumptions, the fundamental principles for the calculation of the two-way bending capacity are that, subjected to a unit OOP deflection:

- The potential crack pattern of a wall is assessed via its geometry and boundary conditions.
- The dissipated internal energy of a single crack is the product of the bending moment capacity on that crack line and the relative rotations of the adjoining rigid flat plates. The dissipated internal energy of a wall is the sum of the dissipated energy along all cracks.
- Assuming the largest deflection of the wall to be 1, the virtual work on a wall is the integral of the OOP load and the deflection of the wall on the surface.
- The virtual work equals the dissipated internal energy of the wall.

The analytical formulation is therefore deducted as shown in the following equations:

$$w = C_{vw} \cdot (P_h M_h + P_d M_d) \tag{6.1}$$

where w is the two-way bending capacity defined as the peak pressure on the wall net area; C_{vw} is the coefficient of virtual work, i.e., the reciprocal of the total volume swept by the deformed wall subjected to the virtual work; P_h and P_d are participating coefficients of the vertical and diagonal crack lines, respectively, i.e., the product of the length of crack lines and the relative rotations of the adjoining rigid flat plates; M_h and M_d are the bending moment capacity of vertical and diagonal cracks per unit length, respectively. Note here, for the convenience of explaining the physical meaning of the equations, the original formulation in AS3700 (2018) is re-formed

so that C_{mv} is related to the deformed surface of the wall and ($P_h M_h + P_d M_d$) is related to the participant of vertical and diagonal cracks.

In AS3700 (2018), the calculations for the coefficients C_{mv}, P_h and P_d corresponding to various types of crack patterns (Figure 6.2) are listed in Table 6.1. Relevant intermediate parameters are illustrated in Figure 6.3 and explained as follows:

- H_d, L_d – the design height and design length of the wall, respectively. If the top edge of the wall is free, the design height is the height of the wall ($H_d = H_w$); otherwise, the design height is half of the height of the wall ($H_d = H_w/2$). If one of the vertical edges is free, the design length is the length of the wall ($L_d = L_w$); otherwise, the design length is half of the length of the wall ($L_d = L_w/2$); if an opening is presented, L_d is the length of the longer panel beside the opening.
- κ_d – the design wall aspect ratio, $\kappa_d = H_d / L_d$.
- G – the assumed slope of the crack line, $G = 2(h_u + t_j) / (l_u + t_j)$.
- h_u, l_u, – brick height, brick length, respectively.
- t_j – mortar joint thickness.
- α – a slope factor that identifies the expected cracking pattern including a vertical central crack in the case $\alpha < 1$, or a horizontal central crack in the case $\alpha \geq 1$. $\alpha = G \cdot L_d / H_d$.
- R_f – the restraint factor of the rotation of the lateral edges. R_f ranges from 0 (hinged) to 1 (clamped). Unless specifically indicated, R_f is set as 0.5, which assumes that the lateral edges of a wall are at an intermediate state between simply hinged and fully restrained. This assumption has been proved to be effective in previous validations of VWM against the experiments (Griffith & Vaculik, 2007; Derakhshan et al., 2018; Graziotti et al., 2019). However, no systematic experimental study has been done to prove its validity. A further discussion regarding R_f is provided in Section 6.4.

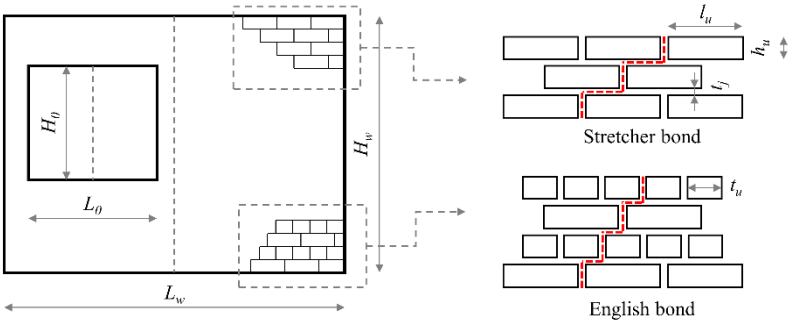

Figure 6.3. Illustrations regarding the commonly used symbols.

Table 6.1. The calculations for the coefficients C_{vw}, P_h and P_d by AS3700 (2018)corresponding to the various types of crack patterns shown in Figure 6.2.

Type of crack pattern (Figure 6.2)	Coefficients		
	C_{vw}	P_h	P_d
A1, A2	$\frac{1}{\frac{{H_d}^2}{\kappa_d}\left(1-\frac{\kappa_d}{3G}\right)}$	$(R_{f1}+R_{f2})G$	$2G\left(1+\frac{1}{G^2}\right)$
B1, B2	$\frac{1}{\frac{{H_d}^2}{\kappa_d}\left(1-\frac{G}{3\kappa_d}\right)}$	$(R_{f1}+R_{f2}+2-2\alpha)\kappa_d$	$2G\left(1+\frac{1}{G^2}\right)$
C1, C2	$\frac{1}{\frac{{H_d}^2}{\kappa_d}\left(1-\frac{\kappa_d}{3G}\right)}$	$2R_{f1}G$	$2G\left(1+\frac{1}{G^2}\right)$
D1, D2	$\frac{1}{\frac{{H_d}^2}{\kappa_d}\left(1-\frac{G}{3\kappa_d}\right)}$	$2R_{f1}\kappa_d$	$2G\left(1+\frac{1}{G^2}\right)$
A with an opening	$\frac{1}{\frac{{H_d}^2}{\kappa_d}\left[\left(1-\frac{\kappa_d}{3G}\right)+\frac{L_0}{2L_d}\right]}$	$2R_{f1}G$	$2G\left(1+\frac{1}{G^2}\right)$
B with an opening	$\frac{1}{\frac{{H_d}^2}{\kappa_d}\left[\left(1-\frac{G}{3\kappa_d}\right)+\frac{L_0}{L_d}\left(1-\frac{G}{2\kappa_d}\right)\right]}$	$2R_{f1}\kappa_d$	$2G\left(1+\frac{1}{G^2}\right)$

The parameters C_{vw}, P_h and P_d assess the geometry and boundary conditions. These include the geometry of the wall (κ_d) and opening (L_0), the dimensions and bond patterns of the bricks (G), and the restrained conditions of the lateral edges (R_f). The calculation of C_{vw} is based on the assumption that the wall consists of several rigid flat plates when it reaches the two-way bending capacity. In this sense, the shape of the deformed wall is assumed as a pyramid, based on which the virtual work is calculated. However, the numerical results in Chapter 4 show that a wall approximates a curved surface rather than a pyramid when it reaches its capacity. Furthermore, when an opening is present in a wall, AS3700 omits the contribution of the smaller panel beside the opening, which may further result in over-conservative estimations. These in total require the reconsideration of C_{vw}.

On the other hand, the material properties are assessed by the horizontal and diagonal bending moment capacity, M_h and M_d. These include the tensile strength of the bricks (f_{bt}) and the flexural strength of masonry having a failure plane parallel to the bed joints (f_{x1}). However, the formulas for M_h and M_d are mostly empirical and dimensionally inconsistent. Besides, some important factors are not taken into account. For example, the contribution of the pre-compression (σ_p) is not included in the calculation of M_d. For a more detailed discussion about the expressions of M_h and M_d in AS3700, readers are referred to Chapter 2.

To assess M_h and M_d based on rational mechanics, updated expressions were proposed by Willis et al. (2006). The basic assumptions of these expressions are that:

- For horizontal bending moment capacity, M_h, two failure modes are considered, namely the line and stepped failure. The former is caused by the bending failure of the bricks, while the latter is caused by the torsional failure of the bed joints. The failure caused by horizontal bending is determined by the worst case of the two modes. Additionally, the bending failure of the head joints is not considered in either failure mode. Additional discussion regarding these aspects is provided in Section 6.4.
- For diagonal bending moment capacity, M_d, the bending and torsional failure of the bed joints are included. The influence of head joints is neglected based on the observation that their failure usually takes place before the wall failure. The bending and torsional failures linearly interact, that is, the sum of the ratios of bending and torsional moments to respective strengths is unity at failure.

According to Willis et al. (2006), the expressions of M_h and M_d are,

$$M_h = lesser\ of \begin{cases} \dfrac{1}{2(h_u + t_j)}\left[(f_{bt} - \nu \cdot \sigma_d) \cdot (h_u + t_j) \cdot \dfrac{{t_w}^2}{6}\right] & \text{(line failure)} \\ \dfrac{1}{h_u + t_j}\left[\tau_u k_b \cdot 0.5(l_u + t_j){t_w}^2\right] & \text{(stepped failure)} \end{cases} \tag{6.2}$$

$$M_d = \frac{\sin\varphi_0}{h_u + t_j}\left[(\sin\varphi_0)^3\,\tau_u k_b + \frac{(\cos\varphi_0)^3\,(f_{x1} + \sigma_d)}{6}\right] \cdot 0.5(l_u + t_j){t_w}^2 \tag{6.3}$$

$$\tau_u = 0.9\sigma_d + 1.6 f_{x1} \tag{6.4}$$

$$\varphi_0 = \tan^{-1} G \tag{6.5}$$

where ν is the Poisson's ratio of masonry; k_b is a coefficient for computing the torsional shear capacity of the bed joints (Willis et al., 2006); f_{bt} is the tensile strength of the bricks; f_{x1} is the flexural strength of masonry having a failure plane parallel to the bed joints; τ_u is the ultimate torsional shear strength of masonry in bed joints; φ_0 is tangent of the assumed slope of the crack line G; σ_d is the pre-compression at the considered position in the wall.

6.1.2 Improved analytical formulation

To address the above-mentioned problems in the VWM and establish an improved analytical formulation, the following modifications are implemented partially based on the numerical study (Chapter 4 and Chapter 5):

- The coefficient of virtual work C_{vw} is calibrated in a way that the two-way bending capacity w is exponentially related to the design wall aspect ratio κ_d, which follows the tendency observed in the numerical study in Chapter 4. This modification essentially reconsiders the deformed shape of walls in the two-way bending capacity based on which the virtual work is calculated. In the original VWM, the shape of the deformed wall is assumed as a pyramid, while the numerical study shows that a wall approximates a curved surface rather than a pyramid when it reaches its capacity.

- A coefficient of opening C_{op} is annexed to the coefficient of virtual work C_{vw}. C_{op} considers the relations between the opening size, shape and position and the two-way bending capacity as observed in the numerical study in Chapter 5. In cases where the opening area is non-covered and non-loaded, these relations include: as the opening size increases, w increases exponentially; as the opening aspect ratio increases, w increases nonlinearly; as the opening moves horizontally from the lateral edge towards the wall central line, w increases linearly. Note that the opening length L_0 is not considered in the design length L_d, as it is in the original VWM, since the presence of an opening is included in the new coefficient C_{op}.

Additionally, the numerical findings in Chapter 4 show that the two-way bending capacity is linearly related to the pre-compression. This relation is automatically satisfied in the original formulations via the expressions of the bending and torsional capacity of bricks and joints. Therefore, no modifications are made for the pre-compression.

Based on the above-mentioned modifications, the improved analytical formulation is introduced as follows. The principal part of the improved analytical formulation is the same as in Equation (6.1) where the participating coefficients of bending moment capacity, P_b and P_d are expressed in Table 6.1. The coefficient of virtual work, C_{vw} is:

$$C_{vw} = \frac{\alpha_0 \cdot e^{(\alpha_1 \cdot \kappa_d)}}{{H_d}^2} \cdot C_{op} \tag{6.6}$$

where α_0 and α_1 are constant coefficients.

$$C_{op} = \begin{cases} \beta_1 \cdot \exp\left(\beta_2 \eta \cdot {\kappa_d}^{\beta_3}\right) \cdot (\alpha^*)^{\beta_4} \cdot (\beta_5 |\lambda_x - 0.5| + \beta_6) + \beta_7 + \Delta \\ 1 \quad (no\ opening) \end{cases} \tag{6.7}$$

$$\Delta = \begin{cases} 0 & (for\ window) \\ \beta_8 \cdot \eta^{\beta_9} \cdot {\kappa_d}^{\beta_{10}} & (for\ door) \end{cases}$$

$$\begin{cases} \beta_1 = 0.14;\ \beta_2 = 5.61;\ \beta_3 = -0.39;\ \beta_4 = 1.03;\ \beta_5 = -0.25; \\ \beta_6 = 0.14;\ \beta_7 = 1.00;\ \beta_8 = 1.74;\ \beta_9 = 3.10;\ \beta_{10} = 1.38 \end{cases}$$

where η is the opening size normalised as the opening length to wall length ($\eta = L_0/L_w$); α^* is the opening shape defined as the aspect ratio ($\alpha^* = H_0/L_0$) for windows; for doors, a nominal height H_0^* is defined as ($2H_0$-H_w), the aspect ratio of the door is defined as $\alpha^* = H_0^*/L_0$; x is the horizontal distance between the opening centroid to the left edge of the wall; λ_x is the opening position defined as the normalised x, see Equation (6.8); $\beta_1 - \beta_{10}$ are constant coefficients; ⊿ is the supplement coefficient of the opening type. The symbols regarding the opening are illustrated in Figure 6.4.

$$\lambda_x = \frac{x - L_0/2}{L_w - L_0} \qquad x \in \left(\frac{L_0}{2}, L_w - \frac{L_0}{2}\right) \tag{6.8}$$

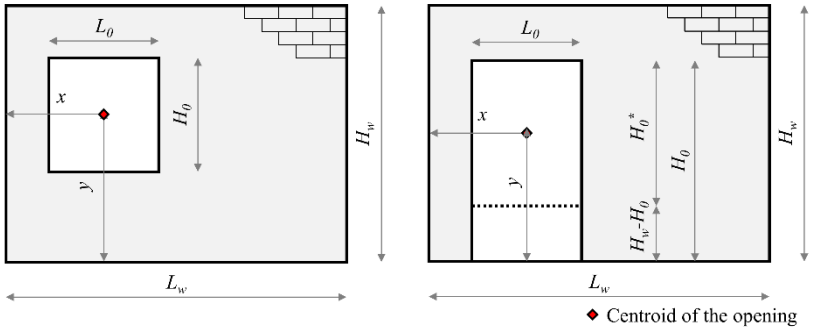

Figure 6.4. The illustration of the symbols regarding the openings.

The horizontal and diagonal bending moment capacities (M_h and M_d) follow those methods introduced by Willis et al. (2006), namely, Equations (6.2) and (6.3).

6.2 Calibration of the improved analytical formulation

Most of the parameters within the improved analytical formulation, such as the designed height and length of walls, can be determined directly before the calculations. The material properties and some of the intermediate parameters, however, need to be evaluated with more caution. The material parameters required are the tensile strength of the bricks f_{bt}, the flexural strength of masonry having a failure plane parallel to the bed joints f_{x1}, the bond strength of masonry f_w and the torsional shear strength of the bed joints τ_u. In the following sections, the methods of determining the material properties are first introduced. Then, the intermediate parameters are determined or calibrated against the numerical results. The intermediate parameters include the constant coefficients for the coefficient of virtual work α_0 and α_1.

6.2.1 Determination of the material properties

The values of the material properties are directly retrieved from the testing data if they are available. Otherwise, these values are evaluated from methods in the literature. In Table 6.2, the tensile strength of bricks f_{bt} is estimated as 0.1 of their compressive strength f_b (NPR9998, 2018; Jafari et al., 2022). The flexural strength of masonry f_{x1} is estimated with different values for clay and calcium silicate masonry (NPR9998, 2018). The bond strength of masonry f_w is estimated to be equal to the flexural strength according to the experiments by Jafari et al. (2022). According to the research by Willis et al. (2004) and Sharma et al. (2021), the ultimate torsional shear strength of masonry in bed joints τ_u is supposed to be evaluated via the formula $\tau_u = f_{v0} + \mu \cdot \sigma_d$, in which f_{v0} and μ are the initial cohesion and initial frictional coefficient of the bed joints, respectively. However, since the companying tests on shear behaviour are very rare in the existing testing campaigns for entire walls, this formula can be substituted with the empirical formulas based on the tests of clay brick and calcium silicate brick masonry proposed by Graziotti

et al. (2019). Even so, it is worth noting that these empirical formulas were based on a limited number of tests on specific batches of bricks, thus possibly causing inaccuracy when they are applied to other types of clay or CS bricks.

Table 6.2. Methods of estimating the material properties.

Material properties	References	Clay bricks	Calcium silicate bricks
f_{bt} (MPa)	NPR9998 (2018); Jafari et al. (2022)	$f_{bt} = 0.1f_b$	
f_{x1} (MPa)	NPR9998 (2018)	0.3	0.15
f_w (MPa)	Jafari et al. (2022)	$f_w = f_{x1}$	
τ_u (MPa)	Graziotti et al. (2019)	$1.55\sigma_d+1.07$	$1.14\sigma_d+1.81$

6.2.2 Calibration based on the numerical results

After determining the methods of estimating the material properties, the only remaining coefficients in the improved analytical formulation are the α_0 and α_1 of the coefficient of virtual work C_{vw} introduced in Equation (6.6). Through the nonlinear regression process referring to the numerical results in Chapter 4, the values of α_0 and α_1 are determined as 0.5304 and 0.7, respectively.

Figure 6.5 presents the comparisons between the numerical results and the predictions by Willis et al. (2006) and the improved analytical formulation. Results of the improved analytical formulation show the two-way bending capacity follows an exponential and linear relation regarding the wall aspect ratio and pre-compression, respectively. Besides, the improved analytical formulation can predict the interdependent relationship between the wall aspect ratio and the pre-compression, as shown in the numerical results (Chapter 4). That is, for a wall with a higher aspect ratio, the same increment of pre-compression can have a larger increment of two-way bending capacity than that of a wall with a lower aspect ratio. Additionally, for a certain wall aspect ratio, the prediction of the influence of the pre-compression by the improved analytical formulation does not perfectly match the numerical results, which can result from a misevaluation of the material properties. As shown by Equations (6.1) - (6.3) and Table 6.1, for a wall with certain dimensions (C_{vw}, P_b and P_d determined), the influence of pre-compression is sensitive to the material properties and has a linear relation with the two-way bending capacity. Since this linear tendency is confirmed by both Willis et al. (2006) and the numerical results, the improved analytical formulation keeps the mechanically deducted formulas regarding the bending moment resistance (M_b and M_d) by Willis et al. (2006). However, the obvious difference between the improved analytical formulation and the numerical results on predicting the influence of pre-compression suggests further study on the consideration of the material properties.

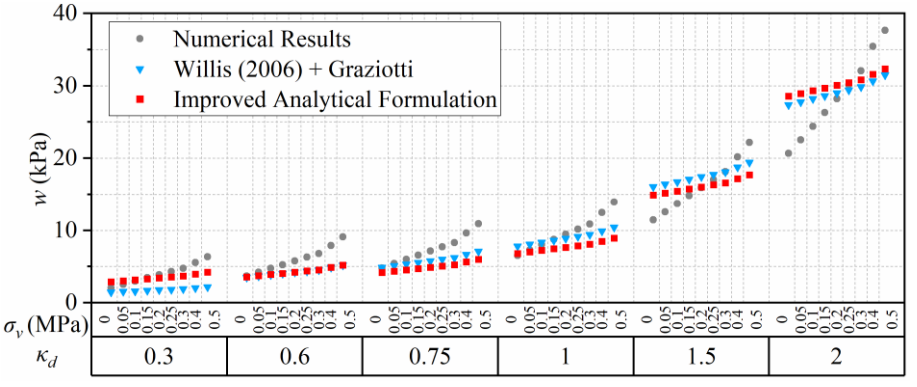

Figure 6.5. Comparisons between the numerical results and the predictions regarding the wall aspect ratio κ_d and pre-compression σ_v by Willis (2006) and the improved analytical formulation. Note here two different sets of input parameters are required for the analytical formulations and numerical models.

6.3 Validation of the improved analytical formulation against experimental results

The improved analytical formulation is applied to predict the two-way bending capacity of the tested walls reported in the dataset in Chapter 2. In total, 46 walls are compared. R_f is set as 0.5 for all the analytical formulations as discussed in the previous section; a discussion on the effect of this parameter is presented in Section 6.4. The torsional shear strength τ_u is determined by Graziotti et al. (2019) for the analytical formulation by Willis (2006). Figure 6.6 shows the normalised value concerning experimental results for the two-way bending capacity evaluated via AS3700 (year), Willis (2006) and the improved analytical formulation. shows the ratios of the predictions by AS3700, Willis (2006) and the improved analytical formulation to the experimental results. N(±20%) denotes the number of predictions that deviates from the testing results by no more than 20%. N(±20%) is marked with the central light grey area in the figure. Results show that compared with AS3700 and Willis (2006), the predictions by the improved analytical formulation are more distributed in the N(±20%) area. Table 6.3 shows that on average in all cases, the ratios of the predictions to the experimental results by AS300 and the improved analytical formulation are much higher than those of Willis (2006) (98% and 88% compared with 85%). Regarding the deviations of the predictions, 27 out of 46 predictions by the improved analytical formulation deviate less than 20% from the experimental results, which has an obvious advantage over the other formulations (17 and 12 out of 46 by AS3700 and Willis (2006), respectively).

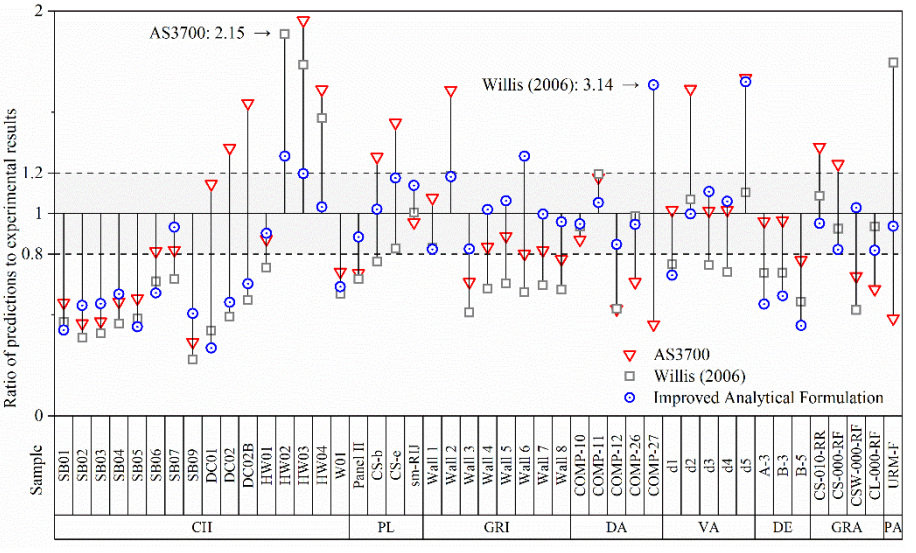

Figure 6.6. The ratio of predictions by AS3700, Willis (2006) and the improved analytical formulation to experimental results. Testing campaigns: CH: Chong (1993); PL: van der Pluijm (1999, 2001); GRI: Griffith et al. (2007); DA: Damiola et al. (2018); VA: Vaculik et al. (2018): DE: Derakhshan et al. (2018); GRA: Graziotti et al. (2019); PA: Padalu et al. (2020).

Table 6.3. The average of ratio of the predictions to the experimental results on all specimens.

Analytical formulations	AS3700	Willis (2006)	Improved analytical formulation
Mean of the ratios of the predictions to the experimental results	98%	85%	88%
Coefficient of variation	0.43	0.59	0.33
N(±20%)*	17	12	27

*N(±20%) denotes the number of predictions that deviates from the testing results by no more than 20%.

The comparisons of the analytical formulations regarding the wall aspect ratio and pre-compression are shown in Figure 6.7. In the experimental database, only the testing campaign by Griffith and Vaculik (2007) provides comparable testing samples. In Figure 6.7, the improved analytical formulation can always indicate the enhancing effect of the increasing pre-compression on the two-way bending capacity, while in some cases AS3700 and Willis (2006) fail to predict this effect, such as with Wall 3, 4 and 5. All the formulations can predict that the wall capacity increases as its aspect ratio increases (Wall 3 and Wall 7; Wall 5 and Wall 8). However, the newly implemented exponential relation between the wall capacity and the wall aspect ratio (see Equation (6.6)) cannot be validated due to the lack of a sufficient number of experimental specimens. Besides, note it is also debatable if wall pairs Wall 3 and Wall 7, Wall 5 and Wall 8 are comparable since the opening positions are different.

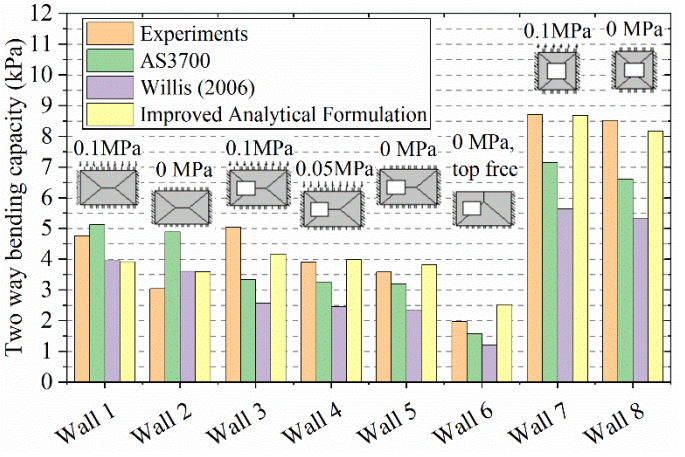

Figure 6.7. Comparisons between the analytical formulations regarding the pre-compression and wall aspect ratio considering the experimental benchmarks by Griffith and Vaculik (2007) (Please note that Wall 2 was retested due to an initial sliding at its bottom edge during the first test).

The comparisons of the analytical formulations regarding the openings are shown in Table 6.4. The opening areas of perforated walls in groups 1-4 are covered and loaded as the remaining masonry part, while those in groups 5-10 are non-covered and non-loaded. Experimental results show that two scenarios exist: when the opening area is covered and loaded, the presence of the opening reduces the wall capacity; when the opening area is non-covered and non-loaded, the presence of the opening increases the wall capacity (Chapter 5). However, the capacity of perforated walls in groups 8-10 is higher than that of their solid counterparts, even though the opening areas are non-covered and non-loaded. Regarding groups 8 and 9, additional timber supports were added to the vertical edges of the solid walls (samples d1 and d2), which could enhance the fixity of vertical boundary conditions, therefore increasing the wall capacity (Vaculik, 2012). Concerning group 10, the solid wall collapsed due to the formation of long vertical line cracks passing through the bricks in the middle and vertical edges of the wall, while the perforated wall only formed local diagonal stepped cracks upon the upper portion of the longer panel beside the opening (Graziotti et al., 2019). This difference is not found in previous testing campaigns in which the solid and perforated walls share the same crack pattern. The formulation proposed by AS3700 and Willis constantly predicts that the presence of the opening reduces the wall capacity except for the C-shape (one lateral edge free) walls, see group 4. The improved analytical formulation, however, constantly predicts that the presence of the opening increases the wall capacity. This is because the improved analytical formulation only considers the seismic scenario in which the opening area is non-covered and non-loaded.

Table 6.4. Comparisons of the analytical formulations regarding the openings.

Group	Sample	Opening		Two-way bending capacity (kPa)	Ratios of the predictions by		
		Area	Position		AS 3700 (kPa)	Willis 2006 (kPa)	Improved analytical formulation (kPa)
					to the experimental results (%)		
1	SB01	-	-	2.80	56	46	43
	SB02	18%	centric	2.40	46	39	55
	SB03	11%	centric	2.30	47	41	55
	SB04	13%	centric	2.20	56	45	60
2	SB06	-	-	7.50	81	67	61
	SB07	11%	centric	5.50	82	68	93
3	DC01	-	-	2.65	115	42	34
	DC02	18%	centric	1.75	133	49	56
4	HW01	-	-	3.70	87	74	90
	HW02	4%	centric	2.80	215	189	129
	HW03	8%	centric	3.30	195	174	120
	HW04	7%	centric	3.70	161	147	103
5	Wall 1	-	-	4.76	108	83	82
	Wall 3	12%	eccentric	5.05	66	51	83
6	Wall 2	-	-	3.04	161	119	118
	Wall 5	12%	eccentric	3.59	89	65	106
7	TUD_COMP-11	-	-	2.45	118	120	105
	TUD_COMP-12	26%	eccentric	3.67	53	53	85
8	d1	-	-	3.95	102	75	70
	d3	13%	eccentric	2.67	101	75	111
9	d2	-	-	2.47	162	107	100
	d5	13%	eccentric	1.61	167	111	165
10	CS-000-RF	-	-	2.65	125	92	82
	CSW-000-RF	27%	eccentric	2.34	69	53	103

Figure 6.8 a and b show the comparisons of the analytical formulations regarding the masonry type and boundary conditions, respectively. The numbers of samples deviating more than 20% of the experimental results (N±20%) in each sub-category are counted and marked on the columns in the figures. Figure 6.8a shows that for both clay (CL) and calcium silicate (CS) brick walls, the improved analytical formulation predicts more precisely than the formulation by AS3700 and Willis

(2006). However, regarding clay brick walls, even the improved analytical formulation only has an accuracy of 50%. This can result from the inaccurate estimation of the material properties, especially regarding the torsional shear capacity of the bed joints to which the horizontal and diagonal bending moment capacities are quite sensitive, see Equations (6.2) and (6.3). Concerning walls with different boundary conditions, the improved analytical formulation performs better than the formulation by AS3700 and Willis (2006) in each sub-category, especially for the O-shape walls (walls supported at all edges). However, all the analytical formulations predict inaccurately for the C-shape wall (walls with one lateral edge free) and the U-shape walls (walls with a top edge free). This problem can arise from the basic assumption of the VWM that an O-shape wall is assumed to be a combination of a U-shape wall and its mirroring part, such as Type B1 and B2 in Figure 6.2. However, the premise of this assumption should be that the top edge of the U-shape wall is rotationally restrained, which is not the case in the experiments. This can lead to a misevaluation of the boundary conditions and therefore results in an inaccurate prediction of the two-way bending capacity.

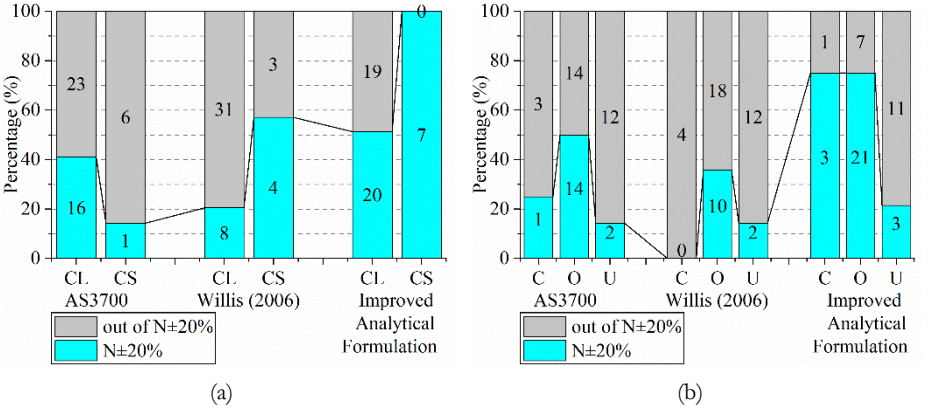

Figure 6.8. Comparisons regarding (a) masonry type and (b) boundary conditions.

6.4 Discussions on the lateral edge's restrain and the head joint behaviour

As discussed in the above-mentioned sections, the improved analytical formulation inherits parts of the original VWM. Among the inherited parts, the rotational stiffness coefficient of the lateral edges R_f, the contribution of the head joints and the failure modes of the vertical cracks can be influential on the two-way bending capacity. This section discusses further regarding these aspects.

The rotational stiffness coefficient R_f determines the contribution of the vertical cracks governed by the lateral boundary conditions. With the VWM, R_f ranges from 0 to 1, representing the lateral edges of a wall being freely rotatable or fully restrained, respectively. Moreover, the value of R_f indicates the contribution of the vertical cracks: with R_f equalling 0, no vertical cracks are considered; with R_f

equalling 1, wall height-long vertical cracks along the vertical edges are taken into account. AS3700 suggests that users are responsible to determine the value of R_f according to their engineering experience. Griffith and Vaculik (2007) and Derakhshan et al. (2018) recommend R_f to be 0.5, which has not been validated by any experimental or numerical studies. In the improved analytical formulation in this study, R_f also takes the value of 0.5 as suggested in the literature.

Since according to the improved analytical formulation, R_f can indirectly affect the influence of pre-compression on the wall capacity, a sensitivity study was conducted to explore this effect. The R_f was set with values of 0, 0.5 and 1. Figure 6.9 shows that for a specific wall, the increase of R_f greatly increases the two-way bending capacity. However, as the pre-compression increases for walls with a certain aspect ratio, the increase of R_f does not influence the increasing tendency of the two-way bending capacity. Nevertheless, the larger the aspect ratio, the larger the relative difference in terms of two-way bending capacity between values of R_f equalling 0 and 1. This suggests that according to the predictions by the improved analytical formulation, the influence of pre-compression on the two-way bending capacity is irrelevant to the rotational stiffness of the lateral edges of walls.

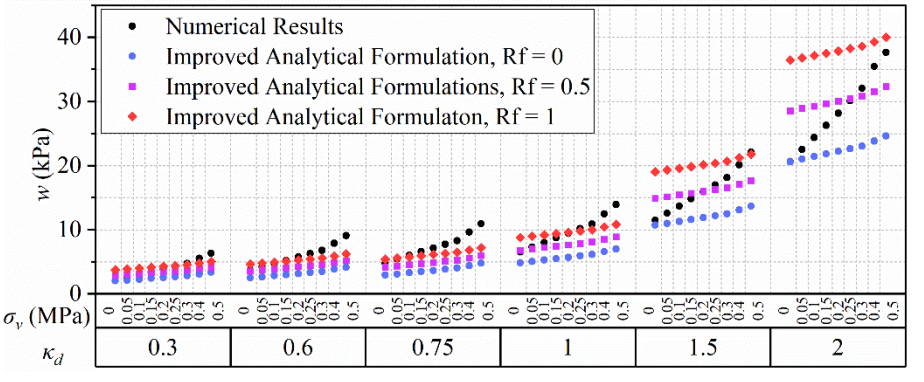

Figure 6.9. Sensitivity study on rotational stiffness coefficient R_f.

Though the updated expressions regarding the bending moment resistance M_b and M_d by Willis are based on rational mechanics, some of the basic assumptions are debatable. First, the bending and torsional contributions of the head joints are ignored. However, according to the numerical results presented in Figure 4.8b in Chapter 4, at the peak capacity, the dissipated energy from the head joints along the predominant cracks can be up to 40% of the total. This suggests that neglecting the contribution of the head joints can lead to a conservative estimation. Besides, the failure caused by horizontal bending is considered either a line or stepped failure. This is also possibly over-conservative since in practice this failure can be a mix of line and stepped failure, as reported by Vaculik (2012) (Figure 6.10).

Figure 6.10. Examples of a mix of line and stepped cracks along the lateral edges of walls (Vaculik, 2012).

Based on the improved analytical formulation, three variation cases of the analytical formulations were studied to check the contribution of the head joints and the failure mode of the vertical cracks: i) head joint failure is considered (Equation (6.11)), while the vertical cracks are either line or stepped (Equation(6.2)); ii) head joint failure is not considered, while the vertical cracks are a mix of line and stepped failure(Equation (6.9)); iii) head joint failure is considered, while the vertical cracks are a mix of line or stepped failure.

$$M_h = 0.5(M_{brick} + M_{head}) + 0.5(T_{bed} + M_{head}) \tag{6.9}$$

$$M_{brick} = \frac{1}{2(h_u + t_j)} \cdot (f_{bt} - \nu\sigma_d) \frac{(h_u + t_j){t_w}^2}{6} \tag{6.10}$$

$$M_{head} = \frac{1}{2(h_u + t_j)} \cdot (f_w - \nu\sigma_d) \frac{(h_u + t_j){t_w}^2}{6} \tag{6.11}$$

$$T_{bed} = \frac{1}{h_u + t_j} \cdot \tau_u k_b \frac{l_u + t_j}{2} {t_w}^2 \tag{6.12}$$

Table 6.5 shows that taking the contribution of head joint failure into account and the consideration of a mix failure mode of the vertical cracks can improve the average accuracy of the prediction. However, all predictions by the variation cases have a larger deviation from the experimental results than the improved analytical formulation in terms of the N(±20%). Figure 6.11 further indicates a closer prediction by the improved analytical formulation than the variation cases. These results suggest that neglecting the contribution of the head joints and considering the vertical cracks as either line or stepped failure is sufficient for the improved analytical formulation. However, experimental or numerical studies are suggested to determine the above-mentioned aspects for further investigating the failure mechanism of walls and improving the accuracy of the analytical formulations.

Table 6.5. The average of ratio of the predictions to the experimental results on all specimens.

Analytical formulations	AS3700	Willis (2006)	Improved analytical formulation	Stepped or lined + head joints	Stepped and lined, no head joints	Stepped and lined + head joints
Mean of the ratios of the predictions to the experimental results	98%	85%	88%	92%	101%	105%
Coefficient of variation	0.43	0.59	0.33	0.33	0.38	0.36
N(±20%)*	17	12	27	24	18	18

*N(±20%) denotes the number of predictions that deviates from the testing results by no more than 20%.

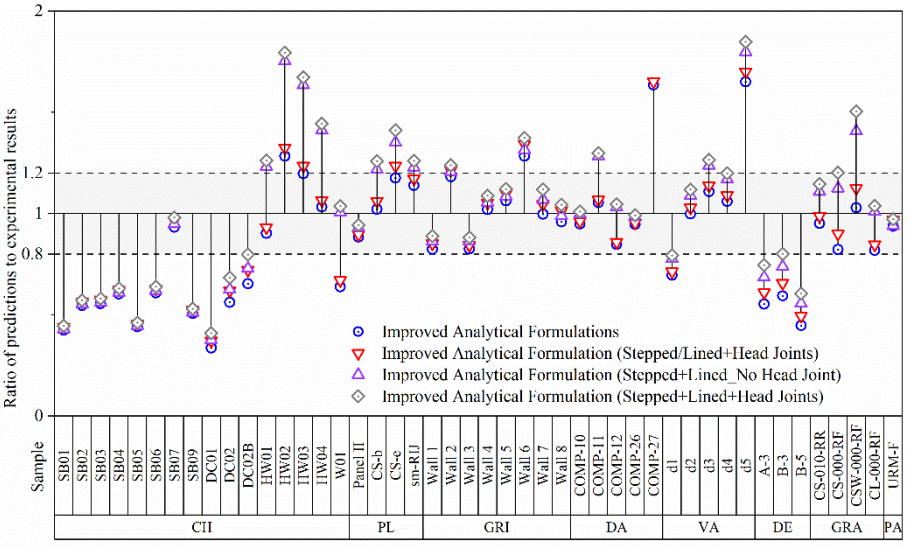

Figure 6.11. Various cases considering the combination of stepped and lined failure and the contribution of the head joints.

6.5 Conclusions, reflections and suggestions

In this chapter, an improved analytical formulation incorporating the numerical findings in Chapter 4 and Chapter 5 is proposed. The modifications mainly concern the wall aspect ratio, pre-compression and openings. Conclusions are:

- Within a dataset of 46 testing samples, the improved analytical formulation assesses the two-way bending capacity of the walls more precisely and with fewer deviations than AS3700 and Willis (2006). This suggests that introducing the tendency between the geometric parameters and the two-way bending capacity from the numerical study to the VWM is promising.

- Neglecting the contribution of the head joints and considering the vertical cracks as either line or stepped failure is sufficient for the improved analytical formulation.

Despite the good performance of the improved analytical formulation, reflections are necessary for the issues existing in the improved analytical formulation. First are some issues resulting from the modifications on the original VWM and the update by Willis et al. (2006):

- The coefficient of virtual work, C_{vw}, is the most important parameter relating to the wall geometry. Essentially, it indicates the total volume swept by the deformed wall subjected to the virtual work. In the improved analytical formulation, C_{vw} follows an exponential relation with the wall aspect ratio. This is based on the numerical observations that the deformed shape of a wall reaching its peak capacity approximates a curved surface. In contrast, the original VWM assumes that the deformed shape of a wall is a pyramid, namely, a combination of several rigid flat plates. However, either assumption of the deformed shape of a wall in its peak capacity does not have any evidence from the experiments.
- The presence of the openings is evaluated by the coefficient of opening C_{op} which is incorporated in the calculation of C_{vw} as a correction factor. This means a perforated wall is firstly evaluated as a solid wall, then its two-way bending capacity is calibrated by C_{op}. Besides, C_{op} is proposed based on the scenario in which the opening area is non-covered and non-loaded, which always leads to a result that the two-way bending capacity of a perforated wall is higher than its solid counterpart. However, the scenario where the opening area is covered and loaded, which is also commonly encountered for the walls subjected to wind loads, has not been incorporated in the improved analytical formulation.

Additionally, the following issues lie both in the improved analytical formulation and the original VWM and the update by Willis et al. (2006) resulting from the inheritance of some assumptions and calculations by the former from the latter.

- The participating coefficients of the horizontal and diagonal bending P_h and P_d follow those of the original VWM. Therefore, P_h and P_d are still calculated based on the assumption that the cracks are in straight lines at the intersections of the rigid flat plates. This is contradictory with the newly proposed C_{vw} in the improved analytical formulation with which the crack lines are curved and the relative rotation along an individual crack between the adjacent cracked wall plates is not constant.
- The improved analytical formulation, following the original VWM, assumes that the upper and lower part of a wall is equivalent to the entire wall. For example, the upper and lower parts of an O-shape wall, which are two U-shape walls, are assumed to be equivalent to the entire wall. And their independently calculated two-way bending capacities are the same by the prediction of the VWM. This assumption, however, is not reliable since the U-shape wall is only equivalent to a half-size O-shape wall when its free edge is rotationally

constrained. In this sense, this equivalent of walls with different boundary conditions can especially overestimate the capacity of a wall with its top edge free.

- The contribution of the head joints is not taken into account in the improved analytical formulations, similarly to the formulation by AS3700 and Willis (2006), based on the assumption that the head joints crack and lost their strength before reaching the wall capacity. However, the numerical results show that at the peak capacity along the predominant cracks, the failure of the head joints is not negligible. This contradiction has not been experimentally investigated. Nevertheless, it should be remarked that in the numerical analyses the same tensile behaviour was assumed for the bed and head joints. This assumption is based on the fact that the walls were constructed with good quality under laboratory conditions. However, such an assumption may not be true with in-situ existing structures where the head joints can be weaker than the bed joints.
- Willis et al. (2006) assume that the vertical cracks are either line or stepped. However, experiments by Vaculik (2012) show that vertical cracks can be a mix of line and stepped failure. If this is the case, assuming the vertical cracks to be either line or stepped failure can lead to overly conservative predictions.
- The improved analytical formulation, like the original VWM, is still sensitive to the material properties, especially the torsional shear strength of the bed joints. The torsional shear strength of the bed joints is suggested by Sharma et al. (2021) to be retrieved from the direct tests. Where its value is not available, it can be estimated via the empirical formulas by Graziotti et al. (2019). However, these formulas were derived from a batch of specific masonry samples including Dutch solid clay and calcium silicate bricks. Considering the large variety of masonry types with different properties, these formulas can produce large errors when predicting the torsional strength of other samples. Therefore, using these formulas can lead to the misevaluation of the wall capacity.

To address the above-mentioned issues, the following aspects are suggested to be explored in future experimental and numerical studies:

- The deformed shapes of walls at the moment of reaching their two-way bending capacity.
- The influence of the openings on the wall capacity.
- The crack patterns of walls with various boundary conditions, especially the rotational stiffness and the free edge.
- The contribution of the head joint failure to the wall capacity.
- The failure mode of the vertical cracks (line, stepped or mix).
- The torsional shear failure mechanisms of the bed joints.

Chapter 7

CONCLUSIONS AND RECOMMENDATIONS

7.1 Conclusions

Investigations on two-way spanning unreinforced masonry (URM) walls subjected to natural hazards, such as earthquakes and wind loads, identify the out-of-plane (OOP) failure as one of the most common failure mechanisms. However, current analytical formulations, such as the one included in the European standard Eurocode 6, the Australian Standard AS3700 and the Dutch Practical Guideline NEN-NPR9998, may inaccurately assess the two-way bending capacity (the peak pressure on the wall net area) of the URM walls and have limited application ranges regarding the geometric parameters, such as the wall aspect ratio, pre-compression, and openings. To address this problem, this research explored the influence of the geometric parameters on the two-way bending capacity of URM walls by employing a 3D simplified brick-to-brick modelling technique. The final goal is to improve the analytical formulations by incorporating numerical results. In this section, the major research processes and contributions are reported.

The research started with the assessment of the accuracy and application range of the current analytical formulations (Chapter 2). A dataset of 46 testing specimens from 8 international testing campaigns was created and used for the assessment. The aim was to indicate the limitations and drawbacks of the current analytical formulations and identify the most influential factors on the two-way bending capacity of the URM walls. Major findings are as follows:

- Compared to the Yield Line Method (YLM), the analytical formulations based on the Virtual Work Method (VWM) provides the most accurate prediction for the testing specimens in the analysed dataset, especially for partially clamped walls and walls with openings.
- The influencing trend of some crucial factors such as the pre-compression predicted by the analytical formulations is contradictory to the testing results, such as the pre-compression.
- The influence of the pre-compression and wall aspect ratio is interdependent, which requires an investigation of their combined effects.
- The application ranges of some crucial factors are limited or not well defined, such as the boundary conditions and the wall thickness/bond patterns.

- The influence of some crucial factors, such as the material properties, and the size, shape and position of the openings, cannot yet be determined due to a lack of systematic experimental study.

To perform for the first time a systematic study on the influence of the crucial geometric parameters, a 3D simplified brick-to-brick modelling approach was adopted. The selection was made in comparison with other modelling strategies and the model was calibrated and validated against quasi-static monotonic tests (Chapter 3). To achieve this goal, nonlinear finite element analysis with a 3D simplified brick-to-brick modelling approach was applied. For interface elements, a Coulomb friction model combined with a tension cut-off and an elliptical compression cap was used. For bricks, a rotating smearing cracking model was employed. The calibration and validation of the model were carried out against quasi-static monotonic experimental data. Besides, the applied approach was compared with other modelling strategies including a continuum modelling approach and a 3D detailed brick-to-brick explicitly considering each brick, mortar joint and brick-mortar interface. The numerical study focuses on strong brick-weak mortar masonry and walls with four-sided restrain. Major findings are:

- A good agreement is found between the numerical and experimental results in terms of the two-way bending capacity, initial stiffness and crack pattern.
- The numerical results show a drop in two-way bending capacity in the post-peak stage, while the quasi-static experiments provide a more ductile post-peak behaviour. This is in disagreement with the selected benchmark (Vaculik, 2012) and with other quasi-static tests, for example, van der Pluijm (1999b); Damiola et al. (2018). However, trends found by the numerical study are reported in other experimental works such as the monotonic static tests by Lawrence (1983) and the shake-table tests by Graziotti et al. (2019) on URM walls in OOP two-way bending that show a sharp decrease in capacity after reaching the peak. Besides, this phenomenon has also been observed in the numerical studies by Karimi Ghaleh Jough and Golhashem (2020), in which a similar modelling approach was adopted. Furthermore, a sensitivity study shows that the post-peak drop is insensitive to the material properties and boundary conditions.
- Compared with the continuum modelling and the 3D detailed brick-to-brick modelling, the 3D simplified brick-to-brick modelling is a good compromise to capture the response at the component level, in terms of wall capacity and crack pattern, with limited computational costs. The employed 3D simplified brick-to-brick modelling approach is concluded to be sufficiently reliable to address the purpose of this study.

With the established numerical models, the influence of the wall aspect ratio and pre-compression on the two-way bending capacity of URM walls was quantified for the first time (Chapter 4). In addition, the numerical results were compared with the current analytical formulations. Major findings are that,

- The two-way bending capacity is exponentially related to the aspect ratio and linearly related to the pre-compression. The influence of the aspect ratio and

pre-compression on the two-way bending capacity is interdependent. That is, as the aspect ratio increases, the same increment of the pre-compression leads to a larger increment of the two-way bending capacity.

- The two-way bending capacity of walls is much higher than the force at the instant of reaching the rigid-plates crack pattern, which is in the post-peak stage; this is the case, especially for low pre-compression values. Consequently, the deformed shapes of the walls at the two-way bending capacity are closer to curved surfaces rather than rigid plane plates. This indicated that the cracking process is not yet completed at the two-way bending capacity in the numerical study whereas a completed localised crack pattern at the two-way bending capacity is assumed in every analytical formulation. It is therefore suggested that the deformed shape of the wall at the two-way bending capacity (especially when the pre-compression is low) should be studied further.
- The torsional failure of bed joints is the predominant failure mechanism for URM walls in OOP two-way bending. As the pre-compression or aspect ratio increases, the proportion of contribution by the torsional capacity of bed joints increases. This suggests that when the aspect ratio increases, the contribution of the torsional behaviour of joints increases, and the increase of the pre-compression enhances this effect thus significantly increasing the two-way bending capacity.

Regarding the openings, the influence of their size shape and location are investigated (Chapter 5). The influence of the arrangement of the opening area, namely, whether the opening area is covered and loaded or not, was investigated by a review of the experimental database and examined via numerical models. A parametric study was carried out to evaluate the influence of the opening geometric parameters, such as type (window or door), size, shape and position on both long and short walls. Major findings are:

- Although limited experimental data is available, by comparing all the available results, the influence of the openings is found to be related to the arrangement of the opening area, namely, being covered and loaded or non-covered and non-loaded. In the former case, the two-way bending capacity of a perforated wall is generally lower than that of its solid counterpart, while in the latter case, the two-way bending capacity of a perforated wall can be higher than that of its corresponding solid wall. The first scenario (covered and loaded) can be considered representative of the action of wind load, while the second scenario (non-covered and non-loaded) can be more representative in the case of seismic loading.
- A preliminary analysis with the YLM and numerical analyses confirm that the arrangement of the opening area substantially influences the two-way bending capacity. This is in agreement with the experimental observations. For the YLM analyses, it should be noted that relatively rough assumptions were made. For example, the moment capacity was assumed to be equal for both horizontal and diagonal cracks. Nevertheless, the numerical results further confirm the

experimental observations and evaluation of the YLM regarding the arrangement of the opening area.

- The numerical parametric study indicates that when the opening area is non-covered and non-loaded, as the opening size (normalised as the ratio of the opening length to the wall length) increases, the normalised two-way bending capacity of the perforated wall (defined as the ratio of the capacity of the perforated wall to that of the solid wall) increases exponentially. With the same opening size, the two-way bending capacity of a wall with a door is higher than that of a wall with a window. As the opening aspect ratio (the opening height to length) increases, the two-way bending capacity increases, and the crack pattern remains similar. The influence of the opening position on the two-way bending capacity is limited. As the opening moves horizontally from the lateral edge towards the wall central line, the two-way bending capacity increases slightly. However, as the opening position varies, either vertically or horizontally on the wall, the diagonal cracks can shift positions, and more secondary diagonal cracks can appear.

Finally, the numerical results were incorporated to propose an improved analytical formulation based on the VWM. To achieve this, the influence of the geometric parameters, namely the wall aspect ratio, pre-compression and openings, on the two-way bending capacity of URM walls observed in the numerical study (Chapter 4 and Chapter 5) was incorporated into the VWM (Chapter 6). After determining the values of required material properties, the improved analytical formulation was calibrated against the numerical study. Then, the validation of the improved analytical formulation was carried out against the experimental dataset presented in Chapter 2. Further, the improved analytical formulation was compared with the Australian Standard AS3700 and its updated version by Willis. Besides, the influences of the lateral boundary conditions and the head joint failure were discussed. Major findings are:

- The improved formulation provides higher accuracy in the prediction of the two-way bending capacity for the dataset collected in Chapter 2. This suggests that introducing the tendency between the geometric parameters and the two-way bending capacity from the numerical study to the VWM is promising.
- Neglecting the contribution of the head joints and considering the vertical cracks as either line or stepped failure is sufficient for the improved analytical formulation.
- The two-way bending capacity predicted by the improved analytical formulation is sensitive to the rotational stiffness coefficient R_f of the lateral boundary conditions. Assigning a value of 0.5 to R_f as recommended in the literature has not been verified by any experiments or numerical studies, which can cause inaccuracy in the evaluation.

7.2 Recommendation for future research

The following aspects are of interest for the further development of this study.

Regarding further experimental studies:

- The influence of the arrangement of the opening area, namely if it is covered and loaded, or non-covered and non-loaded, is suggested to be verified by the tests.
- The torsional behaviour of the bed joints should be investigated with various masonry types. With the same masonry type, the failure modes, such as cracks along with the mortar-brick interface and within the centre of the mortar, are suggested to be studied.
- Other parameters that have not been investigated in this research, such as the rotational stiffness of the lateral edges, the bond patterns and slenderness of the wall, and material parameters deserve more attention.
- The deformed shape at the peak capacity of walls should be re-evaluated. The post-peak response of the URM walls in two-way bending requires further study to validate if it is more ductile or brittle. This is related to the gradual or sudden completion of the final crack pattern and the deformed shape of the wall being curved or rigid plates, which requires further experimental exploration.
- The influence of the rotational stiffness (simply supported, fully clamped or partially clamped) of the lateral boundaries of URM walls is suggested to be studied experimentally.

Regarding further numerical studies:

- The coupling of the tensile cracking, shearing and compression causes numerical instability, especially at the post-peak stage. Efforts are recommended to be put into improving the robustness of the modelling approach.
- The numerical models developed in this research are suggested to be further applied to the weak brick-strong mortar masonry.
- Further detailed comparisons of various modelling techniques, such as the continuum and 3D detailed brick-to-brick modelling approaches can be of interest.
- The trigger of the tensile failure of the bricks can be important. Various modelling techniques, such as modelling an individual brick with the smeared cracking model or a presumed mid-length interface are suggested to be compared.
- The failure of the mortar joints with low compressive strength requires more investigation. Numerical studies at the wallette level can be of interest.

Regarding the further improvement of the analytical formulations:

- Specific values of the rotational stiffness of the lateral edges are suggested to be determined for various types of boundary conditions.

- The torsional shear strength of the bed joints is suggested to be determined either with reliable mechanical deductions or experimental observations as inputs.

Appendix A

TENSILE FAILURE OF THE BRICKS

When applying the 3D brick-to-brick modelling to simulating the URM walls in OOP two-way bending, the failure of the bricks can be modelled with two strategies: i) the bricks are modelled with the smeared cracking model; ii) the bricks are modelled with two linear elastic parts, while the two parts are connected with mid-length brick interface elements. This appendix compares the application of these two strategies via the modelling of the OOP bending of wallettes with DIANA FEA.

Figure A.1 shows the geometry of the models according to NEN-EN 1052-2. Figure A.2 and Figure A.3 show the meshing of the models. Table A.1 concludes the modelling details. Table A.2, Table A.3 and Table A.4 report the input parameters for the bricks and interfaces. Figure A.4, Figure A.5 and Figure A.6 show that applying the input parameters set in Section 3.4, the force-displacement curves, crack patterns and tensile failure of the bricks do not vary when various modelling techniques were employed to simulate the tensile failure of the bricks. This confirms that the modelling strategies in Chapter 3 are suitable for this study.

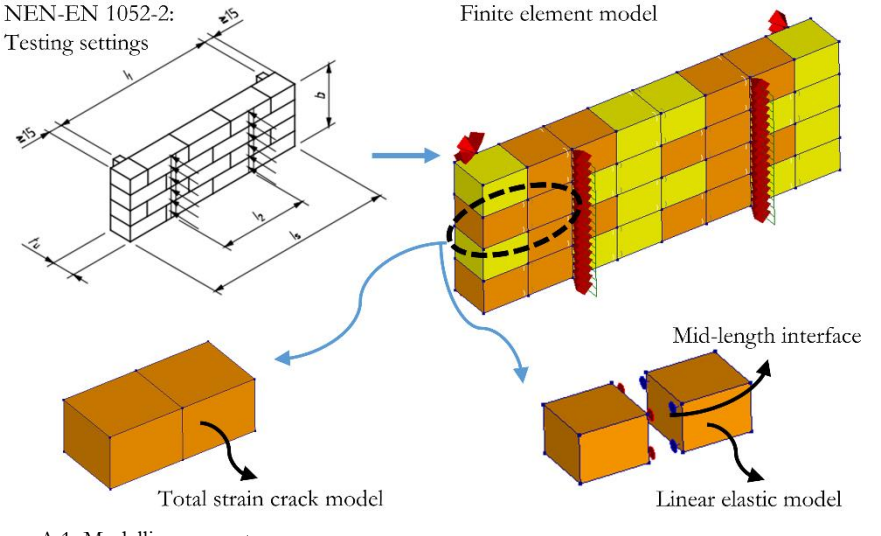

Figure A.1. Modelling geometry

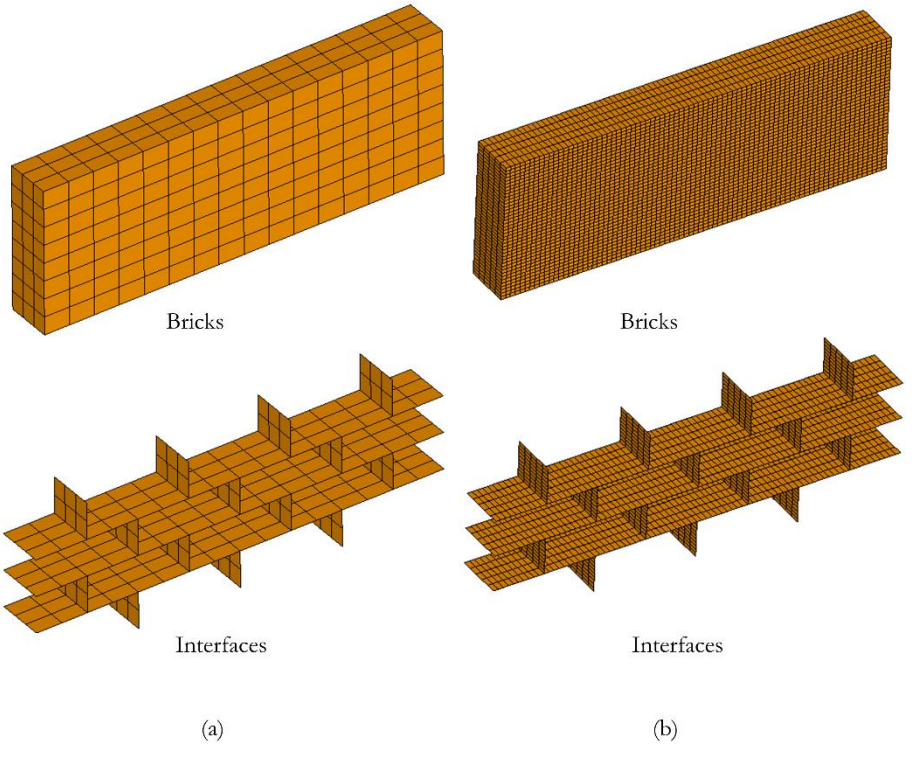

Figure A.2. Mesh size of total strain crack model for bricks. Left: coarse mesh; Right: Fine mesh. Top row: the mesh of the bricks; bottom: the mesh of the interfaces.

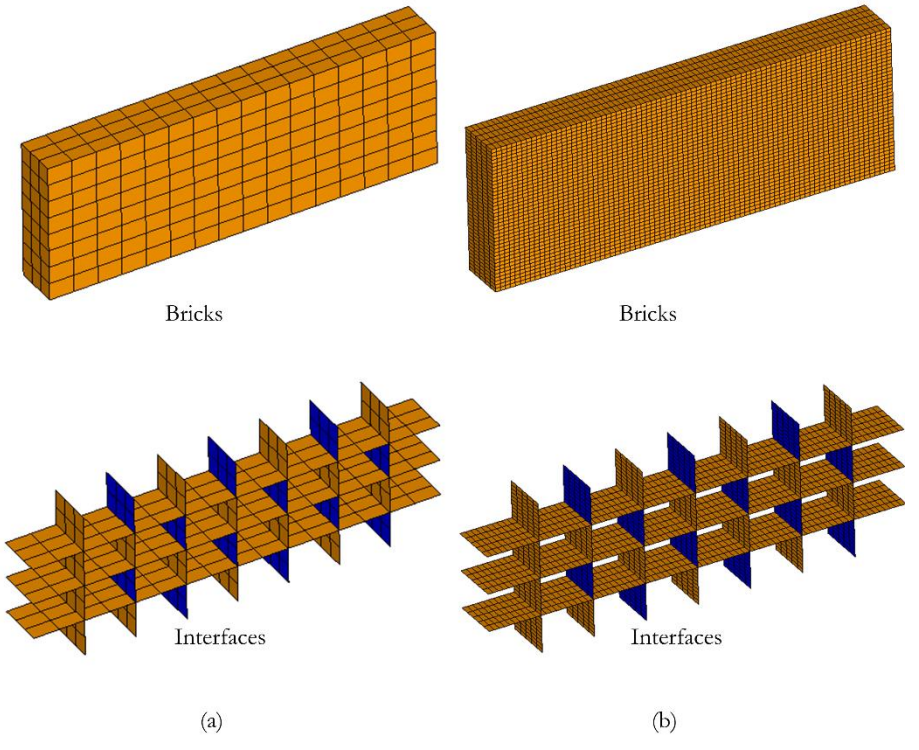

Figure A.3. Mesh size of models in which mid-length brick interfaces are arranged. Left: coarse mesh; Right: Fine mesh. Top row: the mesh of the bricks; bottom: the mesh of the interfaces. Mid-length brick interfaces are high-lightened in blue.

Table A.1. Modelling details

		Models			
		Total strain crack model for bricks – coarse mesh (TSCM-coarse)	Total strain crack model for bricks – fine mesh (TSCM-fine)	Mid-length brick interface – coarse mesh (MidInt-coarse)	Mid-length brick interface – fine mesh (MidInt-fine)
Geometry	Brick size (mm)	Length, height, thickness: 240, 86, 110			
Input parameters	Bricks	Total strain crack model, Table A.2		-	
	Mid-length brick interfaces	Combined cracking-shearing-crushing model, Table A.3			
	Interfaces for mortar joints	-		Discrete cracking model, Table A.4	
Mesh size	Divisions in brick length, height and thickness	4×2×3	20×10×5	4×2×3	20×10×5
Loads		Prescribed displacement			
Iterative methods and convergence norms		Newton-Raphson; force and displacement norms, both satisfied; converging tolerance: 0.01			

Table A.2. Input parameters of bricks (total strain crack model)

Elastic modulus E_b (MPa)	Poisson's ratio υ_b	Density γ (kg/m^3)	Tensile strength f_{bt} (MPa)	Fracture energy $G^I_{f,b}$ (N/mm)
52,700	0.16	1,900	3.55	0.06

Table A.3. Input parameters of interface elements for mortar joints (combined cracking-shearing-crushing model)

Regime	Parameter	Value
Elastic	Normal stiffness k_{nn} (N/mm^3)	70
	Shear stiffness k_{ss} (k_{tt}) (N/mm^3)	30
Tension	Tensile strength f_t (MPa)	0.21
	Mode-I fracture energy G_f^{I} (N/mm)	0.01
Shearing	Initial cohesion c_0 (MPa)	0.21
	Mode-II fracture energy G_f^{II} (N/mm)	0.11
	Friction angle φ (rad)	0.52
Compression	Compressive strength f_c (MPa)	16

Table A.4. Input parameters of mid-length brick interfaces (discrete cracking model)

Regime	Parameter	Value
Elastic	Normal stiffness k_{nn} (N/mm³)	10,000
	Shear stiffness k_{ss} (k_{tt}) (N/mm³)	10,000
Tension	Tensile strength f_t (MPa)	3.55
	Mode-I fracture energy G_f^I (N/mm)	0.06

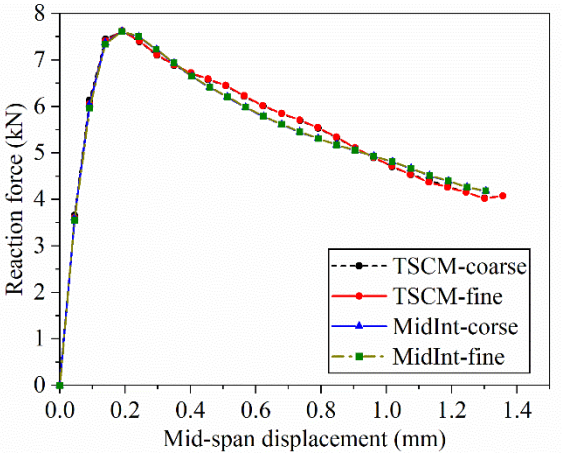

Figure A.4. Force-displacement curves of various models.

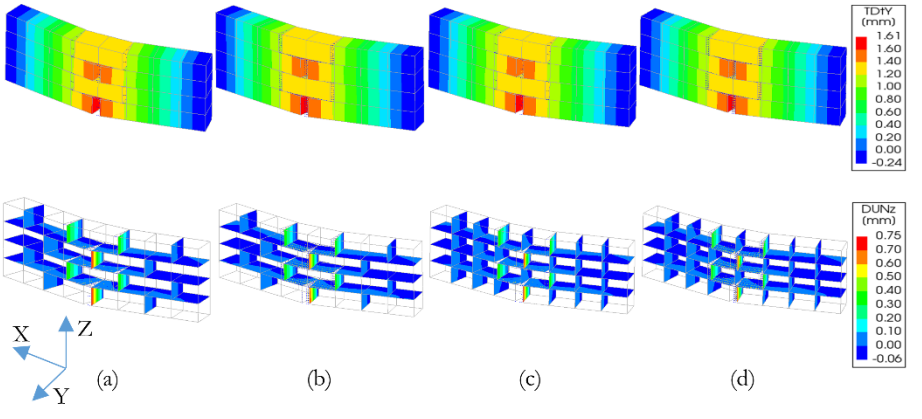

Figure A.5. Deflection and crack pattern of the models: (a) TSCM-coarse; (b) TSCM-fine; (c) MidInt-coarse; (d) MidInt-fine. TDtY: deformation in Y direction; DUNz: normal relative displacement of the interface elements. Deformation factor: 50.

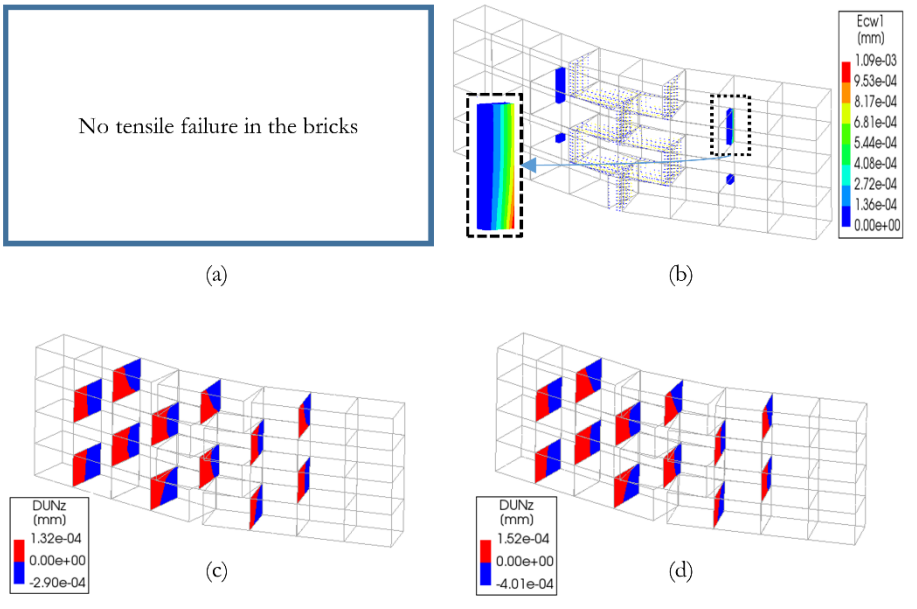

Figure A.6. Tensile failure of the bricks in the models. (a) TSCM-coarse and (b) TSCM-fine: tensile failure of the bricks shown with the smeared cracks in the brick elements. Ecw1: principle crack width. (c) MidInt-coarse and (d) MidInt-fine: tensile failure of the bricks shown with the mid-length interfaces. DUNz: normal relative displacement of the interface elements. Deformation factor: 50.

Bibliography

Abdulla, K. F., Cunningham, L. S., & Gillie, M. (2017). Simulating masonry wall behaviour using a simplified micro-model approach. *Engineering Structures*, *151*, 349-365.

Abrams, D. P., AlShawa, O., Lourenco, P. B., & Sorrentino, L. (2017). Out-of-Plane Seismic Response of Unreinforced Masonry Walls: Conceptual Discussion, Research Needs, and Modeling Issues. *International Journal of Architectural Heritage*, *11*(1), 22-30.

Ahani, E., Mousavi, M. N., Ahani, A., & Kheirollahi, M. (2019). The Effects of Amount and Location of Openings on Lateral Behavior of Masonry Infilled RC Frames. *KSCE Journal of Civil Engineering*, *23*(5), 2175-2187.

Andreotti, G., Graziotti, F., & Magenes, G. (2018). Detailed micro-modelling of the direct shear tests of brick masonry specimens: The role of dilatancy. *Engineering Structures*, *168*, 929-949.

Baker, C., Chen, B., & Drysdale, R. G. (2005). *Failure line method applied to walls with openings*. 10th Canadian Masonry Symposium, Banff, Canada.

Baraldi, D., & Cecchi, A. (2017). A full 3D rigid block model for the collapse behaviour of masonry walls. *European Journal of Mechanics - A/Solids*, *64*, 11-28.

Block, P., & Lachauer, L. (2013). Three-Dimensional (3D) Equilibrium Analysis of Gothic Masonry Vaults. *International Journal of Architectural Heritage*, *8*(3), 312-335.

Bruggi, M., & Taliercio, A. (2015). Analysis of no-tension structures under monotonic loading through an energy-based method. *Computers & Structures*, *159*, 14-25.

Bui, T. T., Limam, A., Sarhosis, V., & Hjiaj, M. (2017). Discrete element modelling of the in-plane and out-of-plane behaviour of dry-joint masonry wall constructions. *Engineering Structures*, *136*, 277-294.

Calò, M., Malomo, D., Gabbianelli, G., & Pinho, R. (2021). Shake-table response simulation of a URM building specimen using discrete micro-models with varying degrees of detail. *Bulletin of Earthquake Engineering*, *19*(14), 5953-5976.

CEN. (1999). *EN 1052-2 - Methods of test for masonry - Part 2: Determination of flexural strength* (Vol. 2).

CEN. (2012). *Eurocode 6: Design of masonry structures, Part 1-1: General rules for reinforced and unreinforced masonry structures*. Brussels, Belgium.

Chang, L.-Z., Messali, F., & Esposito, R. (2020). Capacity of unreinforced masonry walls in out-of-plane two-way bending: A review of analytical formulations. *Structures*, *28*, 2431-2447.

Chang, L.-Z., Rots, J., & Esposito, R. (2020). Numerical modelling of two-way out-of-plane bending tests on URM walls: The influence of lateral boundary conditions. 17th International Brick and Block Masonry Conference -From Historical to Sustainable Masonry, Krakow, Poland.

Chang, L.-Z., Rots, J. G., & Esposito, R. (2021). Influence of aspect ratio and pre-compression on force capacity of unreinforced masonry walls in out-of-plane two-way bending. *Engineering Structures*, *249*.

Chang, L.-Z., Rots, J. G., & Esposito, R. (2022). Influence of openings on two-way bending capacity of unreinforced masonry walls. *Journal of Building Engineering*, *51*.

Chen, B. (2002). *Masonry walls with openings under out-of-plane loading (Master thesis)* McMaster University. Hamilton, Canada.

Chiozzi, A., Milani, G., & Tralli, A. (2017). A Genetic Algorithm NURBS-based new approach for fast kinematic limit analysis of masonry vaults. *Computers & Structures*, *182*, 187-204.

Chisari, C., Macorini, L., Amadio, C., & Izzuddin, B. A. (2018). Identification of mesoscale model parameters for brick-masonry. *International Journal of Solids and Structures*, *146*, 224-240.

Chong, V. L. (1993). *The behaviour of laterally loaded masonry panels with opening* (PhD thesis), University of Plymouth. Plymouth, UK.

D'Altri, A. M., de Miranda, S., Castellazzi, G., & Sarhosis, V. (2018). A 3D detailed micro-model for the in-plane and out-of-plane numerical analysis of masonry panels. *Computers & Structures*, *206*, 18-30.

D'Altri, A. M., Messali, F., Rots, J., Castellazzi, G., & de Miranda, S. (2019). A damaging block-based model for the analysis of the cyclic behaviour of full-scale masonry structures. *Engineering Fracture Mechanics*, *209*, 423-448.

D'Altri, A. M., Sarhosis, V., Milani, G., Rots, J., Cattari, S., Lagomarsino, S., Sacco, E., Tralli, A., Castellazzi, G., & de Miranda, S. (2019). Modeling Strategies for the Computational Analysis of Unreinforced Masonry Structures: Review and Classification. *Archives of Computational Methods in Engineering*, *27*(4), 1153-1185.

D'Ayala, D. F., & Paganoni, S. (2011). Assessment and analysis of damage in L'Aquila historic city centre after 6th April 2009. *Bulletin of Earthquake Engineering*, *9*(1), 81-104.

Damiola, M., Esposito, R., Messali, F., & Rots, J. G. (2018). *Quasi-static cyclic two-way out-of-plane bending tests and analytical models comparison for URM walls*. 10th International Masonry Conference, Milan, Italy.

Damiola, M., Esposito, R., & Ravenshorst, G. J. P. (2017). *C31B67: Quasi-static cyclic out-of-plane tests on masonry components 2016/2017*. Delft, the Netherlands.

Darwin, D., Dolan, C. W., & Nilson, A. H. (2016). *Design of concrete structures*. McGraw-Hill Education New York, NY, USA.

de Vekey, R. C., Bright, N. J., Luckin, K. R., & Arora, S. K. (1986). The resistance of masonry to lateral loading, Part 3: Research results on autoclaved aerated concrete blockwork. *The Structural Engineer*, *64*(11), 332-340.

de Vekey, R. C., Edgell, G. J., & May, I. M. (1996). Lateral load behaviour of walls with openings. The 7th North American Masonry Conference, South Bend, US.

De Villiers, W. I. (2019). *Computational and experimental modelling of masonry walling towards performance-based standardisation of alternative masonry units for low-income housing* Stellenbosch: Stellenbosch University.

Degli Abbati, S., D'Altri, A. M., Ottonelli, D., Castellazzi, G., Cattari, S., de Miranda, S., & Lagomarsino, S. (2019). Seismic assessment of interacting structural units in complex historic masonry constructions by nonlinear static analyses. *Computers & Structures*, *213*, 51-71.

Derakhshan, H., Dizhur, D. Y., Griffith, M. C., & Ingham, J. M. (2014). Seismic assessment of out-of-plane loaded unreinforced masonry walls in multi-storey buildings. *Bulletin of the New Zealand Society for Earthquake Engineering*, *47*(2).

Derakhshan, H., Griffith, M. C., & Ingham, J. M. (2013a). Airbag testing of multi-leaf unreinforced masonry walls subjected to one-way bending. *Engineering Structures*, *57*, 512-522.

Derakhshan, H., Griffith, M. C., & Ingham, J. M. (2013b). Out-of-Plane Behavior of One-Way Spanning Unreinforced Masonry Walls. *Journal of Engineering Mechanics*, *139*(4), 409-417.

Derakhshan, H., Lucas, W., Visintin, P., & Griffith, M. C. (2018). Out-of-plane Strength of Existing Two-way Spanning Solid and Cavity Unreinforced Masonry Walls. *Structures*, *13*, 88-101.

DIANA-BV. (2019). *DIANA user's manual - Release 10.4*. DIANA FEA BV. Delft, The Netherlands.

Dizhur, D., & Ingham, J. (2015). *Seismic Improvement of Loadbearing Unreinforced Masonry Cavity Walls, Report - Branz ER3*. New Zealand.

Doherty, K., Griffith, M. C., Lam, N., & Wilson, J. (2002). Displacement-based seismic analysis for out-of-plane bending of unreinforced masonry walls. *Earthquake Engineering & Structural Dynamics*, *31*(4), 833-850.

Drougkas, A., Licciardello, L., Rots, J. G., & Esposito, R. (2020). In-plane seismic behaviour of retrofitted masonry walls subjected to subsidence-induced damage. *Engineering Structures*, *223*.

Edgell, G. J., & Kjaer, E. (2000). *Lateral load behaviour of walls with openings*. 12th International Brick and Block Conference, Madrid, Spain.

Esposito, R., Messali, F., Ravenshorst, G. J. P., Schipper, H. R., & Rots, J. G. (2019). Seismic assessment of a lab-tested two-storey unreinforced masonry Dutch terraced house. *Bulletin of Earthquake Engineering*, *17*(8), 4601-4623.

Feenstra, P. H. (1993). Computational aspects of biaxial stress in plain and reinforced concrete. *PhD thesis, Delft University of Technology*.

Galvez, F., Sorrentino, L., Ingham, J. M., & Dizhur, D. (2018). *One-Way Bending Capacity Prediction of Unreinforced Masonry Walls With Varying Cross Section Configurations*. 10th International Masonry Conference, Milan, Italy.

Gonen, S., Pulatsu, B., Soyoz, S., & Erdogmus, E. (2021). Stochastic discontinuum analysis of unreinforced masonry walls: Lateral capacity and performance assessments. *Engineering Structures*, *238*.

Graziotti, F., Tomassetti, U., Penna, A., & Magenes, G. (2016). Out-of-plane shaking table tests on URM single leaf and cavity walls. *Engineering Structures*, *125*, 455-470.

Graziotti, F., Tomassetti, U., Sharma, S., Grottoli, L., & Magenes, G. (2019). Experimental response of URM single leaf and cavity walls in out-of-plane two-way bending generated by seismic excitation. *Construction and Building Materials*, *195*, 650-670.

Griffith, M. C., & Vaculik, J. (2007). Out-of-plane flexural strength of unreinforced clay brick masonry walls. *TMS Journal*, *25*(1), 53-68.

Griffith, M. C., Vaculik, J., Lam, N. T. K., Wilson, J., & Lumantarna, E. (2007). Cyclic testing of unreinforced masonry walls in two-way bending. *Earthquake Engineering & Structural Dynamics*, *36*(6), 801-821.

Haseltine, B. A., & Tutt, J. N. (1986). The resistance of masonry to lateral loading, Part 4: Implications of research on design recommendations. *The Structural Engineer*, *64*(11), 341-350.

Haseltine, B. A., Tutt, J. N., & West, H. W. H. (1977). The resistance of brickwork to lateral loading, part II: design of walls to resist lateral loads [Article]. *J. INST. STRUCT. ENG.*, *55*(10 , Oct.1977), 422-430.

Haseltine, B. A., West, H. W. H., & Tutt, J. N. (1977). The resistance of brickwork to lateral loading, Part 2: Design of walls to resist lateral loads. *The Structural Engineer*, *55*(10), 422-430.

Hendry, A. W., Sinha, B. P., & Davies, S. (2017). *Design of masonry structures*. CRC Press.

Isfeld, A. C., Stewart, M. G., & Masia, M. J. (2021). Stochastic finite element model assessing length effect for unreinforced masonry walls subjected to one-way vertical bending under out-of-plane loading. *Engineering Structures*, *236*.

Jafari, S. (2021). *Material characterisation of existing masonry: A strategy to determine strength, stiffness and toughness properties for structural analysis* (PhD thesis), Delft University of Technology. Delft, the Netherlands.

Jafari, S., Rots, J. G., & Esposito, R. (2019). Core testing method to assess nonlinear behavior of brick masonry under compression: A comparative experimental study. *Construction and Building Materials*, *218*, 193-205.

Jafari, S., Rots, J. G., & Esposito, R. (2020). Core testing method to assess nonlinear shear-sliding behaviour of brick-mortar interfaces: A comparative experimental study. *Construction and Building Materials*, *244*.

Jafari, S., Rots, J. G., & Esposito, R. (2022). A correlation study to support material characterisation of typical Dutch masonry structures. *Journal of Building Engineering*, *45*.

Karimi Ghaleh Jough, F., & Golhashem, M. (2020). Assessment of out-of-plane behavior of non-structural masonry walls using FE simulations. *Bulletin of Earthquake Engineering*, *18*(14), 6405-6427.

Lagomarsino, S., Penna, A., Galasco, A., & Cattari, S. (2013). TREMURI program: An equivalent frame model for the nonlinear seismic analysis of masonry buildings. *Engineering Structures*, *56*, 1787-1799.

Lawrence, S., & Marshall, R. (2000). *Virtual work design method for masonry panels under lateral load*. 12th International brick/block masonry conference, Madrid, Spain.

Lawrence, S. J. (1983). *Behavior of brick masonry walls under lateral loading* (Publication Number 1) (PhD thesis), University of New South Wales. Sydney, Australia.

Leonetti, L., Greco, F., Trovalusci, P., Luciano, R., & Masiani, R. (2018). A multiscale damage analysis of periodic composites using a couple-stress/Cauchy multidomain model: Application to masonry structures. *Composites Part B: Engineering*, *141*, 50-59.

Li, J., Masia, M. J., & Stewart, M. G. (2016). Stochastic spatial modelling of material properties and structural strength of unreinforced masonry in two-way bending. *Structure and Infrastructure Engineering*, *13*(6), 683-695.

Li, J., Masia, M. J., Stewart, M. G., & Lawrence, S. J. (2014). Spatial variability and stochastic strength prediction of unreinforced masonry walls in vertical bending. *Engineering Structures*, *59*, 787-797.

Liberatore, L., & AlShawa, O. (2021). On the application of the yield-line method to masonry infills subjected to combined in-plane and out-of-plane loads. *Structures*, *32*, 1287-1301.

Liberatore, L., AlShawa, O., Marson, C., Pasca, M., & Sorrentino, L. (2020). Out-of-plane capacity equations for masonry infill walls accounting for openings and boundary conditions. *Engineering Structures*, *207*.

Liu, Z., & Crewe, A. (2020). Effects of size and position of openings on in-plane capacity of unreinforced masonry walls. *Bulletin of Earthquake Engineering*, *18*(10), 4783-4812.

Lourenco, P. B., Rots, J., & Blaauwendraad, J. (1998). Continuum model for masonry parameter estimation and validation. *Journal of Structural Engineering-Asce*, *124*(6), 642-652.

Lourenco, P. B., & Rots, J. G. (1997). Multisurface interface model for the analysis of masonry structures. *Journal of Structural Engineering-Asce*, *123*(7), 660-668.

Malomo, D., & DeJong, M. J. (2021). A Macro-Distinct Element Model (M-DEM) for simulating the in-plane cyclic behavior of URM structures. *Engineering Structures*, *227*.

Malomo, D., DeJong, M. J., & Penna, A. (2019). Influence of Bond Pattern on the in-plane Behavior of URM Piers. *International Journal of Architectural Heritage*, 1-20.

Malomo, D., Pinho, R., & Penna, A. (2018). Using the applied element method for modelling calcium silicate brick masonry subjected to in-plane cyclic loading. *Earthquake Engineering & Structural Dynamics*, *47*(7), 1610-1630.

Malomo, D., Pinho, R., & Penna, A. (2020). Numerical modelling of the out-of-plane response of full-scale brick masonry prototypes subjected to incremental dynamic shake-table tests. *Engineering Structures*, *209*.

Marfia, S., & Sacco, E. (2012). Multiscale damage contact-friction model for periodic masonry walls. *Computer methods in applied mechanics and engineering*, *205-208*, 189-203.

Messali, F., Esposito, R., Ravenshorst, G. J. P., & Rots, J. G. (2020). Experimental investigation of the in-plane cyclic behaviour of calcium silicate brick masonry walls. *Bulletin of Earthquake Engineering*, *18*(8), 3963-3994.

Messali, F., Ravenshorst, G., Esposito, R., & Rots, J. G. (2017). Large-scale testing program for the seismic characterization of Dutch masonry walls. Proceedings of the 16th European Conference on Earthquake Engineering, 16WCEE, Santiago, Chile.

Miglietta, M., Damiani, N., Guerrini, G., & Graziotti, F. (2021). Full-scale shake-table tests on two unreinforced masonry cavity-wall buildings: effect of an innovative timber retrofit. *Bulletin of Earthquake Engineering*, *19*(6), 2561-2596.

Milani, G., & Lourenço, P. B. (2013a). Simple Homogenized Model for the Nonlinear Analysis of FRP-Strengthened Masonry Structures. I: Theory. *Journal of Engineering Mechanics*, *139*(1), 59-76.

Milani, G., & Lourenço, P. B. (2013b). Simple Homogenized Model for the Nonlinear Analysis of FRP-Strengthened Masonry Structures. II: Structural Applications. *Journal of Engineering Mechanics*, *139*(1), 77-93.

Milani, G., Lourenco, P. B., & Tralli, A. (2006). Homogenization Approach for the Limit Analysis of Out-of-Plane Loaded Masonry Walls. *Journal of Structural Engineering-Asce*, *132*, 1650-1663.

Mojsilović, N. (2011). Strength of masonry subjected to in-plane loading: A contribution. *International Journal of Solids and Structures*, *48*(6), 865-873.

Moon, L., Dizhur, D., Senaldi, I., Derakhshan, H., Griffith, M., Magenes, G., & Ingham, J. (2014). The Demise of the URM Building Stock in Christchurch during the 2010–2011 Canterbury Earthquake Sequence. *Earthquake Spectra*, *30*(1), 253-276.

Morandi, P., Albanesi, L., Graziotti, F., Li Piani, T., Penna, A., & Magenes, G. (2018). Development of a dataset on the in-plane experimental response of URM piers with bricks and blocks. *Construction and Building Materials*, *190*, 593-611.

Nasiri, E., & Liu, Y. (2019). The out-of-plane behaviour of concrete masonry infills bounded by reinforced concrete frames. *Engineering Structures*, *184*, 406-420.

NEN. (2018). *NEN-EN 1996-1-1 National Annex to Eurocode 6*.

Ng, C. L. (1996). *Experimental and theoretical investigation of the behaviour of brickwork cladding panel subjected to lateral loading* (PhD thesis), University of Edinburgh. Edinburgh, UK.

Nie, Y., Sheikh, A., Griffith, M., & Visintin, P. (2022). A damage-plasticity based interface model for simulating in-plane/out-of-plane response of masonry structural panels. *Computers & Structures*, *260*.

Noor-E-Khuda, S., Dhanasekar, M., & Thambiratnam, D. P. (2016). An explicit finite element modelling method for masonry walls under out-of-plane loading. *Engineering Structures*, *113*, 103-120.

NPR9998. (2018). *NPR 9998 - Beoordeling van de constructieve veiligheid van een gebouw bij nieuwbouw, verbouw en afkeuren*.

Padalu, P. K. V. R., Singh, Y., & Das, S. (2020a). Analytical modelling of out-of-plane flexural response of unreinforced and strengthened masonry walls. *Engineering Structures*, *218*.

Padalu, P. K. V. R., Singh, Y., & Das, S. (2020b). Cyclic two-way out-of-plane testing of unreinforced masonry walls retrofitted using composite materials. *Construction and Building Materials*, *238*.

Penna, A., Morandi, P., Rota, M., Manzini, C. F., da Porto, F., & Magenes, G. (2014). Performance of masonry buildings during the Emilia 2012 earthquake. *Bulletin of Earthquake Engineering*, *12*(5), 2255-2273.

Pereira, J. M., Correia, A. A., & Lourenço, P. B. (2021). In-plane behaviour of rubble stone masonry walls: Experimental, numerical and analytical approach. *Construction and Building Materials*, *271*.

Ravenshorst, G. J. P., & Messali, F. (2016). *C31B60: Out-of-plane tests on replicated masonry walls*. Delft, the Netherlands.

Rots, J. G. (1988). *Computational modeling of concrete fracture* (PhD thesis), Delft University of Technology. Delft, the Netherlands.

Rots, J. G., van der Pluijm, R., Vermeltfoort, A. T., & Janssen, H. J. M. (1997). *Structural Masonry - An experimental/numerical basis for practical design rules*. A.A.Balkema.

SAI. (2018). *Australian standard for masonry structures (AS 3700:2018)*. Standards Australia Limited. Sydney, Australia.

Sharma, S., Graziotti, F., & Magenes, G. (2021). Torsional shear strength of unreinforced brick masonry bed joints. *Construction and Building Materials*, *275*.

Sharma, S., Tomassetti, U., Grottoli, L., & Graziotti, F. (2020). Two-way bending experimental response of URM walls subjected to combined horizontal and vertical seismic excitation. *Engineering Structures*, *219*.

Sinha, B. P. (1978). Simplified ultimate load analysis of laterally loaded model orthotropic brickwork panels of low tensile strength [Article]. *Struct Eng Part B*, *56 B*(4), 81-84.

Sorrentino, L., D'Ayala, D., de Felice, G., Griffith, M. C., Lagomarsino, S., & Magenes, G. (2016). Review of Out-of-Plane Seismic Assessment Techniques Applied To Existing Masonry Buildings. *International Journal of Architectural Heritage*, 1-20.

Sousamli, M., Messali, F., & Rots, J. G. (2022). A total-strain based orthotropic continuum model for the cyclic nonlinear behavior of unreinforced brick masonry structures. *International Journal for Numerical Methods in Engineering*, *123*(8), 1813-1840.

Southcombe, C., & Tapp, A. (1988). Investigation of laterally loaded brickwork panels with openings. *Masonry(2) Stoke-on-Trent, 1988*, 112-114.

Standard, B. (2005). *BS 5628-1: 2005* (Vol. 1).

Tapp, A. (1985). *An investigate of laterally loaded fenestrated masonry panels (Master thesis)* Polytechnic South West. Plymouth, UK.

Tomassetti, U., Graziotti, F., Penna, A., & Magenes, G. (2018). Modelling one-way out-of-plane response of single-leaf and cavity walls. *Engineering Structures*, *167*, 241-255.

Vaculik, J. (2012). *Unreinforced masonry walls subjected to out-of-plane seismic actions* (PhD thesis), University of Adelaide. Adelaide, Australia.

Vaculik, J., & Griffith, M. C. (2017a). Out-of-plane load–displacement model for two-way spanning masonry walls. *Engineering Structures*, *141*, 328-343.

Vaculik, J., & Griffith, M. C. (2017b). Out-of-plane shaketable testing of unreinforced masonry walls in two-way bending. *Bulletin of Earthquake Engineering*, *16*(7), 2839-2876.

van der Pluijm, R. (1999a). *Out-of-plane bending of masonry behaviour and strength* (PhD thesis), Eindhoven University of Technology. Eindhoven, Netherland.

van der Pluijm, R. (1999b). *Report TUE-BCO_9903: Test on laterally loaded clay brick panels*. Eindhoven, the Netherlands.

van der Pluijm, R. (2001). *2001-CON-BM-R5015: Laterally Loaded Masonry Panels made with Thin Layer Mortar*. Delft, the Netherlands.

van der Pluijm, R., Rutten, H., & Ceelen, M. (2000). Shear Behaviour of Bed Joints. 12th International Brick/Block Masonry Conference, Madrid, Spain.

Walsh, K. Q., Dizhur, D. Y., Almesfer, N., Cummuskey, P. A., Cousins, J., Derakhshan, H., Griffith, M. C., & Ingham, J. M. (2014). Geometric characterisation and out-of-plane seismic stability of low-rise unreinforced brick masonry buildings in Auckland, New Zealand. *Bulletin of the New Zealand Society for Earthquake Engineering*, *47*(2).

Walsh, K. Q., Dizhur, D. Y., Shafaei, J., Derakhshan, H., & Ingham, J. M. (2015). In Situ Out-of-Plane Testing of Unreinforced Masonry Cavity Walls in as-Built and Improved Conditions. *Structures*, *3*, 187-199.

West, H. W. H., Hodgkinson, H. R., & Haseltine, B. A. (1977). The resistance of brickwork to lateral loading, Part 1: Experimental methods and results of tests on small specimens and full sized walls. *The Structural Engineer*, *55*(10), 411-421.

West, H. W. H., Hodgkinson, H. R., Haseltine, B. A., & de Vekey, R. C. (1986). The resistance of masonry to lateral loading, Part 2: Research results on

brickwork and aggregate blockwork since 1977. *The Structural Engineer*, *64*(11), 320-331.

Willis, C. (2004). *Design of Unreinforced Masonry Walls for Out-of-plane Loading* (PhD thesis), The University of Adelaide. Adelaide, Australia.

Willis, C., Griffith, M., & Lawrence, S. (2004). Horizontal bending of unreinforced clay brick masonry. *Masonry international*, *17*(3).

Willis, C. R., Griffith, M. C., & Lawrence, S. J. (2006). Moment Capacities of Unreinforced Masonry Sections in Bending. *Australian Journal of Structural Engineering*, *6*(2), 133-146.

Xu, H., Gentilini, C., Yu, Z., Wu, H., & Zhao, S. (2018). A unified model for the seismic analysis of brick masonry structures. *Construction and Building Materials*, *184*, 733-751.

Yekrangnia, M., & Asteris, P. G. (2020). Multi-strut macro-model for masonry infilled frames with openings. *Journal of Building Engineering*, *32*.

Zeng, B., Li, Y., & Cruz Noguez, C. (2021). Modeling and parameter importance investigation for simulating in-plane and out-of-plane behaviors of un-reinforced masonry walls. *Engineering Structures*, *248*.

Zhou, Y., Sluijs, L. J., & Esposito, R. (2022). *A microporomechanical model to predict nonlinear material behavior of masonry*. Computational Modelling of Concrete and Concrete Structures, Vienna, Austria.

Zhou, Y., Sluys, L. J., & Esposito, R. (2022). An improved mean-field homogenization model for the three-dimensional elastic properties of masonry. *European Journal of Mechanics - A/Solids*, *96*.

Acknowledgements

I would like to express my warmest gratitude to my promotor Prof. Jan Rots who inspired, encouraged and generously supported me. I am deeply indebted to my daily supervisor Dr Rita Esposito for her patient guidance and selfless help during the whole PhD study. Besides, I would like to appreciate Prof. Karin Lundgren, Prof. Jelke Dijkstra and Prof. Mario Plos for offering me the postdoc position at the Chalmers University of Technology.

My sincere appreciation goes to my lovely officemates Dr Xi Li, Dr Yi Xia, Dr Samira Jafari, Niels Kostense and Dr Satya Sharma. Thanks for the relaxing and pleasant coffee breaks, and for not hating me for putting up a huge but not that pretty poster on the wall. My fantastic next-door-officemates Alfonso Prosperi, Belen Gaggero and Dr Manimaran Pari must be acknowledged here for their perpetual enthusiasm for proposing a beer, their amazing Gangnam Style dance and twisted love for singing Cornutone. Thanks also go to my kind and supportive colleagues Dr Francesco Messali, Dr Anjali Mehrotra, Michele Longo, Dr Michele Mirra, Onur Arslan, Amirhossein Ghezelbash, Paul Korswagen Eguren, Jaap Meijer and Iris Nederhof-van Woggelum.

In particular, I am grateful to Marianthi Sousamli for the music, movies and books she shared, and the talks and debates we had. Thank you for listening to my stories about struggling and helping me to know myself better.

This adventure would not reach its end if the following guys had not appeared: Rui Yan, Dr Huan Wang, Yuxuan Feng, Dr Xiangcou Zheng, Qin Qin, Biyue Wang, Dr Hongpeng Zhou, Dr Chenjie Yu, Quanxin Jiang, Yubao Zhou, Zhaoying Ding, Ren'an Gong, Jun Xu, Fanxiang Xu, Zhe Han, Lu Cheng, Ze Chang. You are reliable friends from whom I learnt a lot not only about research but also life. Thanks for the beers, parties and trips. To those who are still struggling with their PhD studies, I wish you a successful ending. Cheer up, you can achieve that.

In addition, thanks go to the following inspiring and kind friends: Dr Xiao Guo, Dr Yu Chen, Minfei Liang, Dr Fengqiao Zhang, Xiuli Wang, Pei He, Xinyue Chang, Dr Tiantian Du, Mingyan Fu, Dr Yifan Fu, Tianlong Jia, Mengmeng Gao, Dr Yunlong Guo, Min Jiang, Dengxiao Lang, Dr Na Li, Dr Xiao Lin, Cheng Liu, Dr Maolong Lv, Dr Xiaocong Lv, Dr Meng Meng, Dr Wenting Ma, Dr Wang Pan, Dr Kailun Zhu, Fenghua Wang, Dr Guishan Wang, Dr He Wang, Kailan Wu, Jinbao Xie, Jing Xu, Dr Jincheng Yang, Xinling Yue, Dr Hao Yu, Aoxi Zhang, Dr Dadi Zhang, Haoxiang Zhang, Jin Yan.

Xinrui, thanks for being part of my life. With you, for the first time, giving makes me happier than taking. Without you, I would never know being intertwined with another soul can be so wonderful. Our promise was witnessed by the full moon on summer nights. She told me, gently and firmly, that we two together will have a marvellous journey.

At last, I would like to express my deepest love to my parents. Thanks for bringing me to this beautiful world. For years I have been floating away from you, away from home. But like every wave goes back to the ocean, I will be back in your embrace.

List of Publications

Journal publication

1. **Chang, L.-Z.**, Rots, J. G., & Esposito, R. (2022). Influence of openings on two-way bending capacity of unreinforced masonry walls. Journal of Building Engineering, 51.
2. **Chang, L.-Z.**, Rots, J. G., & Esposito, R. (2021). Influence of aspect ratio and pre-compression on force capacity of unreinforced masonry walls in out-of-plane two-way bending. Engineering Structures, 249.
3. **Chang, L.-Z.**, Messali, F., & Esposito, R. (2020). Capacity of unreinforced masonry walls in out-of-plane two-way bending: A review of analytical formulations. Structures, 28, 2431-2447.

Conference publication

1. **Chang, L.-Z.**, Rots, J., & Esposito, R. (2020). Numerical modelling of two-way out-of-plane bending tests on URM walls: The influence of lateral boundary conditions. 17th International Brick and Block Masonry Conference -From Historical to Sustainable Masonry, Krakow, Poland.

Curriculum Vitae

Personal information

Name	Langzi Chang
Email	L.Chang-2@tudelft.nl;
	langzichang@gmail.com
Date of birth	January 26th, 1992
Birthplace	Boli County, Heilongjiang Province, China
Nationality	Chinese

Education

Jul 2018 - present	PhD candidate
	Faculty of Geosciences and Civil Engineering,
	Delft University of Technology, Delft, The Netherlands
Sep 2015 – Dec 2017	Master of Civil Engineering
	Faculty of Civil Engineering,
	Harbin Institute of Technology, Harbin, China
Apr 2016 – Sep 2016	Visiting researcher
	Faculty of Civil Engineering
	Hokkaido University, Sapporo, Japan
Sep 2011 – Jun 2015	Bachelor of Civil Engineering
	Faculty of Civil Engineering,
	Harbin Institute of Technology, Harbin, China